RESPONSE OF COMPOSITE LAMINATES UNDER OUT-OF-PLANE LOADING

Ahmed Wagih Abdallah Abdel Hady

Doctoral Thesis

Response of composite laminates under out-of-plane loading

Ahmed Wagih Abdallah Abdel Hady

2018

Universitat de Girona

Doctoral Thesis

Response of composite laminates under out-of-plane loading

Ahmed Wagih Abdallah Abdel Hady

2018

Doctoral Program in Technology

Advisors:

Dr. Norbert Blanco Villaverde
Universitat de Girona, Spain

Dr. Pere Maimí Vert
Universitat de Girona, Spain

Thesis submitted to the University of Girona for the degree of Doctor of Philosophy

Ahmed Wagih Abdallah Abdel Hady

Response of composite laminates under out-of-plane loading

Doctoral Thesis, 2018
Doctoral Program in Technology
Supervisors: Dr. Norbert Blanco and Dr. Pere Maimí

University of Girona
AMADE Research Group
Dept. of Mechanical Engineering and Industrial Construction
Department of Mechanical Engineering and Industrial Construction
Carrer Universitat de Girona, 4
17003, and Girona

To whom it might concern,

Dr. Norbert Blanco Villaverde and Dr. Pere Maimí Vert, Associate Professors at the the Department of *Enginyeria Mecànica i de la Construcció Industrial* of *Universitat de Girona*

CERTIFY that the study entitled *Response of composite laminates under out-of-plane loading* has been carried out under their supervision by Ahmed Wagih Abdallah Abdel hady to apply for the doctoral degree with the International mention. We also certify that Ahmed Wagih Abdallah Abdel hady was a full time graduate student at Universitat de Girona, Girona, Spain, from September 2015 to present.

Girona, April 2018,

Dr. Norbert Blanco Villaverde
Universitat de Girona, Spain

Dr. Pere Maimí Vert
Universitat de Girona, Spain

IN THE NAME OF ALLAH

To my dear family

"*Genius is one percent inspiration, ninety-nine percent perspiration.*" **Thomas Edison**
- Spoken statement (1903); published in Harper's Monthly (September 1932).

Acknowledgement

I would like to express my gratitude to my advisors, Dr. Pere Maimí and Dr. Norbert Blanco, for the indefatigable help and for the key contributions that have allowed the development of the present thesis.

I would like to thank also Prof. Josep Costa, Dr. Albert Turon, Dr. Dani Trias and Dr. Emilio González, who spent a lot of time revising parts of the present thesis. Of course, I am grateful to all members of the research group AMADE at Universitat de Girona for the help and nice moments that I have received from each one.

I have to do a special mention to my friends at FEUP and INEGI in University of Porto for their help during my research stay. I am also grateful to Prof. Pedro Camanho for his support and making the research stay much more easier and useful.

I would also like to thank my family for the support they provided me through my entire life and in particular, I must acknowledge my parents, my brothers, my wife and my lovely daughter Mariam for their support and being without me for a long time throughout my stay in Girona.

In addition, I would like also to thank my friends Dr. Abdallah Kabeel, Dr. Tamer Sebaey, Mohammed Emara and Mohammed Moawad for their support. For sure I cannot forget the help and support by my professors and colleagues in Zagazig University, Egypt.

Funding

The period of this research has been funded by the Universidad de Girona under a research grant IF-UDG, started in October of 2015 until present.

Also, the present work has been partially funded by the Spanish Government (Ministerio de Economía y Competitividad), the European Union under contracts DPI2012-34465, MAT2013-46749-R and MAT2015-69491-C3-1-R, and by the financial support of ERANet AirTN 01/2012 under the project entitled "Damage tolerance for thin ply textile composites(DAMTEX)".

Part of the work has been carried out during a three months research stay at the University of Porto, under the UdG mobility grant (MOB2016), between February and May 2017.

Publications

The scientific contributions outcome of this thesis are listed below:

- Journal publications

  Published Papers

  1. **Wagih A**, Maimí P, Blanco N, Costa J. A quasi-static indentation test to elucidate the sequence of damage events in low velocity impacts on composite laminates. *Composite Part A: Applied Science and Manufacturing*, 2016; 82: 180-189.

  2. **Wagih A**, Maimí P, González E, Blanco N, de Aja JS, de la Escalera F, Olsson R, Alvarez E. Damage sequence in thin-ply composite laminates under out-of-plane loading. *Composite Part A: Applied Science and Manufacturing*, 2016; 87: 66-77.

  3. **Wagih A**, Maimí P, Blanco N, Trias D. Predictive model for the spherical indentation of composite laminates with finite thickness. *Composite Structures*, 2016; 153:468-477.

  Papers in processing

  4. **A. Wagih**, P. Maimí, N. Blanco, E.V. González. Scaling effects of composite laminates under out-of-plane loading.

  5. **A. Wagih**, P. Maimí, R.P. Issac, A. Turon, N. Blanco, S. M. García-Rodríguez, G. Guillamet, J. Costa. Improving damage resistance and load capacity of thin-ply laminates using ply clustering and small mismatch angles.

- Conference communications

  6. **A. Wagih**, P. Maimí, N. Blanco. Damage scenario of CFRP composite laminates under Quasi-Static Indentation loading. 7th International conference on Composite Testing and Model Identification (Comptest 2015), Madrid, Spain, 7-10th April 2015.

  7. **A. Wagih**, P. Maimí, E.V. González, N. Blanco, J.R. Sainz de Aja, F.M. de la Escalera. Damage sequence in thin-and Ultra-thin-ply composite laminates under out-of-plane loading. 17th European Conference on Composite Materials (ECCM17), Munich, Germany, 26-30th June 2016.

  8. **A. Wagih**, P. Maimí, A. Turon, N. Blanco, R. P. Issac, G. Guillamet, J. Costa. Experimental study on the damage sequence in Non-Crimp-Fabric composite laminates under out-of-plane loading. 8th International con-

ference on Composite Testing and Model Identification (Comptest 2017), Leuven, Belguim, 5-7th April 2017.

List of Figures

List of Tables

Contents

Abstract

The use of composite laminates by the aeronautic industry has increased significantly in the last years. The use of these materials by the largest civil aircraft companies is a real example of this increase. Additionally, the automotive industry has recently started to use this type of material in the structure of the new generation of electric cars to reduce their weight and, therefore, energy consumption. Among the different types of composite materials, carbon fiber reinforced polymers (CFRP), especially those with epoxy matrix, are the most common composite laminates due to their high specific properties like high stiffness or strength to weight ratios. In spite of these advantages, one of the main disadvantages of these materials is the low resistance against impact, which may affect their load capacity performance.

The impacted parts, i.e, airplane body, should be transferred to laboratories to be inspected and evaluate the generated damage, which is really a time and money consuming process. However, the inspection process of the impacted parts can be eliminated, if a reliable scaling tool is available to predict the damage inside the real impacted parts by testing a small coupon in the laboratory.

Hence, the main objective of the thesis is to provide a reliable scaling tool to predict the response of composite structures under out-of-plane loading by testing small coupons. This global objective cannot be achieved without understanding the damage mechanisms and their sequences in composite laminates under out-of-plane loading. The main objective of the thesis has been achieved by considering three different sub-objectives. The first sub-objective is focusing on understanding the damage mechanisms and their sequences in composite laminates made of different ply thicknesses. The damage mechanisms are almost the same for the different ply thicknesses considered. However, the interaction between the damage mechanisms changes by changing the ply thickness.

The second sub-objective focuses on understanding the influence of the laminate design parameters, mismatch angle between plies and ply thickness, on the response of composite laminates under out-of-plane loading. To achieve this sub-objective, a wide range of mismatch angles between plies and also different ply thicknesses are considered. The results of this part show that the maximum load capacity of

the laminate can be increased by using small mismatch angle between plies or thick-plies. However, the damage initiation can be delayed by using large mismatch angle between plies or thin-plies. The mismatch angle has no influence on the damage resistance (projected delamination area). However, the ply thickness has a significant effect on the damage resistance. Before the fiber failure, the thinner the plies are, the lower the projected delamination area is. These observations are used to design a laminate with improved damage resistance and improved load capacity by manufacturing a thin-ply laminate using small mismatch angles between plies and thick plies in the upper part of the laminate.

In the third sub-objective, the contact problem of a stiff spherical indenter with a composite plate was simulated with a 2D axisymmetric model implemented on a commercial software. A parametric study was carried out numerically to study the effect of the different parameters on the force-indentation response. The results show that the indentation response of an orthotropic laminate is material independent and that it strongly depends on the laminate thickness. The lamina thickness has no significant effect on the force-indentation relation. Also, the specimen in-plane size has no effect on the indentation depth. Two simple equations were derived by normalizing and fitting FE results to predict the response of an orthotropic laminate of finite thickness in contact with stiff spherical indenter supported on two different boundary conditions (fully and hollow supported). The predictions of the derived equations were compared with experimental results and the available analytical models in the literature. The presented equations show an excellent correlation with the experimental investigations.

Finally, the scaling tool to predict the response of composite structures under out-of-plane loading is implemented in two steps. First, an analytical model is proposed to predict the quasi-static indentation response during the elastic and delamination regime up to fiber failure. The model is able to predict the load-displacement and the delamination area-displacement responses. Based on a linear relationship with respect to the applied displacement, the model is able to predict the delamination area up to fiber breakage in a good agreement with the experimental observations. Then, the effect of scaling the geometrical parameters such as in-plane dimension and shape, thickness of the laminate, thickness of the plies and indenter radius is taken into account. This scaling approach is developed based on the presented analytical model and the experimental results presented in this thesis and other experimental results available in the literature. As a result, it is possible to predict the response of large panels or composite structures by testing small coupons.

Resum

L'ús de laminats de material compost en la indústria aeronàutica s'ha vist incrementat significativament en els darrers anys. L'ús d'aquests materials per part de les majors companyies d'aviació civil n'és un clar exemple d'aquest increment. Darrerament també la industria ha començat a fer ús d'aquests materials en l'estructura de la nova generació de vehicles elèctrics a fi de reduir-ne el pes i, per tant, el consum energètic. Entre els diferents tipus de material compost, els polímers reforçats amb fibres de carboni (CFRP de l'anglès), sobretot els de matriu epoxi, són els més comunament emprats grècies a les seves elevades propietats específiques, com ara l'elevat rati entre el seu mòdul de rigidesa o resistència respecte el seu pes. Malgrat aquests avantatges, un dels principals desavantatges d'aquests tipus de materials és la seva baixa resistència a l'impacte, cosa que pot arribar a comprometre la seva capacitat de càrrega.

Les parts impactades, i.e., cos de l'aeronau, s'han d'enviar a laboratoris i tallers per tal de ser revisades i avaluar-ne el dany causat, el que comporta un procés car tant en diners com en temps. No obstant, el procés d'inspecció de les parts impactes pot ser eliminat si es pot comptar amb una eina d'escalat fiable per a la predicció del dany intern en parts reals impactades a través de l'assaig de petites provetes en el laboratori.

Així, el principal objectiu d'aquesta tesi és el d'aconseguir una eina d'escalat fiable per a predir la resposta d'estructures de compòsit sota càrregues fora del pla mitjançant l'assaig de petites provetes. Aquest objectiu global no es podria assolir sense comprendre els mecanismes de dany i la seva seqüència en els materials compostos laminats sota càrregues fora del pla. L'objectiu principal de la tesi s'ha assolit considerant tres sub-objectius diferents. El primer sub-objectiu es centra en comprendre els mecanismes de dany i la seva seqüència en laminats de material compost fets amb làmines de diferent gruix. Malgrat els mecanismes de dany són pràcticament els mateixos en tots els casos independentment del gruix de capa, la interacció entre aquests mecanismes sí que canvia segons el gruix de capa.

El segon sub-objectiu es centra en comprendre la influència dels paràmetres de disseny dels laminats, angle de desfasament entre capes i gruix de capa, en la

resposta de compòsits laminats a càrregues fora del pla. Per tal d'assolir aquest sub-objectiu s'ha dut a terme un estudi considerant un ampli rang d'angles de desfasament entre capes i també diferents gruixos de capa. Els resultats d'aquest estudi mostren que la capacitat de càrrega del laminat s'incrementa quan s'utilitzen angles de desfasament entre capes petits o làmines gruixudes. No obstant, la iniciació del dany es pot endarrerir emprant angles de desfasament entre capes grans o làmines amb gruixos petits. Si bé l'angle de desfasament no té influéncia sobre la resistència al dany (projecció de l'àrea delaminada), el gruix de capa sí que té un efecte significatiu sobre la resistència al dany del laminat. Abans de que aparegui el primer trencament de fibres, quan més petit sigui el gruix de capa, més petit serà la projecció de l'àrea delaminada. El resultat d'aquestes observacions permet dissenyar laminats a base de capes primes amb una resistència al dany i una capacitat de càrrega millorades usant angles de desfasament entre capes petits i capes gruixudes en la part superior del laminat.

En el tercer sub-objectiu es va simular el problema del contacte entre un indentador esfèric rígid i una placa de compòsit mitjançant un model axisimètric 2D implementat en un programari comercial. Es va dur a terme un anàlisi paramètric de forma numèrica per tal d'analitzar l'efecte dels diferents paràmetres en la resposta força-indentació. Els resultats mostren que la resposta a la indentació d'un laminat ortotròpic és independent del material però que depèn en gran mesura del gruix del laminat. El gruix de la làmina no té un efecte significatiu en la relació força-indentació. Igualment, la dimensió de la proveta en el pla tampoc té efecte sobre la profunditat d'aquesta indentació. Mitjançant la normalització i l'ajust dels resultats de les simulacions numèriques es va poder derivar dues equacions per predir la resposta d'un laminat ortotròpic de gruix finit en contacte amb un identador esfèric rígid sota dues condicions de contorn (completament suportat i suport buit). Les prediccions obtingudes amb aquestes equacions es van comparar amb resultats experimentals i les prediccions d'altres models analítics presents en la literatura. Les equacions presentades en aquest treball presenten una excel· lent correlació amb els resultats experimentals.

Finalment, l'eina d'escalat per a la predicció de la resposta d'estructures de material compost sota càrregues fora del pla s'implementa en dos passos. Primer es proposa un model analític per predir la resposta a la indentació quasi-estàtica en la part elàstica i de delaminació i fins a l'inici del trencament de fibres. Aquest model és capaç de predir la corba força-desplaçament. En base a una relació lineal amb el desplaçament aplicat, el model pot predir l'àrea delaminada fins a l'aparició de la ruptura de fibres amb bona concordança amb les observacions experimentals. Llavors, es considera l'efecte d'escalar els paràmetres geomètrics, com ara les dimensions en el pla i forma, el gruix del laminat, el gruix de capa i el radi de l'indentador. Aquest procés d'escalat es realitza en base als resultats presentats en aquesta tesi i d'altres resultats

experimentals disponibles en la literatura. En conseqüència, és possible predir la resposta de grans panells o estructures de compòsit mitjançant l'assaig experimental de petites provetes.

Resumen

El uso de laminados de material compuesto en la industria aeronáutica se ha incrementado significativamente en los últimos años. El uso de estos materiales por parte de las mayores compañías de aviación civil así lo demuestra. Últimamente también la industria del automóvil ha empezado a utilizar este tipo de materiales en la estructura de la nueva generación de vehículos eléctricos a fin de reducir peso y, por tanto, consumo energético. Entre los diferentes tipos de material compuesto, los polímeros reforzados con fibras de carbono (CFRP del inglés), sobretodo los de matriz epoxi, son los más comúnmente utilizados gracias a sus elevadas propiedades específicas, como por ejemplo el elevado ratio entre su módulo de rigidez o resistencia respecto a su peso. A pesar de estas ventajas, uno de los principales inconvenientes de este tipo de materiales es su baja resistencia al impacto, cosa que puede llegar a comprometer su capacidad de carga.

Las partes impactadas, i.e., cuerpo de la aeronave, deben ser enviadas a los laboratorios y talleres de reparación para ser revisadas y evaluar el daño causado, lo que comporta un proceso caro tanto en dinero como en tiempo. No obstante, el proceso de inspección de las partes impactadas puede ser eliminado si se puede contar con una herramienta de escalado fiable para la predicción del daño interno en partes reales impactadas a través del ensayo de pequeñas probetas en el laboratorio. Así, el principal objetivo de esta tesis es el de conseguir una herramienta de escalado fiable para la predicción de la respuesta de estructuras de compuesto bajo cargas fuera del plano mediante el ensayo de pequeñas probetas. Este objetivo global no se podría conseguir sin comprender los mecanismos de daño y su secuencia en materiales compuestos laminados bajo cargas fuera del plano. El objetivo principal de la tesis se ha conseguido considerando tres sub-objetivos distintos. El primer sub-objetivo se centra en comprender los mecanismos de daño y su secuencia en laminados de material compuesto fabricados con láminas de distinto espesor. A pesar de que los mecanismos de daño son prácticamente los mismos en todos los casos, independientemente del grosor de capa, la interacción entres estos mecanismos sí que varía según el grosor de capa.

El segundo sub-objetivo se centra en comprender la influencia de los parámetros de diseño de los laminados, ángulo de desfase entre capas y espesor de capa, en la respuesta de materiales compuestos laminados bajo cargas fuera del plano. A fin de conseguir este sub-objetivo se ha llevado a cabo un estudio considerando un amplio rango de ángulos de desfase entre capas y también diferentes espesores de capa. Los resultados de este estudio muestran que la capacidad de carga del laminado se incrementa cuando se utilizan ángulos de desfase entre capas pequeños o láminas gruesas. A pesar de ello, la iniciación del daño se puede retrasar utilizando ángulos de desfase entre capas grandes o láminas con espesores pequeños. Si bien el ángulo de desfase no tiene influencia sobre la resistencia al daño (proyección de la área delaminada), el grosor de capa sí que tiene un efecto significativo sobre la resistencia al daño del laminado. Antes de que aparezca la primera rotura de fibras, cuanto menor sea el grosor de capa, mayor será la proyección del área delaminada. El resultado de estas observaciones permite diseñar laminados a base de capas finas con una resistencia al daño y una capacidad de carga mejoradas utilizando ángulos de desfase entre capas pequeños y capas gruesas en la parte superior del laminado.

En el tercer sub-objetivo se simuló el problema del contacto entre un indentador esférico rígido y una placa de material compuesto mediante un modelo axisimétrico 2D implementado en un programa comercial. Se llevo a cabo un análisis paramétrico de forma numérica para poder analizar el efecto de los distintos parámetros en la respuesta fuerza-indentación. Los resultados muestran que la respuesta a la indentación de un laminado ortotrópico es independiente del material pero dependiente en gran medida del grosor del laminado. El grosor de lámina no tiene ningún efecto significativo en la relación fuerza-indentación. Igualmente, la dimensión de la probeta en el plano tampoco tiene efecto sobre la profundidad de esta indentación. Mediante la normalización y el ajuste de los resultados de las simulaciones numéricas se pudo derivar dos ecuaciones para predecir la respuesta de un laminado ortotrópico de grosor finito en contacto con un indentador esférico rígido bajo dos condiciones de contorno (completamente soportado y soporte hueco). Las predicciones obtenidas con estas ecuaciones se compararon con los resultados experimentales y las predicciones de otros modelos analíticos presentes en la literatura. Las ecuaciones presentadas en este trabajo presentan una excelente correlación con los resultados experimentales.

Finalmente, la herramienta de escalado para la predicción de la respuesta de estructuras de materiales compuestos bajo cargas fuera del plano se implementa en dos pasos. Primero se propone un modelo analítico para predecir la respuesta a la indentación cuasi-estática en la parte elástica y de delaminación y hasta el inicio del rompimiento de fibras. Este modelo es capaz de predecir la curva fuerza-desplazamiento. En base a una relación lineal con el desplazamiento aplicado, el modelo puede predecir el área delaminada hasta la aparición de la ruptura de fibras

con buena concordancia con las observaciones experimentales. Luego se considera el efecto de escalar los parámetros geométricos, como son las dimensiones en el plano y forma, el grosor del laminado, el grosor de capa y el radio del indentador. Este proceso de escalado se realiza en base a los resultados presentados en esta tesis y de otros resultados experimentales disponibles en la literatura. En consecuencia, es posible predecir la respuesta de grandes paneles o estructuras de material compuesto mediante el ensayo experimental de pequeñas probetas.

1 Introduction and objectives

1.1 Overview

A composite material can be defined as a combination of two or more materials that results in better properties than those of the individual components used alone. The two constituents are a reinforcement and a matrix. Composite materials can be classified based on the reinforcement type and the matrix type. Based on the reinforcement type, composites were classified into different categories such as particle reinforced, fiber reinforced and structural composites [1] as shown in Figure 1.1.

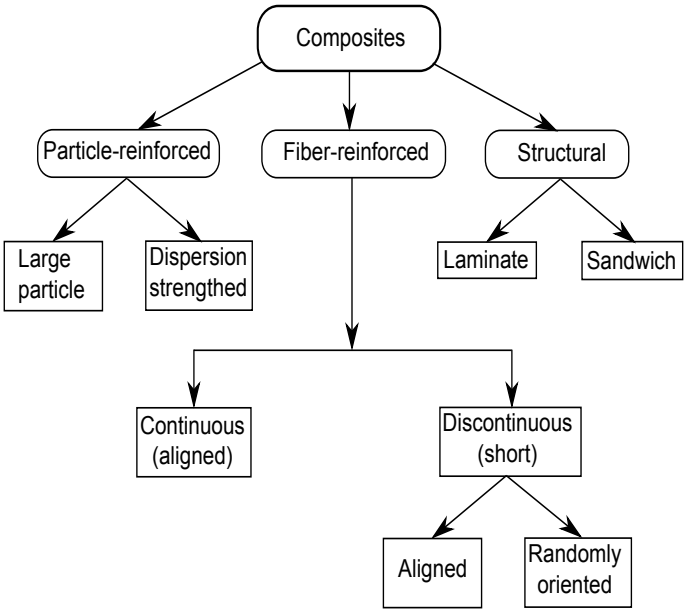

Fig. 1.1: Classification of composites [after [1]].

In all the kinds of composites, the applied load is transmitted and distributed to the reinforcement via the matrix phase. It is the control of the reinforcement geometry and distribution which are important parameters for high strength and stiffness to be attained. Particle-reinforced composites are composed of particles which have dimensions that are approximately equal in all directions. They may be spherical, platelets, or any other regular or irregular geometry. Particle composites tend to be much weaker and less stiff than continuous fiber composites, but they are usually much less expensive. In the particle reinforcement, it is not easy to obtain an excellent distribution of the reinforcement in the matrix phase which in

most cases negatively affects the final composite response. A fiber has a length that is much greater than its diameter. The length-to-diameter ratio is known as the aspect ratio and can vary greatly. Continuous fibers have long aspect ratios, while discontinuous fibers can have short aspect ratios. Continuous-fiber composites normally have a preferred orientation, while discontinuous fibers generally have a random orientation. Examples of continuous reinforcements include unidirectional, woven cloth and helical winding, while examples of discontinuous reinforcements are chopped fibers and random mat. In the fiber reinforced matrix, it is much easier to obtain uniform distribution of the fibers in the matrix especially for continues fibers. Structural composites are composed of several plies which must be stacked together with different fiber orientations to form a laminate. In the structural composites, the control of the strength and stiffness can be achieved not only by the reinforcement volume ratio but also, by changing the staking sequence of the plies or changing the mismatch angle between the adjacent plies or changing the ply thickness. For this reason, structural composites have been paid attention in the industrial applications.

The matrix phase, in most cases, provides some ductility to the final composites. The most typical common matrix is polymers to produce Polymeric Matrix Composite (PMC), metals to produce Metal Matrix Composite (MMC), and ceramics to form Ceramic Matrix Composite (CMC).

This thesis, focuses on a small area of composite materials in which the PMC is reinforced by long fibers using for example Glass Fiber Reinforced Epoxy (GFRP) or Carbon Fiber Reinforced Epoxy (CFRP). This kind of materials can be manufactured in the form of laminates (composite laminates); which consists of two or more plies stacked together, where each one has the reinforcement oriented at a given direction. The orientation of each ply is changed suitably in order to stand the mechanical design requests.

There are several methods of manufacturing composite laminates that are widely used in aerospace industry including spray-up, filament winding, autoclave curing, pultrusion and vacuum assisted resin transfer moulding. The decision of choosing one of these methods is taken according to the project requirement such as low cost, mass production, high quality of the product, the complexity of the laminates and also, the most important for structural applications, final mechanical properties. The choice between these methods was discussed in several papers in the literature [1–4].

CFRP composites are one of the most widely used composites in aerospace structures, including military and commercial aircraft, due to their high specific properties like high stiffness or strength to weight ratios and good fatigue tolerance [2, 5, 6]. Despite these advantages, externally exposed airframe structures are prone to

damage caused by impacts such as tool drops or bird strikes, which may impair their load capacity performance [5]. Another source of impacts which is more likely to happen is the ground accidents. The aviation industry has acknowledged the risks associated with serious ground operation incidents and accidents. Consequences of these events result in aircraft damage, delays and financial direct and indirect cost to the industry. Direct costs are those related to the actual cost of repairing the damage and indirect costs include lost revenue, lost work time, disruption of the flight schedule and consequent negative customer feedback. In 2000, the Airports Council International reported that US$3 billion losses were caused by airport ground vehicles hitting aircraft, hitting each other or other objects around the airport [7]. Narrowing down the focus on aircraft damage during ground operations, it has been reported that 50% of the major damage was caused by baggage vehicles while 60% of the minor damage was caused by collision of aircraft with ground vehicles [8]. Figures 1.2 and 1.3 show some impact events on aircraft during ground operations. However, these high losses due to ground operations, this type of damage is not as dangerous as damage caused by tool drops or so, which cannot be detected from the outside but do compromise the integrity of the structure.

Fig. 1.2: Flock of birds strikes during aircraft take-off [9].

Studies on composite laminates under out-of-plane loading have been founded since the 1970s. For example, but not limited to, Cantwell et al. [11–16], Doyle et al. [17], Sankar et al. [18], Olsson et al. [19–21] have investigated the effects of impact events on composite laminates. One of the conclusions of these studies is that the residual tensile and compressive strengths of composite laminates are influenced by the damage area and the different damage mechanisms induced by this impact. Olsson [19] investigated the effect of large and small mass impactors and observed that the large mass impactor generated a quasi-static response, whereas a small mass impact response was wave controlled which generate a dynamic response. Later, Olsson [20] and Yigit and Christoforou [22] suggested a criteria for classifying low and high velocity impacts. For low velocity impacts, the impact response is governed

Fig. 1.3: Ground service vehicle impacts [10].

by impactor/plate mass ratio rather than the impact velocity while for higher impact velocities, the short impact time results in a response governed by wave propagation phenomena. All these studies have illustrated that the impact response is a complex phenomenon even in isotropic materials. This phenomenon depends on a large number of parameters such as: the nature and the characteristics of the impactor and the structure, contact time, impactor velocity, thickness, wave propagation, etc. Furthermore, composite variables such as: lay-up, fiber volume fraction, geometry of the specimen, mismatch angle between plies, etc. have a significant influence on the damage formation and propagation.

The work done in this thesis focuses on the elastic response and damage evolution in composite laminates under low velocity impacts and quasi static indentation test. Ballistic impact, a low mass high velocity impact, is beyond the scope of this thesis.

1.2 Motivation

As shown in the previous section, externally exposed airframe structures are prone to damage caused by impacts. As reported by Pringle [7], large mass impacts, i.e. ground operation incidents and accidents, causes billions dollars of losses for aircraft companies. This kind of damage can be easily detected and repaired accordingly, even if expensive. However, smaller impacts, such as caused by tool drops, cannot be detected easily and generate internal damage which is difficult to be inspected in the working site. Hence, the impacted parts should be transferred to laboratories to be inspected against impact which is really time and money consuming process. The inspection process of the impacted parts can be eliminated, if a reliable scaling tool is available to predict the damage inside the real impacted parts by testing a small coupon in the laboratory. Implementing a reliable scaling tool cannot be achieved without the understanding of the response of composite laminates under

impact loading. For this reason, a large number of studies on this field were done during the last two decades. These studies basically deal with the effect of different parameters on the response of composite laminates under impact loads. However, a limited number of studies were found to deal with the understanding of the damage behaviour during the impact event.

There are several models available in the literature that enable predicting the response of composite laminates under impact loads. Finite element based models are accurate and can handel complex geometries. However, they are computationally expensive and very time consuming which makes them not suitable for the industry where the results must be obtained quickly. Experimental work is reliable but it is also very expensive, time consuming and complicated due to the dynamic effects. On the other hand, it is well known that the analytical models have the privilege over the other models for their ability to predict the behavior of a structure in a few minutes. However, the results of the analytical models are not accurate enough to be applicable in the industry. So, it is important to find a low cost and reliable tool to predict the response of composite laminate under out-of-plane loading with good accuracy. In order to deal with this demand, better understanding for the different damage mechanisms and their sequence during an impact event is mandatory. This better understanding indirectly reflects a better design of laminates with high damage tolerance and lower weight which is the main demand of aeronautics industry. Also, this better understanding might help for developing a reliable scaling approach to obtain the response of large composite laminate or real structure in the industry subjected to out-of-plane loading by testing a small coupon in the laboratory.

Composite laminates can be found in many applications; in which contact stresses can be found between two composite laminates. For example, contact between a composite fan blade and its disc, or in rotating components such as ball bearings against a composite housing, or in applications in which a composite plate slides between a pair of rollers. Many such cases involve a composite laminate in contact with other surfaces, and they can be idealised as a contact problem between a stiff indenter and a composite plate of finite thickness. There are several analytical models available in the literature that enable the prediction of the elastic response of a composite laminate in contact with stiff indenter. However, the accuracy of these models are not enough to be applicable in the industry. Also, there are finite element based models which can predict the response with a good accuracy but they are computationally expensive. So, a try to develop a closed form solution which will be able to predict the elastic response of composite laminate of finite thickness in contact with stiff indenter in short time with a good accuracy is valuable for industry.

1.3 Objectives

Based on the proposed motivations, the main objective for this thesis is to implement a reliable scaling tool for predicting the response of large structure composite laminates under out-of-plane loading by testing a small coupon in the laboratory. In the way to achieve this global objective, three sub-objectives need to be accomplished.

The first sub-objective focuses on understanding the damage mechanisms and their sequence during impact event on composite laminates with different ply thicknesses. A step loading Quasi-Static Indentation (QSI) test on a quasi-isotropic laminate with a typical ply thickness is used in this study. After each step, the test is stopped and specimens are unloaded and analyzed by means of Scan Electron Microscope (SEM), Optical Microscope (OM) or Computed Tomography (CT) to investigate the damage generated in the material. A non-destructive ultrasonic inspection technique (C-scan) was used to capture the different delamination areas and their through the-thickness position in the laminate. The indentation depth of the tested specimens was measured after different periods of the tests to study the relaxation of the material after the test.

Recently, the application of thinner plies has shown better properties than the thicker ones such as: unnotched tensile strength, bearing strength and compression after impact strength which highlight its importance and probability to be applicable in the aeronautic industry. The response of this kind of laminates under low velocity impact is still not well understood and the experimental results which explain the damage evolution and its sequence are rare. Therefore, the same procedure was used to understand the damage sequence in the thin-ply laminates under impact event. Two laminates with two different ply thicknesses are considered to study the effect of ply thickness on the damage sequence. Moreover, the damage sequence is studied in three different materials, AS4D/8852, Tenax/RTM6 TeXtrem thin-plies and T700GC/M21 NCF thin-plies, which are applicable in many applications.

There is large number of parameters affecting the impact response, i.e; impactor size, ply clustering, mismatch angle between plies, specimen in-plane dimension, etc. Understanding the influence of theses parameters is mandatory to provide a reliable scaling approach for this test. From this sense, the second sub-objective is to to understand the influence of mismatch angle and ply thickness on the impact response.

The third sub-objective is to derive a closed from solution to predict the indentation depth of composite laminates in contact with stiff spherical indenter which is of immense importance in many applications especially for determining the whole impact response. With this aim, the contact problem of a stiff spherical indenter with a composite plate was simulated with a 2D axisymmetry model implemented on a

commercial software. A parametric study was carried out numerically to study the effect of the different parameters on the force-indentation response. Two different situations are considered: i) the composite laminate is fully supported on a rigid substrate and ii) the composite laminate is supported on a hollow substrate.

After understanding the damage mechanisms and its sequence in composite laminates under out-of-plane loading and the effect of the different parameters on the response, the global objective of the present work can be achieved. The objective is to provide a reliable scaling tool to predict the response of a large composite panels or real structures under out-of-plane loading by testing small coupons. Therefore, an analytical model is developed to predict the load-displacement response during loading and unloading stages and the delamination area inside the impacted laminates. The developed model and the experimental data available in the literature are used to predict the response of a larger in-plane and thickness specimen impacted by large indenter by testing a small scale coupon which is known as "scaling effects". The importance of this scaling approach is the high reduction in the test and materials cost and the high results accuracy.

Figure 1.4 shows a flowchart illustrating the procedure followed to achieve the promising objectives. The first sub-objective is achieved by experimental tests on a unidirectional ply laminate combined with numerical simulations for clarifying some issues observed in the experimental tests. The second sub-objective is achieved through experimental tests on a thin- and ultra-thin-ply laminates and the results of the first experiments is used for clarifying the results. The numerical simulation is used to achieve the third sub-objective. The experimental results obtained in the first sub-objective were used to validate the numerical model. The global objective is achieved by implementing analytical model for quasi-static indentation test and uses this model combined with the experimental data available in the literature for scaling the quasi-static indentation test and low velocity impact. The results obtained from the first two sub-objectives are used to model the damage during the quasi-static indentation test.

1.4 Thesis Layout

In Chapter 2 a general review on the categories of the out-of-plane loading including static, quasi-static indentation, low-velocity impact and high-velocity impact on composite laminates. Then, a detailed review on the damage mechanisms during impact and quasi-static indentation tests is introduced. Also, a review on the local deflection of composite laminates (indentation response) is introduced. By the end of this chapter, a summary of the main findings in the literature is introduced.

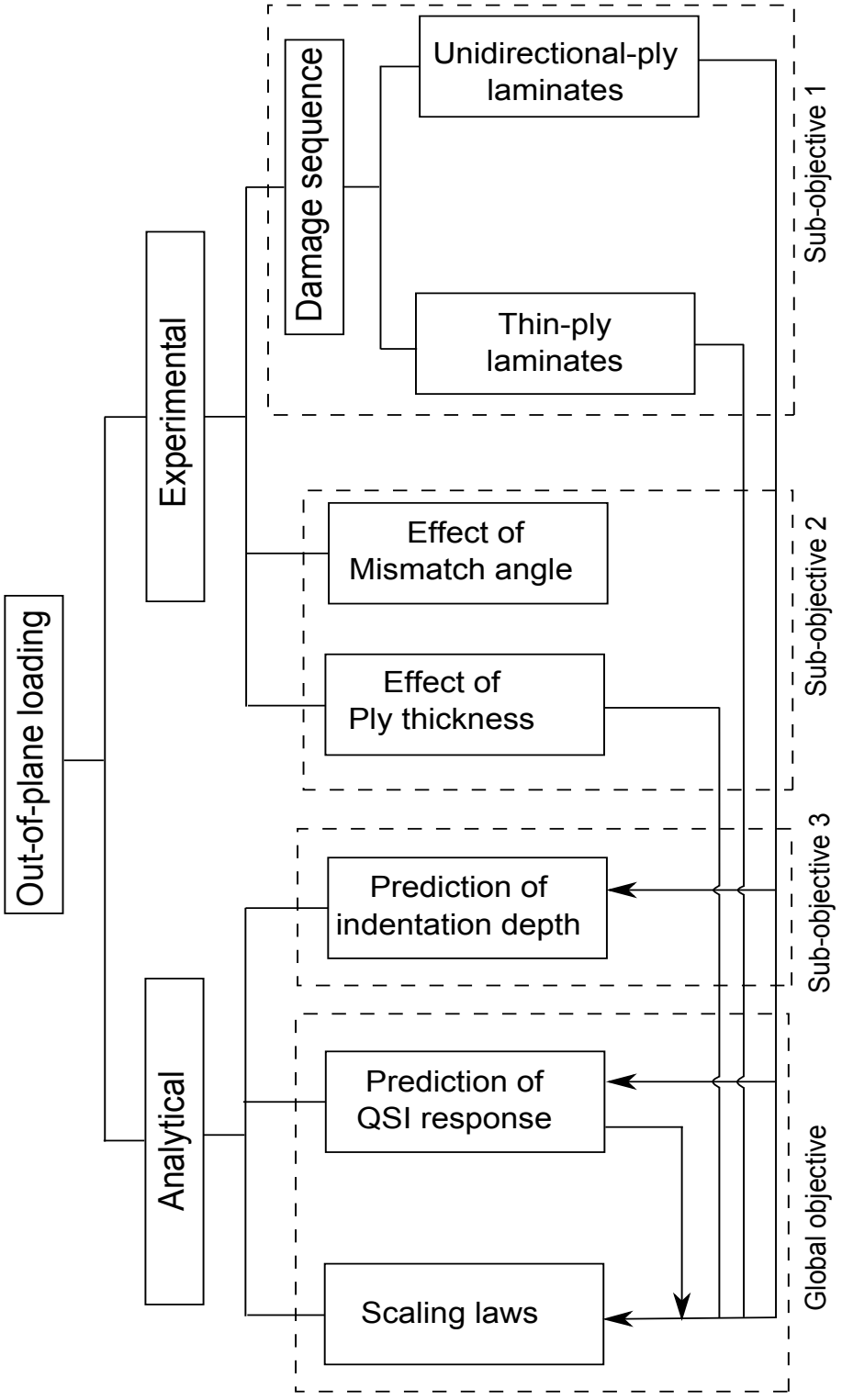

Fig. 1.4: Flowchart showing the tasks done during this work.

Based on the analysis done in Chapter 2, this thesis is divided in two main parts: experimental and analytical. In part I, experimental observations, the damage mechanisms and their sequence in composite laminates under out-of-plane loading is

experimentally studied. This part extends from Chapter 3 to Chapter 6. In Chapter 3 a detailed study of QSI tests on carbon fiber laminated composites manufactured from unidirectional plies is presented. Matrix cracks and delaminations were investigated, at different indentation displacements, by means of Scanning Electron Microscopy (SEM) and ultrasound C-scan inspections with the aim of understanding the initiation and the propagation of both damage mechanisms. The evolution of the indentation profile with time after the QSI test was monitored by means of a 3D surface inspection technique.

Recently, the application of thinner plies in composite laminate manufacturing have shown better properties such as: unnotched strength, bearing strength and compression after impact strength which highlight its importance and probability to be applicable in the aeronautic industry. The response of this kind of laminates under low velocity impact is still not well understood and the experimental results which explain the damage evolution and its sequence are rare. Therefore, in Chapter 4 the same procedure followed in Chapter 3 was used to understand the damage sequence in the TeXtrem thin-ply laminates under impact event. Two laminates with two different ply thicknesses are considered to study the effect of ply thickness on the damage sequence. In Chapter 5, the damage mechanisms and their interactions in NCF thin-ply composite laminates during QSI tests is experimentally studied. Also, the influence of mismatch angle on the response of NCF thin-ply laminates is experimentally studied in this chapter. With the aim of improving the damage resistance of NCF composite laminates, the effect of combining small and large mismatch angle in the same laminate and also combining thin and thick plies in the same laminate is presented in Chapter 6

Part II, analytical models, deals with the derivation of analytical models to simulate the QSI tests. In Chapter 7, an elastic 2D axisymmetric contact model was implemented using a commercial software to simulate the elastic response of orthotropic composite laminates of finite thickness in contact with stiff indenter and supported with two different boundary condition: fully and hollow support. Parametric studies were performed using the introduced Finite Element (FE) model to investigate the effect of each parameter on the elastic response of indentation problem. Two equations were derived to predict the response of an orthotropic composite laminate with finite thickness by normalizing the parameters influencing the problem and fitting of the normalized FE results.

In Chapter 8, an analytical model is proposed to predict the QSI response during the elastic and delamination regime up to fiber failure. The predicted load-displacement responses correlate well with the experimental results presented in the literature. The effect of scaling the geometrical parameters as in-plane dimension and shape, thickness of the laminate, thickness of the plies and indenter radius is analyzed.

This scaling approach is developed based on the presented analytical model and the experimental results available in the literature.

Finally, in Chapter 9 conclusions are drawn and topics for future work are suggested.

Literature review

2

2.1 Introduction

Impact behaviour of various materials has been studied throughout history. Several studies have been carried out on isotropic plates, orthotropic plates and anisotropic plates to understand the damage mechanics during this test [13, 23–31]. All these studies have illustrated that the impact response is a complex phenomenon even in isotropic materials. This phenomenon depends on a large number of parameters such as: the nature and the characteristics of the impactor and the structure, contact time, impactor velocity, thickness, wave propagation, etc. Furthermore, composite variables such as lay-up, fiber volume fraction, geometry of the specimen and mismatch angle between plies have a significant influence on the damage formation and propagation.

With the aim of clarifying and summarizing the effort done in the literature to characterize the response of composite laminates under out-of-plane loading, a comprehensive review of the literature concerning composite laminates subjected to out-of-plane loading is introduced. This chapter is presented in three main sections; definition and classification of out-of-plane loading, impact and QSI damage mechanics and scaling laws. In the first section, the out-of-plane loading is defined showing the different classifications and the limits of each. The second section presents a detailed experimental and analytical review on the damage modes during QSI and low-velocity tests. The third section, summarizes the effort done in the literature to scale out-of-plane loading tests. Finally, the chapter is finished with summary and conclusions from the review of the literature.

2.2 Out-of-plane loading

Out-of-plane loading is a loading condition in which the load is applied in the transverse direction of the specimen (thickness direction). Out-of-plane loading was classified in the literature according to initial velocity, because collisions at different velocities can lead to different dynamic responses and damage in the target. Sierakowski et al. [32] have proposed a classification of the different loading conditions as shown in Figure 2.1. This classification basically depends on the loading velocity.

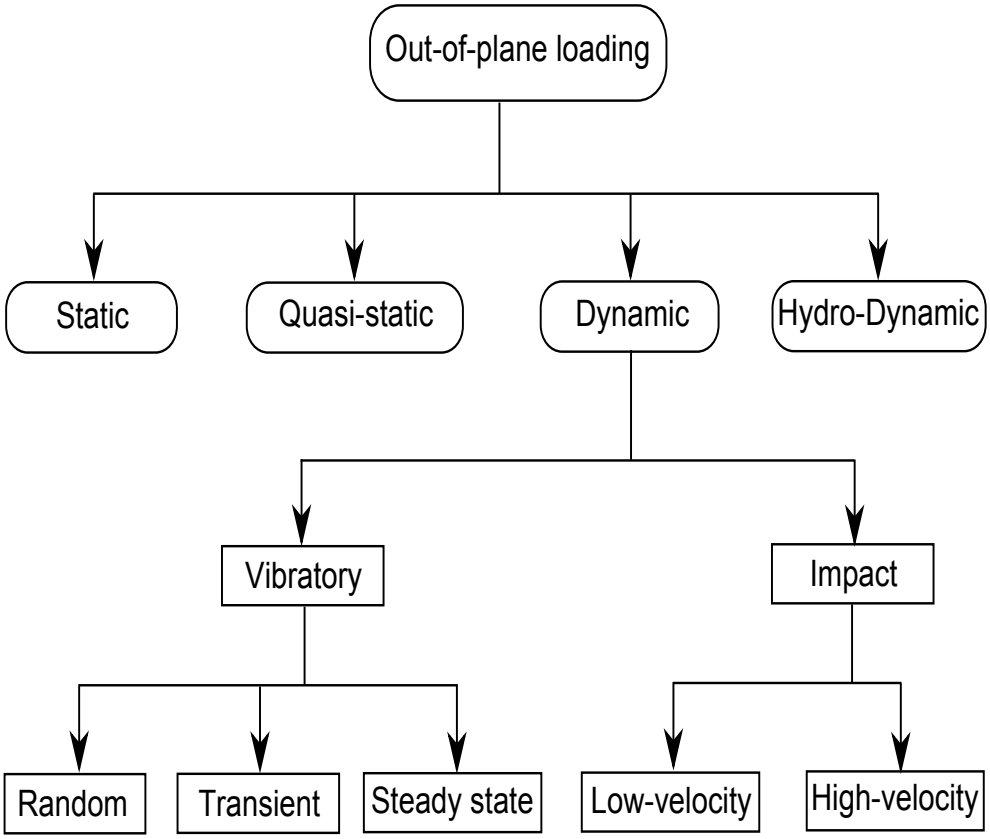

Fig. 2.1: classification of the out-of-plane loading based on load velocity [32].

Another classification was presented by Olsson [33]. According to his study, an impact event initiates stress waves propagating from the impact point, where the influence of the waves gradually fade away due to material damping and wave scattering. For impact times close to the time required for the waves to propagate through-the-thickness direction, the response is dominated by three-dimensional wave propagation (see Figure 2.2a). For longer impact times, flexural and shear waves govern the response (see Figure 2.2b). For times much longer than the time needed by these waves to reach the plate boundaries, the lowest vibration mode of the impactor-plate system predominates (see Figure 2.2c). Eventually, the deformation mode approaches a purely static deformation.

The response dominated by through-the-thickness waves is typically associated with ballistic impact (see Figure 2.2a), which in most cases, causes localized and easily detectable damage [33]. Related to the impacts that might affect an aircraft, the response in Figure 2.2b is typical for impacts by hail and runway debris, whereas the response in Figure 2.2c is typical for dropping of heavy tools or ground accidents.

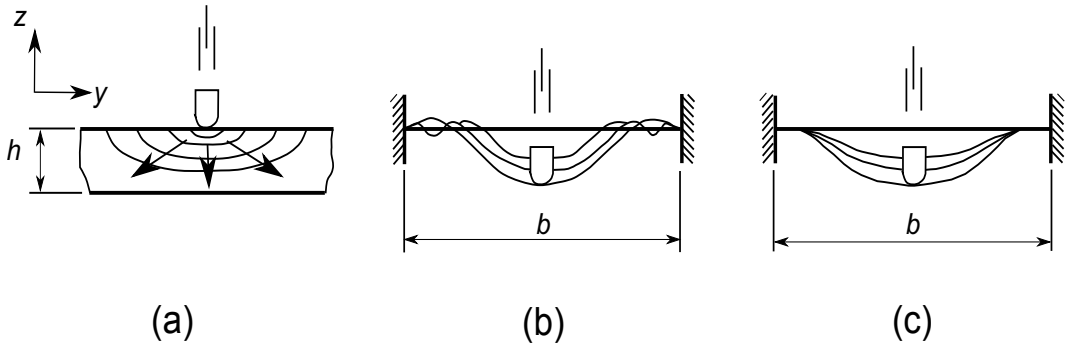

Fig. 2.2: Impact responses (after Olsson [33]): (a) dominated by dilatational waves, (b) dominated by flexural and shear waves, and (c) quasi-static response.

2.2.1 Low-velocity impact

Low-velocity impacts can cause barely visible impact damage which is difficult to detect during routine inspections especially in composite laminates. Many researchers have carried out experimental studies on low-velocity impacts on composite laminates. For example but not limited to, Cantwell et al. [11–16], Doyle et al. [17], Sankar et al. [18], Olsson et al. [19–21] have investigated the effects of impact events on composite laminates. All of them agreed on the fact that the residual tensile and compressive strengths of composite laminates are influenced by the damage area and the different damage mechanisms induced by this impact.

At least three definitions of low-velocity impact can be found in the literature. The one proposed by Robinson and Davies [34] and adopted by Abrate [35] is based on the propagation of elastic waves through the thickness of the impacted laminate. When the ratio between initial velocity and wave velocity is smaller than the strain which causes failure in the thickness direction, the role played by this kind of wave is considered negligible and impact velocity is said to be "low". This defines a low velocity collision, in which possible damage is caused by overall deformation of the laminate, thought of as a two-dimensional solid, rather than by local compression of the material at the impact point, which should be treated as a three-dimensional phenomenon. Another definition is proposed by Sjoblom et al. [36]: "by low velocity we mean an impact velocity low enough to justify a static analysis of the response of the structure". Hence, a collision should be said to take place at low velocity if the contact duration is much greater than the time required for flexural elastic waves to reach the boundary and be reflected back, as pointed out in [37, 38]. Later, Olsson [20] and Yigit and Christoforou [22] suggested a criteria for classifying low and high velocity impacts. They stated that "for low velocity impacts, the impact response is governed by impactor/plate mass ratio rather than the impact velocity while for higher impact velocities, the short impact time results in a response governed by wave propagation phenomena".

2.2.2 Quasi-static indentation

Quasi-static indentation loading can be defined when the impact duration is much longer than the time required by the propagating waves to travel from the impact site to the supports or free edges [33]. Fortunately, low velocity impacts caused by large masses can be treated as a static indentation problem because the impact duration is much longer than the time required by the propagating waves to travel from the impact site to the supports or free edges. Indeed, experimental results correlate well with this assumption for low and medium impact energies [39]. The limits of using QSI to represent low-velocity impact are established by Swanson [40], Bucinell et al. [41], Olsson [19] and Yigit and Christoforou [22].

Low velocity impact tests do not allow one to observe the succession and evolution of the degradation mechanisms within the plate, since the plate can only be inspected upon the completion of impact testing. For this reason, a number of researchers have turned their attention to QSI tests. These tests have been demonstrated to give similar global behaviour and damage states as low velocity impact tests [42–45]. Since they are static tests, they can be easily interrupted at different stages to observe the damage evolution within the plate. Lammerant and Verpoest [46] analyzed the interaction between matrix cracks and delaminations by means of QSI tests. More recently, Guan et al. [47] showed good correlation between impact and QSI tests when comparing composites with different constituents. The information gathered in QSI experiments might be used to validate numerical efforts to describe damage mechanisms and their interaction during impact events [47–53]. It may also be the driving criteria in optimizing ply sequences or foreseeing the effect of emerging composite concepts such as thin ply laminates or the use of hybrid reinforcements. Therefore, QSI tests can provide meaningful evidence of the damage events occurring during a low velocity impact as well as its sequence and interactions.

2.3 Impact/QSI damage mechanics

2.3.1 Damage modes

Composites behave in a different way as compared to conventional metallic materials. When traditional engineering materials such as steel or aluminum are subjected to low velocity impacts, the energy is typically absorbed as a plastic deformation. However, this deformation is permanent and it does not significantly reduce the load carrying capability of the structure [54].

Polymer matrix composites such as carbon fiber composites exhibit very little or no plastic deformation during low velocity impact. This is due to the low strain to failure of the fiber. During a low velocity impact event, the impact energy is

absorbed through the global bending of the composite laminate [48, 54, 55]. Many researchers have paid attention to the behaviour of the composite laminates under low velocity impact [11–16, 56]. They found that the energy is absorbed by the composite laminates through out several damage modes caused by the stresses during the global bending of the laminate. Other studies have been done on the post impact compressive strength of the delaminated composites [13, 27, 28, 57–61]. They concluded that the strength of the post-impacted laminates is highly affected by the delaminations inside the laminate.

The impact event generates two kinds of damage modes; a local damage and a global damage. Figure 2.3 shows the different damage modes as presented by Sierakowski [32]. Local damage can lead to fiber breakage which can be stable or unstable behaviour. The stable behaviour occurs when the laminate can withstand high operating loads after suffering impact damage, which does not cause a catastrophic failure. Unstable bahaviour is defined when the fiber breakage propagates and leads to catastrophic failure or complete failure of the laminate. In another words, fiber failure occurring in the local damage is stable if the remaining fibers can sustain the load. However, fiber fracture in laminates which are unable to sustain the operating loads leads to catastrophic failure defined as unstable behaviour. The global damage mode can lead to matrix cracking, delaminations and permanent indentation. The matrix cracking and permanent indentation lead to quite stable behaviour, since after occurring both, the laminate can withstand high operating loads. However, for delamination, the stable behaviour can occur when the impacted laminate can sustain the operating load.

Matrix damage, delamination and fiber breakage are very hard to detect while the laminate is in service. However, the permanent indentation is easy to be detected by visual inspection which can give some information about the global behaviour of damage. Thus, definition of the damage modes guides us to evaluate the different damage mechanisms. Damage mechanisms in local and global modes include different kinds of failure which might occur successively or simultaneously. The understanding of the cause, formation and sequence of damage arising from a low velocity impact is essential for the effective use of polymer matrix composites in high performance applications.

2.3.2 Damage mechanisms

In order to understand impact damage development, it is important to determine how the damage initiates and grows during impact. Many damage mechanism, such as matrix cracking, delamination and fiber breakage can occur during an impact event on composite laminates. A number of studies were conducted to determine the exact nature of the damage, the sequence of damage accumulation, and the

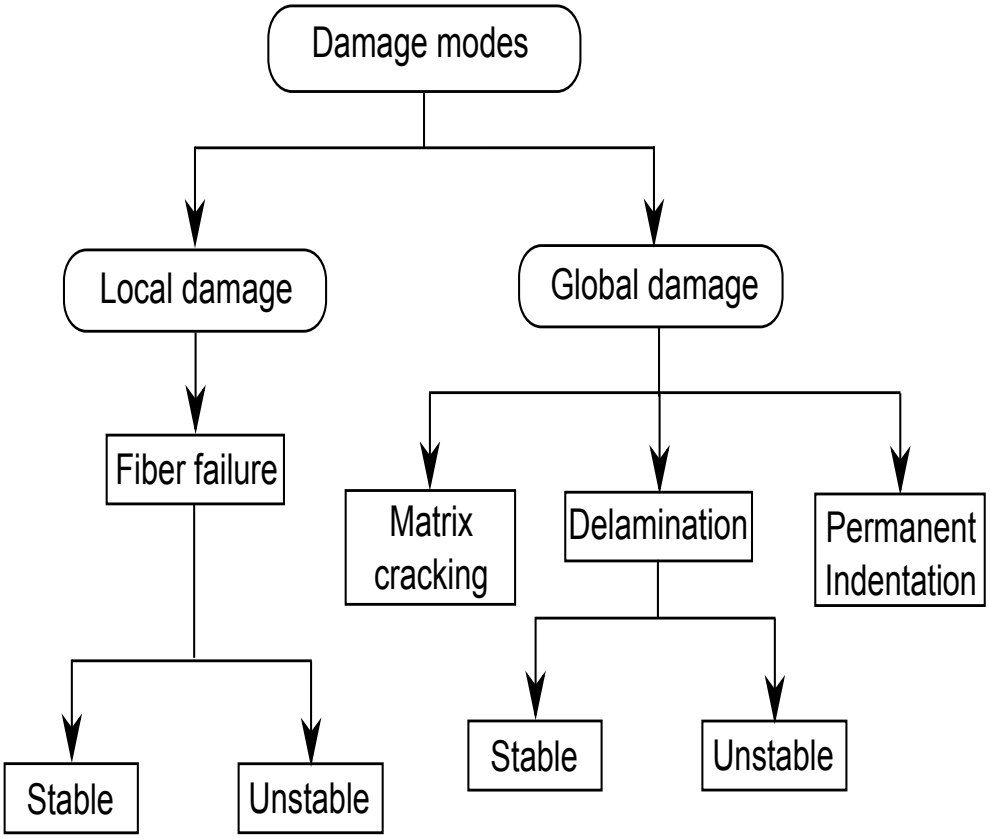

Fig. 2.3: Different damage modes as presented by Sierakowski [32].

influence of various parameters such as impactor shape and velocity. Damage initiation, propagation and perforation threshold values are important from the point of view of designing a composite laminate with improved properties against impact. The evolution of the type and the size of the damage with the kinetic energy or the applied displacement of the impactor are also of interest. Based on the experimental observations available in the literature, the damage during an impact event on composite laminates can be classified in four damage mechanisms: matrix cracking, delamination, fiber breakage and perforation. In the following subsections, a detailed review is introduced for each of these different damage mechanisms.

(i) Matrix cracking

Matrix cracking is the first damage mechanism during an impact event [62]. It was reported that this matrix damage is induced by transverse low-velocity impact, and usually occurs at low energy levels. This matrix damage always takes the form of matrix cracking and also debonding between fiber and matrix. Matrix cracks occur due to property mismatching between the fiber and matrix, and are usually oriented in planes parallel to the fiber direction in unidirectional layers. Joshi and Sun [63] reported that the matrix cracks can be found under the edges of the impactor, shear cracks, and in the bottom layer

of the laminate, tensile bending cracks. Matrix shear cracks are formed by the very high transverse shear stress due to the contact force, and are inclined at approximately 45° [64, 65]. The tensile bending cracks at the bottom layer are induced by the high tensile bending stresses in this layer. The bending stress is closely related to the flexural deformation of the laminate [66]. This conclusion was confirmed in several studies later [28, 67–72].

Cantwell and Morton [11] emphasized that the type of matrix cracking is dependent on the global structure of the impacted specimens. For example, for long thin specimens bending cracks in the lower layers occur due to excessive transverse deflection and subsequent membrane effects predominate, whereas short thick specimens are stiffer and so higher peak contact forces induce transverse shear cracks under the impactor in the upper plies. Wu and Springer [73] reported detailed locations of matrix cracking for graphite/epoxy plates of various stacking sequences under impact loading. Abrat [74] proposed a schematic drawing of the matrix cracking initiation and propagation in thin and thick composite laminates. In his study, he claimed that the matrix cracks for thicker composite laminates have a pine-pattern shape (Figure 2.4a). However, for thinner laminates, a reversed-pine-pattern-shape can be observed (Figure 2.4b). Crossman and Wang [75] reported that the matrix cracks are dependent on the ply thickness. This damage mechanism can be delayed or even prevented in thin-ply laminates [76–78].

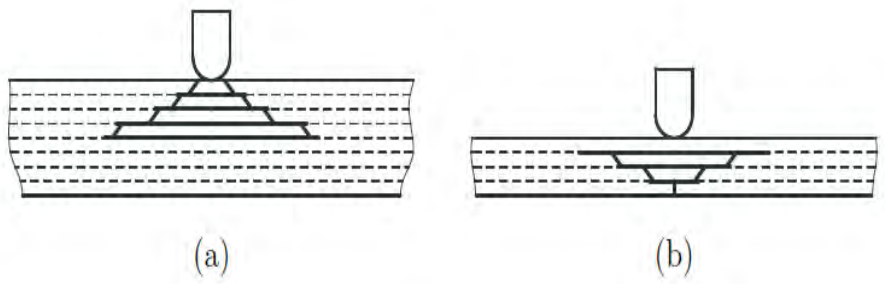

Fig. 2.4: Matrix cracks damage mechanism patterns [74], (a) pine-tree and (b) reversed-pine-tree.

Olsson et al. [21, 79] proposed a simple threshold load for matrix cracking due to the through-the-thickness shear stress created by a static concentrated contact load. The threshold load is calculated by considering the Hertz distribution of the contact pressure, and the corresponding maximum value of the shear stress in the through-the-thickness direction and within the contact radius. In the same way of the simplified shear stress field indicated by Davies et al. [80], the distribution of the through-the-thickness shear stress is assumed parabolic

with the maximum located in the middle plane. The shear cracks threshold load is defined as:

$$F_s = \frac{4}{3}\pi c \cdot h \cdot \tau_u \tag{2.1}$$

where c is the contact radius, h is the laminate thickness, and τ_u is the out-of-plane shear strength.

It is valuable to point out that most of the available studies have assumed that matrix cracking has a slight influence on the stiffness which can be neglected during calculations [13, 19, 20, 33, 60, 61, 74, 79, 81, 82]. However, other studies have shown that matrix shear cracks and the tensile cracks have a significant influence on the stiffness of the impacted laminates [83–85].

(ii) Delamination

During an impact event, when the applied energy exceeds the amount that the material can absorb due to the matrix cracks, delaminations grow between plies of different fiber orientation [73, 86, 87]. These delaminations seriously reduce the compressive strength of the composite and also allow more paths for progressive damage.

Many studies were conducted to understand how delaminations initiate and how they grow. For understanding delamination initiation, Takeda et al. [88] and Joshi and Sun [63] presented microscopic observations showing delaminations and matrix cracking. In their study, they showed that the material consume a small amount of the applied energy in matrix cracks. When the cracks reach an interface between two plies, a delamination starts to grow between these two plies consuming largest portion of the applied energy. Liu [89] investigated experimentally the delamination behavior in [0/90] laminates under impact event. In his study, he explained that delamination was a result of the bending stiffness mismatch between adjacent layers, i.e. the different fiber orientations between the layers. Also, he found that delamination areas were generally oblong shaped with their major axis being coincident with the fiber orientation of the layer below the interface. Later, these results have been widely reported elsewhere in the literature [50, 60, 61, 64, 73]. Moreover, he defined a bending mismatch coefficient between the two adjacent layers which includes bending stiffness terms and predicts the peanut shape reported for [0/90] laminates. Also, he concluded that, the greater the mismatch angle is, the greater the delamination area is.

Other studies [64, 90–92] were done and they concluded that delamination was initiated as a mode I fracture process due to very high out-of-plane normal

stresses caused by the presence of the matrix cracks and high interlaminar shear stresses along the interface. However, Davies and Robinson [80, 93], in a highly simplified isotropic axisymmetric analysis for the threshold force for growth of an internal circular delamination in the mid-plane, showed that mode II strain energy release rate is independent of delamination radius. The prediction of their proposed hypothesis was in a good agreement with their experimental results for quasi-isotopic laminates. Also, they showed that the initiation of delamination is independent of indenter size. To simplify the development of the model, static loading conditions were considered, the laminate was treated as isotropic, only small deflections were considered (membrane effects were neglected), and the through-thickness distributed delaminations were collapsed into a single and perfectly circular mid-plane delamination. Based on these assumptions, the threshold load for a mid-plane circular delamination, F_{d1}, can be approximated as:

$$F_{d1} = \pi \sqrt{\frac{32 D G_{\mathrm{IIc}}}{3}} \tag{2.2}$$

where D is the bending stiffness and G_{IIc} is the mode II fracture toughness.

This hypothesis for delamination initiation was followed by many researchers [19, 21, 79, 81, 82, 94]. In addition, experimental and numerical results indicate that the delamination threshold load is independent of the boundary conditions and the in-plane size of the laminate [79, 95, 96].

Schoeppner and Abrate [96] proposed an empirical relation between delamination threshold load and laminate thickness using approximately 500 low-velocity impact force histories from the Air Force Research Laboratory low-velocity impact database and is expressed as follows:

$$F_{d1} = C \cdot h^{3/2} \tag{2.3}$$

where C is a curve fit coefficient determined with the impact curves, and h is the laminate thickness.

Sutherland and Guedes Soares [97] developed a simplified shear delamination model to predict the onset of interlaminar fracture in marine-grade composite materials. They showed that the damage threshold load is related to the interlaminar shear strength and not related to the mode II fracture toughness. The prediction of the proposed hypothesis correlates well with their experimental

results. A strength criterion that defines the onset of cracking or delamination for hemispherical indenters is:

$$F_{\mathrm{d1}} = \sqrt{\frac{6\tau_{\mathrm{s}}^3\pi^3h^3r}{E}} \tag{2.4}$$

where τ_{s} is the interlaminar shear strength of the laminate, h is the laminate thickness, r is the impactor radius and E is the contact modulus which can be computed as $\frac{1}{E} = \frac{1-\nu_1^2}{E_1} + \frac{1-\nu_2^2}{E_2}$, where the subscripts 1 and 2 refer to the indenter and the laminate, respectively.

Regarding understanding delamination growth, Choi and Chang [64] reported that delamination growth was governed by interlaminar longitudinal shear stress (σ_{13}) and transverse in-plane stress (σ_{22}) in the layer below the delaminated interface and by the interlaminar transverse shear stress (σ_{23}) in the layer above the interface. Several studies were carried out confirming the hypothesis reported by Choi and Chang [64] which considers the delamination growth is basically dependent of the interlaminar shear stress and the transverse in-plane stress [66, 98, 99].

Some research has been also carried out in order to relate the delamination growth to the mode II fracture toughness. Razi and Kobayshi [100] performed a numerical simulation of impact-induced delamination growth. They concluded that the mode II fracture toughness was the dominant parameter for propagation of delaminations. Later, several studies were done and reached the same conclusion [19, 20, 33, 59–61, 79, 101], which has been set as a reference for modeling the delamination growth. Suemasu and Majima [81, 82] performed numerical simulations to predict the load after the damage initiation, F_{dn}, which can be defined as:

$$F_{dn} = \pi\sqrt{\frac{32DG_{\mathrm{IIc}}}{n+1}} \tag{2.5}$$

where n is the number of equally delaminated interfaces which is assumed to be 1 for determining the delamination initiation load, F_{d1}. Fractographic results, e.g. in [102], indicate that $n = 0.3\ N$, being N is the number of interfaces, for conventional tape prepreg laminates. In the work developed by Olsson [21, 95], Equation 2.5 was used for orthotropic plates by simply changing the isotropic plate stiffness D by the effective plate stiffness D^* for orthotropic plates.

Olsson et al. [79] developed a fracture mechanics criterion for dynamic growth of an arbitrary number nd of delaminations in a transverse isotropic plate. The

load after delamination growth for dynamic test (low-velocity impact), F_{dn}^{imp}, can be computed as:

$$F_{dn}^{imp} = \frac{F_{dn}}{\sqrt{1 - \frac{7\pi^2}{216}}} \approx 1.213 F_{dn} \tag{2.6}$$

(iii) Fiber breakage

Fiber breakage is considered as a catastrophic failure damage mechanism. After this damage mechanism, the material can not withstand the design loads [12, 13, 16]. This damage mechanism generally occurs much later in the fracture process than matrix cracking and delamination. Since research has concentrated on the damage mechanisms due to low-energy impacts, there is less information available in the literature on this damage mechanism . Fiber failure initiates in two regions: i) under the impactor due to locally high shear stresses due to contact and compressive stress and ii) in the non impacted face due to the higher normal bending stresses [14, 15, 21]. Belingardi and Vadori [103] defined the term of saturation impact energy, which is the maximum energy bearable by the material without perforation.

Sjoblem [104] has proposed a criterion to compute the critical load for fiber breakage due to the shear stresses. This criterion was formulated in a more straight forward form by Abrate [74]. By considering the Hertz contact law and a uniform distribution of the through-the-thickness shear stress, the fiber breakage due to shear stresses can be computed as:

$$F_r = (\pi S_L h)^{3/2} \sqrt{\frac{6r}{E}} \tag{2.7}$$

where S_L is the shear strength, h is the laminate thickness, r is the indenter radius and E is the effective contact modulus.

Recently, Olsson [21] has developed a closed form equation to compute the critical load for fiber breakage during impact and quasi-static indentation loading. The hypothesis followed to derive this equation is that large deflections result in membrane strains, which reach a peak at the boundary of the concentrated load. Delamination causes a more or less complete loss of the bending stiffness so that the laminate deforms around the impactor at a constant curvature. This results in a uniform contact pressure and membrane stress in the contact region, which can be used to derive the following critical load, F_r for rupture

(tearing) of the fibers in the laminate. The critical fiber breakage load, F_r, can be computed as:

$$F_r = \frac{4\pi r h E_r \varepsilon_t^2}{1 - \nu_r} \tag{2.8}$$

where r is the indenter radius, h is the laminate thickness, E_r and ν_r are the average membrane Young modulus and Poisson's ratio in the membrane loading of the laminate and ε_t is the tensile failure strain of fibers in the laminate.

Aktas et al. [105] experimentally investigated the damage sequence in composite laminates made of unidirectional plies under low-velocity impact test. They summarized the damage sequence in six stages. The first stage is permanent indentation having semi-spherical shape under the impactor, along with interlayer and intralayer matrix cracks. The second stage is delamination at interior interfaces due to different fiber orientations of adjacent plies. The third stage is splitting among undamaged fibers due to deformation around impact point. The fourth stage is fiber fracture resulting from bending and/or stretching of fibers. The fifth stage is edge delaminations occurring around the point of impact. The last stage is delamination at the bottom layer, resulting from vertical displacement of the broken and unbroken fibers. This sequence of damage is presented as a schematic drawing in Figure 2.5.

(iv) Perforation and penetration

After the fiber breakage damage mechanism, the load decreases by increasing the applied displacement until the indenter penetrates the laminate. In the literature penetration and perforation are sometimes confused. According to the approach proposed in [106], the penetration occurs when the striker passes completely through the entire laminate. Cantwell and Morton [11] showed that the impact energy penetration threshold increases rapidly with specimen thickness for CFRP laminates. They also analysed the penetration process to calculate the energy absorbed by shear-out. This simplified analysis predicted shear-out as the major form of energy absorption (50-60% depending on plate thickness). El-Habak [107] tested a variety of GFRP composites at penetration loads and concluded that the glass fiber treatment played a key role in determining the perforation load. Although the matrix had little effect, polyester was preferable to epoxy. Lui et al. [108] performed low-velocity impact tests on CFRP laminates with different thicknesses. They studied the influence of increasing the laminate thickness by different joining techniques, i.e. mechanical riveting, adhesive bonding and joining, on the penetration threshold. From their study, they concluded that using joining techniques to

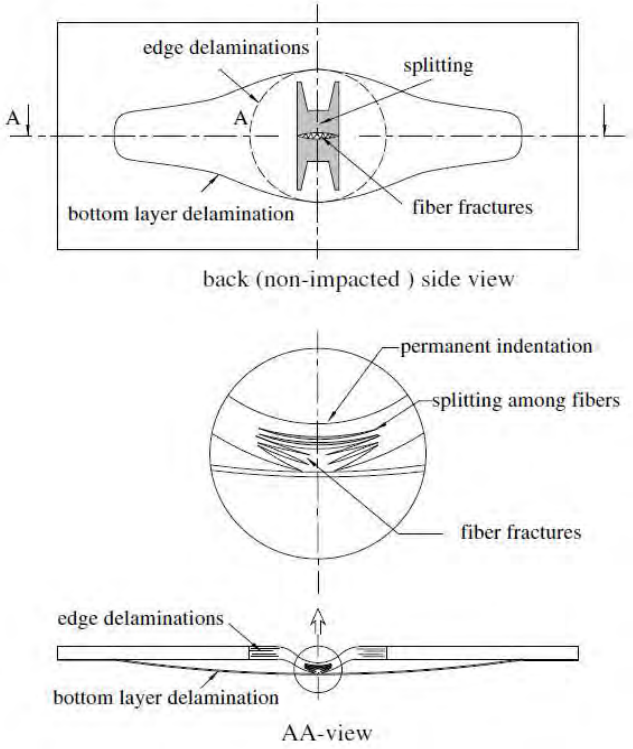

Fig. 2.5: Schematic illustrations for different damage modes as presented by Aktas et al. [105].

obtain a thick laminate has the advantage of higher penetration energy over the thick laminated composite laminates.

Caprino and Lopresto [109] proposed an empirical correlation that describes the effect of laminate thickness, fiber volume fraction and impactor diameter on the penetration energy by a unique power law. The relationship was initially assessed for glass fiber reinforced laminates and then validated for carbon fiber reinforced laminates on the basis of experimental data available in the literature. The proposed empirical equation assumes a dependence of the penetration energy on three specific parameters, laminate thickness, impactor diameter and the fiber volume fraction. The penetration energy for a composite laminate under impact-loading can be computed as:

$$U_P = \gamma \cdot (h \cdot V_f \cdot D_I)^{\beta} \tag{2.9}$$

U_P is the penetration energy, h is the laminate thickness, V_f is the fiber volume fraction, D_I is the impactor diameter and γ and β are two parameter that depend on the material.

The data presented by Caprino and Lopresto [109] refers to a quite large variety of carbon fibers, thickness, boundary conditions, geometry of the speci-

mens and striker diameters. Results indicate that the exponent of the power law, which is close to 3/2, seems to be independent of the particular material. Moreover, the relationship was found to hold valid even for polycarbonate panels, though polycarbonate is isotropic and prone to extensive plastic yielding before failure. Therefore, if the exponent were confirmed being unaffected by the considered material, each material might be characterized in terms of penetration energy, by a unique constant.

2.3.3 Indentation evaluation

The permanent indentation depth is a key parameter in damage assessment procedures for the aeronautical industry. Indeed, it is used as a direct indication of the severity of the damage induced by a low velocity impact and its intensity is used to decide on the need for repair or not. In particular, the indentation depth referred to as Barely Visible Impact Damage - BVID (it is assumed that it might not be found during heavy maintenance general visual inspections) is considered neither to impair the loading capability of the structure nor to cause detrimental damage growth during service. However, there has been little attention to permanent indentation by the research community. A better knowledge on the permanent indentation and its correspondence to the damage scenario inside the laminate is fundamental in improving damage tolerance procedures. In 2012 Singh et al. [110] introduced a method for evaluating the 3D indentation profile based on the measurement of the flight time of an ultrasonic pulse between the transducer and the first wave reflection.

Impact on monolithic plates involves local and global deflection. Therefore, impact damage may be caused due to local contact stresses and/or stresses resulting from the structural response. It is valuable highlighting that the indentation depth caused by QSI test is always larger than that caused by low velocity impact test due to the larger contact time between indenter and plate during QSI test [20, 106]. Figure 2.6 shows the two different responses: local deflection, indentation (α), and the global deflection (u).

In 1882, Hertz published for the first time a solution for the problem of frictionless contact between homogeneous elastic bodies under normal loading [111]. In his work, the applied force was related to the indentation depth as:

$$F = K\alpha^q \tag{2.10}$$

where K is the contact stiffness, q is a power parameter, and α is the indentation depth.

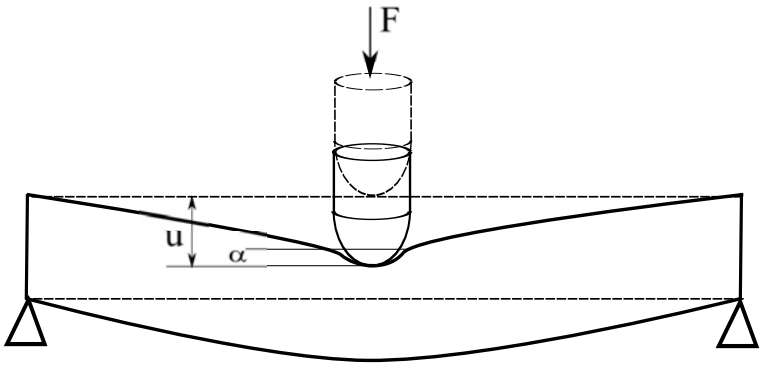

Fig. 2.6: Schematic drawing of QSI problem showing the local deformation (indentation) and the global deformation.

The elastic contact problem of a sphere and a homogeneous isotropic material is now well understood and has been summarized by Jonhson [112]. However, solutions for non-isotropic materials are much less available. Contact problems for transversely isotropic materials have been investigated by Green and Zerna [113], Leknitskii [114], Sveklo [115], Dahan and Zarka [116] and Turner [117], among others.

One of the most widely used elastic contact laws for laminated plates was presented by Yang and Sun [118] based on Hertz theory. They assumed that the contact pressure and contact area could be obtained from the usual formulas for isotropic materials, but using the orthotropic modulus of the material in loading direction instead of the isotropic modulus of elasticity. However, this model solves the contact problem as a half space problem without taking into account the plate thickness effect. They proposed an approximation for the contact deformation of a composite laminate indented by a rigid sphere. The formulation is the same introduced by Hertz, Equation 2.10, by considering the power parameter, q, equal 1.5 and the contact stiffness can be approximated as:

$$K = \frac{4}{3}\sqrt{r}E_3 \tag{2.11}$$

where r is the indenter radius and E_3 is the young modulus of the upper ply in the thickness direction.

A general solution for contact loading of transversely isotropic materials was presented by Swanson [119] based on Turner theory [117]. The model showing that the contact parameters may be found from formulae similar to the classical Hertz law for isotropic materials, if the isotropic modulus is replaced by a combination of the

transversely isotropic properties. Thus for a normal contact force F, the indentation response can be expressed as:

$$F = \frac{4\sqrt{c}E_T}{3}\alpha^{1.5} \tag{2.12}$$

where c is the contact radius and E_T is the effective elastic modulus for transversally isotropic materials.

The effective elastic modulus of transversally isotropic martials is computed in the literature by two expressions proposed by Turnner [117] or Greszczuk [120]. So, E_T can be computed based on Turner theory [117] as:

$$E_{\mathrm{T}} = \frac{2}{\alpha_1\alpha_3} \tag{2.13}$$

The parameters α_1 and α_3 can be determined as:

$$\alpha_1 = \sqrt{\frac{\frac{E_{\mathrm{xx}}}{E_{\mathrm{zz}}} - \nu_{\mathrm{xz}}^2}{1-\nu_{\mathrm{xy}}^2}}$$

$$\alpha_2 = \frac{\frac{E_{\mathrm{xx}}}{2G_{\mathrm{xz}}} - \nu_{\mathrm{xz}}(1+\nu_{\mathrm{xy}})}{1-\nu_{\mathrm{xy}}^2}$$

$$\alpha_3 = \frac{2(1-\nu_{\mathrm{xy}}^2)}{E_{\mathrm{xx}}}\sqrt{\frac{\alpha_1+\alpha_2}{2}} \tag{2.14}$$

where E_{xx}, E_{zz}, G_{xz}, ν_{xy}, ν_{xz} are the three-dimensional effective elastic constants of transversely isotropic materials or composite laminate (z is the thickness direction and x and y are the in-plane directions).

Or it can be obtained according to Greszczuk derivation as [120]:

$$E_{\mathrm{T}} = \frac{2\sqrt{\frac{G_{rz}}{C_{rr}}}(C_{rr}C_{zz} - C_{rz}^2)}{\sqrt{(\sqrt{C_{rr}C_{zz}} + G_{zr})^2 - (C_{rz}+G_{zr})^2}} \tag{2.15}$$

where:

$$C_{rr} = \frac{E_r(1-\nu_{rz}\nu_{zr})\beta}{(1+\nu_{rr})}$$

$$C_{rz} = E_r\nu_{zr}\beta$$

$$C_{zz} = E_z(1 - \nu_{rr})\beta$$

$$\beta = \frac{1}{(1 - \nu_{rr} - 2\nu_{rz}\nu_{zr})} \tag{2.16}$$

Recently, Chen et al. [121] have proposed a modification on the model presented by Yang and Sun [118] to deal with the problem of contact between rigid indenter and laminated plate taking in to account the plate thickness. This model can be expressed in this form:

$$w(x_0, y_0, F) - w\left(x_0 + \left(\frac{F}{K}\right)^{1/3}\sqrt{r}, y_0, F\right) + \left(\frac{F}{k}\right)^{2/3} = \frac{3F}{4E_T\sqrt{r}} \tag{2.17}$$

where $w(x, y, F)$ is the plate deflection function, the subscript 0 refer to the initial contact points.

Comparing the results of Yang and Sun model [118] and Chen et al. model [121] with the experimental results presented by Wu and Shyu [98] as shown in Figure 2.7, the predictions of Chen et al. [121] model agree well with the experimental results for small indentation depth. However, the predictions of Yang and Sun model deviate from the experimental results at lower indentation depths. Moreover, Chen et al. model shows better correlation with the experimental results for small thickness (h = 2 mm). However, for the larger laminate thickness (h = 4 mm), the correlation became worst.

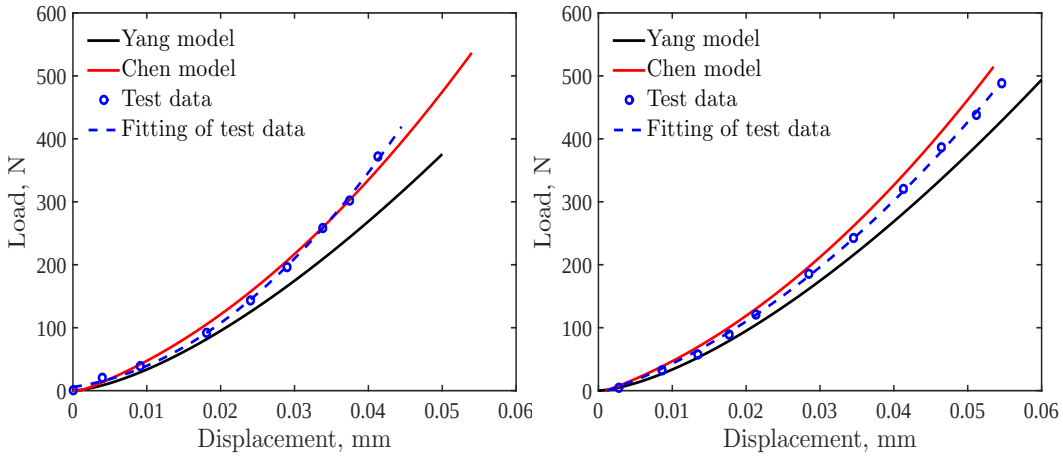

(a) h = 2 mm **(b)** h = 4 mm

Fig. 2.7: Comparison between Yang and Sun model [118], Chen model [121] and Wu and Shyu [98] experimental results.

Efforts have been done to correlate the contact force and the plate response by use of the functions and integral equations proposed by Green and Zerna [113]. Apart from these efforts, Wu and Yen [122] and Chao and Tu [123] have used the solution proposed by Pagano [124] for approximating a point load and then numerically associated the resulting surface displacements to the indenter geometry. With such an approach they related the static indentation of a cross-ply laminate to the contact force exerted by a rigid sphere. Sankar [125] derived an approximate function for surface displacement in an orthotropic beam. This function was used to formulate the integral equation for the problem of smooth contact between a rigid cylinder and an orthotropic beam. Some researchers proposed a general method to approach the contact problem of anisotropic plates. This method is based on the combination of an elastic solution which describes the local contact phenomenon and the classical theory for the global response. For instance, Cairns and Lagace [126] have used the stress function proposed by Leknitskii [114] to study the thick composite laminates subjected to lateral loading. Their experimental results were found to be in good agreement with their predictions. As indicated by Swanson [127], using this method is difficult and it is difficult to assess the resulting accuracy.

On the other hand, some researchers use the Finite Element Method to predict the response of laminated plates subjected to indentation loads. Jung [128] introduced an axisymetric FE model to study the response of laminated composite plates under static indentation load and a progressive damage failure between a circular plate and a rigid hemispherical tip indenter. Ye et al. [129] developed a 3D FE model to numerically predict the dent depth in composite laminates subjected to static indentation. Good agreement between the numerical results and the experimental results was found for larger indentation depths than those achieved in [128, 130]. Gan et al. [131] introduced a 2D FE analysis to study the indentation response of composite laminate supported on rigid substrate and indented by cylindrical and spherical indenters. From this study, an empirical formula was introduced to predict the contact radius between the indenter and the composite laminate.

Typically, in an any kind of loading the force increases to a maximum value and then decreases back to zero (unloading stage). During the unloading stage, Yang and Sun [132, 133] found that the Hertzian contact law was not adequate. The unloading phase is significantly different from the loading phase due to permanent indentation. In order to account this effect, Crook [134] proposed the following equation:

$$F_c = F_m \left(\frac{\alpha - \alpha_0}{\alpha_{max} - \alpha_0} \right)^{5/2} \tag{2.18}$$

where F_m is the contact force at the start of unloading, α_{max} is the maximum indentation depth, α_0 is the permanent indentation depth.

2.4 Scaling of impact/QSI test

Scaling is an important aspect of every physical theory [135] and scaling laws are commonly used in many physical and engineering problems. A historical review of scaling was introduced by Bažant et al. [135]. Moreover, understanding scaling laws allows extrapolating testing results to large scale real structures. The scaling technique has two important advantages: i) reduce the experimental cost by testing a specimen with smaller in-plane and out-of-plane dimensions and ii) increase the accuracy of analytical models by considering an experimental result as an input of the model. Although several researchers [136–144] have paid attention to scaling of composite laminates under in-plane loading, applying this idea for specimens under out-of-plane loading is a complex task even when considering only a linear elastic response. Morton [145] applied the classical scaling laws for the elastic behaviour (undamaged) of transversely impacted carbon-fiber beams. Qian et al. [146] developed scaling laws for the elastic response (undamaged) of the impacted composite laminates. In their study, an experimental analysis was carried out by increasing the initial in-plane size by a factor of five to validate their laws. They also considered that the damage process in composite laminates is too complex so the damage part of the response can not be scaled with analytical laws. Sankar [147] provided a method for nondimensionalizing the impact problem. In this study, the impact problem of a plate was defined by five dimensionless parameters. Although good agreement was found between these laws and the experimental results, their use is limited to predict the elastic response and the maximum impact force. Liu et al. [148] have studied the size effects on impact experiments. In their study, the influence of the laminate thickness and the in-plane dimension was studied. They concluded that the thickness effect is much more significant than the in-plane dimensional effect. Recently, Abisset et al. [68] have done an attempt to give some preliminary interpretations based on simplified analytical models of the main scaling effects by observing experimental QSI. Having a look to the parameters that affect the QSI test, the in-plane dimension is the most effective parameter to be scaled to reduce the size of the tested specimens reducing testing and computational costs.

From this short review it can be concluded that the available scaling laws are only valid to scale the elastic response of the impact test and the maximum impact force. However, there is a lack of knowledge in the scaling of the damage threshold load, the response of the damaged laminates and the damage size. The present work is an effort in this direction.

2.5 Summary and conclusions

As a summary of this chapter, quasi-static indentation tests can provide meaningful evidence of the damage events occurring during a low velocity impact as well as its sequence and interactions. Four main damage mechanisms can be detected during impact/quasi-static indentation on composite laminate which can be summarized as: matrix cracking, delamination, fiber breakage and perforation. The sequence of these four damage mechanisms is not clear yet and the interaction between them also is not clear. There is a lack of knowledge on the fiber breakage damage mechanism because most of the available experimental work deals with low energy levels which are below the energy required to break the fibers. There are too many parameters affecting this kind of loading, i.e., in-plane size, impactor size and shape, plate thickness, ply thickness, stacking sequence and mismatch angle between plies. The influence of these parameters is not clear in the literature.

The prediction of the indentation depth is important in many engineering applications. The available analytical models are able to predict the indentation depth. However, the predictions of these models correlate well with the experimental results for a small indentation depth, while for large indentations the agreement between experimental results and predictions is poorer.

From this comprehensive review it can be concluded that the available scaling laws are only valid to scale the elastic response of the impact test. However, there is a lack of knowledge in the scaling of the response of damaged laminates and the damage size.

Part I

Experimental investigations

3 Damage sequence in unidirectional-ply laminates

3.1 Introduction

In this chapter, a detailed study of QSI tests on carbon laminated composites is presented. Matrix cracks and delaminations were investigated, at different indentation displacements, by means of Scanning Electron Microscopy (SEM) and ultrasound C-scan inspections. The evolution of the indentation profile with time after the QSI test was monitored by means of a 3D surface inspection technique. In view of the results, four stages in the sequence of damage mechanisms during a low velocity impact event are clearly established and properly explained.

3.2 Materials and methods

The material used in this study was a UD tape prepreg AS4D/TC350 carbon/epoxy from which a laminate with stacking sequence $[45/0/-45/90]_{3s}$ was manufactured at the Dutch National Aerospace Laboratory-NLR (The Netherlands) using fiber placement technology following standard aeronautical procedures. The unidirectional material properties were measured following the corresponding ASTM standards in a previous work by Sebaey et al. [59]. The unidirectional elastic properties are summarized in Table 3.1. The out-of-plane Poisson's ratio, ν_{23}, is assumed to be equal 0.5, since it is not provided by Sebaey et al. [59]. The specimen dimensions for the QSI tests were 80 $\times$ 80 $\times$ 4.46 mm. No thermal or moisture conditioning was performed before or during the tests.

Tab. 3.1: Elastic and thickness properties of the AS4D/TC350 carbon/epoxy plies [59].

Elastic modulus in the fiber direction, E_{11}	135.4 GPa
Elastic modulus in the transverse direction, E_{22}	9.3 GPa
Shear modulus, G_{12}	5.3 GPa
Poisson's ratio, ν_{12}	0.32
Ply thickness, t_{ply}	0.184 mm

The QSI tests consisted of step-loading bending indentation tests, which were performed using a 100 kN MTS universal testing machine. Figure 3.1 illustrates the experimental setup with the sample location, indenter, and the fixture (centrally-

hollow support). The indenter was a stainless steel hemisphere of 12.7 mm in diameter according to ASTM standard [149]. Basically, the fixture consists of two hollow cylindrical plates with a 50 mm diameter hole clamping the specimen. The specimen is clamped between both plates to prevent the separation of the specimen edges from the base during loading. The set of clamping plates and specimen is mounted on top of three columns to allow the direct measurement of the deflection of the specimen with a displacement transducer (Transducer 2 in Figure 3.1a). The indentation load is centrally applied (see Figure 3.1b). The QSI tests were carried out under displacement control at a loading rate of 0.5 mm/min. To avoid the testing machine compliance influencing the results, the displacement of the indenter was measured directly using a displacement transducer (Transducer 1 in Figure 3.1a).

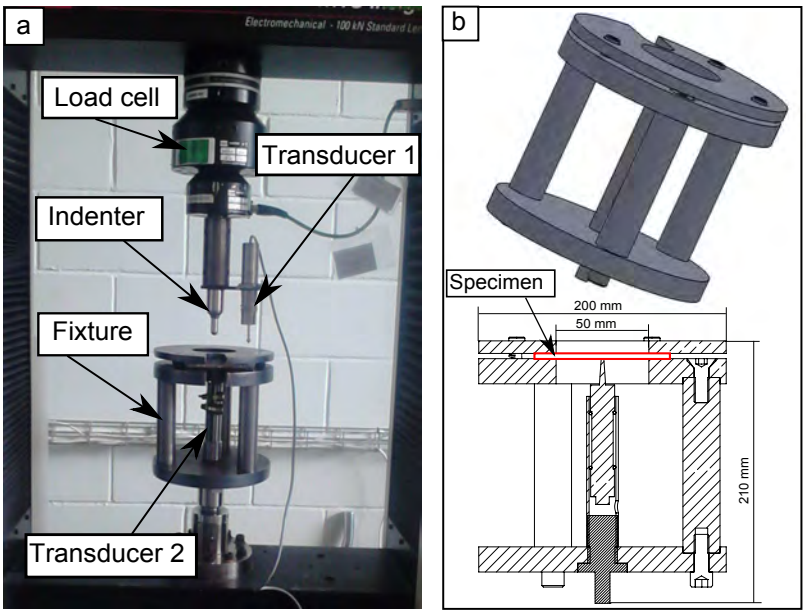

Fig. 3.1: Experimental set up of the QSI test: (a) indentation test set-up and (b) schema of the indentation fixture.

The test campaign was organized into 5 batches of 3 specimens (15 specimens in total). Each batch was loaded up to a certain displacement level: d = 0.8, 1.0, 2.0, 3.2 and 3.9 mm. When the consigned displacement was reached, some specimens were unloaded and analyzed by means of SEM to investigate the damage generated in the material. A Zeiss EM910 Field Emission Gun, 40 kV acceleration voltage, 0.3 nm resolution and a magnification range (1000×:500000×) was employed to this end. Two of the tested specimens for each set were cut at the middle of the indentation area to analyze their cross-sections. In all cases, the surfaces of the specimens to be analyzed were put in resin and coated with gold to make them conductive.

The indentation depth of the tested specimens was measured 48 h after the QSI tests using Crysta-Apex C 3D surface roughness measuring machine which, according to the manufacturer's specifications, measures to an accuracy of 0.02 mm. This machine uses a tiny probe that moves along the indented area and measures the relative coordinates (X,Y,Z) of each point. The machine was programmed to measure 900 points in the indented area (30×30 mm^2) to obtain a complete profile. The repeatability of the measurement was checked by acquiring the indentation profile of one specimen three times in the same day and the scatter was not found to be relevant. In order to study the relaxation of the indentation, the same test was repeated at 2, 3, 6, 14, and 30 days after the QSI test.

A non-destructive ultrasonic inspection technique (C-scan) was used to capture the different delamination areas and their through-the-thickness position in the laminate. During this inspection, ultrasonic waves were emitted in the through-the-thickness direction of the specimen and the intensity of the reflected waves were recorded and compared to the initially emitted ones.

An elastic 2D axisymmetric contact model was generated using a commercial software to simulate the stress and strain distributions in the elastic stage of response. It is considered that a laminate with 24 plies is enough close to an homogeneous transversely isotropic material to its mechanical response be approximated by an axisymmetric model. The indenter and specimen were meshed using 2D 4-node structural elements. A convergence study of the FE results was conducted to ensure that the mesh refinement in the composite laminate was fine enough to capture the stresses, strains and deformations with reasonably accuracy. As a result, a graded mesh was created with a finer mesh close to the contact region (the mesh size was 0.1×0.1 mm at the contact area). The interaction between the indenter and the specimen was modeled as a contact pair with no friction between the indenter and the specimen. Geometric non linearities was conducted in this model. No damage models of the material were implemented. The boundary condition was assumed as a fixed support at the hole diameter (assuming no slipping between the two rigid substrates and the specimen). The 3D homogenized elastic properties of the laminate [150] summarized in Table 3.2 were introduced into the model. To calculate these 3D laminate properties the transverse shear modulus of the lamina, G_{23}, was calculated considering that the unidirectional ply was transversely isotropic.

Tab. 3.2: 3D homogenized elastic properties of the AS4D/TC350 $[45/0/-45/90]_{3s}$ laminates.

$E_{xx} = E_{yy}$ GPa	E_{zz} GPa	ν_{xy}	$\nu_{xz} = \nu_{yz}$	G_{xy} GPa	G_{xz}=G_{yz} GPa
52.6	11.1	0.307	0.322	20.1	4.25

3.3 Results and discussion

3.3.1 Sequence of damage events

Figure 3.2 shows a load-displacement curve representative of each batch; with each batch corresponding to a predetermined displacement (d = 0.8, 1.0, 2.0, 3.2 and 3.9 mm). As each curve overlaps the curves with smaller displacement, this figure illustrates the excellent repeatability of the QSI tests. On the whole, the load-displacement behaviour is characterized by a mainly elastic increase of load up to a local load maximum, $F^{\mathrm{m}}_{\mathrm{max}}$, at a displacement of around 0.85 mm, at which there is then a sudden load drop. Following this initial drop, the load grows monotonically until a second load drop occurs at d close to 3.4 mm.

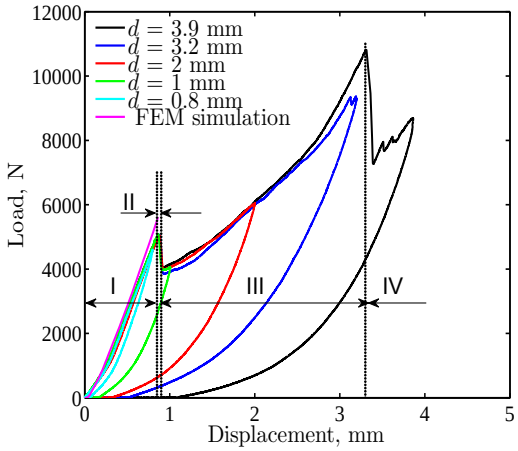

Fig. 3.2: Load-displacement curves from QSI tests of AS4D/TC350 specimens.

The average indentation depth (α_0), total energy (E_{T}), absorbed energy (E_{A}) and projected delamination area (A) of each batch tested is shown in Table 3.3. The total energy is calculated by integrating the area under the loading curve. The absorbed energy is calculated by subtracting the area under the unloading curve from the total energy. Representative SEM micrographs of the specimens' cross-section, and the corresponding C-scans of the four displacements of interest (d = 1.0, 2.0, 3.2 and 3.9 mm) are shown in Figures 3.3 and 3.4. In summary, these results show matrix cracking and no delamination for d = 1.0 and progressively increasing delaminations for d = 2.0 and d = 3.2 mm. In addition to these damage mechanisms, the specimen tested up to d = 3.9 mm exhibits extensive fiber breakage on the bottom side of the specimen. In view of these findings, QSI load-displacement curves can be divided into four different stages, termed here as I, II, III and IV.

The first stage (I), here referred to as the elastic stage, spans a displacement of 0 to 0.85 mm and is associated with the increase in the indentation load according to the Hertzian contact and bending response up to a local maximum load $F^{\mathrm{m}}_{\mathrm{max}}$ (the first

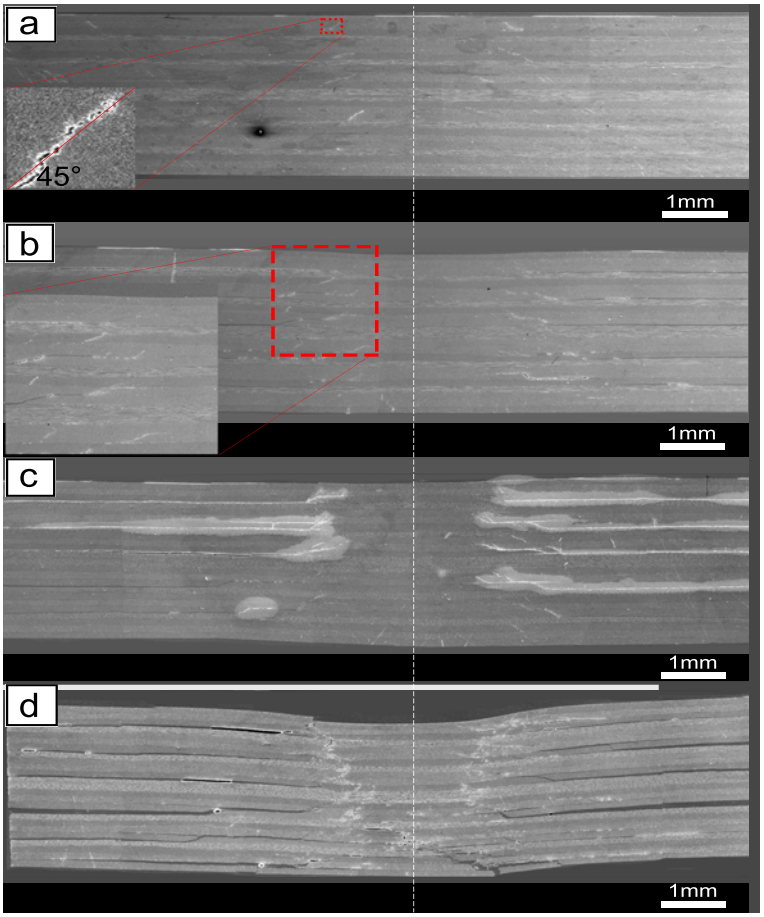

Fig. 3.3: SEM micrographs of the specimens' cross-section at different displacement levels: (a) $d = 1$ mm (b) $d = 2$ mm, (c) $d = 3.2$ mm, and (d) $d = 3.9$ mm. (The specimens were cut along the 90° direction. The dashed white line represents the center of the indentation).

Tab. 3.3: Related indentation damage parameters.

Stage	displacement d (mm)	Ind. depth α_0 (mm)	Total energy E_T (J)	Abs. energy E_A (J)	Projected delamination area A (mm^2)
I	0.8	0.194 ± 0.005	1.59 ± 0.54	0.328 ± 0.02	0
II	1	0.229 ± 0.016	2.57 ± 1.4	1.13 ± 0.63	0
III	2	0.412 ± 0.029	7.17 ± 2.6	4.14 ± 1.2	1015 ± 55
III	3.2	0.505 ± 0.033	14.8 ± 3.1	7.28 ± 2.3	2205 ± 84
IV	3.9	0.621 ± 0.019	22.6 ± 2.2	16.2 ± 1.6	2350 ± 140

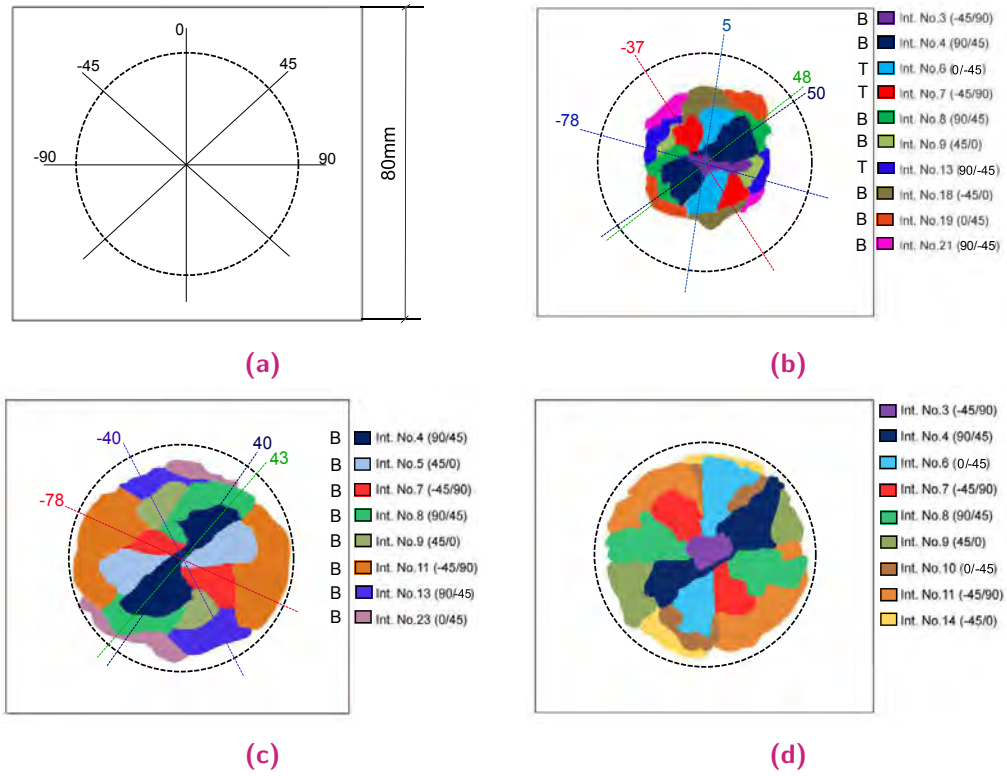

Fig. 3.4: Through-the-thickness position and extension of individual delaminations of specimens tested at different displacement levels: (a) d = 1 mm, (b) d = 2 mm, (c) d = 3.2 mm, and (d) d = 3.9 mm (dash circles represent the hole diameter, symbol (B) refers to the delamination dominated by the bottom ply orientation, symbol (T) refers to the delamination dominated by the top ply orientation; e.g, interface 3 (-45/90), the first angle refers to the ply above the interface, while the second angle refers to the ply below.

peak of the indentation load-displacement curve in Figure 3.2). There is no evidence of any form of damage in the SEM or C-scan prior to this load peak. Furthermore, the numerical load displacement curve obtained by the FEM has the same shape than the experimental response. The fact that it is a little more stiffer is associated to the idealized clamped boundary conditions in the FEM model.

The second stage (II), corresponds to a sudden load drop at 0.85 mm. In view of extensive matrix cracking being observed immediately after this load drop, Figure 3.3a, we termed it the matrix cracking stage. Matrix cracks grow in an almost $45°$ direction from the end of contact area in the transverse plies (see Figure 3.3a). No delaminations were observed either by SEM (Figure 3.3a) or by C-scan (Figure 3.4a). Therefore, these microstructural findings provide evidence that the sudden drop in the load-displacement response is due to the oblique matrix cracks.

As mentioned in the previous section, a FEM model was generated for the better understanding of the location and orientation of the matrix cracks. Figure 3.5 shows the resulting distribution of the principal strains for a displacement of the indenter $d = 0.85$ mm. The principal strain trajectories under tension and compression are also plotted in this figure. Taking into account that matrix cracks are more prone to appearing perpendicularly to tensile strains where the shear stress level is higher, the results of the simulation indicate that the first cracks to appear should be located close to the indenter contact area and at an angle of about $45°$. This is in good agreement with the SEM images taken. Therefore, after comparing the SEM inspections at 0.8 mm (not included as they did not exhibit any evidence of damage) and 1 mm displacements, observing the C-scans of these specimens (Figure 3.4a) and taking into account the FE results, it can be concluded that oblique matrix cracks through the specimen thickness are responsible for the observed load drop at 0.85 mm. Some researchers [20, 60, 96] assume that the first load drop in low velocity impact tests corresponds to the "delamination threshold". The argument is that a first delamination appears at the middle of the laminate, where the shear stresses reach a maximum. The load required to delaminate is [21]:

$$F_{\mathrm{d1}} = \pi \sqrt{\frac{32 G_{\mathrm{IIC}} D^*}{n+2}} \tag{3.1}$$

where D^* is the equivalent bending stiffness and n is the number of equally distributed delaminations. For the first delamination, $n = 1$. Once the first delamination is created, other delaminations appear at different interfaces and P_{DEL} decreases, resulting in the load drop observed in the experiments. Regarding the shear matrix cracks, it is assumed that, in spite of admitting their presence, they are believed not to have an effect on the load displacement curve. However, the absence of delaminations after the first load drop goes against this hypothesis. On the contrary, it confirms the results reported in [83–85] that defined the first drop as "Hertzian

failure and shear cracks". In summary, the load drop is not caused by the reduction of bending stiffness linked to delaminations, but to the sudden reduction of the shear stiffness due to matrix cracks. That is, delamination should be taken as a subsequent phenomenon to matrix cracking, rather than being related to the load drop.

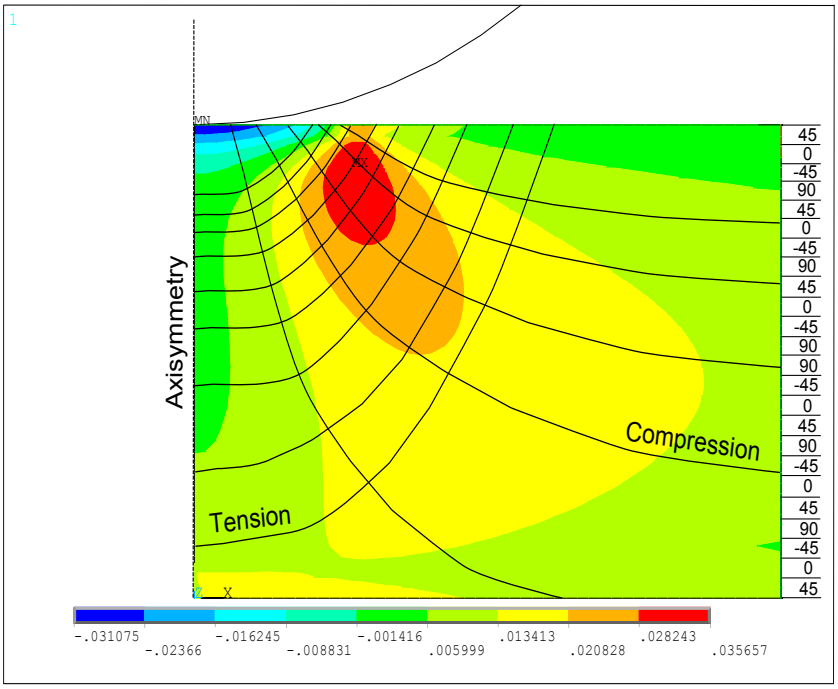

Fig. 3.5: Principal strain distribution and directions at stage II predicted by the FE simulation.

The third stage (III), within 1 mm $< d <$ 3.3 mm, is termed delamination propagation. During this stage the load once again increases with the applied displacement but at a lower slope than that of the elastic stage (I). Meanwhile, delaminations grow progressively (Figure 3.3b and Figure 3.4b). Although Equation 3.1 predicts a constant load when a given number of delaminations grow, the observed hardening in the load-displacement curve is due to geometrical non linearities [81, 82]. According to the SEM observation, the matrix cracks grow until they reach the interface with longitudinal plies for this cross-section, from which delaminations start to grow. This trend is also observed during the C-scan inspections. Figure 3.4b shows the extension and the through-the-thickness location of the delaminations for a displacement d = 2 mm. Delaminations grow dominated by the direction of the fibers of the adjacent plies. The projected delamination area is almost circular, likewise to the results reported in [60, 61, 151]. It is noticeable that delaminations appeared and propagated in all the interfaces, starting from interface number 3 to interface number 9 (almost all the interfaces above the midplane). Due to the configuration of the C-scan, interfaces 1 and 2 were not detectable and the interfaces below the midplane are mostly hidden by the interfaces above them. Towards the end of stage

III, d = 3.2 mm, a higher crack density and a larger extent of delaminations is easily observable both by SEM (Figure 3.3c) and C-scan (Figure 3.4c).

Figure 3.6 shows the experimental c-scan observations at interfaces 7 and 13 at two different displacements; 2 and 3.2 mm. The dashed lines in the figure represents the hidden part of the delamination under the upper layer. The progression of the delamination shape from d = 2 mm to d = 3.2 mm provides evidence that the delamination starts following the direction of the reinforcement in the upper ply and then, for larger displacements, propagated towards the direction of the fiber in the lower ply. The interface 7 is located in the region of the maximum shear stresses (Figure 3.5) and the interface 13 is just below the the laminate centerline in which the 90 ply is clustered, resulting in a larger shear crack. To explain the projected delamination onset and propagation mechanism in interface 7, between $[-45/90]$, and interface 13, between [90/-45], a schematic drawing, Figure 3.6b, was generated based on our results and the results in Chen et al. [152], and Shyr et al. [84]. First, shear matrix cracks appear in the top and bottom layers as represented with number 1 in Figure 3.6b, and then the delamination grows following the orientation of the top layer, represented by number 2 in the figure. As the load increases, delamination grows according to the orientation of the bottom layer, represented by number 3 in the same figure.

The fourth stage (IV), extends from d = 3.3 mm to 3.9 mm. We termed it the fiber breakage stage. It is characterized by a sudden load drop at 3.3 mm. The SEM micrograph taken at d = 3.9 mm (Figure 3.3d) shows two damage mechanisms: a shear cone formation, in which plies are broken in the upper part of the laminate (the upper 2/3 of the laminate) and the tensile failure of plies at the bottom of the laminate (bottom 1/3 of the laminate). The conical damage at the upper 2/3 of the laminate follows the same path as the initial shear matrix cracks of stage II. This finding suggests that matrix cracks not only are important for the initiation of delaminations but they also drive fiber failure at this stage (IV).

The projected delamination area is often taken as a direct quantitative indication of the extent of damage caused by a low velocity impact [60], although recent works suggest that it is not a robust indicator [59]. Figure 3.7 summarizes the relation between the projected delamination area and the maximum displacement of the indenter. The initial impair of load capacity related to matrix cracking (stage II) is not accompanied by an increase in the projected delamination area. During stage III, the projected delamination area increases with the indenter displacement, indicating a stable delamination growth. However, in the last stage (IV), the conical failure is completely formed (see Figure 3.3d).

Figure 3.8 summarizes the sequence of damage events observed in the QSI tests along with its correlation with the load-displacement curve. The load displacement

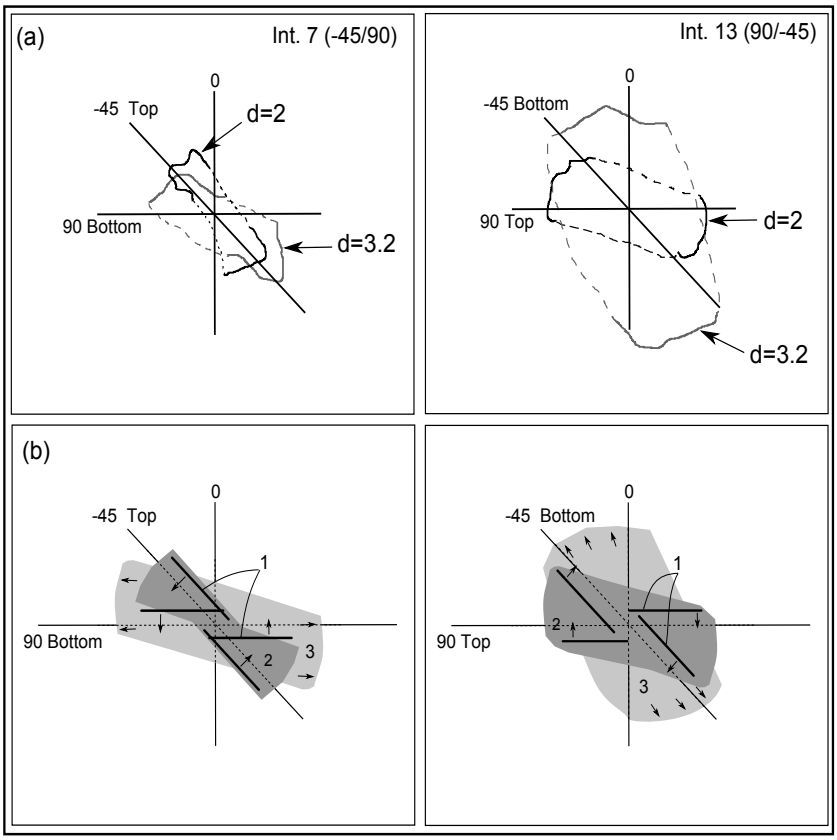

Fig. 3.6: Schematic drawing for the delamination propagation (a) projected delaminated area in interfaces 7 and 13, respectively, at displacements 2 and 3.2mm, (b) sequence of damage events, 1, shear matrix cracks, 2, delamination growth governed by upper plies and 3, damage evolution governed by bottom plies.

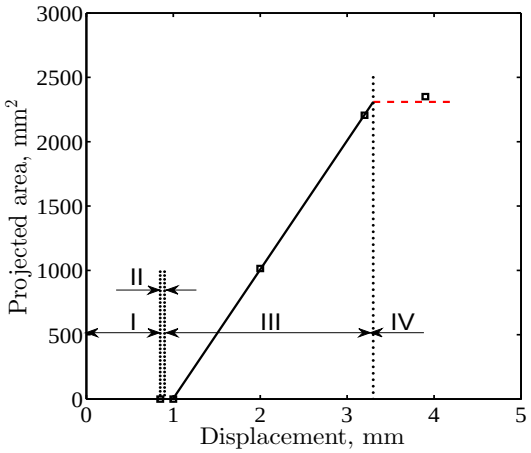

Fig. 3.7: Projected delamination area as a function of the maximum indenter displacement.

curve is plotted using four different colors, each color corresponding to the damage mechanism represented in Figure 3.8a of the same color.

It is worth noting that this sequence of events is not significantly affected by the size of the clamping device. Indeed, the initial forms of damage are matrix cracking and, subsequently, delaminations. According to Equation 3.1, the load for the onset of delamination does not depend on the size of the hole. On the other hand, the load for shear matrix cracks can be approximated by [21]:

$$F_s = \frac{4}{3}\sqrt{\frac{d}{2E^*}}(\pi h \tau_U)^{3/2} \tag{3.2}$$

where E^* is the equivalent contact Young modulus, d is the diameter of the indenter (spherical), h is the laminate thickness and τ_U the shear strength.

The two analytical expression, Equation 3.1and Equation 3.2, show none of the critical loads for shear matrix cracks or delaminations depend on the opening window (unsupported area of the specimen). On the other hand, the effect of the specimen thickness scales for both expressions with $h^{(3/2)}$. Therefore the use of a thicker specimen must increase the onset of the critical load accordingly. Other damage mechanisms, such as those related to the tensile stresses at the bottom of the specimen (matrix cracks or fibre failure), are more sensitive to the thickness of the specimen and window size of the fixture.

This comprehensive background explains the behaviour of thin-ply laminates under low velocity impacts [76], when shear matrix cracking is reduced, the shear stiffness is not impaired, so the first load drop in the load-displacement curve is not present. Furthermore, the absence of the shear cone in thin plies promotes that fiber failure is dominated by the tensile stresses at the bottom of the laminate [76, 153].

The variation of the total, elastic, and absorbed energy versus the indentation displacement is represented in Figure 3.9. During stage I, the absorbed energy is almost zero, which means that all the applied force is stored as elastic energy (Hertzian contact and bending response). At stage II, the absorbed energy begins to increase. This is due to the energy absorbed by the first observed damage mechanism (matrix cracking). As the indentation displacement grows, the absorbed energy is linearly increased due to the formation and propagation of delaminations (stage III). At an indenter displacement of 3.9 mm the elastic energy exhibits a large drop related to fiber breakage. Upon the progression of fiber damage, the material loses the capability to withstand more pressure and most of the applied energy is dissipated, until the complete failure of the specimen.

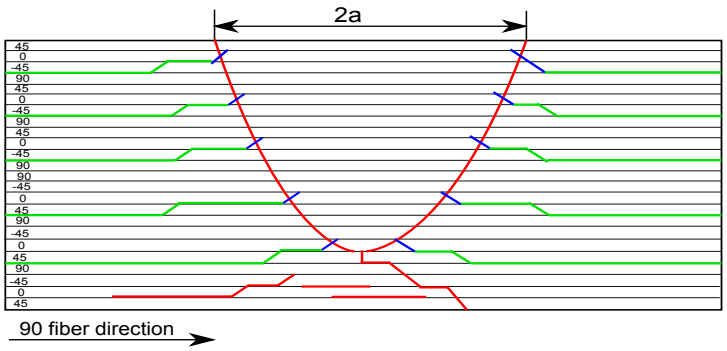

(a) Schematic drawing of the indentation damage

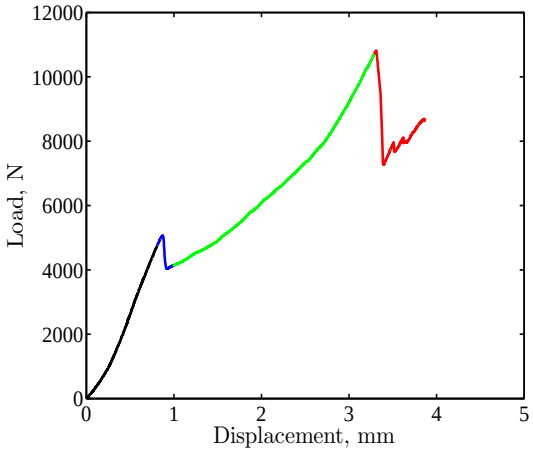

(b) Related load displacement curve

Fig. 3.8: Summary of the QSI damage in composite laminates (each color in the load displacement curve refers to the corresponding damage in the schematic drawing).

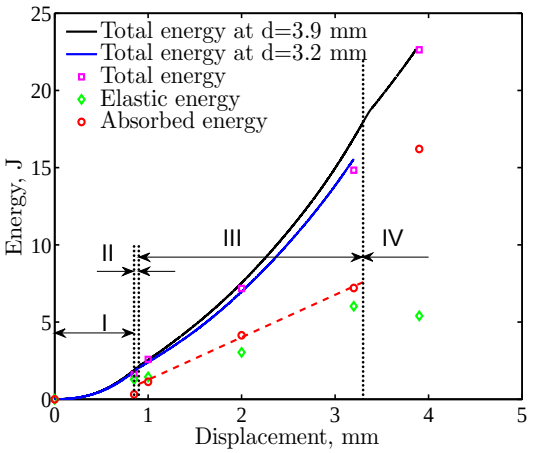

Fig. 3.9: Total, elastic, and absorbed energies vs. indenter displacement.

3.3.2 Permanent indentation

The results of the 3D scanning of the indentation footprints measured 48 h after the test are shown in Figure 3.10. For the smallest indenter displacement, $d = 1$ mm, the measured indentation depth was 0.21 mm, whereas for $d = 3.9$ mm it reached 0.62 mm. In all the cases the indentation profile follows a concentric-circles pattern unaffected by the orientation of the upper ply. The relaxation of the indentation depth was monitored by measuring it 2, 3, 6, 14, and 30 days after the QSI test. The evolution of the measured indentation depth, and its normalized value (α/α_0), is characterized by a rapid decrease until a steady state is reached after 14 days (Figure 3.11). The decreasing rate of the measured indentation is almost the same for all the indentation energies regardless of the damage level attained (Figure 3.11b). Therefore, it should be related to the intrinsic relaxation of the viscoelastic matrix.

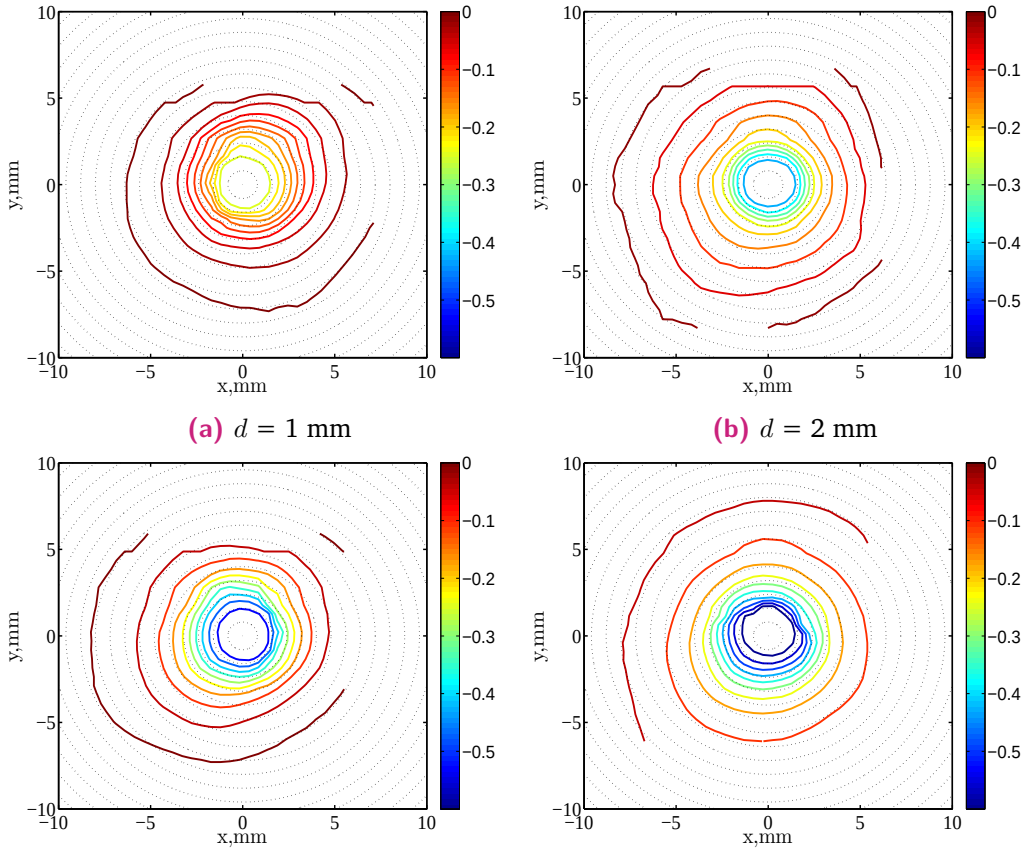

(a) $d = 1$ mm **(b)** $d = 2$ mm

(c) $d = 3.2$ mm **(d)** $d = 3.9$ mm

Fig. 3.10: Indentation profiles of the CFRP laminates at different displacements of the indenter. The color bars indicate the indentation depth.

After 10 days, all measured indentation depths fall below the Barely Visible Indentation Damage (0.6 mm, as proposed in [154]). Only the indentation depth of the specimen tested up to $d = 3.9$ mm and measured after 2, 3 and 6 days was greater than this threshold. The combination of a measured indentation depth below the BVID and the observed damage mechanisms (delaminations in most of the interfaces

and the extensive fibre breakage for $d = 3.9$ mm) raise some concerns about the interpretation of the BVID threshold as a damage level with no detrimental effect on the subsequent load capability of the structure.

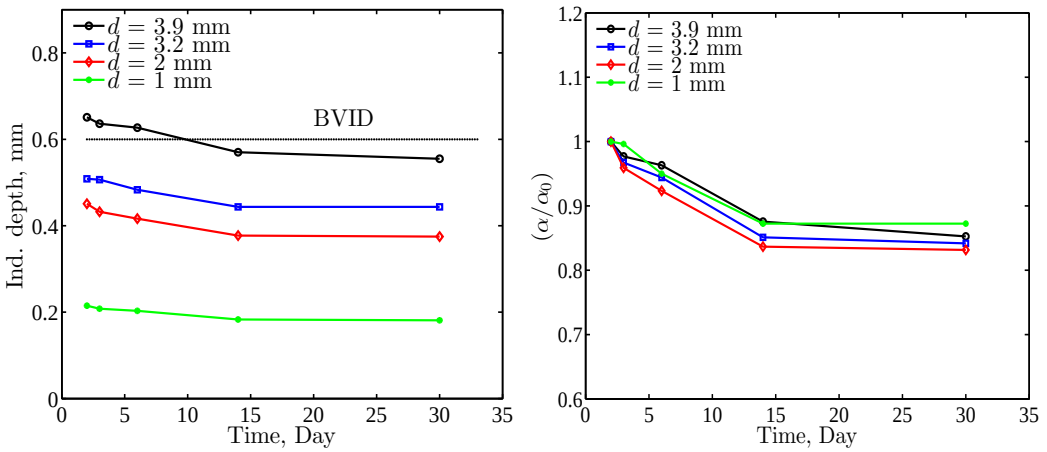

(a) Residual indentation **(b)** Normalized residual indentation (α/α_0)

Fig. 3.11: Relaxation of the measured indentation vs. time (α_0 defined as α at day 2).

3.4 Conclusions

A series of Quasi-Static Indentation tests on quasi-isotropic carbon reinforced composite laminates have been performed to investigate the damage scenario during a low velocity impact event. The microstructural analysis using SEM and the C-scan inspections after the tests, pointed to four different stages in the development of damage in the material samples. For indentation displacements below 0.85 mm, stage I, the specimens mainly behaved elastically with no evidence of any form of damage. Stage II, at 0.85 mm, was characterized by a sudden drop in load related to the onset of matrix cracking, whereas no evidence of delaminations was observed at this stage. Matrix cracks were located in stress concentration areas with high tensile principal stress components. Stage III was characterized by the progressive growth of delaminations initiated at the matrix crack tips. Load and delamination extension progressed until fiber failure took place on the bottom of the specimens, which was then followed by a drastic load drop.

The indentation profile was almost circular for all indentation displacements and the indentation depth relaxed significantly during the first 14 days after the test. These observations might help in establishing appropriate inspection or maintenance intervals regarding the detectation of indented composite parts.

4 Damage sequence in thin-ply laminates

4.1 Introduction

With the aim of delaying the onset and propagation of damage, reducing the ply thickness has been reported to have benefits in lessening intra-laminar [75, 155–158], inter-laminar [159, 160] and splitting damage [136, 161], without using special resins and/or fiber architectures [21, 69, 77, 162]. The use of thin- or ultra-thin-ply laminates, with thicknesses below 0.1 mm, has been analyzed in the recent years by several authors [153, 157]. In addition, the strength performance in other well-known tests on composite material coupons is enhanced when using thin-ply technology. Some examples from the literature are: Unnotched Tension [69, 76, 77], Bearing [76], Open-Hole Compression [69, 76, 77], and Compression After Impact [60, 77, 78]. The results of these tests for thin- and thick-ply laminates are summarized and compared in Table 4.1; as can be observed, significant strength improvement is obtained for thin-ply laminates.

For the particular case of damage resistance assessment in low-velocity impact loading, Yokozeki et al. [69, 163] reported that the overall extent of delamination is independent of the ply thickness. However, the projected delamination areas reported by González et al. [60] showed a clear effect of the ply thickness on the damage resistance: the thicker the ply thickness is, the larger the delamination area is. Saito et al. [78] and Amacher et al. [76] reported that the ply thickness has a great effect on the delamination area: the thicker the ply thickness is, the smaller the delamination area is. In any case, the understanding of the appearance and growth of the different damage mechanisms present in an impact event, as well as their interactions, has not been sufficiently consolidated. More studies should be carried out in order to improve the damage resistance and the damage tolerance of composite structures that are susceptible to impact.

This chapter analyzes the associated damage mechanisms and their sequence in thin- and ultra-thin TeXtreme® plain weave ply composite laminates under QSI tests. Inspections by Optical Microscopy and ultrasonic C-scan technique were performed to identify the different damage mechanisms that occur at different indenter displacements. Also, indentation profiles of the indented surfaces were measured after the tests by means of a 3D coordinate measuring machine. Moreover,

Tab. 4.1: Strength performance on quasi-isotropic laminates: Unnotched Tension (UT), Bearing (B), Open-Hole Compression (OHC), and Compression After Impact (CAI).

Ref.	Material	Fabric	Ply thickness [mm]		UT [MPa]		B [MPa]		OHC [MPa]		CAI [MPa]	
			t_{thick}	t_{thin}	Thick	Thin	Thick	Thin	Thick	Thin	Thick	Thin
[77]	T800S/BT250E-1	Unidirectional	0.125	0.040	700	980	-	-	547	490	-	-
[69]	MR50K/#1063EX	Unidirectional	0.160	0.080	812	974	-	-	296	323	228	246
[60]	AS4/8552	Unidirectional	0.728	0.182	-	-	-	-	-	-	105	133
[78]	TR50S/#350	Unidirectional	0.150	0.038	-	-	-	-	-	-	380	450
[76]	M40JB/80EP(CF)	Unidirectional	0.300	0.030	595	847	476	584	215	255	-	-

the relaxation of the damaged material was measured by means of a dent-depth gauge.

4.2 Materials and methods

The fiber material used in this study was Tenax®-E HTS45 12K 800tex of 240 GPa tensile modulus, presented as TeXtreme® plain weave with 20 mm wide yarn fabrics, manufactured by Oxeon AB. TeXtreme® plies are dry cross-ply non-crimp fabrics, where the excess of resin pockets is minimized. Thus the weight and strength are improved in comparison with conventional woven plies. It can be considered that the behaviour of this type of plies is a combination of that of woven and unidirectional type plies since the yarns are wide. Two different ply thicknesses were considered: 0.08 mm and 0.16 mm (with 80 gsm and 160 gsm areal weights, respectively), which correspond to a yarn thickness of 0.04 mm and 0.08 mm, respectively. In the following, these plies are respectively identified as Ultra-Thin-Ply (UTP) and Thin-Ply (TP). The fibers were impregnated by HexFlow® RTM 6 mono-component epoxy system, supplied by Hexcel® by means of Resin Transfer Moulding (RTM) process. The curing temperature was 180 °C during 90 minutes. The glass transition T_g temperature of the RTM6 resin is 195 °C. The plies were coated with a binder, Bisphenol A with high molecular weight, to improve the interface properties in the laminate and to avoid the movement of the fibers during the manufacturing process. The manufactured laminated plates with UTP and TP both resulted in a fiber volume fraction of 57 %, using EN 2564:1998 [164].

The stacking sequence of the manufactured plates was $[((45/-45)/(0/90))_n]_s$, with n equal to 7 and 14 for TP and UTP laminates, respectively; for both cases, the nominal laminate thickness was of 4.5 mm. The ASTM D7136 [165] test method for drop-weight impact event was taken as reference in order to define the specimen dimensions and the QSI clamping system. Therefore, the in-plane specimen dimensions were 150 mm $\times$ 100 mm, where the orientation $0°$ was aligned with the major in-plane dimension, i.e. 150 mm. The clamping system consists of a flat base

with a 125 mm $\times$ 75 mm rectangular cut-out and four clamps with rubber tips which fix the specimen during the QSI tests. The indenter was hemispherical-shaped with a diameter of 16 mm and made of stainless steel. Figure 4.1 illustrates the QSI test set-up with the clamping system, the specimen location, and the indenter. As can be observed, a laser displacement transducer MEL M70LL was used to measure the back-face displacement of the plate just in the indentation point. A white tape was glued on the back-face of the specimen to reduce the voltage noise and so improve the displacement measurement resolution. According to the ASTM D6264 standard [149], the QSI tests were carried out under displacement control at a loading rate of 0.5 mm/min by means of an electromechanical testing machine MTS Insight 100 equipped with a 100 kN load-cell.

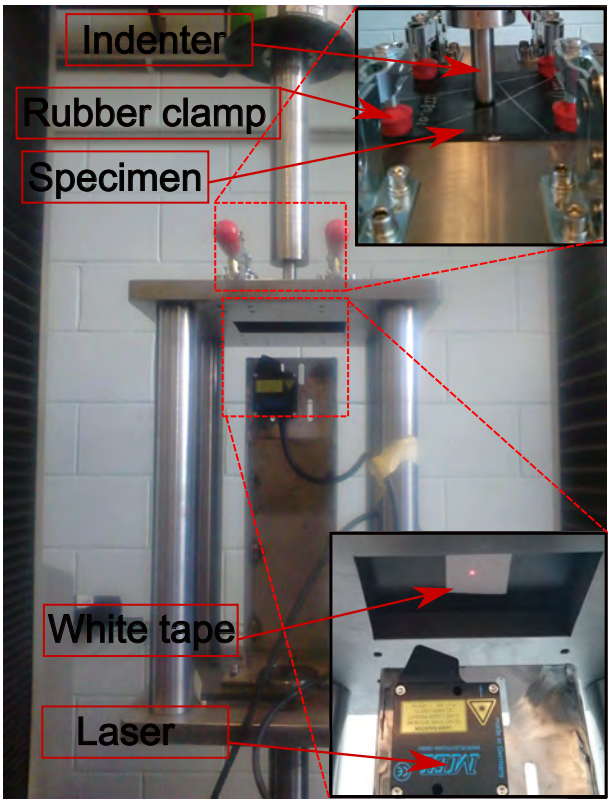

Fig. 4.1: Experimental test set-up of the QSI test.

The test campaign was organized into nine batches for the TP laminates and seven batches for the UTP laminates. Each batch was loaded up to a selected displacement level: d = 2.0, 2.8, 3.5, 4.0, 5.8, 7.8 and 8.5 mm for both laminates. Additionally, for the TP laminates, two extra displacements of 1.5 and 5.0 mm were considered. For each batch, one specimen was tested except for displacements of 4.0, 5.8 and 7.8 mm, where two specimens were considered. These displacements were defined based on previous experimental results of drop-weight impact tests and on the observation of an indentation test until complete perforation (d = 8.5 mm) to detect evidences on the load-displacement measurements. When the selected displacement was

reached, the specimens were unloaded and the indentation depth of the specimens was measured half-an-hour after the QSI tests by means of a dent-depth gauge. Afterwards, the specimens were inspected by ultrasonic C-scan technique to capture the different delamination areas and their through-the-thickness location. Finally, some of the specimens were cut at the middle of the indentation area to analyze the generated cross-section damage by means of optical microscope type LEICA DMR-XA of 0.2 μm resolution and a magnification range (5×:100×).

In order to study the relaxation of the indentation, the measurement with the dent-depth gauge was repeated with some specimens at: 0.5, 1.0 and 2.0 hours; and 1, 2, 4, 7, 14, 20 and 25 days after the QSI test. The storage conditions, humidity and temperature, were 48.5 % RH and 22.5 °C, respectively. Also, a Mitutoyo Crysta-Apex C 3D coordinate measuring machine with a resolution of 0.02 mm was used to measure 400 points in the indented area (20 mm × 20 mm) after 1 day of the indentation test to obtain a complete 3D profile.

4.3 Results and discussion

4.3.1 Sequence of damage events

A sample of the load-displacement curve for each batch of the TP and UTP laminates is shown in Figure 4.2. Since each curve overlaps the curves with smaller displacement, it indicates a good repeatability of the QSI tests for both type of laminates. On the whole, the load-displacement behavior is characterized firstly by an elastic increase of load up to a local maximum load, F_{d1}, at which there is a change in the response. Following this initial change, the load grows monotonically until a large load drop occurs. Finally, a fairly plateau-shaped stage takes place until the complete perforation of the specimen.

The mean values of the indentation depth (α_0), the total energy (E_{T}), the dissipated energy (E_{D}) and the projected delamination area (A) of each batch tested are shown in Tables 4.2 and 4.3 for TP and UTP laminates, respectively. The total energy is calculated by integrating the area under the load versus displacement curves; the elastic energy is calculated by the area under the unloading curve; and the dissipated energy is obtained by subtracting the elastic energy from the total energy.

Optical microscope micrographs of the cross-sections of the specimens and the corresponding C-scan inspections at the selected displacements for both laminates are shown in Figure 4.3 to Figure 4.6. These results show the damage sequence for both materials which can be described as: matrix cracking and delamination onset at d = 1.5 and 2.0 mm for TP and UTP laminates, respectively; progressively increasing delaminations up to d = 4.3 and 3.6 mm for TP and UTP laminates, respectively.

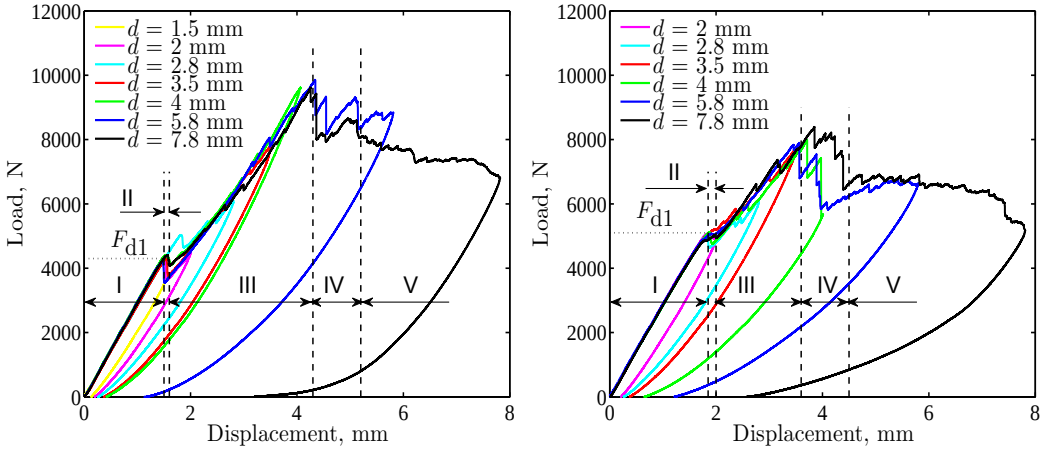

(a) Thin-Ply (TP) laminate **(b)** Ultra-Thin-Ply (UTP) laminate

Fig. 4.2: Load-displacement curves from QSI tests for TP and UTP laminates. The specimens tested at $d = 5.0$ mm and 8.5 mm for TP laminate and $d = 8.5$ mm for UTP laminate are not shown since they not give additional meaningful data.

Tab. 4.2: Related indentation results for TP laminate.

Stage	d (mm)	α_0 (mm)	E_T (J)	E_D (J)	A (mm^2)
II	1.5	0.131	3.5	1.1	142
III	2.0	0.153	5.3	1.8	372
III	2.8	0.201	9.9	3.5	781
III	3.5	0.241	14.6	5	1499
III	4.0	0.511	19.9	6.3	1695
V	5.8	0.965	35.1	20.6	2046
V	7.8	2.273	49.7	40.5	2302

Tab. 4.3: Related indentation results for UTP laminate.

Stage	d (mm)	α_0 (mm)	E_T (J)	E_D (J)	A (mm^2)
II	2.0	0.151	5.6	1.7	458
III	2.8	0.221	9.9	3.5	747
III	3.5	0.255	15.3	5.5	1245
IV	4.0	0.540	18.6	11.2	1376
V	5.8	1.135	31.1	19.7	2576
V	7.8	2.531	42.4	35.6	3582

It is worth noting that delaminations can occur between and also inside plies due to the woven architecture of the TeXtreme® plies. The specimens tested until 5.8 mm show extensive fiber breakage on the top and the bottom sides for both types of laminates. Finally, specimens tested until 8.5 mm are completely damaged. In view of these findings, QSI load-displacement curves can be divided into five different stages, referenced here as: I, II, III, IV, and V (see Figure 4.2).

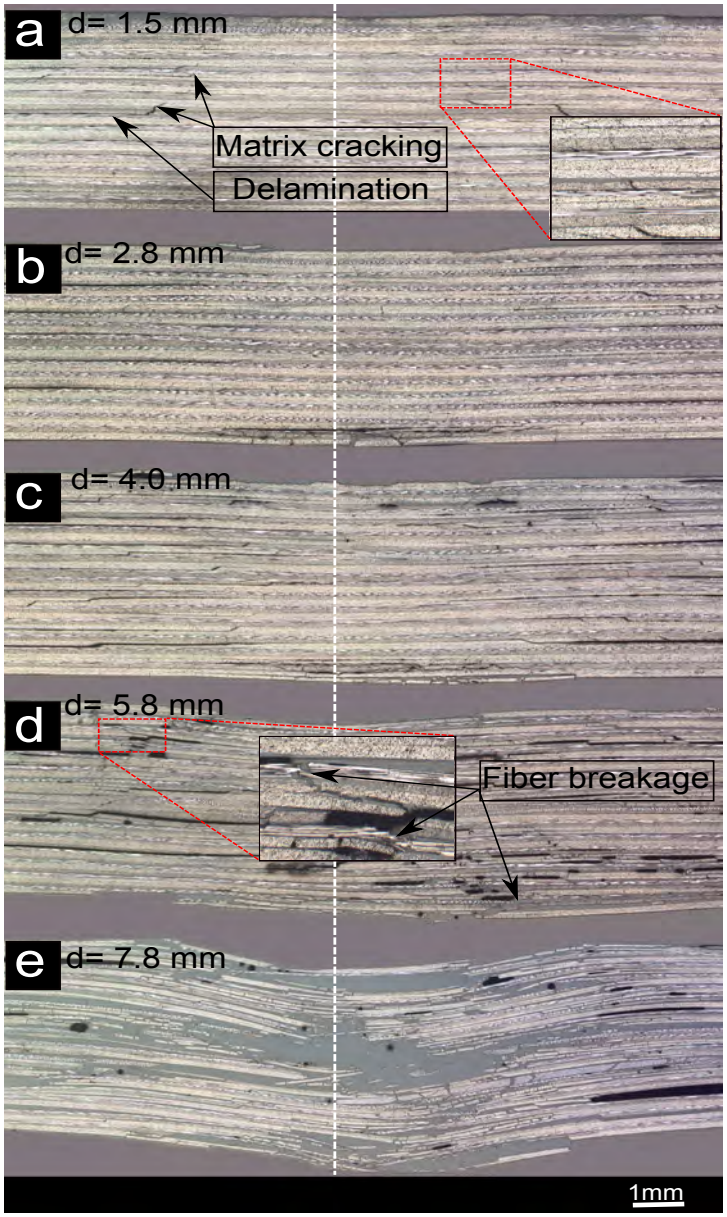

Fig. 4.3: Optical microscope micrographs of the cross-section of the Thin-Ply specimens (TP) at different displacement levels (the dashed white line represents the center of the indentation).

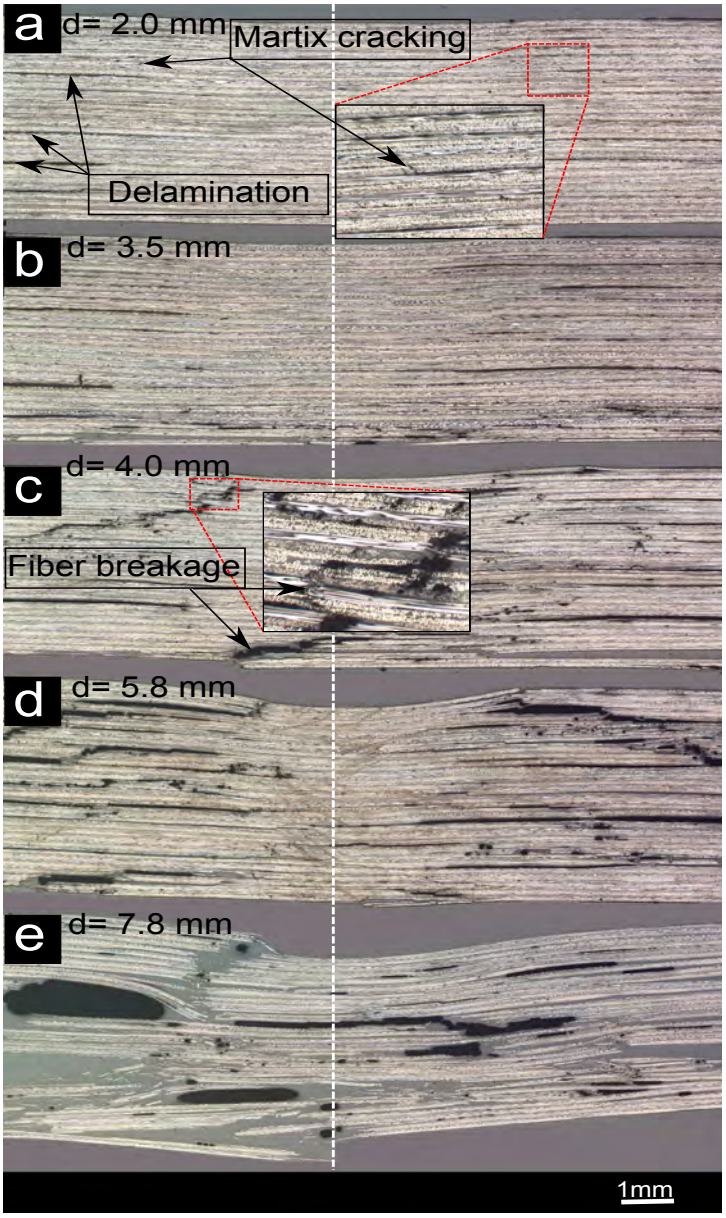

Fig. 4.4: Optical microscope micrographs of the cross-section of the Ultra-Thin-Ply specimens (UTP) at different displacement levels (the dashed white line represents the center of the indentation).

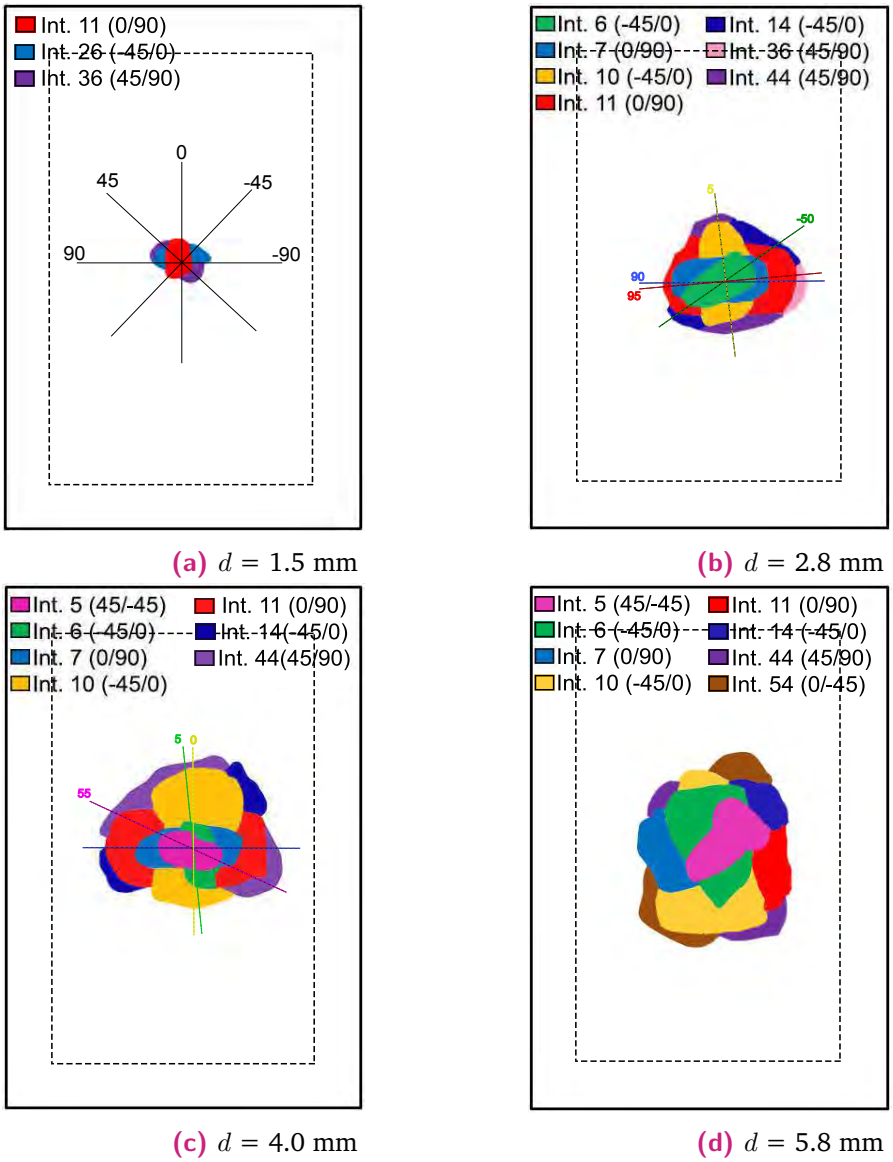

(a) $d = 1.5$ mm **(b)** $d = 2.8$ mm

(c) $d = 4.0$ mm **(d)** $d = 5.8$ mm

Fig. 4.5: Through-the-thickness position and extension of individual delaminations of TP specimens tested at different displacement levels (the dashed lines represent the rectangular hole dimension). Each C-scan corresponds to a different specimen.

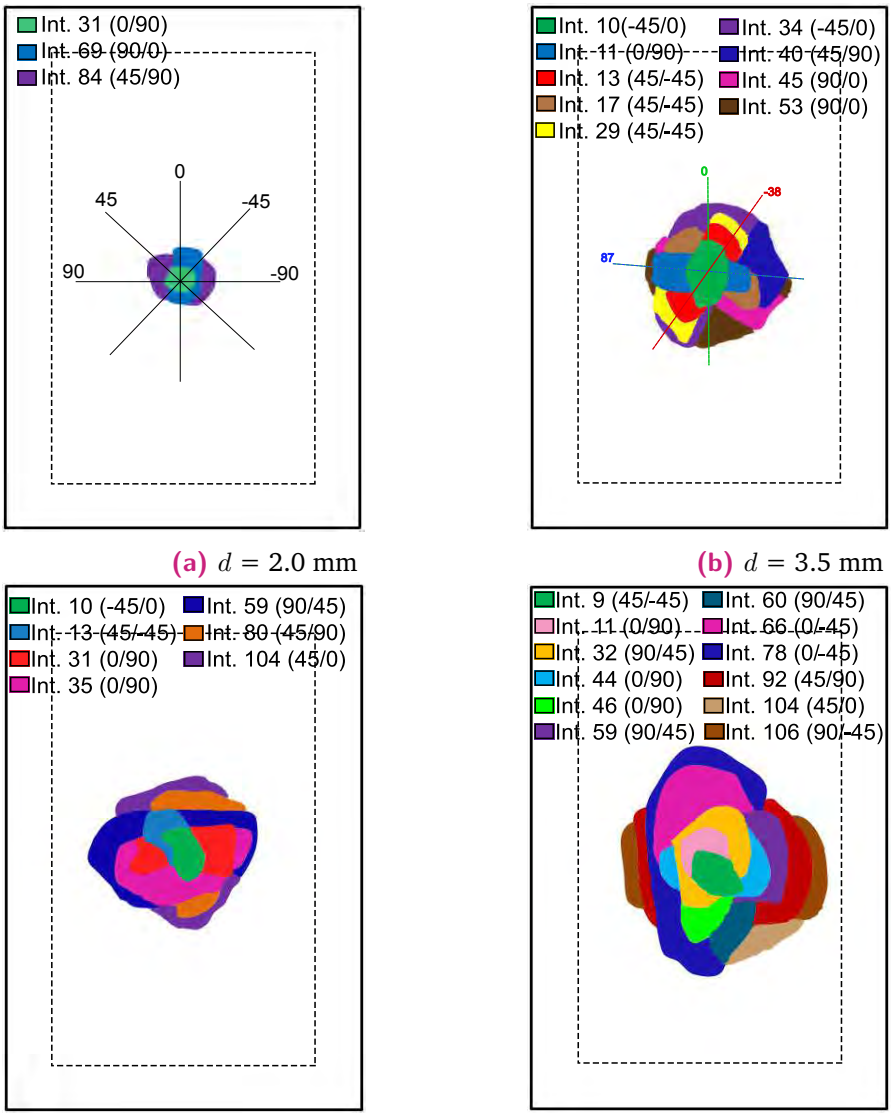

(a) $d = 2.0$ mm **(b)** $d = 3.5$ mm

(c) $d = 4.0$ mm **(d)** $d = 5.8$ mm

Fig. 4.6: Through-the-thickness position and extension of individual delaminations of UTP specimens tested at different displacement levels (the dash lines represent the rectangular hole dimension). Each C-scan corresponds to a different specimen.

Stage I: elastic response

Stage I, termed as the elastic stage, covers the displacement range from 0.0 to 1.5 mm, and from 0.0 to 2.0 mm, for TP and UTP laminates, respectively. This stage is associated with the increase of the indentation load according to the Hertzian contact and bending response, up to the threshold load F_{d1}. It is worth noting that F_{d1} for the UTP laminates is 16.7 % higher than for TP laminates , i.e. a difference of 0.9 kN.

Stage II: matrix cracking and delamination onset

Stage II corresponds to a sudden load drop at 1.5 mm for TP laminates. Extensive matrix cracking and induced delaminations can be observed according to Figure 4.3a and Figure 4.5a. For UTP laminates, a softer change of the load is observed around F_{th} according to Figure 4.2b at 2.0 mm. This zone is associated to the appearance of delaminations and also matrix cracks, as can be observed in Figure 4.4a and Figure 4.6a. These results are in accordance with the results presented by Yokozeki et al. [163].

Matrix cracks grow in an almost 45° direction from the edge of the contact area in the off-axis plies (see Figure 4.3a, and Figure 4.4a). The size and the density of the cracks in the TP laminates is much larger than for the UTP laminates. However, the projected delamination area after the first load drop for TP laminates is smaller than that for UTP laminates as can be seen in Figure 4.5a and Figure 4.6a, with the same number of delaminated interfaces. In view of these results, the results presented in Chapter 3 and previous findings [83, 84], we can conclude that the first clear drop in the load-displacement curve is related to the matrix cracking induced delaminations, as we can see for TP laminates. However, for the UTP laminates, the matrix cracking damage mechanism is delayed [76, 153], and the load drop evolves to a smooth load change which can be attributed to delamination onset.

Stage III: delamination propagation

Stage III, is termed delamination propagation, and takes place within 1.5 mm $< d <$ 4.3 mm, and 2.0 mm $< d <$ 3.6 mm, for TP and UTP laminates, respectively. During this stage, the load again increases with the applied displacement but with a lower slope than that of Stage I due to the growth of the delaminations. However, the stiffness can increase at this stage due to membrane effects. Associated results for TP laminates are shown in Figures 4.3b and 4.5b and Figures 4.3c and 4.5c, at $d = 2.8$ and 4.0 mm, respectively; and for UTP in Figsure 4.4b and 4.6b at $d = 3.5$ mm. Due

to the configuration of the C-scan, interfaces 1 to 4 for the TP laminates and 1 to 8 for the UTP laminates are not detectable. In addition, the delaminated interfaces below the midplane are mostly hidden by the delaminated interfaces above them with larger areas. As can be observed, for both laminates, delaminations start to grow in the already delaminated interfaces and then new delaminations appear and grow. Moreover, for the TP laminate, some delamination migrations were observed. At the end of this stage, higher crack density and larger delaminations are observed for both laminates according to optical microscope inspections (see Figure 4.3c and Figure 4.4b) and C-scan inspections (see Figure 4.5c and Figure 4.6b). Also, a larger amount of matrix cracks and fiber splitting was observed in the bottom quarter of both laminates (see Figures 4.3c and 4.4b), which justifies the small load drops in the load-displacement curve during this stage. It is also noted that the range of this stage is much longer for TP laminates than that for UTP laminates.

Based on the experimental evidence observed, we can conclude that for the TP laminates, delaminations are mainly onset by matrix crack tips. These cracks are caused by the shear stress due to contact, especially in the upper part of the laminate and the shear stresses due to bending in the middle part of the laminate (see Figure 4.3a). At larger loads, another source of delamination appears in the bottom part of the laminate as large tensile stresses produce matrix cracks that also act as delamination initiators (see Figure 4.3b). For the UTP laminates, the same trend is observed, but since matrix cracking is delayed this response occurs at larger displacements (see Figure 4.4a and b). Furthermore, several delaminations could be observed to appear without shear matrix cracks, especially in the middle of the laminate. This suggests that shear stress due to bending loads can be the source of these delaminations (see Figure 4.4a).

Stage IV and V: fiber breakage and perforation

In Stage IV, the ranges of displacement correspond 4.3 mm $< d <$ 5.2 mm and 3.6 mm $< d <$ 4.5 mm for TP and UTP laminates, respectively. During this stage a large load drop can be observed in the load-displacement curves. The optical microscope micrographs at indentation displacements in the range of Stage IV, or at higher displacements (e.g. Figure 4.3d for TP and Figure 4.4c for UTP), show that this load drop corresponds to the fiber breakage in the upper and lower parts of the specimens. The fiber breakage of the upper part is due to compressive stresses, although shear stresses due to contact also contribute to this breakage as they can reduce the compressive strength of the material. For the bottom part of the laminate, the fiber breakage is due to the bending tension stress. It is important to point out that this stage starts earlier in terms of displacement and load in the UTP laminate

than in TP laminates as can be seen in Figure 4.2. This can be due to a higher fracture toughness of the TP laminate since thicker plies are used [166].

Stage V starts from 5.2 mm and 4.5 mm until the complete perforation event, for TP and UTP laminates, respectively. In this stage, the load decreases as the displacement increases, until the indenter perforates the laminate. Extensive fiber breakage and delaminations can be observed in the optical microscope micrographs (see Figure 4.3e, and Figure 4.4d and e).

4.3.2 Damage summary

Figure 4.7 summarizes the relation between the projected delamination area and the displacement of the indenter for both laminate types. The delamination onset is observed during Stage II for both types of laminates. As noted in Section 4.3.1, this stage starts earlier for TP laminates than for UTP laminates. During Stage III, the projected delamination area increases linearly with the indenter displacement. During this stage, delaminations in TP laminates grow slightly faster than in UTP laminates. In stage IV, the fiber breakage stops the delamination growth in the TP laminates. However, delaminations in the UTP laminates continue to grow with the same rate of Stage III. During the final stage, Stage V, the delamination area for the TP laminates again increases but with a lower slope than that of Stage III. In contrast, for the UTP laminates, the delamination area increases with the same slope of that observed in Stage III. A possible reason for this is that after Stage III, the delaminations grow with a higher rate in the bottom half for both laminates, resulting in a "pine tree pattern" shape, especially for UTP laminates (see Figures 4.5d and 4.6d).

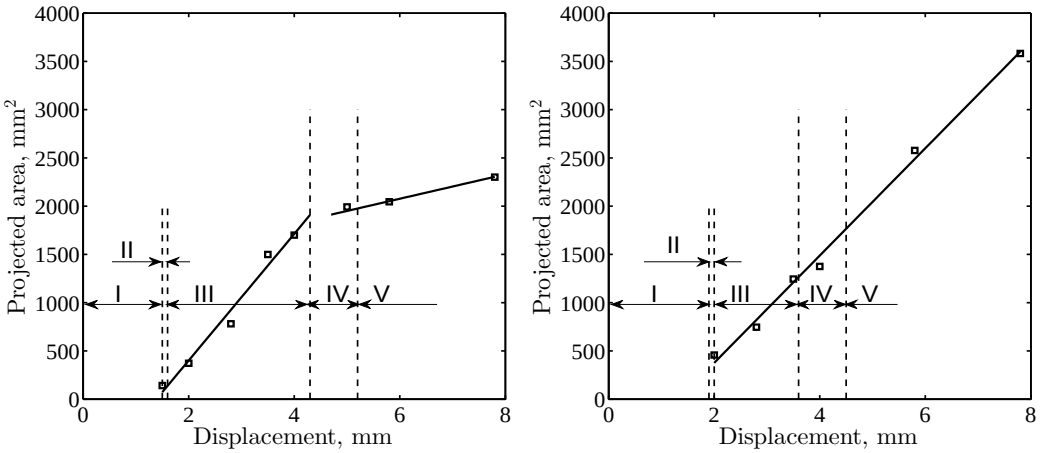

(a) Thin-Ply (TP) laminate **(b)** Ultra-Thin-Ply (UTP) laminate

Fig. 4.7: Projected delamination area as a function of the indenter displacement.

Figures 4.8a and 4.8b summarize the sequence of damage events observed in the QSI tests along with its correlation with the load-displacement curve for TP and UTP laminates, respectively. The load displacement curves are plotted using four different colors, where each color corresponds to a damage mechanism represented in the schematic drawings. These figures explain the expected behaviour of TP and UTP laminates under low-velocity impacts.

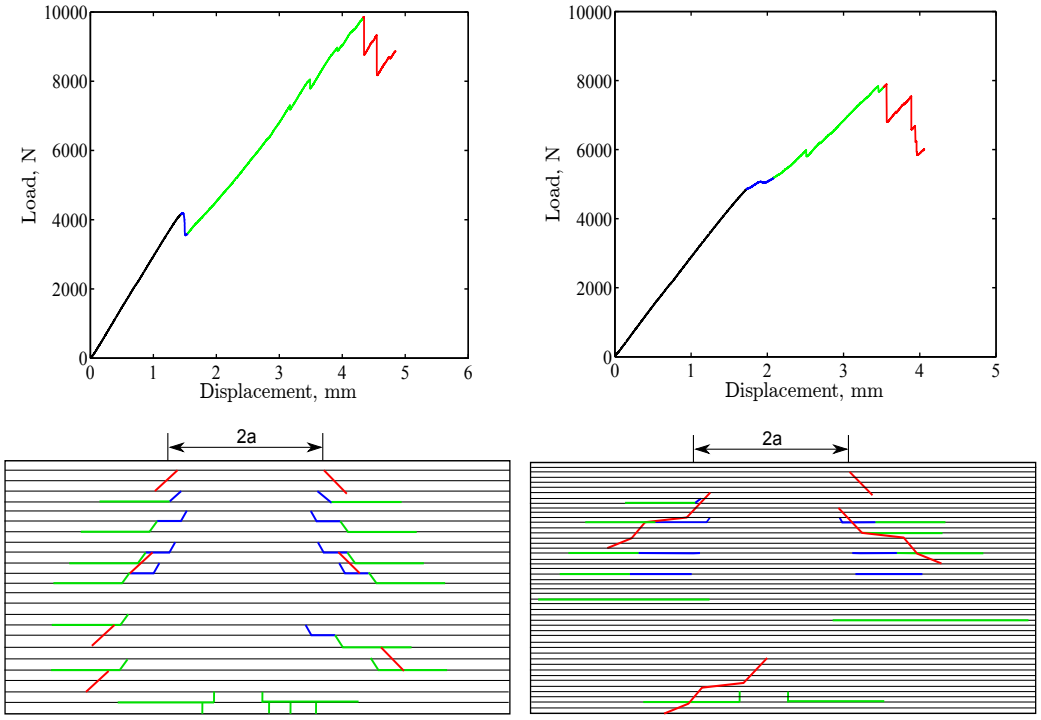

(a) Thin-Ply (TP) laminate **(b)** Ultra-Thin-Ply (UTP) laminate

Fig. 4.8: Summary of the QSI damage in TP and UTP composite laminates. Each color in the load displacement curves (upper figures) refer to the corresponding damage in the schematic drawings (lower figures).

The variations of the total, the elastic, and the dissipated energy versus the indenter displacement are shown in Figure 4.9 for both laminates. During Stage I, the dissipated energy is almost zero, which means that all the applied force is stored as elastic energy. At Stage II, the dissipated energy increases. This is due to the energy dissipated by the first observed damage mechanisms, i.e. matrix cracking and delamination onset. In Stage III, the dissipated energy increases linearly as the indenter displacement increases for both laminates due to the growth of delaminations. It is worth to notice that the slope of the dissipated energy curve during Stage III is equal for both materials. During Stage V, the dissipated energy rapidly increases due to the increase of the fiber damage. The material loses the capability to withstand more pressure and most of the applied energy is dissipated.

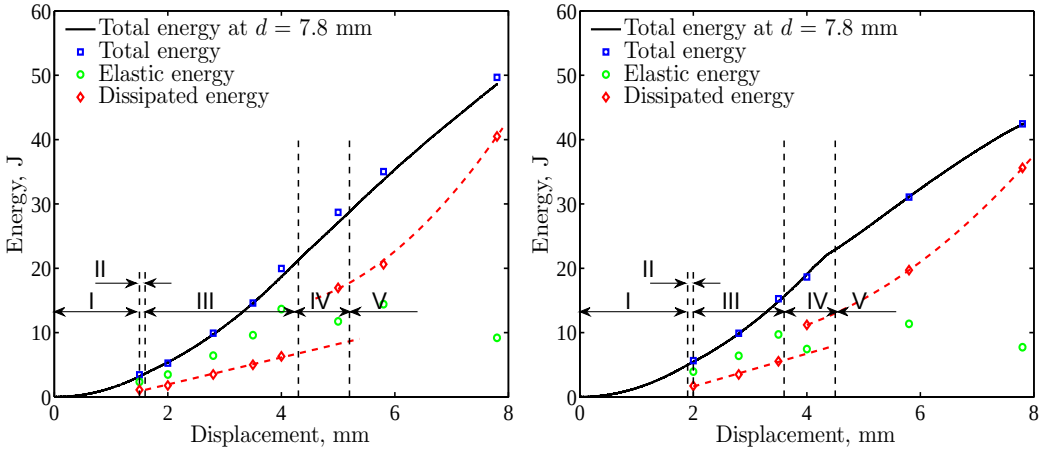

(a) Thin-Ply (TP) laminate **(b)** Ultra-Thin-Ply (UTP) laminate

Fig. 4.9: Total, elastic, and dissipated energies as a function of the indenter displacement.

Figure 4.10 includes the load-displacement curve, the projected delamination area, and the dissipated energy to facilitate the comparison between both laminate types. Before Stage IV, the projected delamination area for TP laminates is larger than that for UTP laminates at small indentation displacements; however, after Stage IV the delamination area for the UTP laminates is larger than for the TP laminates, with a growing difference as the displacement increases. These results correlate with the findings reported by Saito et al. [78] and Amacher et al. [76]. It is also important to highlight that the energy dissipated in Stage V due to fiber fracture in the TP laminates is larger than for the UTP laminates. This result can be related to two different effects: the fiber pull-out mechanism, which for TP laminates is expected to be higher than for UTP laminates [166] and the differences in the damage mechanisms. Figure 4.11 shows an image of the cross-section for two tested specimens at $d = 8.5$ mm. The TP laminate presents a shear failure in all the laminate (as can also be observed in Figure 4.3e at $d = 7.8$ mm). The UTP laminate shows a brittle failure mainly due to tensile and compressive failure at the top and bottom of the laminate (see Figure 4.4e at $d = 7.8$ mm). This observation can be related to the fact that matrix cracking allows the rotation of the fibers which results in a ductile shear failure of the fibers. This behaviour can explain the ability of the TP laminates to dissipate more energy than the UTP laminates in spite of having less delaminations.

According to the experimental observation of the damage sequence of TP and UTP laminates, we can conclude that the damage starts earlier in TP laminates but once initiated it propagates faster in UTP laminates. The maximum load capacity of TP laminates is higher than that of UTP laminates providing some additional ductility to TP laminates. Moreover, the projected delamination area before fiber failure, which

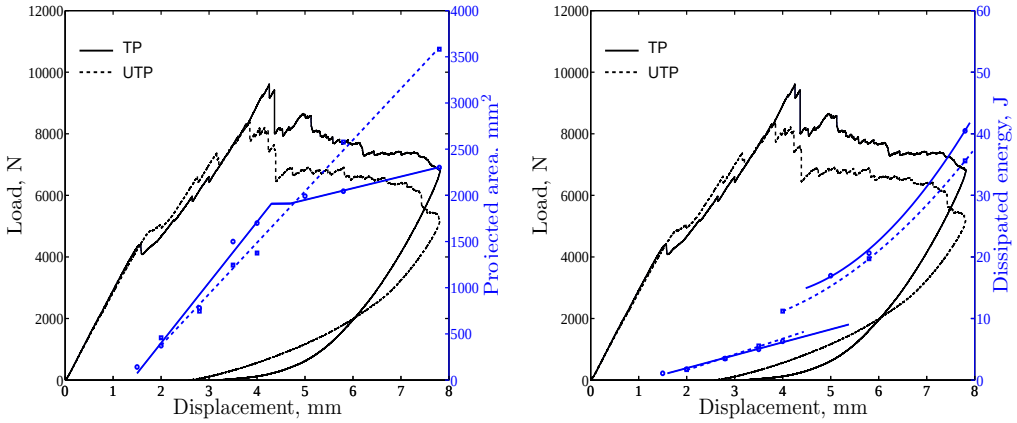

(a) Projected delamination area **(b)** Dissipated energy

Fig. 4.10: Summary of the load-displacement curves, the projected delamination area, and the dissipated energy.

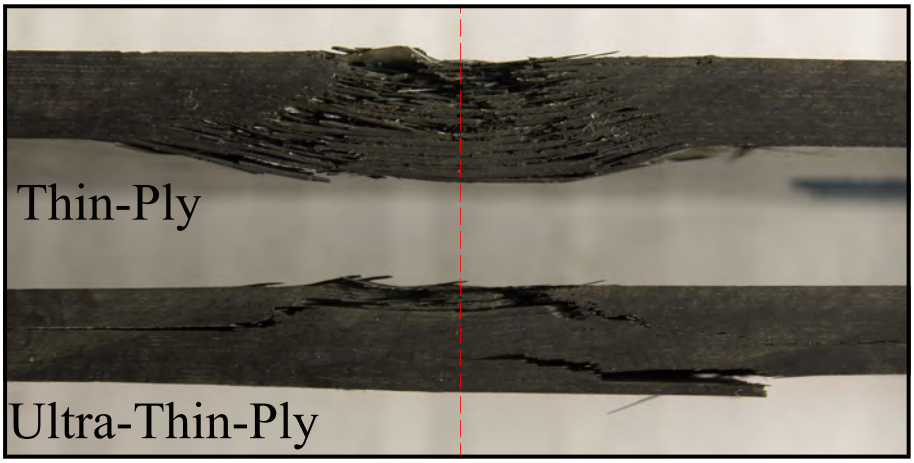

Fig. 4.11: Photographs of the specimens' cross section at $d = 8.5$ mm (the dashed red line represents the center of the indentation).

is usually used to express the damage resistance, is smaller for the UTP laminates than for the TP laminates.

4.3.3 Permanent indentation

The results of the 3D scanning of the indentation footprints measured 24 h after the tests are shown in Figures 4.12 and 4.13 for TP and UTP laminates, respectively. The figures show the profiles of the indentation isolines. At the same indenter displacement, the indentation depth for the UTP laminates is a bit larger than for the TP laminates. The maximum indentation depth is about 0.20 and 0.22 mm at d = 2.8 mm, for TP and UTP laminates respectively. The indentation profile follows a concentric-circle pattern for small displacements; however, it is observed to take an elliptical shape at d = 5.8 mm. This observation might be related with the fiber breakage damage mechanism. Actually, after the start of the fiber breakage, the indentation profile almost takes the shape of the broken fibers on the top surface of the specimens. Moreover, as the indentation depth is increased the response of the laminate is dominated by the top ply of the laminate [131]. Some noise is observed in these profiles due to the fiber architecture of the plies and due to the surface finishing after plate manufacturing.

The indentation depth was measured at: 0.5, 1 and 2 hours; and 1, 2, 4, 7, 14, 20 and 25 days after the QSI test. In order to get a general idea about the relaxation of the indented specimen, the indentation depth, α, was normalized with the indentation depth after 0.5 h, α_0, for all the specimens, as shown in Figure 4.14. The indentation depth is rapidly decreased with increasing time until reaching a steady state after 5 days. The decreasing rate of the measured indentation is almost the same for all the indentation displacements regardless of the damage level attained. Similar results were reported in Chapter 3 for laminates with unidirectional plies. The relaxation time is quite similar for TP and UTP laminates (Figures 4.14a and 4.14b), which indicates that for the material tested the ply thickness has not a big influence on the relaxation time.

The permanent indentation depth is an interesting parameter for the damage assessment. It is used as an indication of the severity of the internal damage induced by impact, e.g. size of delaminations. Figure 4.15 shows the relation between the projected delamination area and the indentation depth 0.5 h after the test. The results for both laminates are fitted with bi-linear curves with the aim of clarify. Up to stage IV, the indentation depth can give a good indication of the delamination area inside the laminate for both laminates, especially at small indentation depth. At this stage, the slopes of the lines are almost equal for both laminates. After, the slope for the UTP laminates is larger than for the TP laminates.

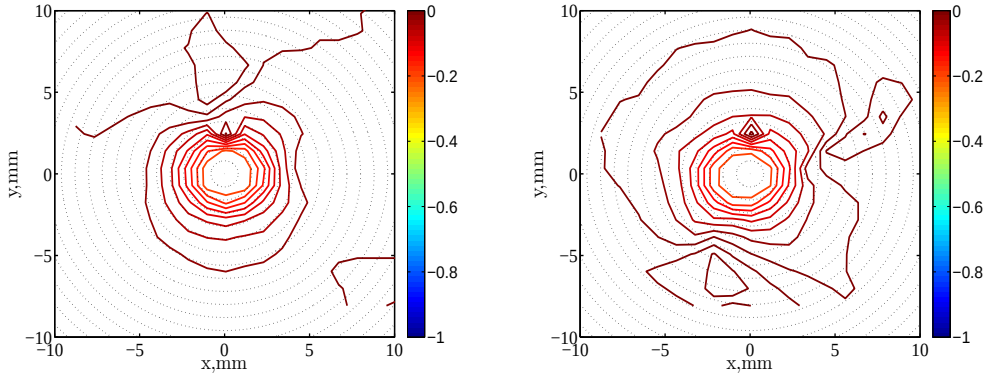

(a) $d = 2.8$ mm **(b)** $d = 3.5$ mm

(c) $d = 4.0$ mm **(d)** $d = 5.8$ mm

Fig. 4.12: Indentation profiles of the TP laminates at different displacements of the indenter after 1 day. The color bars indicate the indentation depth.

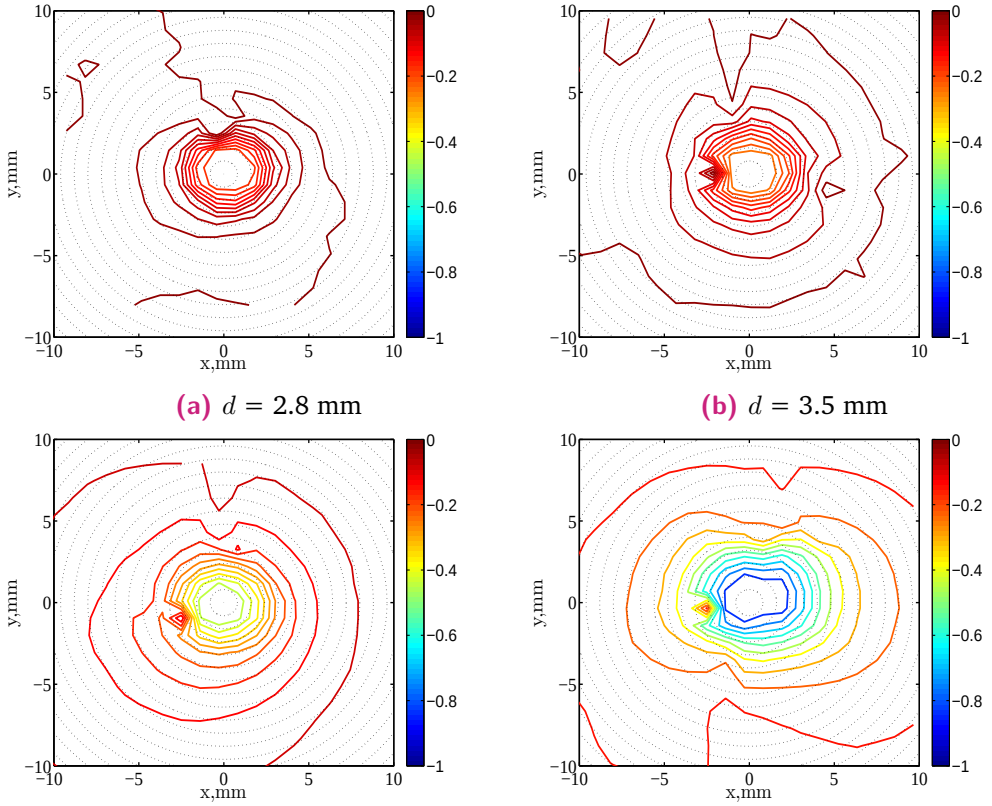

(a) $d = 2.8$ mm **(b)** $d = 3.5$ mm

(c) $d = 4.0$ mm **(d)** $d = 5.8$ mm

Fig. 4.13: Indentation profiles of the UTP laminates at different displacements of the indenter after 1 day. The color bars indicate the indentation depth.

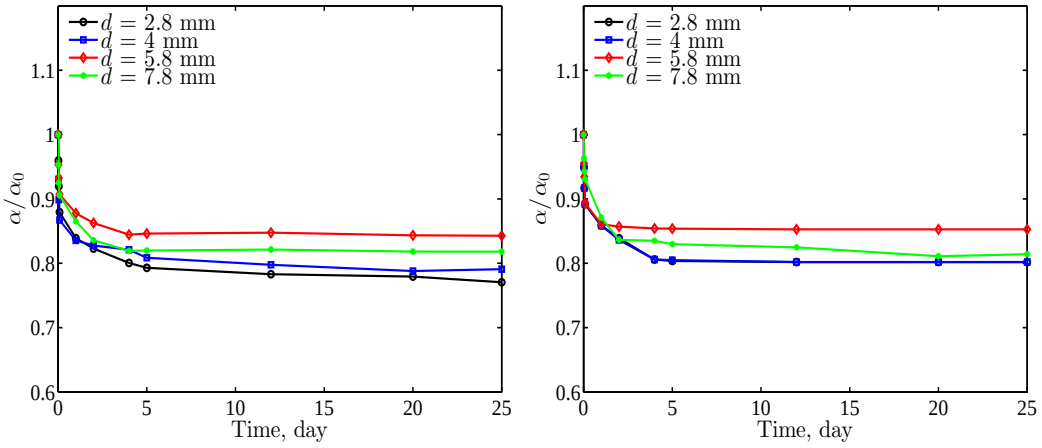

(a) Thin-Ply (TP) laminate **(b)** Ultra-Thin-Ply (UTP) laminate

Fig. 4.14: Relaxation of the measured indentation versus time (α/α_0 is the normalized indentation depth, where α_0 is the indentation depth after 0.5 h).

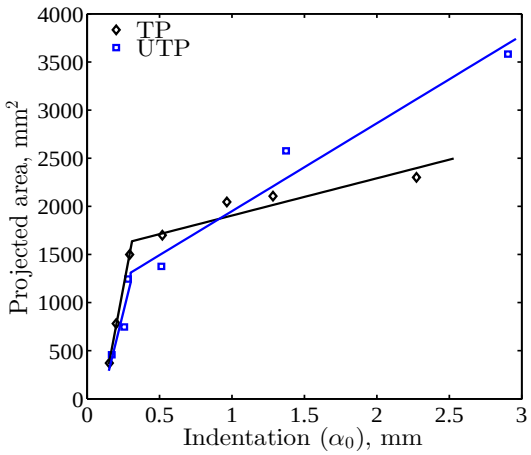

Fig. 4.15: Projected delamination area versus the indentation depth, measured 0.5 h after the test.

The delamination area after an indentation test can be estimated by relating the relaxation curve in Figure 4.14 with Figure 4.15. As an example, if we measure the indentation depth after 10 days from the test, easily, we can enter to the chart in Figure 4.14 and get the indentation depth 0.5 h after the impact test (α_0). Then, entering this data in Figure 4.15, the corresponding projected delamination area is obtained.

It is worth noting that Figure 4.14 and Figure 4.15 are not valid for any test set-up, they apply for the case considered in the present paper, with: hemispherical indenter with 16 mm diameter, center contact location, support with four point clamps and 125 mm $\times$ 75 mm rectangular cut-out which offers simply supported boundary conditions [167].

4.4 Conclusions

A series of quasi-static indentation tests have been carried out on TeXtreme® carbon/epoxy composite laminates to identify the damage mechanisms and their sequences in Thin-Ply (TP) and Ultra-Thin-Ply (UTP) laminates. Combining the microscope photographs and the C-scan results with the load-displacement curves, the complex mechanisms of the penetration process can be summarized in five stages. Stage I corresponds to the elastic response of the material. Stage II is the damage initiation. For TP laminates, a sudden drop in the load-displacement curve takes place which is related to the formation of matrix cracks and the onset of induced delaminations, starting at the end of the contact area due to the high transverse shear stresses. For UTP laminates, the first damage mechanism to appear is delamination with very few matrix cracks. Stage III is termed as delamination propagation, and the load increases again with displacement at a lower slope than

in Stage I. As the loading continues, a large load drop in the load-displacement curve occurs due to the fiber breakage, Stage IV. Stage V, the fibers are sheared out to form a plug for TP laminates, whereas for UTP, the fibers fail under tensile and compressive stresses yielding to a brittle laminate failure. Starting from Stage II until Stage V, the UTP laminates present a linear delamination growth as a function of the indentation displacement, whereas the TP laminates show three different phases for delamination growth which correspond to Stages III, IV and V.

It is important to point out that although the damage onset in the TP laminate takes place earlier than in the UTP laminates, the fiber breakage damage mechanism in the UTP laminates occurs earlier.

The indentation profile was almost circular for both laminates for all indentation displacements below the corresponding displacements for fiber breakage. After the onset of fiber breakage, the indentation profile take an elliptical shape. The indentation depth relaxed significantly during the first 5 days after the test. The ply thickness has no influence on the relaxation time of the impacted specimens.

As a final conclusion of this work, and from the point of view of applicability, it is important to obtain test results linked to the damage tolerance of both laminates to give a robust recommendation for aero-structures. However, as a preliminary recommendation based on damage resistance, UTP laminates show better damage resistance than TP laminates although the maximum load capacity is larger for the TP laminates. So, the selection between one of these two materials should depend on the requirements of the designer.

5 Effect of mismatch angle

5.1 Introduction

Non-Crimp Fabrics (NCFs) provide numerous benefits over unidirectional tapes, such as easy laminate homogenization and simpler ply stacking, a reduction in processing time, cost, waste and stacking errors [153, 168–170]. Moreover, a remarkable improvement in strength can be achieved by using thin-ply NCF laminates. For example, Tsai et al. [169] reported that using NCF laminates improves the open-hole strength. Arteiro at al. [171] reported that notched strength, open-hole strength and bearing strength were improved by using thin-ply NCF laminates [171]. It was also found that this type of laminates can delay or even suppress some damage mechanisms, i.e matrix cracking, which improves the strength of the laminate [153].

For the particular case of NCFs under out-of-plane loading, to the best knowledge of the authors, the publications on this case are rare. Shyr and Pan [84] studied the load and energy histories during low-velocity impact on glass NCF composites. According to this study, comparing the NCF composites with other E-glass woven fabrics and non-woven mat reinforced laminates, NCF had the greatest delaminated areas. Yang et al. [172] carried out low-velocity impact tests and compression after impact test on biaxial NCF composites. They concluded that the failure modes present in compression after impact tests are different from those appearing in compression tests of undamaged specimens. Bibo et al. [173] concluded that the damage mechanisms in this material are different than the damage mechanisms in laminates manufactured using unidirectional prepreg tapes. However, the damage resistance and the damage tolerance are the same for both laminates. Chen and Hodgkinson [174] compared the response of composite laminates with different fiber architectures (3D woven and NCF) under low- and high-velocity impacts. They concluded that the 3D woven fabric composites have better damage resistance and tolerance in low-velocity impact. However, NCF composites have the best damage resistance and damage tolerance in high-velocity impacts. In spite of this important conclusion, they were not able to explain the reason of this contrary behavior in low- and high-velocity impact tests.

The effect of mismatch angle between the adjacent plies on the response of composite laminates under out-of-plane loading has been addressed in several papers [30, 61, 175–180]. Some authors [178, 179] concluded that the mismatch angle has an

insignificant effect on the damage resistance of CFRP composites whereas, others [30, 61, 176, 180] reported that increasing the mismatch angle between plies, improves the damage resistance of composite laminates. Therefore, this is a subject still under debate. In any case, the understanding of the mismatch angle effect on the response of composite laminates under out-of-plane loading must depart from better understanding the damage mechanisms and their sequence during loading.

This chapter analyses the sequence of damage mechanisms in thin-ply NCF composite laminates under QSI tests. Three different mismatch angles between plies are considered to highlight its influence on the damage sequence and the damage resistance. Inspections by micro-Computerized Tomography (μCT) and ultrasonic C-scan techniques were performed to identify the damage mechanisms occuring at different indenter displacements. Also, the indentation depths of the indented surfaces were measured after the tests. Finally, the chapter concludes with a summary of the main findings of the study.

5.2 Material and procedure

The material used in this study is a NCF C-Ply^{TM} T700GC/M21 carbon/epoxy prepreg of tow plies [0/45] and [0/-45] provided by Chomarat^{TM}, with an areal weight of 150 g/m^2 per bi-angle layer (or 75 g/m^2 per ply). The elastic material properties of the ply, summarised in Table 5.1, were measured following the corresponding ASTM standards in a previous work by Huchette [181]. Based on the results of Wagih et al. [182], which conclude that the in-plane size has no influence on the response of composite laminates under out-of-plane loading, a nonstandard specimen size, 100 $\times$ 75 mm, was used for the the QSI tests. No thermal or moisture conditioning was performed before or during the tests.

Tab. 5.1: Elastic properties and thickness of the NCF C-Ply^{TM} T700GC/M21 carbon/epoxy plies [181].

Elastic modulus, E_{11}	130 GPa
Elastic modulus in the transverse direction, E_{22}	8.3 GPa
Shear modulus, G_{12}	4.5 GPa
Poisson's ratio, ν_{12}	0.32
Ply thickness, t_{ply}	0.075 mm

Aiming at clarifying the influence of the mismatch angles on the QSI response, three different mismatch angles between bi-angle layers were considered: 15°, 45° and 90°. In the following, these three laminates are respectively defined as L15, L45 and L90. These three configurations are quasi-isotropic and symmetric, with 48 unidirectional plies (24 bi-angle layers) with a total laminate thickness of 3.6 mm.

The three laminates have the same in-plane elastic properties and the difference between the flexural properties is within 10%. The staking sequences were designed using the ant colony optimization algorithm [183, 184] by Guillamet [185]. The objective function, f, was selected to minimize the difference in flexural properties between the three configurations, and can be defined as:

$$f = \mid D_{11} - D_{22} \mid + \mid D_{11} - D_{12} - 2D_{66} \mid + \mid D_{16} \mid + \mid D_{26} \mid + 1 \tag{5.1}$$

D_{ij} are the bending stiffness matrix coefficients.

The mismatch angle between bi-angle layers was introduced as a constraint of the optimization procedure. Table 6.1 shows the stacking sequence and the corresponding mismatch angles for the three laminates. Figure 5.1 shows the polar plot of the engineering elastic constants of the three laminates. The in-plane elastic modulus, E, and shear modulus, G, of all three configurations are 49.78 GPa and 18.98 GPa, respectively. The flexural modulus, E_f, of laminates L15, L45 and L90 are shown in blue, orange and green dashed lines, respectively. Detailed explanation of the parameters used in the optimization process can be found in [185].

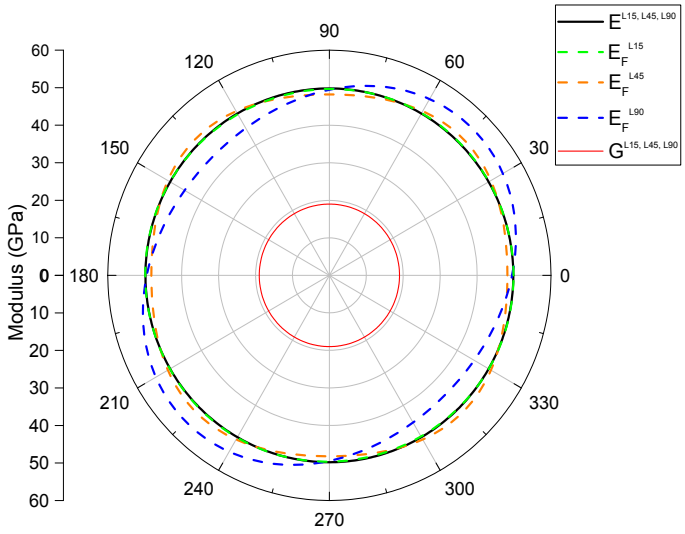

Fig. 5.1: Polar diagram of the elastic, flexural, and shear modulus for the three laminates.

The QSI tests consisted of step-loading indentation tests, which were performed using a 100 kN MTS universal testing machine. Figure 5.2 shows the experimental setup with the sample location, the indenter, and the fixture. The indenter was a stainless steel hemisphere of 16 mm in diameter according to ASTM standard [149]. The specimen was placed between the specimen support (two rectangular plates) with a 50 mm diameter hole in the center, to prevent the separation of it's edges from the base during loading. The specimen along with the specimen supports were rigidly clamped between the upper and lower plates of the fixture. The fixture was then mounted on the testing machine and the indentation load was centrally applied

Tab. 5.2: Stacking sequence and mismatch angle for the tested laminates obtained by ant colony optimization algorithm. In the table * refers to the mismatch angle within the non-crimp-fabrics (bi-angle layer)

Laminate		
L15	Stacking sequence	$[(45/90)/(75/30)/(15/-30)/(-45/0)/(-15/-60)/(-75/-30)/(-15/-60)/(-45/90)/(-75/60)/(75/30)/(15/60)/(45/0)]_s$
	Mismatch angle	$[45^*,15,45^*,15,45^*,15,45^*,15,45^*,15,45^*,15,45^*,15,45^*,15,45^*,15,45^*,15,45^*,0]_s$
L45	Stacking sequence	$[(-45/90)/(45/0)/(-45/90)/(45/0)_3/(-45/90)_3/(45/0)/(-45/90)/(45/0)]_s$
	Mismatch angle	$[45^*,45,45^*,45,45^*,45,45^*,45,45^*,45,45^*,45,45^*,45,45^*,45,45^*,45,45^*,45,45^*,0]_s$
L90	Stacking sequence	$[((45/90)/(0/-45)/(45/0)/(90/-45))_2/(45/0)/(90/-45)/(45/0)/(90/-45)]_s$
	Mismatch angle	$[45^*,90,45^*,90,45^*,90,45^*,90,45^*,90,45^*,90,45^*,90,45^*,90,45^*,90,45^*,90,45^*,0]_s$

on the specimen. The tests were carried out under displacement control at a loading rate of 1 mm/min.

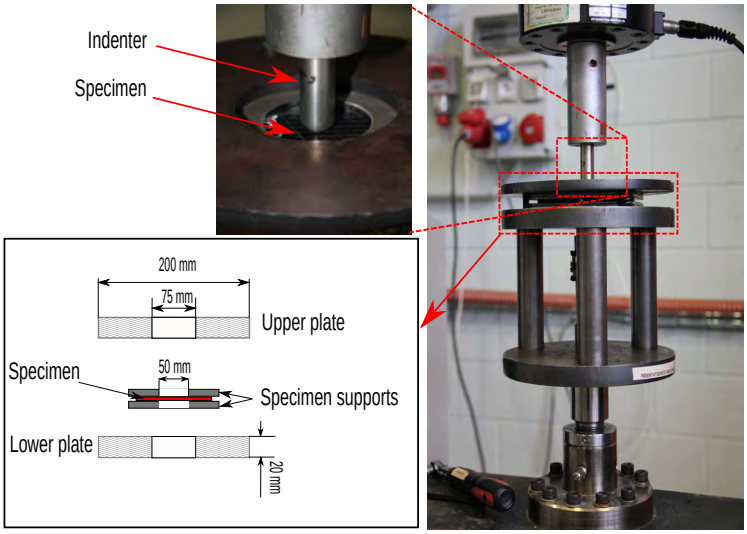

Fig. 5.2: Experimental set up of the QSI test.

For each laminate, one specimen was initially tested until complete perforation (7.5 mm). Based on the detection of failure mechanism suggested by the respective load-displacement curves, 6 different displacement levels were defined for each laminate type. One specimen was tested per displacement level and laminate type. The considered displacements levels were d = 1.1, 2, 2.8, 4.5, 4.9 and 6.0 mm for laminate L15, d = 1.1, 2, 3, 4, 4.9 and 6.0 mm for laminate L45 and d = 1.2, 1.8, 2.4, 3.9, 4.1 and 6.0 mm for laminate L90. When the selected displacement was reached, the specimen was unloaded and the indentation depth was measured within half-an-hour after the QSI tests by means of a dent-depth gauge. Afterwards, the specimens were inspected by ultrasonic C-scan technique to capture the different delaminated areas and their through-the-thickness location. Finally, some of the specimens were inspected by μCT technique to capture the different damage mechanisms. For those specimens to be μCT inspected, to reduce the width to thickness aspect ratio,

thus reducing variations in X-ray path length during the acquisition of projections, the specimens were cut to a 65 $\times$ 75 mm section across the impact damaged site (determined by ultrasonic C-scans) with a diamond cutting wheel. The resulting specimens after cut were then stacked in triples to be scanned together in one operation using the following inspection parameters: 60 KV voltage, 70 μA intensity, 7 μm voxel size and 16.8 mm field of view. Afterwards, the specimen indented at the lowest displacement for each laminate was cut to 15 $\times$ 75 mm across the damaged impact site and inspected again by the μCT technique for an improved resolution using the following inspection parameters: 55 KV voltage, 80 μA intensity, 5 μm voxel size and 11.8 mm field of view. In those specimens inspected at the smallest displacements, binarization process was applied to detect the extension of cracks and delamination. In all cases, 1400 projections (3 integrations per projection) were acquired as the sample rotated over 360°. No contrast agent was used.

5.3 Results

The load-displacement curves for each batch of laminates L15, L45 and L90 are shown in Figure 5.3a, 6.2a and 5.3c, respectively. Since each curve overlaps the curves with smaller displacement, the repeatability of the QSI tests is good. Generally, the load-displacement curves are characterized firstly by an elastic increase of load up to a local maximum point, F_{th}, at which there is a change in the slope. Following this initial change, the load grows monotonically until reaching the maximum load capacity of the laminate, F_{m}, at which a large load drop occurs. Finally, the curve continues with a fairly plateau-shaped stage until the perforation load, F_{p}, due to the friction between the indenter and the laminate. Figure 5.3d shows the load displacement curve for the three tested laminates at d = 7.5 mm. From this figure, it can be seen that the three laminates have the same elastic response which prove that the in-plane and flexural properties of the three laminates are practically equal. The response after the damage initiation for the three laminates differs slightly due to differences in the damage mechanisms inside each laminate.

μCT micrographs of the cross-sections (two orthogonal different directions) of the tested specimens at different displacement levels for the three laminates are shown in Figures 5.4, 5.5 and 5.6 for laminates L15, L45 and L90, respectively. These figures show that the damage is quite similar in both directions, 0 and 90°. The C-scan inspections for the three laminates at different applied displacements are shown in Figure 5.7.

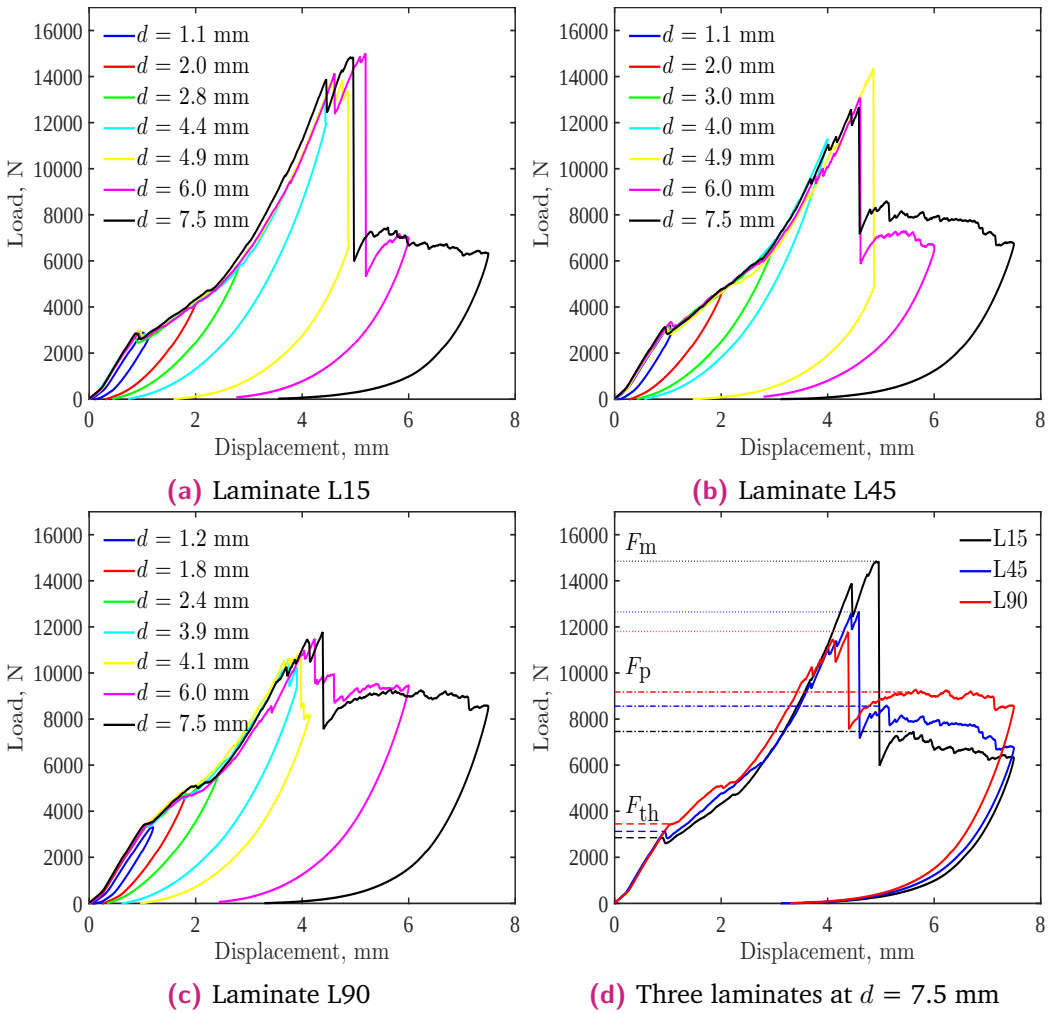

(a) Laminate L15 **(b)** Laminate L45

(c) Laminate L90 **(d)** Three laminates at $d = 7.5$ mm

Fig. 5.3: Load-displacement curves from QSI tests for laminates L15, L45 and L90. In (d) dashed horizontal lines represent the damage threshold (F_{th}), dotted lines represent the maximum loads (F_{m}) and the dash dot lines represent the perforation load (F_{p}).

5.4 Discussion

The load displacement curves and the damage sequence in the three laminates, L15, L45 and L90, are quite similar. Elastic theory governs the first part of the load displacement curve until the damage threshold load (F_{th}), about 3000 N, where a change in the slope of the load displacement curve is clearly observed. After this point the delaminated area increases until the maximum load capacity (F_{m}) (or up to the load for which the delaminations reach the boundary conditions). When the laminate reaches its maximum load capacity, a large amount of fiber failures is observed. Finally, the penetration of the indenter is characterized with a more or less constant load (F_{P}). Also according to a previous study [182], these characteristic loads are independent of the in-plane size of the plates. These three characteristic loads are plotted in Figure 5.8.

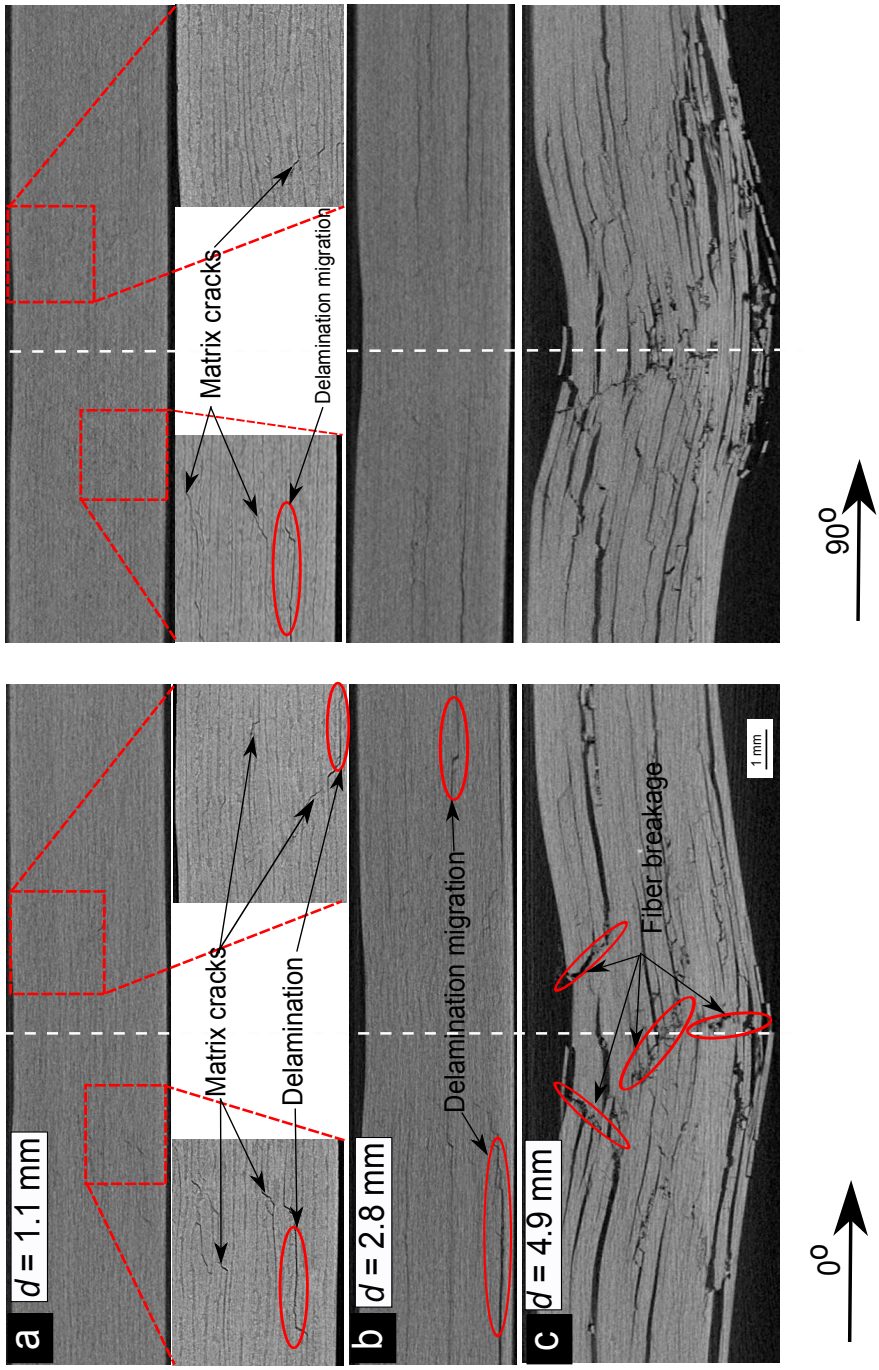

Fig. 5.4: μCT micrographs of the cross-section of laminate L15 at different displacement levels (the dashed white line represents the center of the indentation). The arrows below the images indicate the 0° and 90° direction of the laminates.

The load-displacement curves for the three laminate configurations (Figure 5.3), show that an initial load drop corresponding to the threshold load (F_{th}) can be observed for laminates L15 and L45. No load drop but a slight slope change can be observed for laminate L90. The average value of (F_{th}) for the seven specimens

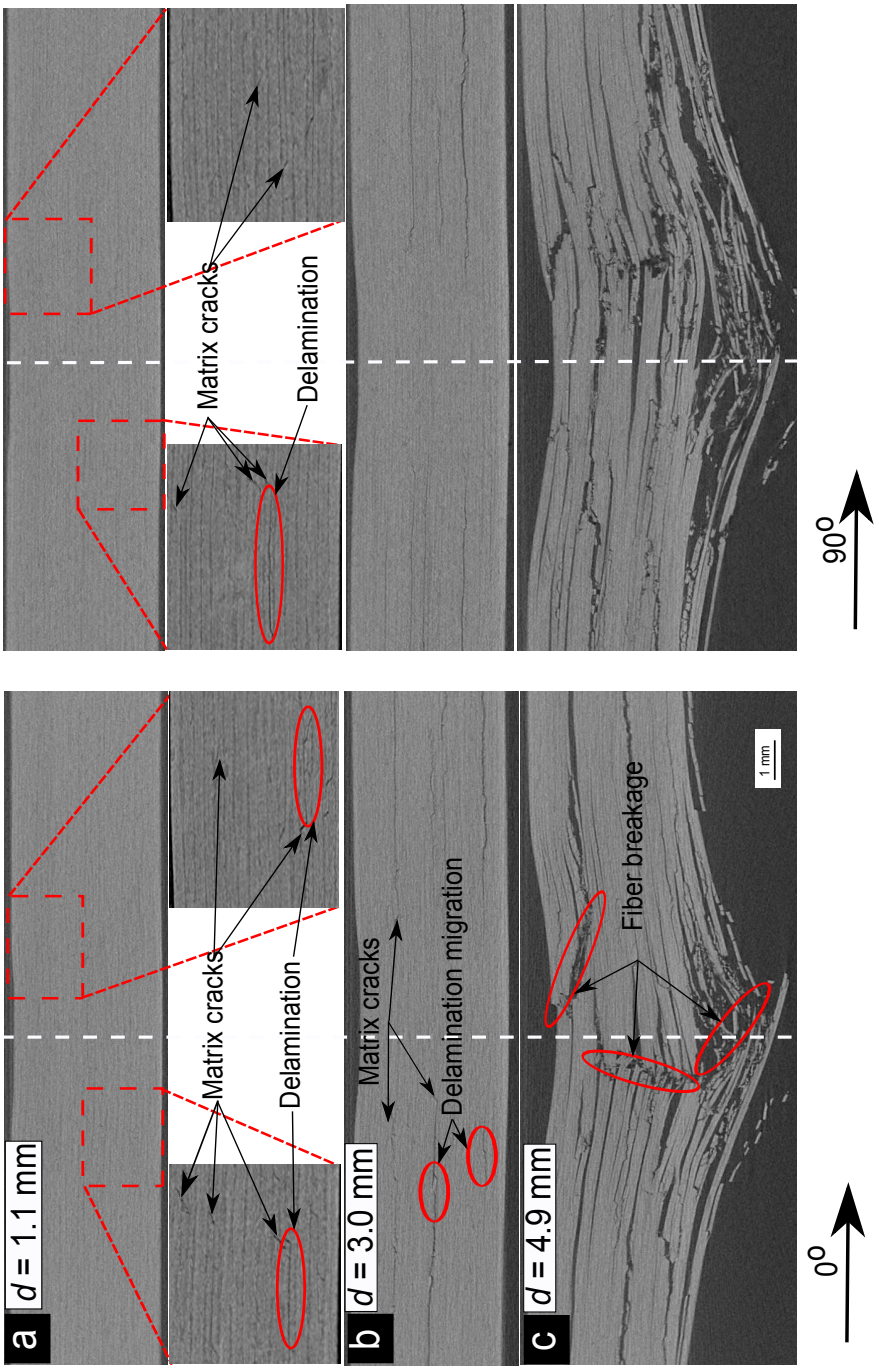

Fig. 5.5: μCT micrographs of the cross-section of laminate L45 at different displacement levels (the dashed white line represents the center of the indentation). The arrows below the images indicate the 0° and 90° direction of the laminates.

tested for each laminate increases slightly with the mismatch angle, from 2850 ± 113 N for laminate L15 to 3368 ± 62 N for laminate L90 (see Figure 5.8).

When analyzing the damage just after the threshold load, L15 and L45 show more matrix cracks (see Figure 5.4a, 5.5a and 5.6a), from which larger delamination areas grow (see Figure 5.7a(i), b(i) and c(i)). Matrix cracks in laminates with small

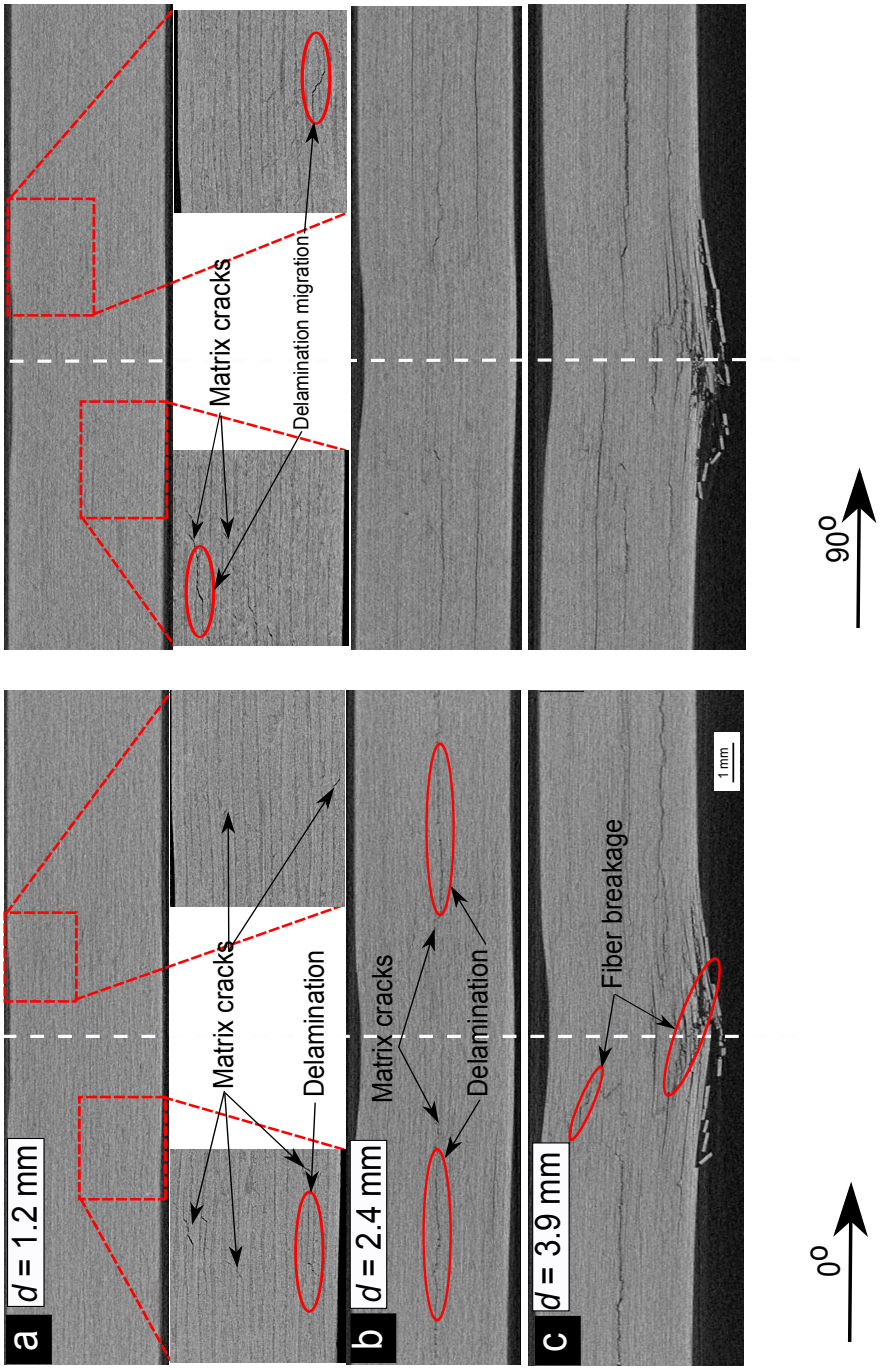

Fig. 5.6: μCT micrographs of the cross-section of laminate L90 at different displacement levels (the dashed white line represents the center of the indentation). The arrows below the images indicate the 0° and 90° direction of the laminates.

mismatch angles expand through several layers, acting as a clustered ply, as it is shown in Figure 5.9a for laminate L15. However, for large mismatch angles, L90, the cracks expand only in a single layer, as it is shown in Figure 5.9c. A 3D μCT micrograph for laminate L15 at $d = 1.2$ mm is shown in Figure 5.10 to elucidate the expansion of matrix cracks through several layers. In this figure, the laminate

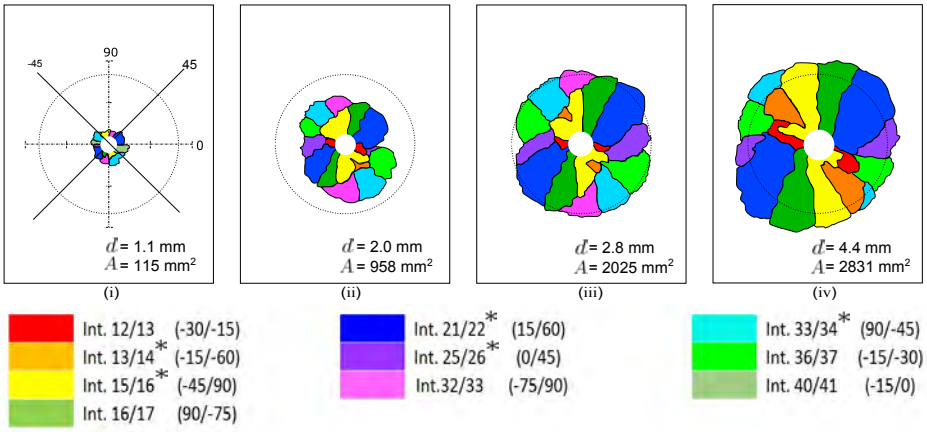

(a) Laminate L15

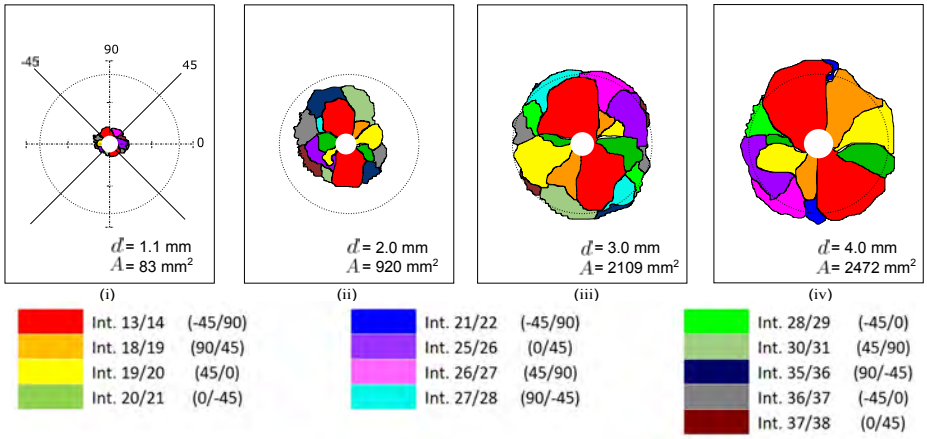

(b) Laminate L45

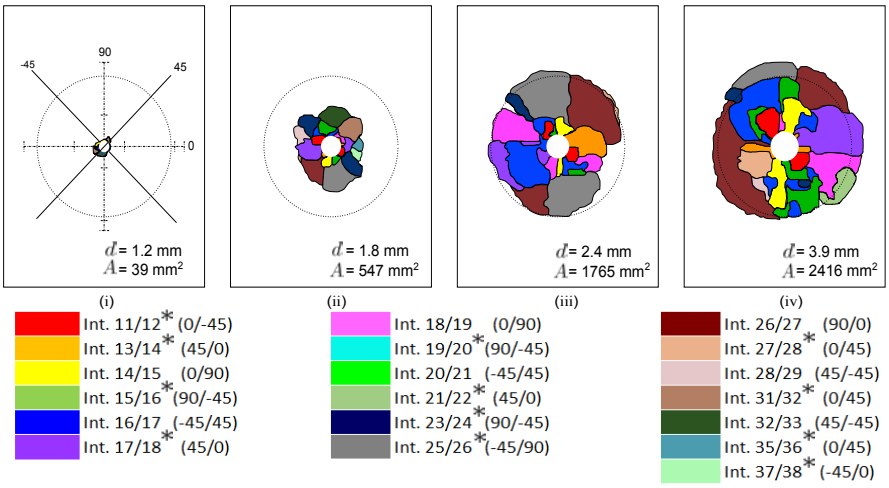

(c) Laminate L90

Fig. 5.7: Through-the-thickness position and extension of individual delaminations of laminate L15, L45 and L90 at different displacement levels (the interfaces are counted form the impacted face, the dashed lines represent the circular boundary hole dimension of the fixture and * refers to the mismatch angle within the non-crimp-fabrics (bi-angle layer)). Each C-scan corresponds to a different specimen.

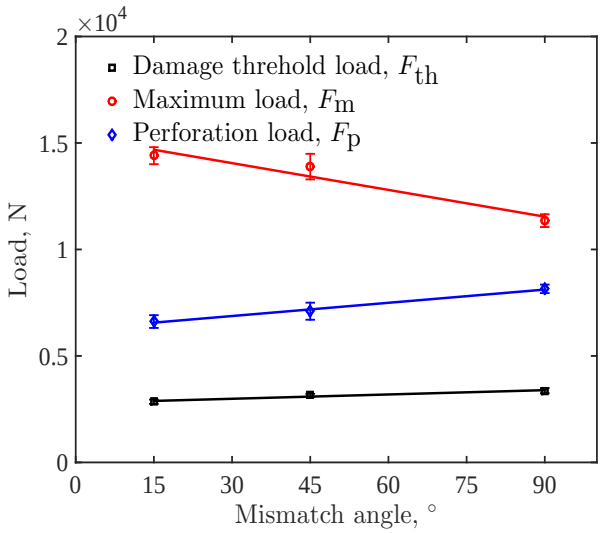

Fig. 5.8: Damage threshold load, Maximum load and perforation load as a function of the mismatch angle. The lines represent the linear fitting of the results.

was divided in four quarters to highlight the different damage mechanisms. The first quartile of the laminate (at impact face), only contains matrix cracks. Delaminations and matrix cracks can be observed in the rest of the laminate. It is worth noting that the cracks in adjacent plies intersect at some points which appear as single crack through two layers in the cross section inspections (see Figure 5.9a).

In Figure 5.8, the average of the maximum load for the three specimens tested at higher displacements is plotted against the mismatch angle. The maximum load (F_m) decreases significantly with respect to the mismatch angle. This is due to the increase of the number of delaminations as the mismatch angle increases (see Figure 5.7). When delaminations grow inside a laminate, they divide the laminate into sublaminates which reduce the ability of the material to withstand load. So, the resistance of the material for fracture decreases and the maximum load capacity decrease too.

After the maximum load capacity of the laminate is reached, a large load drop is observed until the perforation load (F_p). Figure 5.8 also shows the average value of the perforation load (F_p) for the last two specimens as function of the mismatch angle. In this case F_p increases with respect to the mismatch angle. It is observed that small mismatch angles delay fiber failure but they lead to a reduced ability to dissipate energy during the penetration process. After F_m, laminates with small mismatch angles, L15 and L45, show clustered plies of broken fibers through the specimen thickness (see Figure 5.4c and 5.5c, respectively). On the other hand, for laminate L90, the fibers at the bottom part of the laminate are completely broken but there exist several plies without fibre damage (see Figure 5.6c).

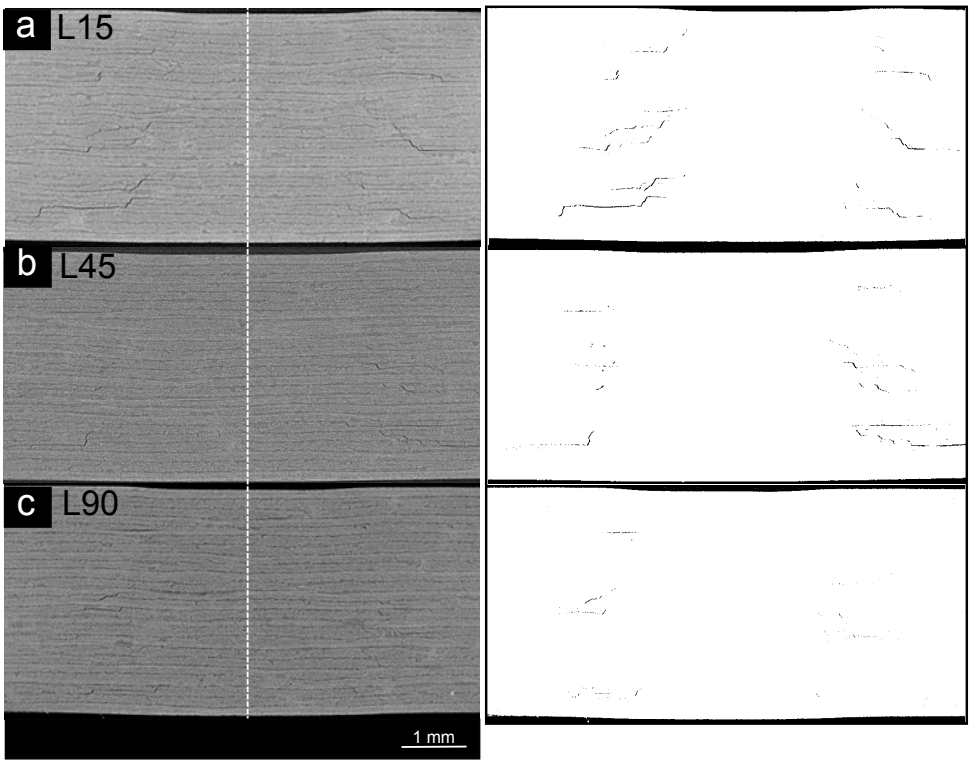

Fig. 5.9: μCT micrographs of the cross-section of L15, L45 and L90 laminates at $d = 1.1$, 1.1 and 1.2 mm, respectively, in the left side of the figure. (the dashed white line represents the center of the indentation). In the right side of the figure, the segmented damage is presented

After the threshold load, the projected delaminated area increases almost linearly with respect to the applied displacement (Figure 5.11) until the boundary of the fixture is reached. If there were not boundaries effects, previous research by Wagih et al. [182, 186] and Sebaey et al. [61] suggests that this linear increase continues until the maximum load. For the laminates tested in this study the delamination area is almost equal for each laminate, which highlights the idea that the mismatch angle has no influence on the projected delamination area for NCF materials. Similar results were reported Davies et al. [178] and Soutis and Curtis [179] for unidirectional ply laminates.

It is noticeable that the delaminations in the three laminates are mainly initiated by matrix crack tips. These cracks are caused by the shear stress due to contact in the upper part of the laminates and by the tensile stress due to bending in the lower parts. By increasing the applied load, new cracks appear in the lower part of the laminate from which new delaminations grow. This is due to the large tensile stresses in the lower part of the laminate which produce matrix cracks that act as delamination initiators. Furthermore, several delaminations could be observed to appear without shear matrix cracks, especially in laminate L90. It is worth noting

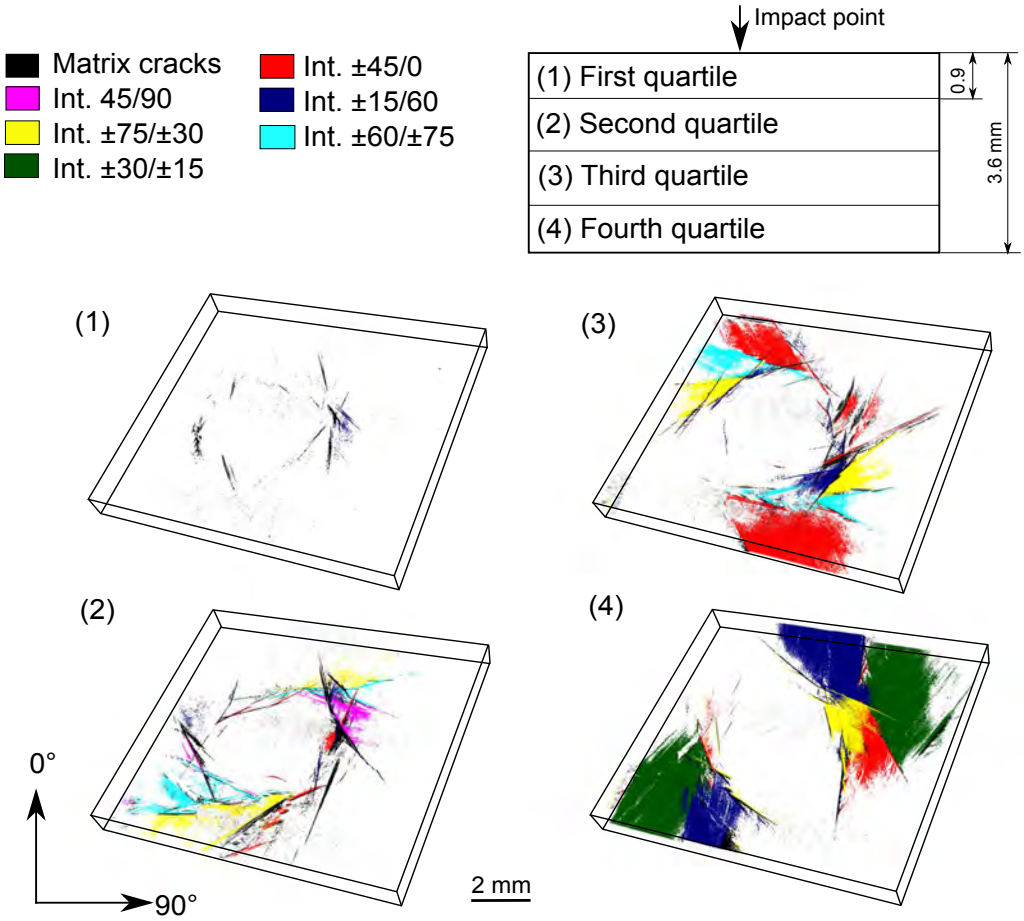

Fig. 5.10: 3D μCT micrograph of laminate L15 at $d = 1.1$ mm.

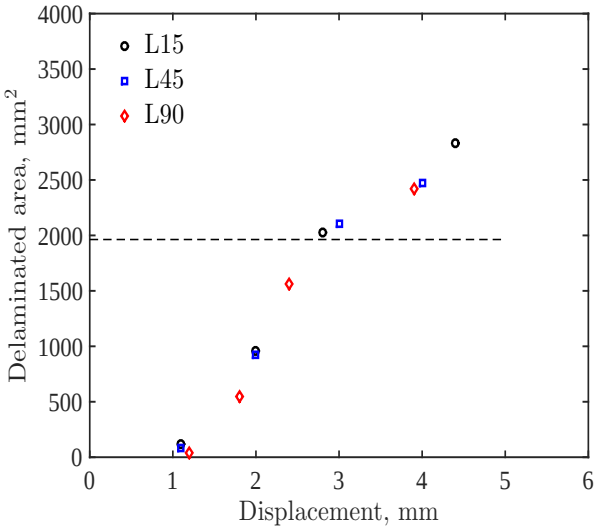

Fig. 5.11: Projected delaminated area as a function of the indenter displacement. The dashed line represent the displacement at which the delamination reach the boundaries of the fixture.

that the delaminations grow not only between the NCF layers but also inside the bi-angle layers.

The total and the dissipated energy for the three laminates are presented as a function of the applied displacement in Figure 5.12. The total energy is calculated by integrating the area under the load versus displacement curves; the elastic energy is calculated by the area under the unloading curve; and the dissipated energy is obtained by subtracting the elastic energy from the total energy [186]. For the three laminates, before the damage starts (first load drop in the load-displacement curve), the dissipated energy is close to zero, which means that all the applied work is stored as elastic energy. After the damage starts at $d = 1.1$ mm for laminates L15 and L45 and $d = 1.2$ mm for laminate L90, the dissipated energy increases. This is due to the formation of matrix cracks and delaminations as shown by the μCT micrographs in Figures 5.4a, 5.5a and 5.6a and in the C-scan observations shown in 5.7ai, 5.7bi and 5.7ci. By increasing the applied load, the dissipated energy increases linearly with the indenter displacement due to delamination propagation until fiber breakage appears. When the applied load reaches the maximum load capacity of the laminate, a jump is observed in the dissipated energy for the three laminates due to fiber breakage (see Figures 5.4c, 5.5c and 5.6c). Afterwards, the dissipated energy rapidly increases due to the increase of fiber breakage until complete perforation and to the increase of the friction force between the indenter and the laminate. The total energy is almost equal for the three laminates. The dissipated energy due to delamination propagation is almost equal for laminates L45 and L15. For similar displacement levels the dissipated energy tends to be slightly higher for laminate L90. This is attributed to the fact the number of delaminated interfaces in laminate L90 is larger than for laminates L45 and L15 (see Figure 5.7).

The indentation depth is an interesting parameter for damage assessment. It is used as an indication of the severity of the internal damage induced by impact, e.g. localized matrix cracks around the indenter and size of delaminations [187]. Moreover, it can be used to predict the damage tolerance of the impacted laminates as presented by Caprino and Lopresto [188]. Figure 5.13a shows the permanent indentation depth measured within 0.5 h after the test as a function of the indenter displacement. In this figure, it is observed that the permanent indentation is almost equal for the three laminates before the fiber breakage starts. After the fiber breakage, at the largest applied displacement, $d = 7.5$ mm, the larger the mismatch angle, the deeper the indentation. Similar results were reported by Caprino et al. [106] for unidirectional ply laminates. This result agrees well with the fact that for an indenter displacement $d = 7.5$ mm, the dissipated energy is larger for laminate L90 (see Figure 5.12b).

Figure 6.14b shows the projected delaminated area as a function of the permanent indentation depth. The figure shows that, at the same indentation depth level, the

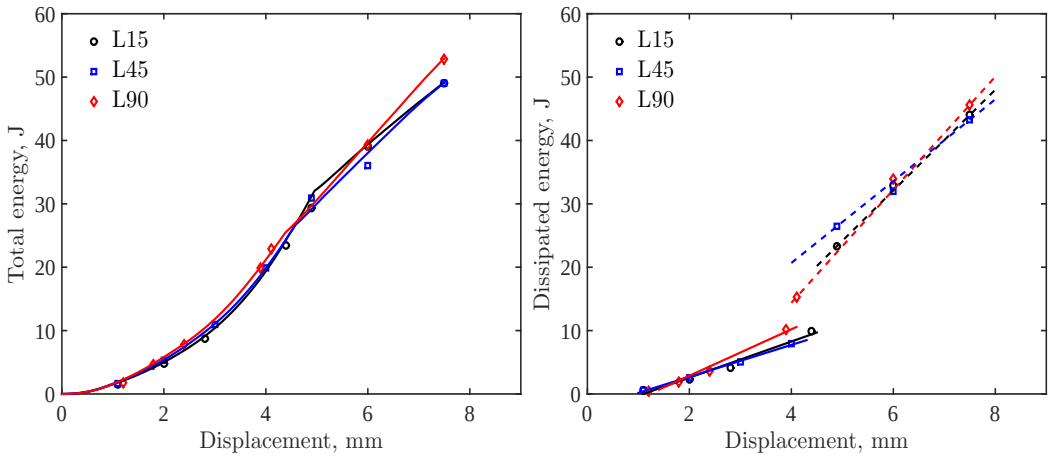

(a) Total energy **(b)** Dissipated energy

Fig. 5.12: Total and dissipated energy as a function of the applied displacement for laminates L15, L45 and L90. In (b) the solid lines are the linear fitting of the dissipated energies before fiber breakage and the dashed lines are the linear fitting of the dissipated energies after fiber breakage.

larger the mismatch angle is, the larger the delamination area is. Furthermore, from this figure, it is observed that the permanent indentation depth for laminate L90 is more expressive for the damage inside the laminate.

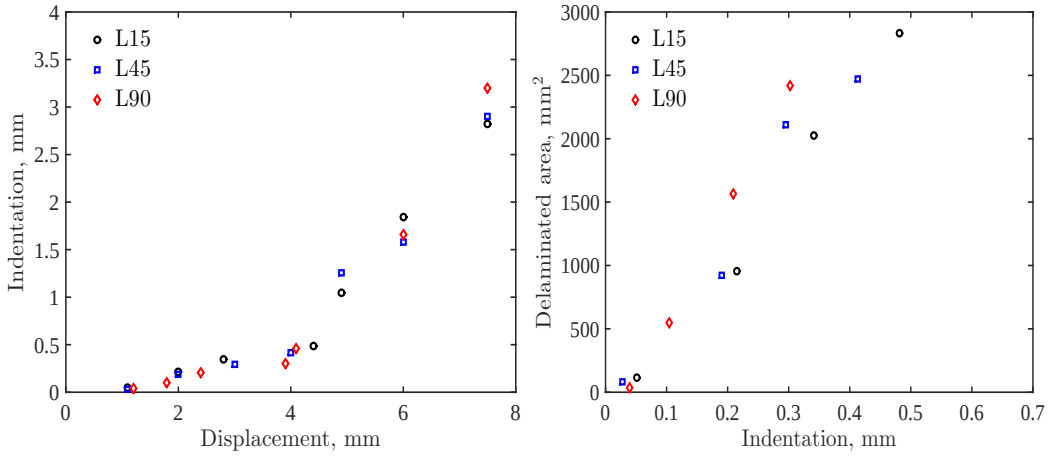

(a) **(b)** Dissipated energy

Fig. 5.13: Permanent indentation as a function of displacement and projected delamination area.

5.5 Conclusions

A series of quasi-static indentation tests has been carried out on thin-ply non-crimp-fabric carbon/epoxy composite laminates to identify the damage mechanisms during low-velocity impact test. Three different laminates, L15, L45 and L90,

corresponding to three different mismatch angles, 15°, 45° and 90° between the NCF layers, were considered in this study. The three laminates were defined to be quasi-isotropic laminates with the same in-plane elastic properties and to minimize the difference between the flexural properties of the three laminates. Combining the load-displacement curves with μCT and C-scan inspections, the damage sequence during an indentation event could be identified.

The load-displacement curves are characterized by a first elastic increase of load up to the damage threshold at which there is a change in the response. For laminates L15 and L45, at the damage threshold load a sudden drop occurs due to extensive matrix cracks from which delaminations grow. However, for laminate L90, at the damage threshold load, no load drop is observed but only a small change in the slope due to the lower density of matrix cracks and smaller delamination area. After this initial change, the load grows monotonically with a lower slope than the elastic response. During this stage, delaminations propagate until reaching the boundaries of the fixture or until the maximum load capacity of the laminate is reached, when a large load drop occurs. This large load drop corresponds to the fiber breakage in the three laminates. For laminate L15, the maximum load was higher than that for laminates L45 and L90. Finally, a fairly plateau-shaped takes place in the three laminates until the complete perforation of the specimen, corresponding to the friction load between the indenter and the laminate.

It is worth highlighting that damage onset increased slightly with the mismatch angle. However, the fiber breakage occurs earlier in laminate L90 and retard by reducing the mismatch angle. Moreover, the load drop after the fiber breakage is reduced as the mismatch angle increased which means a more catastrophic failure as the mismatch angle is decreased.

The projected delaminated area is almost equal for the three laminates which reflects no influence of the mismatch angle on the damage resistance of NCF thin-ply laminates. However, the number of delaminated interfaces is reduced by decreasing the mismatch angle. The permanent indentation depth is also not affected by the mismatch angle before the fiber breakage starts. However, after fiber breakage starts, the larger the mismatch angle is, the deeper the indentation is, which makes the permanent indentation depth for larger mismatch angle more expressive on the damage inside the laminate. Therefore, for laminates with large mismatch angles between plies, the depth of the permanent indentation is a clear indication of the extension of internal damage.

As a final conclusion of this work, the damage mechanisms and their sequence in thin-ply NCF laminates are almost the same as those observed for unidirectional thin-ply laminates. From the point of view of structural application, as the three laminates have the same strength, the choice between them should depend on the

requirements of the application itself. If the main requirement is to delay damage initiation, laminate L90 would be the selection. However, if the main requirement is increasing the maximum load capacity, laminate L15 would be the selection. Taking this into account, in the authors' opinion it would be worth exploring if the combination of large mismatch angles, to increase the damage threshold load, with small mismatch angles, to increase the maximum load capacity and reduce the number of delaminated interfaces, could result in improved laminate designs.

Improving damage resistance

6

6.1 Introduction

Based on the results and suggestions presented in Chapter 5 and to avoid the brittle nature of thin-ply laminates, the objective of the present paper is to design a thin-ply NCF laminate with improved damage resistance by combining small and large mismatch angles and thin- and thick-plies in a single laminate. Seven different lay ups are considered in this study. Three of these lay ups are designed to have a combination of large and small mismatch angles in different parts of the laminate and two lay ups are designed to have a combination between thick and thin-plies in different parts of the laminate. Also, with the aim of comparison, a lay up with constant mismatch angle, 45° and a nonsymmetric laminate with 10-20° mismatch angle are considered. QSI test was used for the application of the out-of-plane loading and ultrasonic C-scan technique was performed to quantify the damage resistance of the tested laminates by measuring the projected delamination area. Indentation depth of the indented surfaces were measured after the tests. Finally, the chapter concludes with a summary of the main findings of the study.

6.2 Material and procedure

The material used in this study is a NCF C-Ply^{TM} T700GC/M21 carbon/epoxy prepreg of tow plies [0/45] and [0/20] provided by Chomarat^{TM}, with an areal weight of 150 g/m^2 per bi-angle layer (or 75 g/m^2 per ply). The unidirectional material properties were summarized in Chapter 5. Based on the results presented in a previous work [182], which conclude that the in-plane size has no influence on the response of composite laminates under out-of-plane loading, a nonstandard specimen size, 100 $\times$ 75 mm, was decided for the the QSI tests. No thermal or moisture conditioning was performed before or during the tests.

Considering the previous results presented in Chapter 5 on the advantage of using small mismatch angle to improve the maximum load capacity of the laminate and the advantage of using large mismatch angles to delay the damage initiation, new laminates were manufactured by combining both large and small mismatch angles in the same laminate. The damage resistance of the proposed laminates was compared with laminates made with 45° mismatch angle and a nonsymmetric laminate with 10-20° mismatch angle. The first lay up is a symmetric laminate with a constant

mismatch angle of 45°, referred here the baseline laminate (BL). The second lay up (LO) is designed to also be a symmetric laminate with large mismatch angles, 45°-75°, between the outer NCF layers and small mismatch angle between the inner NCF layers, 15°. The third lay up (NS) is designed to be a nonsymmetric laminate with small mismatch angles, 10-20°. The fourth lay up (NLU) is also designed to be a nonsymmetric laminate with large mismatch angles in the upper part of the laminate, 90°-45°, and small mismatch angles in the lower part of the laminate, 10-20°. The fifth lay up (NLL) is designed to be just the opposite of NLU: a small mismatch angles in the upper part of the laminate, 10-20° and large mismatch angles in the lower part of the laminate, 90°-45°. The maximum absolute value of B_{ij} in the B-matrix was computed in the optimization process and equal 739.4 MPa for laminate NS and equal 688.6 MPa for laminates NLU and NLL.

With the aim of avoiding the brittle failure of thin-ply laminates, two more lay ups were manufactured from both thick and thin-plies. The sixth lay up (NCU) is designed to have clustered plies at the upper part of the laminate and thin-plies at the rest of the laminate with 10-20° mismatch angles. The seventh lay up (NCL) is designed to be just the opposite of NCU: clustered plies are located at the lower part of the laminate and thin-plies at the rest of the laminate with 10-20° mismatch angles. Theses two lay ups have an absolute value of B-matrix equal to 693.5 MPa. The idea of these two lay ups was build based on the results presented in Chapters 3 and 4 and another work available in the literature [60, 61]. In Chapters 3 and 4, the results indicated that the first damage mechanism is shear matrix cracks which appear in the upper part of the laminate due to contact shear stress and the compressive stresses. These cracks work as delamination initiators, which dissipates most of the impact energy. In the work of González et al. [60] and Sebaey et al. [61], it was suggested that the dissipation of impact energy by different damage mechanisms close to the outer surfaces of the laminate might result in a central block of undamaged plies. In this way, this central block of plies can withstand higher compression after impact loads, and consequently, the damage tolerance is improved. In order to force the location of damage in the more external plies of the laminate, thicker, or clustered, plies were used near the surfaces.

These seven configurations considered are quasi-isotropic laminates with 48 uni-directional plies (24 bi-angle layers) with a total laminate thickness of 3.5 mm. The seven laminates have the same in-plane elastic properties and the difference between the flexural properties of the seven laminates is within 10%. The staking sequences of the seven laminates, shown in Table 6.1, were found by means of the ant colony optimization algorithm, introduced in [183, 184]. The objective function,

f, was selected to minimize the difference in flexural properties between the three configurations, which can be defined as:

$$f = \mid D_{11} - D_{22} \mid + \mid D_{11} - D_{12} - 2D_{66} \mid + \mid D_{16} \mid + \mid D_{26} \mid +1 \tag{6.1}$$

D_{ij} is the bending stiffness matrix coefficients.

Table 6.1 shows the stacking sequence and the mismatch angle for the seven laminates.

Tab. 6.1: Stacking sequence and mismatch angle for the tested laminates obtained by ant colony optimization algorithm. In the table * refers to the mismatch angle within the non-crimp-fabrics (bi-angle layer).

Laminate		
BL	Stacking sequence	$[(-45/90)/(45/0)/(-45/90)/(45/0)_3/(-45/90)_3/(45/0)/(-45/90)/(45/0)]_s$
	Mismatch angle	$[45^*,45,45^*,45,45^*,45,45^*,45,45^*,45,45^*,45,45^*,45,45^*,45,45^*,45,45^*,0]_s$
LO	Stacking sequence	$[((90/-45)/(60/-75)/(-30/15)/(30/-15))/(0/45)/(60/15)//(0/-45)/(-60/75)/(90/45)/(30/-15)/(-30/-75)/(-60/75)]_s$
	Mismatch angle	$[45^*,75,45^*,45,45^*,15,45^*,15,45^*,15,45^*,15,45^*,15,45^*,15,45^*,15,45^*,0]_s$
NS	Stacking sequence	$[(-80/-60)/(-40/-20)/(-10/10)/(20/40)/(50/70)/(50/70)/(80/-80)/(-70/-50)/(-30/-10)/(10/30)/(20/40)/(60/80)]_2$
	Mismatch angle	$[20^*,20,20^*,10,20^*,10,20^*,10,20^*,20,20^*,10,20^*,10,20^*,20,20^*,20,20^*,10,20^*,20,20^*,20]_2$
NLU	Stacking sequence	[(90/45)/(-45/90)/(-45/90)/(45/90)/(-80/-60)/(-40/-20)/(-30/-10)/(10/30)/(10/30)/(20/40)/(20/40)/(50/70)/ (60/80)/(60/80)/(-80/-60)/(-50/-30)/(-10/10)/(0/20)/(10/30)/(50/70)/(50/70)/(90/-70)/(-80/-60)/(-50/-30)]
	Mismatch angle	[45*,90,45*,45,45*,45,45*,10,20*,20,20*,10,20*,20,20*,20,20*,10,20*,20,20*,10,20*,10, 20*,20,20*,20,20*,10,20*,20,20*,10,20*,10,20*,20,20*,20,20*,20,20*,10,20*,10,20*]
NLL	Stacking sequence	[(-30/-50)/(-60/-80)/(-70/90)/(70/50)/(70/50)/(70/50)/(20/0)/(10/-10)/(-30/-50)/(-60/-80)/(80/60)/(80/60)/ (70/50)/(40/20)/(40/20)/(30/10)/(30/10)/(-10/-30)/(-20/-40)/(-60/-80)/(90/45)/(90/-45)/(90/-45)/(45/90)]
	Mismatch angle	[20*,10,20*,10,20*,20,20*,20,20*,10,20*,10,20*,20,20*,10,20*,20,20*,20,20*,10, 20*,10,20*,20,20*,10,20*,20,20*,20,20*,10,20*,20,20*,10,45*,45,45*,45,45*,90,45*]
NCU	Stacking sequence	[(45/90)/(90/-45)/(-45/90)/(90/45)/(-80/-60)/(-40/-20)/(-30/-10)/(10/30)/(10/30)/(20/40)/(20/40)/(50/70)/ (60/80)/(60/80)/(-80/-60)/(-50/-30)/(-10/10)/(0/20)/(10/30)/(50/70)/(50/70)/(90/-70)/(-80/-60)/(-50/-30)]
	Mismatch angle	[45*,0,45*,0,45*,0,45*,55,20*,20,20*,10,20*,20,20*,20,20*,10,20*,20,20*,10,20*,10, 20*,20,20*,20,20*,10,20*,20,20*,10,20*,10,20*,20,20*,20,20*,20,20*,10,20*,10,20*]
NCL	Stacking sequence	[(-30/-50)/(-60/-80)/(-70/90)/(70/50)/(70/50)/(70/50)/(20/0)/(10/-10)/(-30/-50)/(-60/-80)/(80/60)/(80/60)/ (70/50)/(40/20)/(40/20)/(30/10)/(30/10)/(-10/-30)/(-20/-40)/(-60/-80)/(45/90)/(90/-45)/(-45/90)/(90/45)]
	Mismatch angle	[20*,10,20*,10,20*,20,20*,20,20*,10,20*,10,20*,20,20*,10,20*,20,20*,20,20*,10, 20*,10,20*,20,20*,10,20*,20,20*,20,20*,10,20*,20,20*,55,45*,0,45*,0,45*,0,45*]

A 100 kN MTS universal testing machine was used to preform the step-loading QSI tests. Figure 6.1 shows the experimental setup with the indenter and the fixture. The indenter was a stainless steel hemisphere of 16 mm diameter according to ASTM standard [149]. The specimen was placed between the 100 mm $\times$ 100 mm specimen support (two rectangular plates) with a 50 mm diameter hole in the center, to prevent the separation of its edges from the base during loading. The specimen along with the specimen supports are rigidly clamped between the upper and lower plates of the fixture by using three screws. The fixture was then mounted on the testing machine and the indentation load is centrally applied on the specimen. The tests were carried out under displacement control at a loading rate of 1 mm/min.

Six different displacement levels were defined for laminates BL, LO and NS and five different displacement levels for laminates NLU, NLL, NCU and NCL. The considered displacement levels were: d = 1.1, 2.0, 3.0, 4.0, 4.9 and 7.5 mm for laminate BL, d = 0.95, 2.1, 3.0, 4.2, 4.7 and 7.5 mm for laminate LO, d = 1.1, 2.0, 3.0, 4.2, 4.5 and

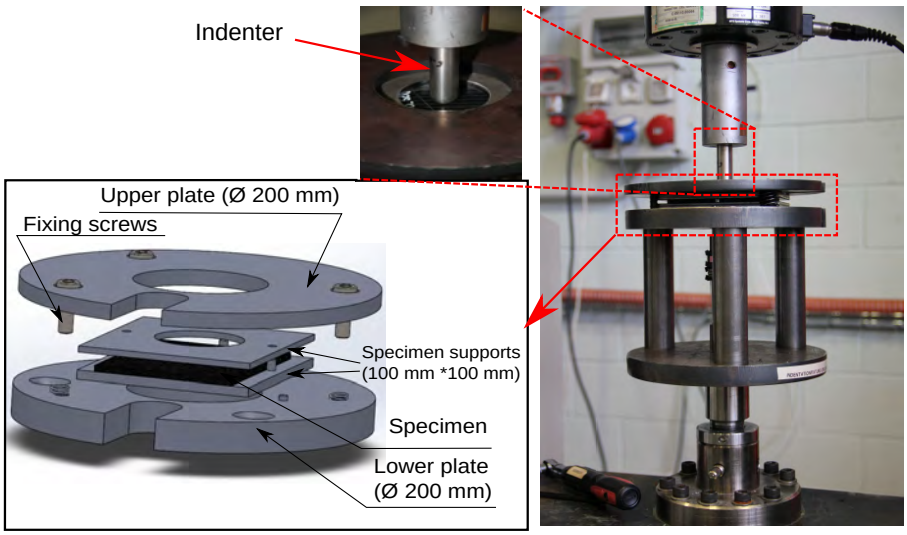

Fig. 6.1: Experimental set up of the QSI test.

7.5 mm for laminate NS, d = 1.2, 3.0, 4.4, 4.7 and 7.5 mm for laminate NLU, d = 1.2, 2.7, 3.8, 4.6 and 7.5 mm for laminate NLL, d = 1.2, 2.5, 3.6, 4.8 and 7.5 mm for laminate NCU and d = 1.3, 2.3, 3.2, 4.9 and 7.5 mm for laminate NCL. For all the laminates, one specimen was tested. These displacements were defined based on the observation of an indentation test until perforation (d = 7.5 mm) to detect evidences on the load-displacement measurements. When the specified displacement were reached, the specimens were unloaded and the indentation depth was measured within half-an-hour after the QSI tests by means of a dent-depth gauge. Afterwards, the specimens were inspected by ultrasonic C-scan technique to capture the different delaminated areas and their through-the-thickness location.

6.3 Results

The load-displacement curves for each batch of the seven tested configurations are shown in Figures 6.2 and 6.3. Since each curve overlaps the curves with smaller displacement, the repeatability of the QSI tests is good, which is common situation in such test [52, 186]. The load-displacement curves of the seven tested laminates follow the same trend. By applying displacement, the load increases elastically up to a certain point commonly known as the threshold load, F_{th}, at which a small load drop occurs due to the initiation of the damage. Following this initial change, the load grows monotonically until reaching the maximum load capacity of the laminate, F_{m}, at which a large load drop occurs due to fiber breakage. After this load drop, a fairly plateau-shaped stage, F_{p}, takes place until the complete perforation of the specimen. In Figures 6.2f and 6.3c, the load-displacement response of laminates BL, LO, NS, NLU and NLL and laminates NS, NCU and NCL, respectively, are plotted

showing the difference between the three characteristic loads, F_{th}, F_m and F_p, for the seven tested laminates. It is valuable noting that the load-displacement curves for the seven laminates overlap before the damage threshold load, F_{th}, which proof the reliability of the optimization algorithm.

The extension of the resulting delaminations and their respective through-the-thickness position for the seven tested configurations at different displacements up to the fiber breakage measured by C-scan technique are shown in Figures 6.4 to 6.10.

Figure 6.11 shows photographs of the specimens' back face after the largest load drop in the load-displacement response.

6.4 Discussion

6.4.1 Combining small and large mismatch angles

For this study five different laminates, BL, LO, NS, NLU and NLL are considered. Figure 6.12a shows the average value of the damage threshold load, F_{th}, for these five laminates. There is no significant difference between laminates BL, NS, NLU and NLL. However, laminate LO shows lower damage threshold load (2880 $\pm$ 75 N for laminate LO and 3215 $\pm$ 83 N for laminate BL). This is due to the initiation of larger number of simultaneous delaminations growing in the upper and lower parts of the laminate. The initiation of delaminations in the upper part of the laminate is originated by the matrix crack tips caused by the higher shear stresses due to contact and compression at this zone [186]. However, these delaminated interfaces in the upper part are difficult to be observed by C-scan due to the machine set up. The lower part delaminations initiate at interface 44/45 and 46/47 (see Figure 6.5) with larger mismatch angles resulting in lower interlaminar shear strengths.

The maximum load capacity of the laminates is shown in Figure 6.12b. Laminates LO and NLL show lower maximum load capacity than laminates BL, NS and NLU. This is due to the growth of delaminations at the bottom of the laminate in which the first fiber breakage occurs due to the higher tensile bending stresses [186] (see Figure 6.13). Contrariwise, laminate NLU shows the highest load capacity among these five tested laminates. This is because in this laminate, delaminations are mainly concentrated in the upper part of the laminate and no delaminations are observed in the lower part of the laminate which is exposed to higher normal bending stresses (see Figure 6.13) resulting in less fiber fracture at the lower part of the laminate (see Figure 6.11(e)). In view of these results, the laminate maximum load capacity can be increased by preventing delaminations growth in the lower part of the laminate. This can be achieved by reducing the mismatch angle between plies in the lower

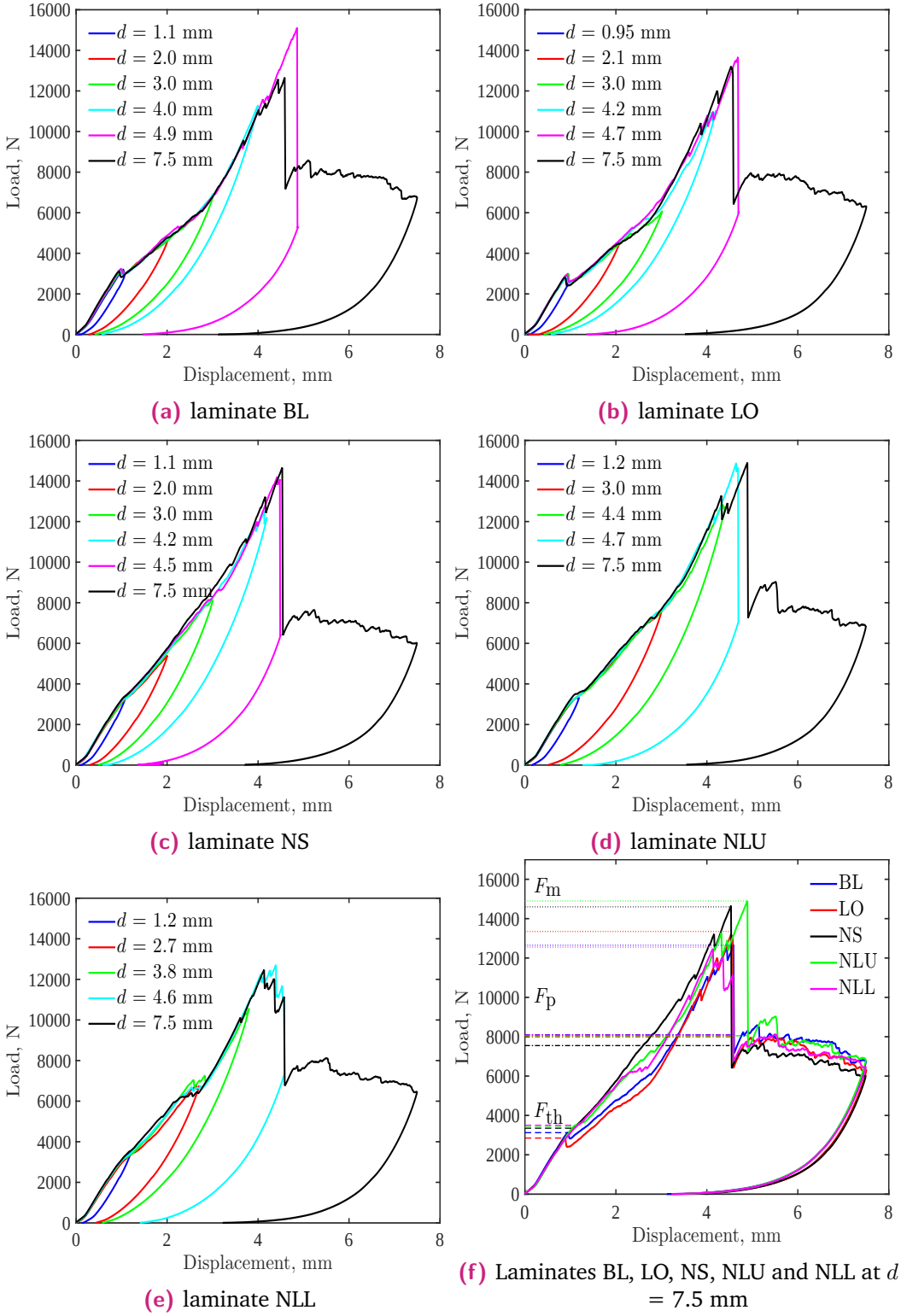

(a) laminate BL

(b) laminate LO

(c) laminate NS

(d) laminate NLU

(e) laminate NLL

(f) Laminates BL, LO, NS, NLU and NLL at d = 7.5 mm

Fig. 6.2: Load-displacement curves from QSI tests for BL, LO, NS, NLU and NLL laminates. In (f) dashed horizontal lines represent the damage threshold, dotted lines represent the maximum loads and the dash dot lines represent the load after the fiber breakage.

part of the laminate and using large mismatch angles in the upper part to dissipate more energy in this part by the initiation and growth of delaminations.

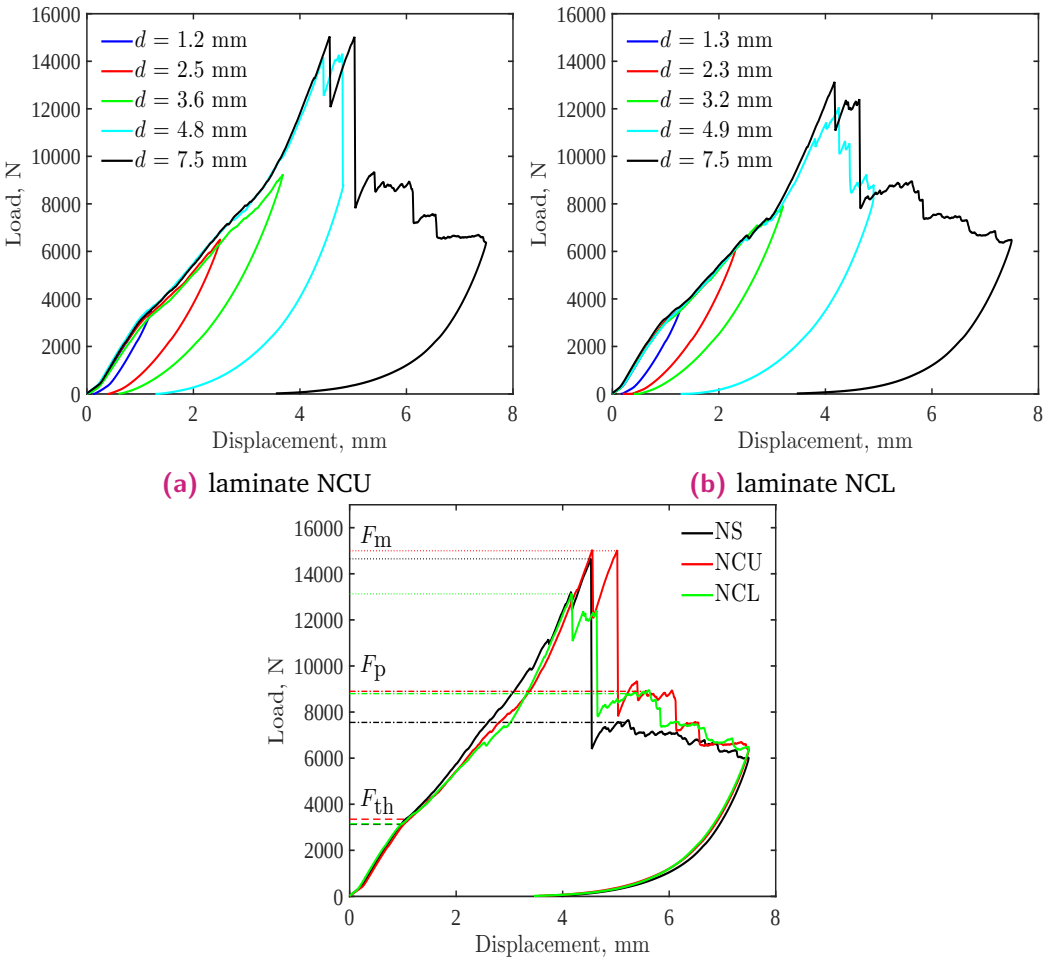

(a) laminate NCU

(b) laminate NCL

(c) Laminates NS, NCU and NCL at d = 7.5 mm

Fig. 6.3: Load-displacement curves from QSI tests for laminates NCU and NCL. In (e) dashed horizontal lines represent the damage threshold, dotted lines represent the maximum loads and the dash dot lines represent the load after the fiber breakage.

A large load drop is observed after the maximum load until F_p. This load, F_p, gives an indication on the ability of the laminate to sustain out-of-plane loads after fiber breakage. Laminate NS shows slightly lower F_p than the other four laminates due to the lower mismatch angles in this laminate, which causes larger amount of fiber breakage through the whole laminate thickness [189].

Figure 6.14a summarizes the relation between the projected delamination area and the displacement of the indenter for laminates BL, LO, NS, NLU and NLL. Generally, it is observed that the projected delamination area increases linearly with the indenter displacement. This observation is in accordance with the available experimental results [61, 186] and the analytical model presented by Wagih et al. [182]. Laminates NS, NLU and NLL have slightly smaller projected delamination area than laminates BL and LO. This can be attributed to the reduction of the

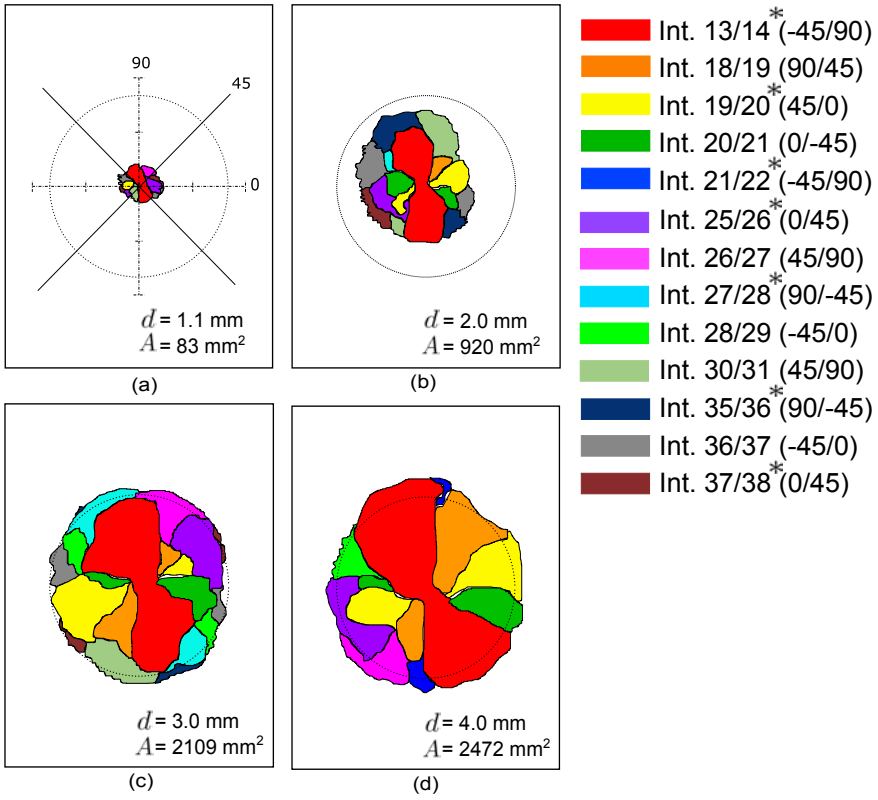

Fig. 6.4: Through-the-thickness position and extension of individual delaminations of BL laminate at different displacement levels up to fiber fracture (the dashed circles represent the circular hole dimension and * refer to the mismatch angle within the non-crimp-fabrics (bi-angle layer)). Each C-scan corresponds to a different specimen.

clustered plies in the central plane of the laminate which reduces the probability of delamination in this area.

In the authors' opinion, using the relation between the projected delamination area and the applied displacement or the impact energy to judge the laminate damage resistance is a misleading parameter. To have a fair judgement on the damage resistance of a laminate, the relation between the projected delamination area and the indentation depth combined with the shape of the delaminations and their through-the-thickness position should be taken into account. Figure 6.14b shows the projected delamination area as a function of the indentation depth. At the same indentation level, laminates NS, NLU and NLL have almost equal projected delamination area and lower than laminates BL and LO. Considering the evolution of the projected delamination area (Figure 6.14a), in which laminates NS, NLU and NLL have almost equal projected delamination area and smaller than laminate BL and LO, we can conclude that permanent indentation is a clear indicator of the level of internal damage.

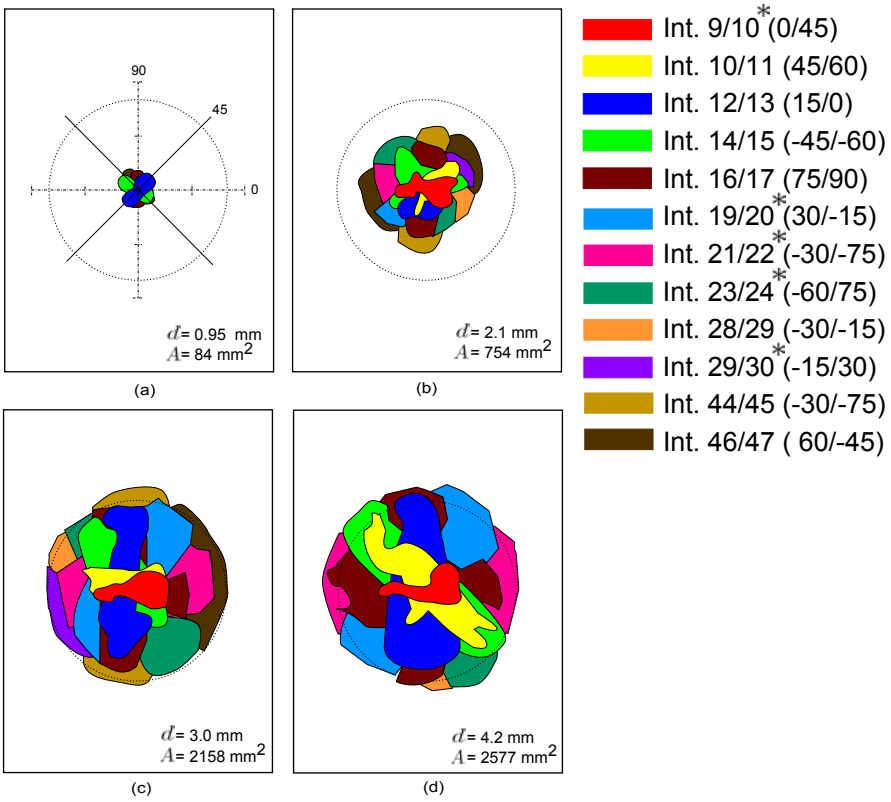

Fig. 6.5: Through-the-thickness position and extension of individual delaminations of LO laminate at different displacement levels up to fiber fracture (the dashed circles represent the circular hole dimension and * refer to the mismatch angle within the non-crimp-fabrics (bi-angle layer)). Each C-scan corresponds to a different specimen.

The through-the-thickness position of individual delaminations at different displacements up to the fiber breakage for the five considered laminates is presented in Figures 6.4, 6.5 to 6.8. Due to the configuration of the C-scan, the first 8 interfaces closed to the indenter for the four laminates are not detectable. For all the laminates, a few number of delaminations were observed for small indenter displacements. For laminates NS and NLU, these delaminations were concentrated in the upper half of the laminate (before interface 24), Figure 6.6(a) and Figure 6.7(a). This is due to the higher shear stresses at the upper part of the laminate which originated form matrix cracks [186]. These matrix cracks trigger delamination in the adjacent interface. However, for laminates LO and NLL, delaminations were observed not only in the upper half of the laminate, but also in the last interface of the laminate in which the mismatch angle is 90° and 75°, respectively. By increasing the applied displacement, delaminations grow in the already delaminated interfaces and also new new delaminations appear at other interfaces dissipating the applied energy until the fiber breakage starts. The projected delamination area for the five laminates corresponds to the well-known circular profile, which is a projection of individual peanut shape delaminations [43].

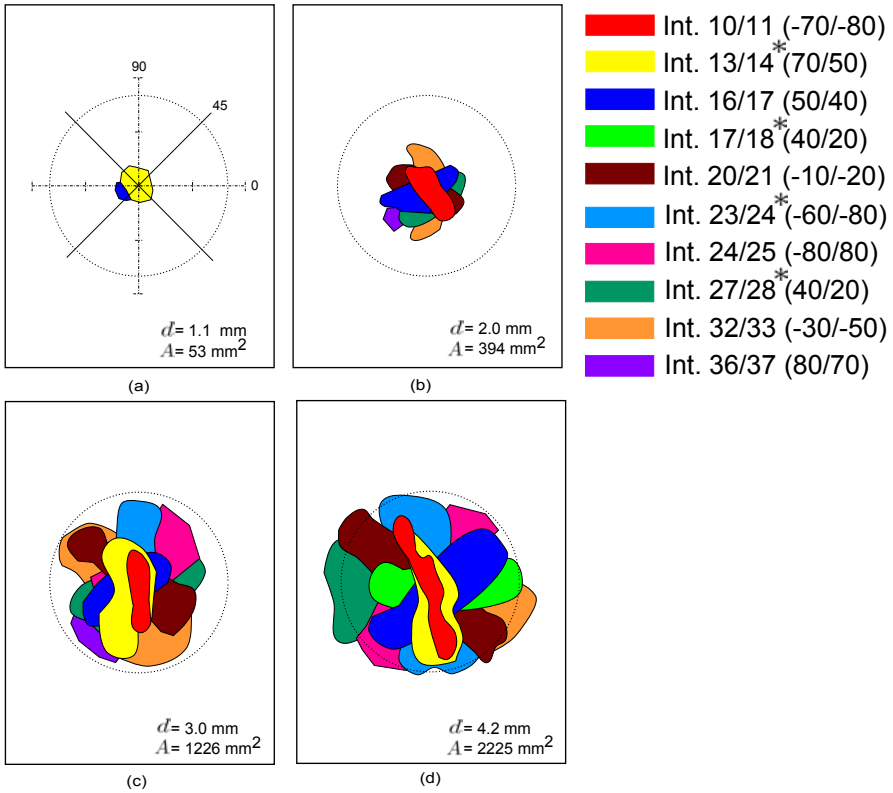

Fig. 6.6: Through-the-thickness position and extension of individual delaminations of NS laminate at different displacement levels up to fiber fracture (the dashed circles represent the circular hole dimension and * refer to the mismatch angle within the non-crimp-fabrics (bi-angle layer)). Each C-scan corresponds to a different specimen.

Figure 6.15 shows a comparison between the total and the dissipated energy for the five considered laminates. The total energy is calculated by integrating the area under the load versus displacement curves; the elastic energy is calculated by the area under the unloading curve; and the dissipated energy is obtained by subtracting the elastic energy from the total energy [186]. The total energy is almost equal for the five tested laminates during the elastic response. After the damage starts, laminate NLU shows the highest total energy. The dissipated energy due to delamination is larger for laminates NS, NLU and NLL than the other two laminates. At the maximum displacement, laminate NLU shows the largest dissipated energy.

In order to summarize this section, according to the experimental observations presented, laminates BL, NS, NLU and NLL show higher damage threshold load, while laminates NS and NLU present higher maximum load and the lowest projected delamination area is found for laminates NS, NLU and NLL.

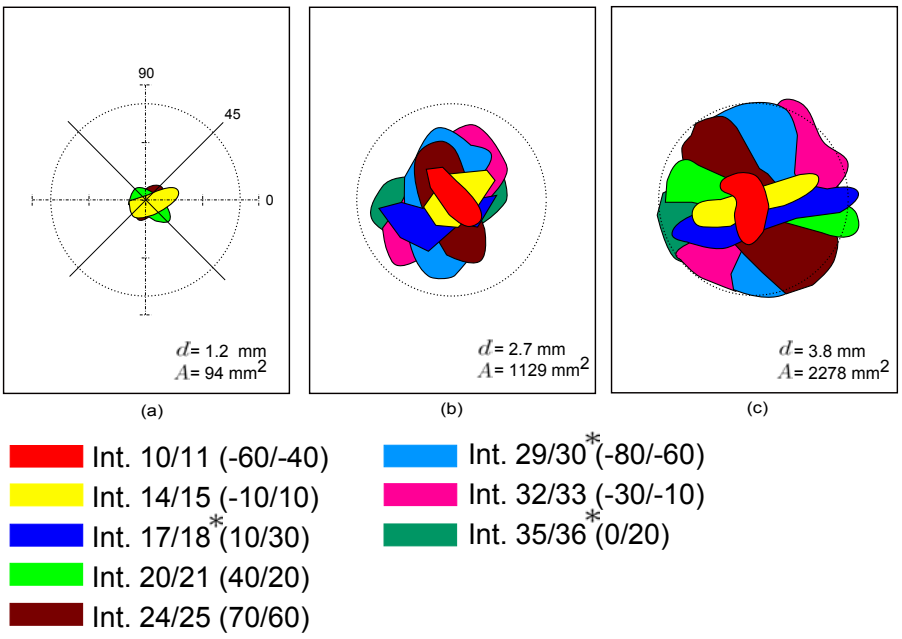

Fig. 6.7: Through-the-thickness position and extension of individual delaminations of NLU laminate at different displacement levels up to fiber fracture (the dashed circles represent the circular hole dimension and * refer to the mismatch angle within the non-crimp-fabrics (bi-angle layer)). Each C-scan corresponds to a different specimen.

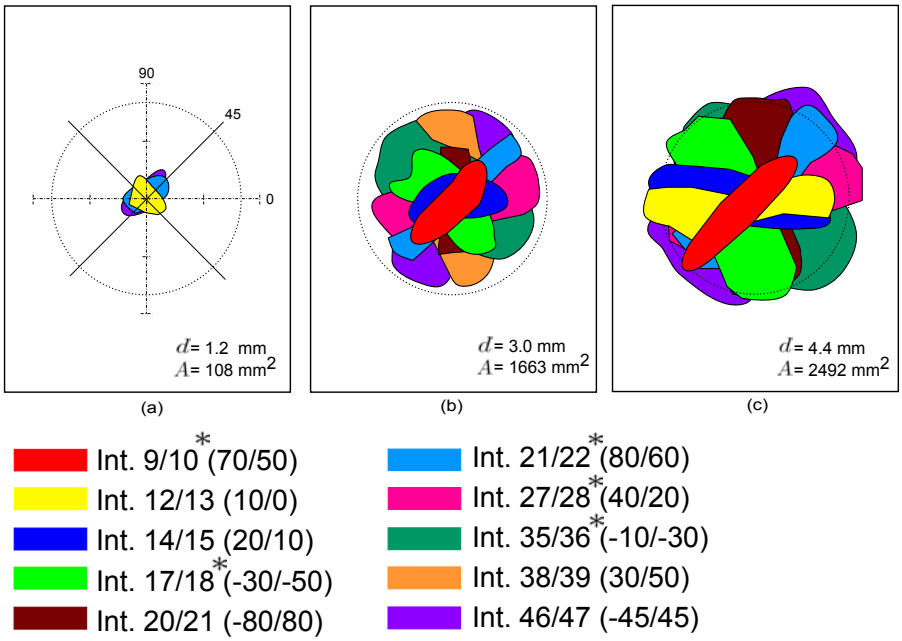

Fig. 6.8: Through-the-thickness position and extension of individual delaminations of NLL laminate at different displacement levels up to fiber fracture (the dashed circles represent the circular hole dimension and * refer to the mismatch angle within the non-crimp-fabrics (bi-angle layer)). Each C-scan corresponds to a different specimen.

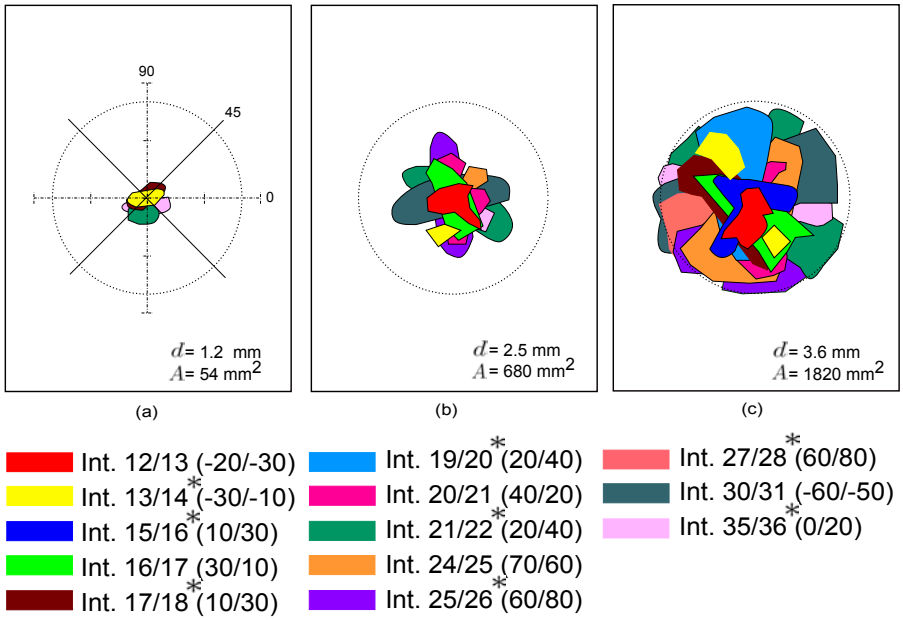

Fig. 6.9: Through-the-thickness position and extension of individual delaminations of NCU laminate at different displacement levels up to fiber fracture (the dashed circles represent the circular hole dimension and * refer to the mismatch angle within the non-crimp-fabrics (bi-angle layer)). Each C-scan corresponds to a different specimen.

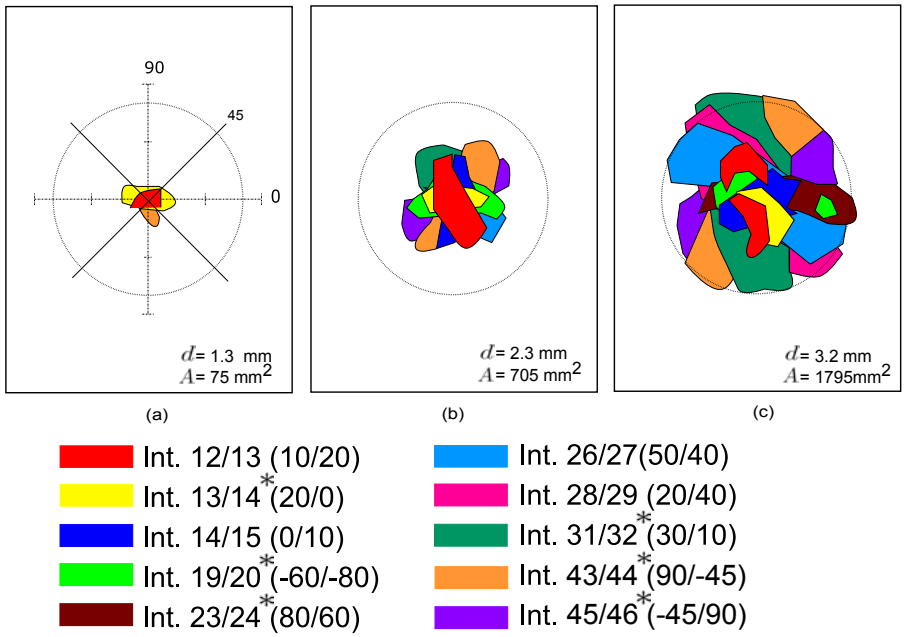

Fig. 6.10: Through-the-thickness position and extension of individual delaminations of NCL laminate at different displacement levels up to fiber fracture (the dashed circles represent the circular hole dimension and * refer to the mismatch angle within the non-crimp-fabrics (bi-angle layer)). Each C-scan corresponds to a different specimen.

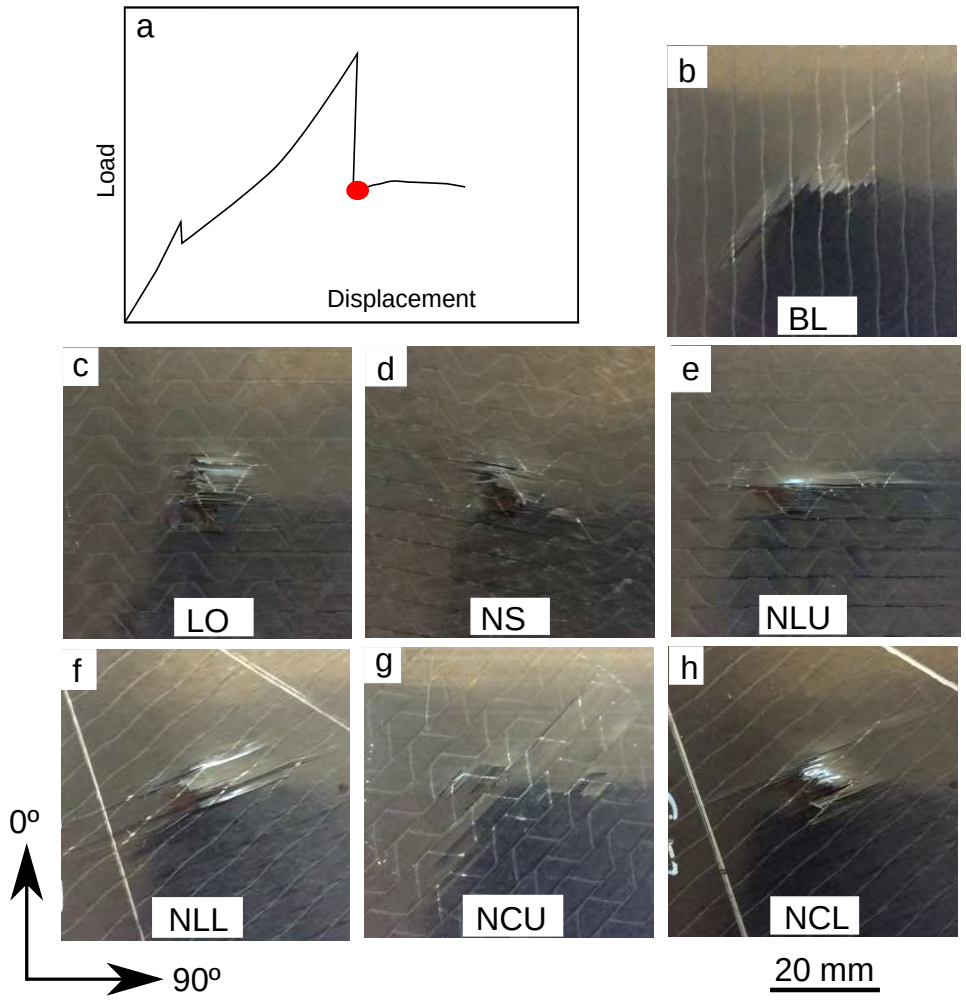

Fig. 6.11: Photographs of the specimens' back face after the largest load drop in the load-displacement response. In (a) a typical load-displacement curve for composite laminate under QSI test indicating the point at which all the images have been taken.

6.4.2 Combining small mismatch angel with ply clustering

For this study, two configurations are considered, laminates NCU and NCL. Laminate NS is also considered with the aim of comparison. Figure 6.16a shows the damage threshold load for laminates NS, NCU and NCL. The damage threshold load is almost the same for laminates NS and NCU, while for laminate NCL is sightly lower. This slight decrease can be related to the clustering of the lower plies in which matrix cracks are more likely to grow due to the bending tensile stresses [60] and as a result more delaminations can appear at this interfaces (see Figure 6.10).

The maximum load capacity, F_{m}, and the perforation load, F_{p}, for laminates NS, NCU and NCL are shown in Figure 6.16b. The maximum load capacity of laminate NCU is slightly larger than that value for laminate NS. This is due to the growth

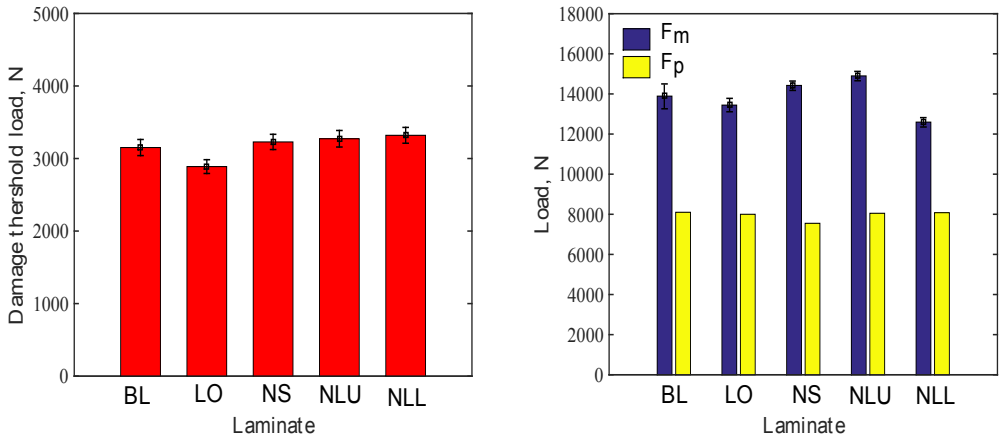

(a) F_{th} **(b)** F_{m} and F_{p}

Fig. 6.12: Comparison of the a) damage threshold load and b) maximum load and the load after the fiber breakage for laminates BL, LO, NS, NLU and NLL.

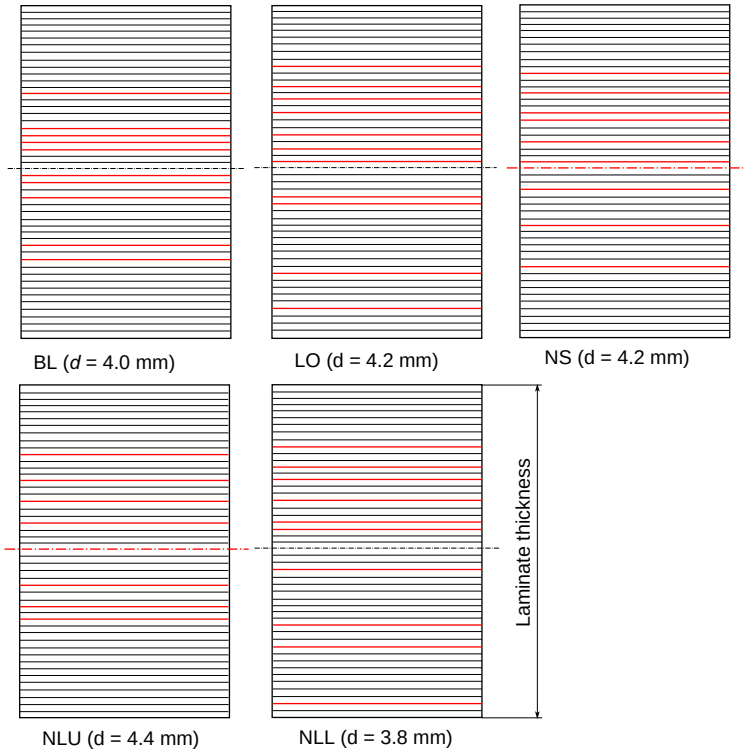

Fig. 6.13: Schematic representation of the through-the-thickness delamination positions (red lines) in laminates BL, LO, NS, NLU and NLL at displacement just before that corresponds to the maximum load.

of larger number of delamination in the upper part of the laminate (see Figure 6.17) which dissipate a large portion of the applied energy and as a result delay the fiber breakage. Also, the concentration of delaminations in the upper part keep the lower part of the laminate without delaminations, which reduces the possibility of

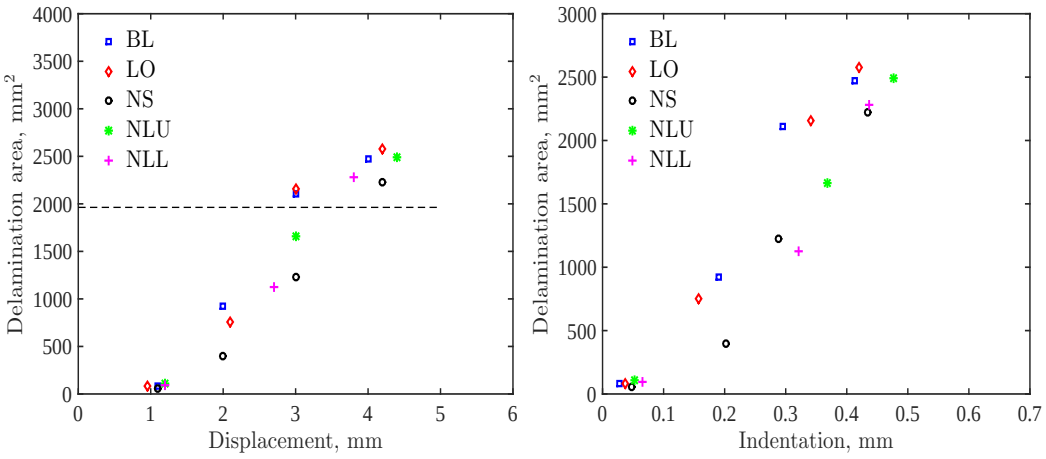

Fig. 6.14: Projected delamination area for laminates BL, LO, NS, NLU and NLL as a function of the indenter displacement and the indentation depth. The dash line in (a) represent the displacement at which the delamination reach the boundary condition.

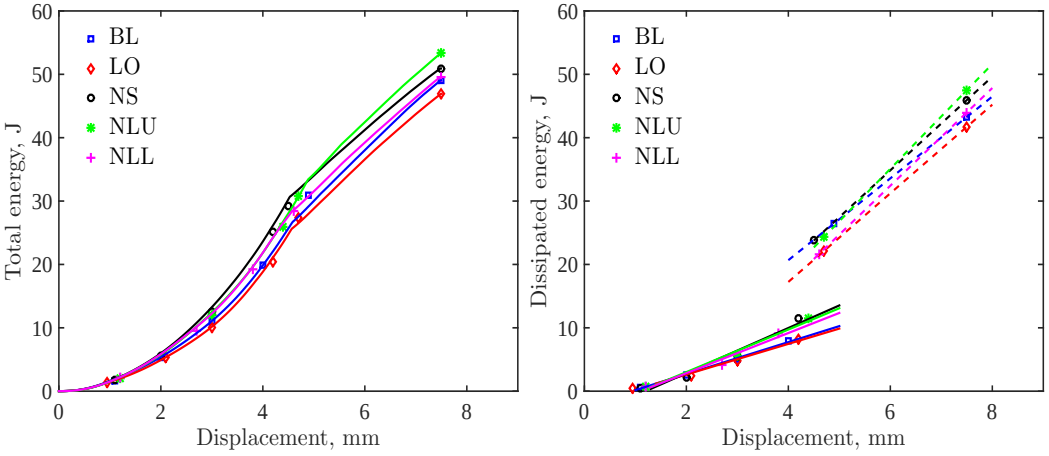

Fig. 6.15: Total and dissipated energy as a function of the applied displacement for all the tested laminates. In (b) the solid lines are the linear fitting of the dissipated energies before the fiber breakage and the dash lines are the linear fitting of the dissipated energies after the fiber breakage.

fiber breakage in this zone subjected to larger tensile stresses (see Figure 6.11 (g)). However, NCL laminate shows much lower maximum load capacity. This is due to the growth of matrix cracks in the clustered plies at the lower part of the laminate, which act as delamination initiators in the interfaces below the clustered plies (see Figure 6.10). These delaminations reduce the ability of the plies in the lower part of the laminate to withstand tensile stresses, causing earlier fiber breakage (see Figure 6.11 (h)).

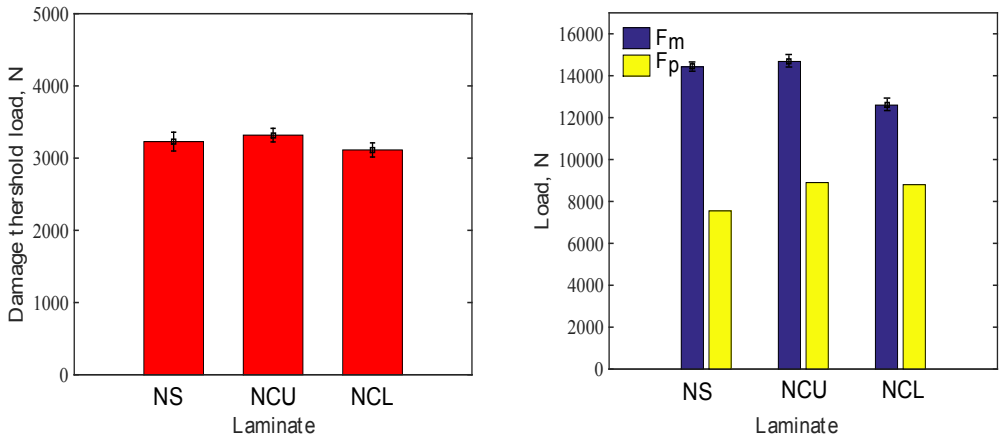

(a) F_{th} **(b)** F_{m} and F_{p}

Fig. 6.16: Comparison of the a) damage threshold load and b) maximum load and load after the fiber breakage for laminates NS, NCU and NCL.

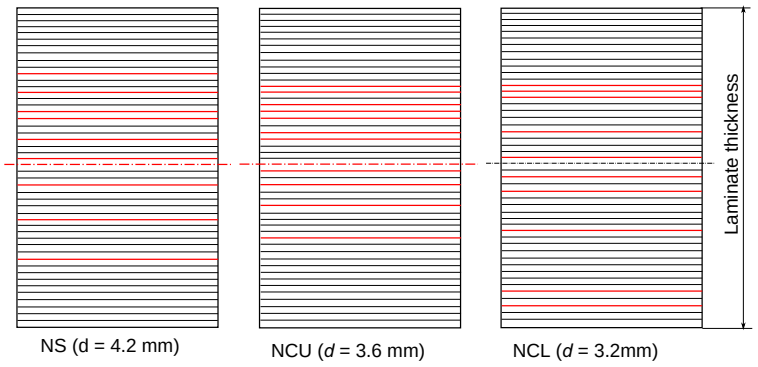

Fig. 6.17: Schematic representation of the through-the-thickness delamination positions (red lines) in laminates NS, NCU and NCL at displacement just before that corresponds to the maximum load.

Figure 6.16b also shows the perforation load, F_{P}, for the three considered laminates. It is observed that laminates NCU and NCL have almost equal F_{p} and larger than laminate NS. This can be attributed to the accumulation of the damage in the upper or the lower part of the laminate in laminates NCU and NCL which keep a large portion of the laminate without damage. This portion without damage make the laminate able to sustain more load than laminate NS.

A comparison between the amount of energy applied and dissipated due to damage in laminates NS, NCU and NCL as a function of the applied displacement is shown in Figure 6.18. Before the fiber breakage, the plots do not show advantage to any of the three laminates given that the values are almost the same for the three laminates with small deviation. At the largest displacement, $d = 7.5$ mm, the applied energy and the dissipated energy is quite larger for laminate NCU than the other

two laminates. This can be attributed to the larger number of delaminated interfaces which dissipate more energy in laminate NCU than the other three laminates. This implies that the absorbed energy by the different damage mechanisms is almost the same for laminate NS and NCL.

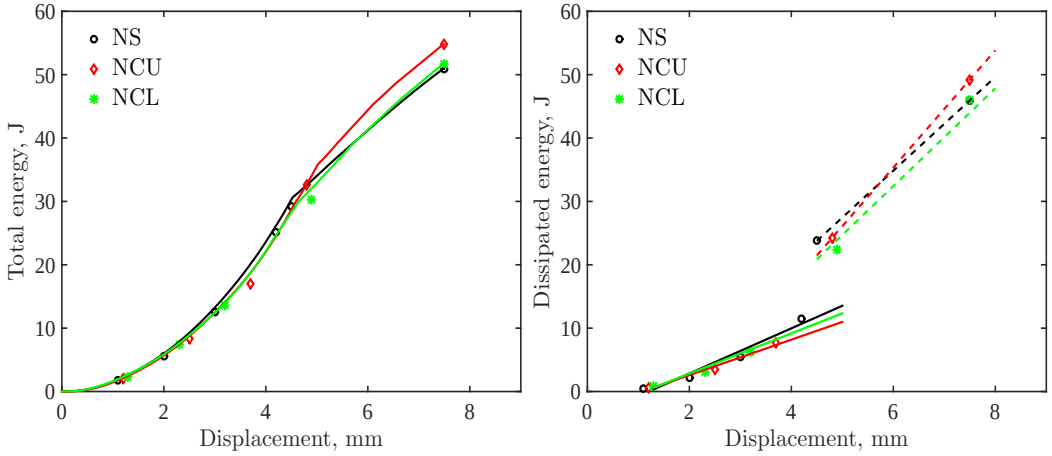

(a) Total energy **(b)** Dissipated energy

Fig. 6.18: Total and dissipated energy as a function of the applied displacement for laminates NS, NCU and NCL. In (b) the solid lines are the linear fitting of the dissipated energies before the fiber breakage and the dash lines are the linear fitting of the dissipated energies after the fiber breakage.

Figure 6.19a summarizes the relation between the projected delamination area and the applied displacement for laminates NS, NCU and NCL. The projected delamination area is almost equal for the three laminates when represented versus the applied displacement. However, comparing the projected delamination area with the indentation depth, Figure 6.19b, laminate NCU shows the lowest projected delaminated area among the three considered laminates. This can be attributed to the presence of clustered plies in the upper part of the laminate, which makes this part of the laminate more prone for the initiation and growth of both intralaminar and interlaminar cracks. These two damage mechanisms cause more local deformation and permanent indentation in laminate NCU.

Analyzing the through-the-thickness individual delaminations for laminates NCU and NCL, Figures 6.9 and 6.10, show the advantage of laminate NCU of having the last quarter of the laminate without delaminations. However, in this laminate more delaminated interfaces can be observed compared to laminates NS and NCL. These delaminated interfaces are concentrated in the upper and the middle parts of the laminate, keeping the lower quarter of the laminate without delaminations. The prevention of delmainations growth in the lower quarter of the laminate lead to lower fiber breakage in the back face of the laminate (see Figure 6.11 (g)). In the case of laminate with delaminated interfaces concentrated in one part of the laminate, a cluster of plies can be found inside the laminate without delaminations which can

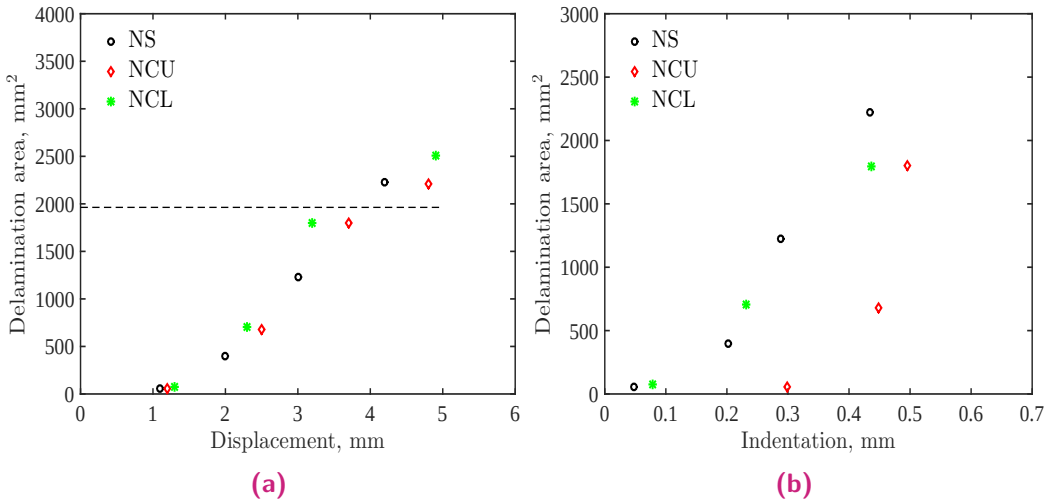

Fig. 6.19: Projected delamination area as a function of the indenter displacement and the indentation depth for laminates NS, NCU and NCL. The dash line in (a) represent the displacement at which the delamination reach the boundary condition.

withstand more loads and show much larger load capacity [189]. Moreover, this cluster of plies without damage lead to better damage tolerance [190] due to the ability of this clusters to resist buckling during a compression after impact test.

In view of the evaluation of the damage threshold load, the maximum load capacity, the projected delamination area with respect to the applied displacement and the indentation depth and also the through-the-thickness individual delamination, the damage threshold load and the maximum load capacity is lower for laminate NCL than laminate NS and NCU. Laminate NCU shows lower projected delaminated area as a function of the indentation depth. Moreover, the advantage of this laminate appears clearly for having a cluster of 12 plies in the lower part of the laminate without delaminations which improve not only the damage resistance but also the damage tolerance. Moreover, the amount of fiber breakage in the back face of the laminate after the largest load drop is small compared to the other two laminates.

6.5 Conclusions

A series of quasi-static indentation tests have been carried out on Non-Crimp-Fabric thin-ply carbon/epoxy composite laminates with seven different lay ups. The tested laminates were designed to have a combination between large and small mismatch angles and clustered plies. An ant colony optimization algorithm was used during the design process of the laminates in order to ensure the same in-plane elastic properties a difference in the flexural properties within 10%.

The results show that the damage threshold load and the maximum load capacity are increased in the laminates with larger mismatch angle in the upper part of the laminate and also by using clustered plies in the upper part of the laminate. Using larger mismatch angles or clustered plies in the upper layers allow delamination initiation and growth in this part of the laminate which is subjected to compressive stresses. The growth of this delamination dissipate large portion of the applied energy which prevent initiation and growth of delamination in the lower part of the laminate. As a result, a cluster of plies can be found inside the laminate without delaminations which can withstand more loads and show much larger load capacity.

Regarding the damage resistance, the laminates with larger mismatch angles in the upper part and also laminates with clustered plies in upper part show lower projected delaminated area as a function of applied displacement compared to the other laminates. Moreover, the laminate with clustered plies in the upper part of the laminate shows lower projected delaminated area as a function of indentation depth compared to the other laminates. In addition, this laminate, NCU, has a cluster of plies without damage in the lower part of the laminate which might improve the damage tolerance as well.

As a final conclusion, designing a nonsymmetric laminate with small mismatch angle and clustered plies in the upper part of the laminate improves the load capacity and the damage resistance of the laminate.

Part II

Analytical models

Indentation depth prediction

7

7.1 Introduction

This chapter introduces a parametric study on the indentation problem using a 2D axisymetric FE model. This study aims to numerically derive a closed form equation for the elastic force-indentation depth relation, F-α, for composite laminates of finite thickness in contact with stiff spherical indenter of a given radius. Two different situations are considered: i) the composite laminate is fully supported on a rigid substrate and ii) the composite laminate is supported on a hollow substrate. Based on different analytical models presented in the literature without the thickness effect, two equations are numerically derived and validated with experimental results. The presented equations predict the response of composite laminates, F-α, under indentation load taking into account the effect of lamina and laminate thickness for both cases previously mentioned (full and hollow support).

7.2 Indentation response

7.2.1 Hertzian contact law for half space

As proposed by Swanson [119], the relation between the contact force (F) and indentation depth (α) for a half space laminated plate can be calculated with:

$$F = K\alpha^{1.5} \tag{7.1}$$

where K is the Hertzian contact stiffness for half space that can be approximated as $K = \frac{4}{3}\sqrt{r}E_{\mathrm{T}}$, r is the radius of the rigid spherical indenter and E_T an effective modulus for transversely isotropic materials.

Turner [117] introduced a method for calculating the effective modulus for transversally isotropic materials E_T as follows:

$$E_{\mathrm{T}} = \frac{2}{\alpha_1\alpha_3} \tag{7.2}$$

The parameters α_1 and α_3 can be determined as:

$$\alpha_1 = \sqrt{\frac{\frac{E_{xx}}{E_{zz}} - \nu_{xz}^2}{1 - \nu_{xy}^2}}$$

$$\alpha_2 = \frac{\frac{E_{xx}}{2G_{xz}} - \nu_{xz}(1 + \nu_{xy})}{1 - \nu_{xy}^2}$$

$$\alpha_3 = \frac{2(1 - \nu_{xy}^2)}{E_{xx}} \sqrt{\frac{\alpha_1 + \alpha_2}{2}}$$

where E_{xx}, E_{zz}, G_{xz}, ν_{xy}, ν_{xz} are the three-dimensional effective elastic constants of transversely isotropic materials or composite laminate (z is the thickness direction and x and y are the in-plane directions).

As a result, the effective modulus, E_T, can be calculated if the three-dimensional effective elastic constants of the laminate are known. A number of methods has been developed to theoretically calculate the three dimensional properties of composite laminates based on the lamina properties [124, 150, 191, 192]. However, as none of these methods is easy to be implemented, a simple model to compute the three dimensional properties of orthotropic laminates is proposed here. The equations of this model are summarised in Appendix 1.

7.2.2 General indentation problem

The most important step in studying a problem is identifying the parameters that influence this problem. The parameters that influence a general indentation problem on a quasi-isotropic laminate can be summarized as follows:

$$F(\alpha, r, t, R, t_{ply}, \mathbf{E}_{ply}) \tag{7.3}$$

where F is the applied force (N), α is the indentation depth (mm), t is the laminate thickness (mm), R is the hole radius (mm) for the hollow supported case, t_{ply} is the lamina thickness (mm) and $\mathbf{E}_{ply}$ is the elastic properties of the ply.

If the ply thickness is small enough compared to other problem dimensions, the homogenized material properties can be used resulting in:

$$F(\alpha, r, t, R, \mathbf{E}_{Lam}) \tag{7.4}$$

where $\mathbf{E}_{Lam}$ includes the five independent material properties for transversely isotropic materials. In this case, the elastic problem is considered axisymmetric.

Turner's [117] solution for half-space shows that this set of elastic properties can be reduced to the effective transverse modulus E_T defined in Equation 7.2. Based on this, the response can be defined as:

$$F(\alpha, r, t, R, E_T) \tag{7.5}$$

According to Buckingham-π theorem [193], the latter equation can be normalized as follows: $\bar{F} = F/(E_T r^2)$, $\bar{\alpha} = \alpha/r$, $\bar{t} = t/r$ and $\bar{R} = R/r$, resulting in:

$$\bar{F}(\bar{\alpha}, \bar{t}, \bar{R}) \tag{7.6}$$

It is known that for the half-space problem, Equation 7.1 works properly. Applying the normalization procedure, it is possible to define $\bar{F} = \frac{4}{3}\bar{\alpha}$ for large $\bar{t}$. To validate the hypothesis of E_T as the only significative elastic property, several material systems are considered (Table 7.1). In Section 7.3, a numerical analysis is performed to determine the load indentation law for composite laminates under fully and hollow support boundary conditions. Equation 7.6 assumes that the problem is axisymmetric, which is true if ply thickness is thin enough to assume that the homogenized properties can be used. On the other hand, if $\bar{t}_{ply} = t_{ply}/r$ is large, the indentation response might depend on the elastic properties of independent plies and problem is no longer axisymmetric. To validate this hypothesis in quasi-isotropic materials a three dimensional model is defined considering several materials and ply thicknesses.

7.3 Numerical modeling

An elastic 2D axisymmetric contact model was developed using a commercial software to obtain the elastic indentation response of a composite laminate. The specimen were meshed using 2D four node structural elements PLANE 182. As a considerably fine mesh is required to ensure accurate results and convergence, a convergence study of the FE results was conducted to ensure that the mesh refinement in the composite laminate is fine enough to capture the stresses, strains and deformations with reasonably accuracy. As a result, a graded mesh was created with a finer mesh close to the contact region. The interaction of the indenter and the specimen was modeled as a contact pair with no friction. Contact element TARGET169 is applied to the indenter and CONTACT175 to the specimen. A nonlinear analysis was conducted in this model. Displacement control technique is used to apply the displacement to the indenter in y-direction. The same model was built with two different boundary conditions. The first, acts as a fully supported specimen

(specimen on a rigid substrate) and the other, acts as a hollow support specimen (specimen between two rigid substrates with a central hole). The boundary condition for the second case was modeled as a fixed support at the hole perimeter (assuming no slipping between the two rigid substrates and the specimen); so, the actual part was modeled just as the part of the specimen on the hole; dimension R. Figure 7.1 shows the models used for this study with the meshing and the applied boundary conditions.

The indentation depth was found as the output of the simulation. For the fully supported case the indentation depth (α_0) is the displacement of the indenter reference point, and for the hollow supported case the indentation depth can be computed from this equation:

$$\alpha_0 = D_1 - D_2 \tag{7.7}$$

where D_1 is the displacement of the indenter reference, point 1, and D_2 is the displacement of point 2 (see Figure 7.1).

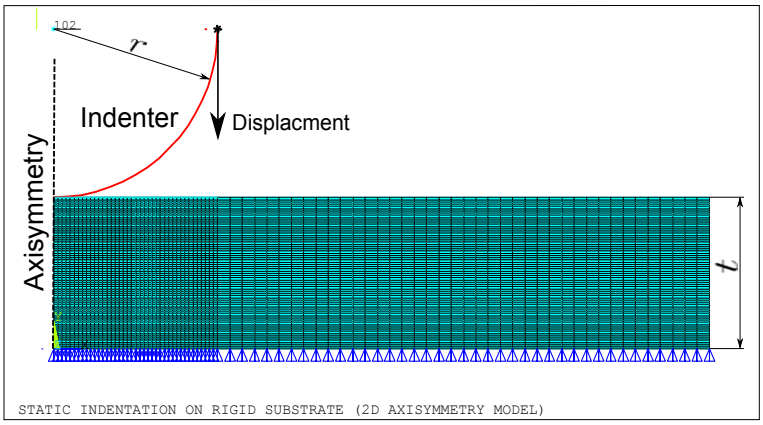

(a) Fully supported (specimen on a rigid substrate)

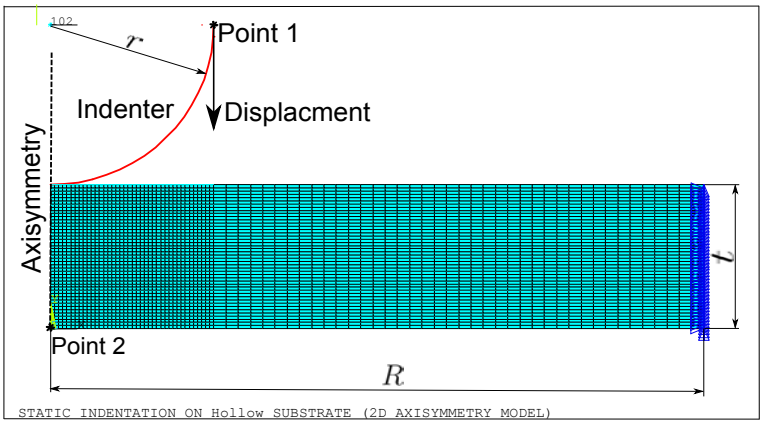

(b) Hollow supported (specimen on a rigid substrate with central hole)

Fig. 7.1: Meshing pattern and boundary conditions for the indentation FE models.

Before numerically deriving a relation (F-α) for a composite laminate of finite thickness, it is instructive to check the agreement between an analytical effective modulus as given by Equation 7.2 and that obtained from FE analysis for an orthotropic halfspace. In order to meet the half-space requirement, orthotropic solid FE models (thickness t = 50 mm) were built such that the ratio of contact radius to model thickness is less than 0.05, and the ratio of contact radius to model length is less than 0.02 for all load cases [131]. Four different quasi-isotropic materials were investigated. As mentioned in Section 7.2.2, the 3D homogeniezed elastic properties of the laminate summarised in Table 7.2 were calculated based on the elastic properties of the different materials mentioned in Table 7.1 and the equations shown in Appendix 1. The corresponding effective modulus, E_T, were calculated by fitting the FE results with the contact Hertz law. The obtained values of E_T were in a good agreement with the corresponding analytical values derived from Equation 7.2, which provides a validation means to numerically determine the contact stiffness for composites of different thicknesses.

Tab. 7.1: Material properties of a unidirectional ply for different composite material

Material	Stack sequence	E_{11} (GPa)	E_{22} (GPa)	ν_{12}	G_{12} (GPa)
AS4D/TC350	$[45/0/-45/90]_{2s}$	135.4	9.3	0.32	5.3
Carbon/Epoxy [98]	$[0/45/90/-45]_{2s}$	148	10	0.31	4.74
Carbon/Epoxy [132]	$[0/45/90/-45]_{2s}$	120.7	7.93	0.3	5.52
Glass/Epoxy [194]	$[0/45/90/-45]_{2s}$	45.4	15.2	0.281	6.03

Tab. 7.2: The three-dimensional effective elastic constants.

Material	$E_{xx} = E_{yy}$ (GPa)	E_{zz} (GPa)	ν_{xy}	$\nu_{xz} = \nu_{yz}$	G_{xy} (GPa)	G_{xz}=G_{yz} (GPa)	E_T (GPa)
AS4D/TC350	52.6	11.1	0.307	0.322	20.1	4.25	11.70
Carbon/Epoxy [98]	56.5	10.75	0.316	0.249	21.47	4.29	12.07
Carbon/Epoxy [132]	86.7	8.6	0.3	0.143	15.77	4.28	4.50
Glass/Epoxy [194]	25.1	15.6	0.292	0.251	9.7	5.9	16.56

To study the effect of laminate thickness on the response of the composite laminate and derive a F-α relation, the contact problem was solved numerically due to the non-linear behaviour and the presence of rigid boundary constraint. Parametric studies were performed using the same FE model introduced with three variable parameters for the fully supported case, i.e. the material properties, the indenter radius r (mm) and the laminate thickness t (mm). For the hollow supported case, four variable parameters were considered; i.e. the three parameters considered for the fully supported case and a new parameter which represent the hole radius R (mm).

Two quasi-isotropic laminates $[45/0/-45/90]_{ns}$ with distinctive material properties were studied, carbon/epoxy AS4D/TC350 and glass/epoxy. The unidirectional ply

properties of both materials are shown in Table 7.1. Four indenter radius, r = 5, 7.5, 10, and 12.5 mm; and four laminate thicknesses were considered: t = 1, 2, 4 and 8 mm that correspond to n = 1, 2, 4 and 8. The hole radius for the hollow supported case was taken as R = 5, 10, 12.5, 25, 37.5 and 45 mm. In total, 224 numerical runs were performed.

7.4 Experiment

The material used in this study was UD tape prepreg AS4D/TC350 carbon/epoxy plies with stacking sequence $[45/0/-45/90]_{3s}$. The unidirectional elastic properties are summarized in Table 7.1, which also includes the elastic properties of other UD composite plies that will be used later in this study for validation.

Quasi-static indentation test was used to introduce the response of composite laminate with a 100 kN MTS universal testing machine. Figure 7.2 shows the indentation experimental setup with configuration of the sample, indenter, and the fixture (centrally-hollow support, and rigid base). The indenter was stainless steel hemisphere of 12.7 mm diameter according to the ASTM standard [149]. Basically, the fixture for the centrally hollow support consists of two hollow cylindrical plates with a 50 mm diameter hole clamping the specimen. The specimen was clamped between both plates to prevent the separation of the specimen edges from the base during loading. The set of clamping plates and specimen were mounted on top of three columns to allow the direct measurement of the deflection of the specimen with a displacement transducer (Transducer 2 in the figure). The indentation load was centrally applied. The fixture for the fully support was taken as a stainless steel plate, Figure 7.2b. The QSI tests were carried out under displacement control at a loading rate of 0.5 mm/min. To avoid the testing machine compliance influencing the results, the displacement of the indenter was measured directly using a displacement transducer (Transducer 1 in the figure). When the displacements reached the value of d = 0.2 and 0.8 mm for the fully and hollow supported experiments respectively, the specimens were automatically unloaded.

In order to investigate both experiments; specimen with fully supported boundary condition and specimen with hollow supported boundary condition (specimen between two rigid plates with central hole), two sets of specimens were prepared. The first set with dimensions 40 $\times$ 40 mm to suit the fully supported case and the second set 80 $\times$ 80 mm to suite the hollow supported case. In both cases, the thickness of the specimens was 4.416 mm. Three specimens were tested for each set. The dimension of the fully supported case were taken based on the stress distribution in the specimen. The stresses in the in-plane dimension tends to zero at 16 mm distance from the indenter.

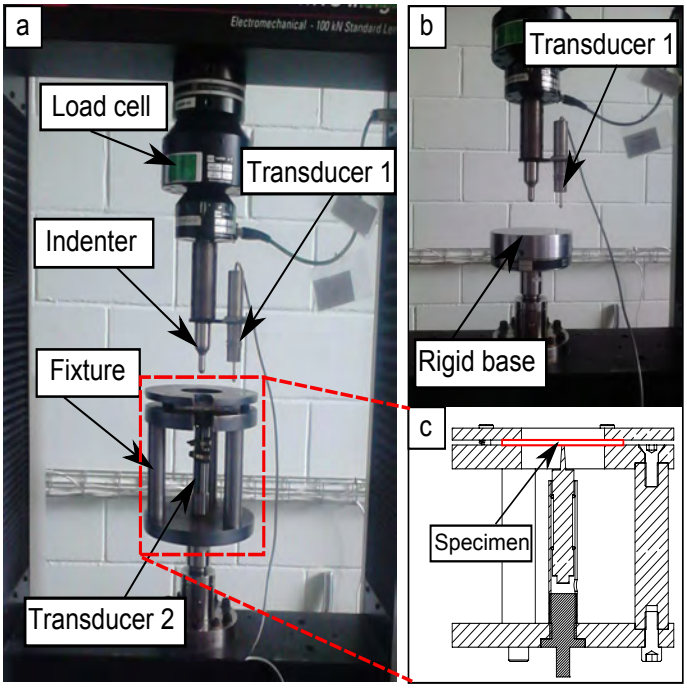

Fig. 7.2: Experimental set up of the QSI test: (a) Hollow supported test, (b) Fully supported test, and (c) The hollow support fixture working drawing.

In the indentation test with full support, the indentation depth was regarded as the same as the displacement of Transducer 1. However, for the hollow support condition, the deformation due to indentation, α_h, taking place in the specimen was not the same as the total displacement, D_t, measured by the indenter displacement (Transducer 1). Therefore, the structural deformation, D_{str},was measured using a second transducer, and the deformation due to indentation was calculated from the following equation [195]:

$$\alpha_h = D_t - D_{str} \tag{7.8}$$

7.5 Modified contact law for a plate of finite thickness

7.5.1 Fully supported experiment

As will be derived and explained later, for this experiment the hole radius is not considered. Additionally, there is no significant effect of the ply thickness on the response. So, Equation 7.6 can be simplified to:

$$\bar{F}(\bar{\alpha}, \bar{t}) \tag{7.9}$$

The Hertzian contact law for infinite plate as previously mentioned in Equation 7.1 can be expressed in function of dimensionless parameters as follow:

$$\bar{F} = \frac{4}{3}\bar{\alpha}_f^{1.5} \tag{7.10}$$

The result from the FE simulation were plotted on Log-Log scale and fitted for different values of $\bar{t}$ to derive a formula of the indentation response of a quasi-isotropic laminate with finite thickness. Figure 7.3 shows an example of Log ($\bar{F}$)-Log ($\bar{\alpha}$) for two different values of $\bar{t}$ with two different materials. The results were observed to completely fit linear relations on the Log-Log scale which gives an indication about the best fitting function.

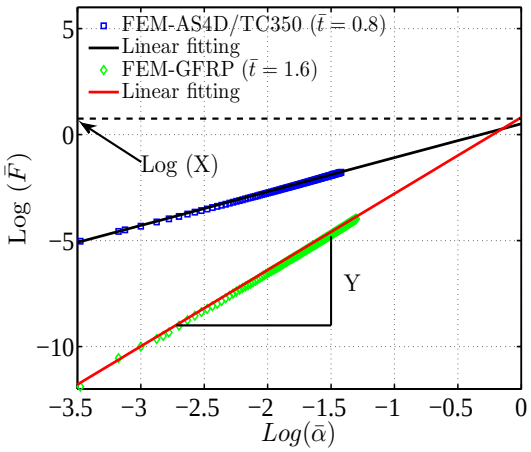

Fig. 7.3: Log ($\bar{\alpha}$)-Log ($\bar{F}$) for different values of $\bar{t}$ and two different materials.

Consequently, the FEM results could be fitted with an exponential function in this form:

$$\bar{F} = X\bar{\alpha}_f^Y \tag{7.11}$$

where X, and Y are two parameters that depend on $\bar{t}$. The values for X, and Y were computed for different values of $\bar{t}$ and plotted in Figure 7.4. The results of X, and Y were fitted with the following equations:

$$X = \frac{4}{3} + b \cdot \bar{t}^{-a}$$

$$Y = 1.5 + d \cdot \bar{t}^{-c} \tag{7.12}$$

where a, b, c, and d are the fitting parameters as shown in Figure 7.4. For large $\bar{t}$ values, the half-space response is recovered and the values of X and Y will be $\frac{4}{3}$ and 1.5, respectively, and Equation 7.11 will lead to Equation 7.10.

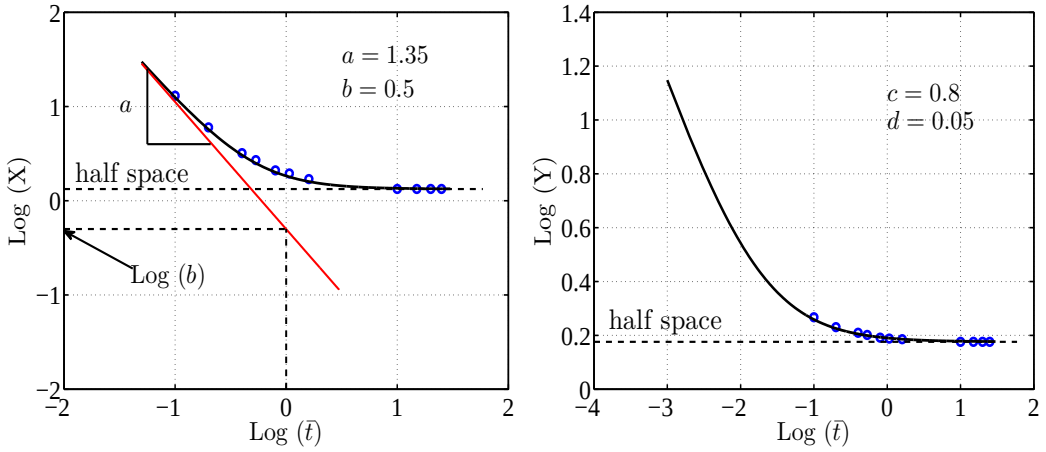

(a) X parameter **(b)** Y parameter

Fig. 7.4: Fitting parameters (a, b, c, and d) for fully supported experiment.

In order to check the validity of the derived equation the $\bar{F} - \bar{\alpha}$ curve was plotted for different $\bar{t}$ from both the FE results and the equation predictions. Figures 7.5a, 7.5b and 7.5c show a good agreement between the FE results and the derived $\bar{F} - \bar{\alpha}$ relation, equation 7.11. Figure 7.5d shows a comparison between the equation prediction and the experimental results done during this work on the AS4D/TC350 with dimensionless thickness $\bar{t}$ =0.695. The predictions of the proposed equation correlate well with the experimental results up to the damage initiation.

The effect of the laminate thickness on the contact response is shown in Figure 7.6. In this figure it can be seen that small variations in thickness is small have a great influence on the $\bar{F} - \bar{\alpha}$ response in the case of thin laminates. However, for thicker laminates, the response tends to the half-space one and the effect of thickness variation is minimized.

7.5.2 Hollow support experiment

Effect of hole radius

The effect of hole radius can be divided into three main parts: $\bar{R} = 0$, $0 < \bar{R} < 1$ and $\bar{R} \geq 1$. For $\bar{R} = 0$, the problem is solved as a fully supported problem and the indentation response can be computed as shown in Section 7.5.1. For $0 < \bar{R} < 1$, to the authors knowledge, there is no real application for indentation problem in this range, so this range is out of interest. To study the effect of hole radius in the range of interest, $\bar{R} \geq 1$, the $\bar{F}$-$\bar{\alpha}$ curves obtained for different values of $\bar{R}$ (1, 2, 4 and 6)

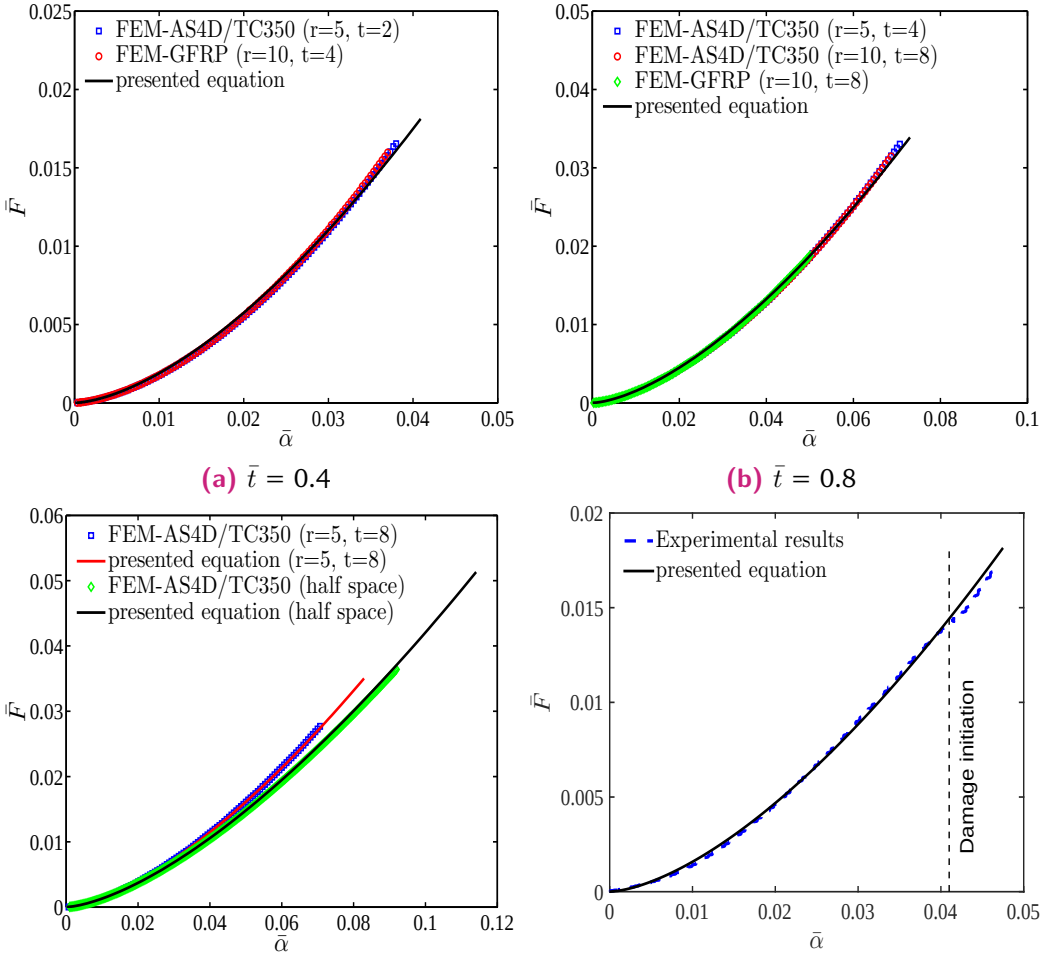

(a) $\bar{t} = 0.4$ (b) $\bar{t} = 0.8$

(c) $\bar{t} = 1.6$ and half space (d) AS4D/TC350 with $\bar{t} = 0.695$

Fig. 7.5: Comparison between FEM results, experimental results and the presented equation predictions.

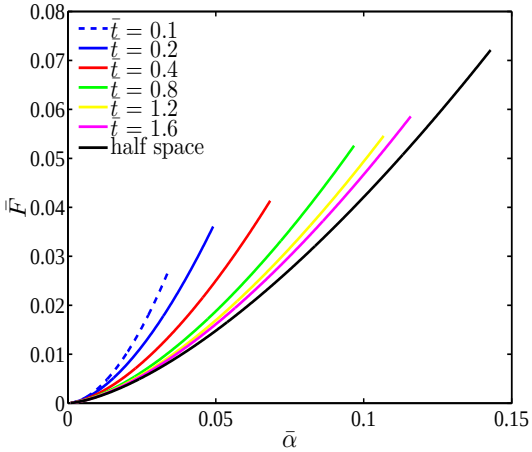

Fig. 7.6: Effect of laminate thickness on the load indentation relation.

and two different values of $\bar{t}$, 0.2 and 0.4, were represented together. As it is shown in Figure 7.7 there is no significant effect of the hole radius on the load indentation curve. Similar results were reported by Chen et al. [121]. In their study, the effect of the hole shape was studied for two different shapes (circular, and square). In consequence, the parameter $\bar{R}$ can be eliminated from the equation.

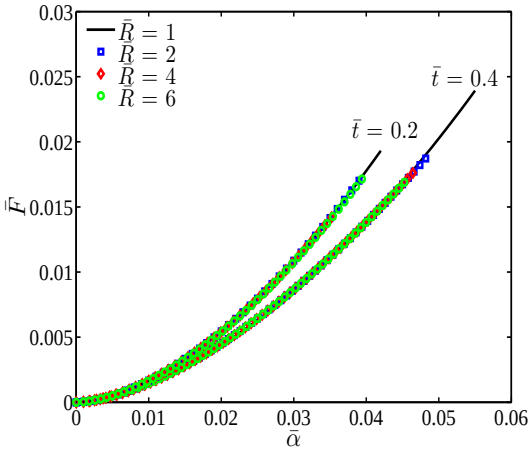

Fig. 7.7: Effect of the hole radius on the load indentation relation for different values of $\bar{t}$.

Effect of lamina thickness

In order to study the effect of lamina thickness on the response, a 3D FE model was implemented to simulate the elastic response of the indentation experiment with the fully and hollow supported boundary conditions. The material used for this study was AS4D/TC350 with stack sequence of $[45_n/0_n/-45_n/90_n]_{ms}$. The lamina thicknesses considered were 0.125, 0.25 and 0.5, corresponding to $n = 1$, 2 and 4, respectively. The global laminate thickness was 4 mm, where $m \times n = 4$. The simulation was done for the four indenter radii considered in the parametric study (r = 5, 7.5, 10, and 12.5 mm) and three hole radii (R = 5, 10 and 25 mm) , see Section 7.3. Figure 7.8 shows that there is no significant effect of the lamina thickness on the elastic response of the hollow support experiment. The same effect was observed for the fully supported experiment.

$F - \alpha$ relation derivation

The general equation for the indentation experiment, Equation 7.6, can be reduced to deal with the indentation experiment with a hollow support boundary condition. Neglecting the effect of lamina thickness and the hole radius, the equation for the hollow supported case can be also reduced to that considered for the fully supported case presented in Equation 7.9. The result from the FE simulation was plotted on

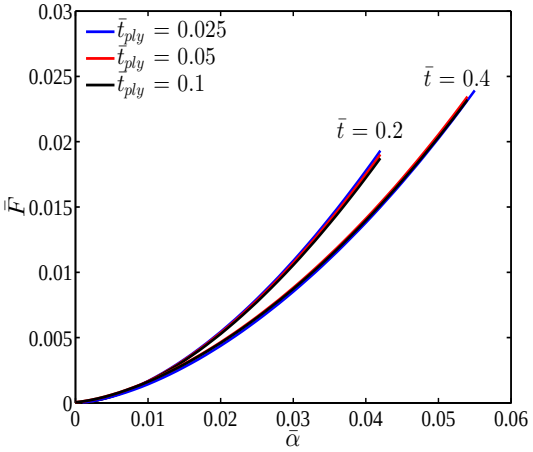

Fig. 7.8: Effect of the lamina thickness on the load indentation relation for different values of $\bar{t}$.

Log-Log scale and fitted for different values of $\bar{t}$ to derive a $\bar{F}$-$\bar{\alpha}$ relation for the indentation response of a quasi-isotropic laminate with finite thickness. Figure 7.9 shows an example of Log ($\bar{F}$)-Log ($\bar{\alpha}$) for $\bar{t} = 0.4$ with the aim of explanation of the derivation procedure.

Based on Figure 7.9, the FEM results can be fitted in this form:

$$\bar{F} = \left[(X_1 \bar{\alpha}_h^{Y_1})^B + (X_2 \bar{\alpha}_h^{Y_2})^B\right]^{\frac{1}{B}} \tag{7.13}$$

where X_1, Y_1, X_2 and Y_2 are fitting parameters that depend on $\bar{t}$ and which can be obtained as shown in Figure 7.9. B is a fitting parameter to fit the transition between the two functions ($X_1 \bar{\alpha}_h^{Y_1}$ and $X_2 \bar{\alpha}_h^{Y_2}$). The first part of the equation ($X_1 \bar{\alpha}_h^{Y_1}$), represented in red line in Figure 7.9, fits the first part of the response (small indentations) and the second part of the equation ($X_2 \bar{\alpha}_h^{Y_2}$), represented in blue line in the figure, fits the final part of the response (large indentations).

The values of X_1, Y_1, X_2 and Y_2 were computed for different values of $\bar{t}$ and fitted with the same procedure followed in Section 7.5.1 with the following resulting equations:

$$X_1 = 0.97 + 0.3\bar{t}^{-1.5}$$

$$Y_1 = 1.5 + 0.03\bar{t}^{-1.2}$$

$$X_2 = 1.05 + 1.5\bar{t}^{-2}$$

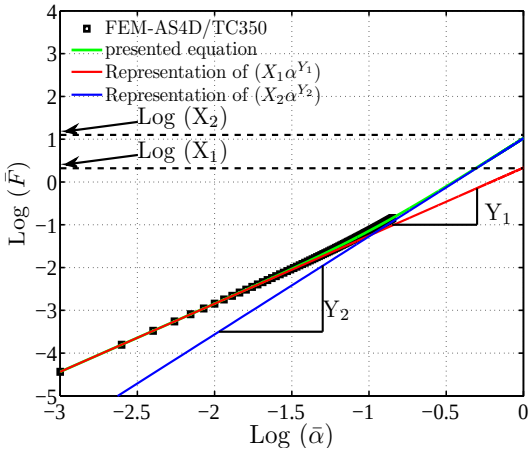

Fig. 7.9: Log $(\bar{F})$-Log $(\bar{\alpha})$ for hollow supported AS4D/TC350 material with $\bar{t} = 0.4$.

$$Y_2 = 1.5 + 0.2\bar{t}^{-1.5} \tag{7.14}$$

The value of the fitting parameter B was computed for different values of $\bar{t}$. This parameter was observed to be independent of the value of $\bar{t}$ and can be approximated to a fixed number, $B = 2.5$. For $\bar{t} \to \infty$, Equation 7.13 leads to Equation 7.10.

In order to check the validity of the derived equation, the $\bar{F} - \bar{\alpha}$ curve was plotted (Figure 7.10) for different values of $\bar{t}$ for both the FE results and Equation 7.13 predictions. Figure 7.10 shows a good agreement between the FE results and the equation predictions. Figures 7.11a, (b) and (c) show a comparison between the represented equation predictions, the experimental results reported by Wu and Shyu [98], Chen et al. model [121] and Yang and Sun model [118] for different values of $\bar{t}$. Figure 7.11d shows a comparison between the presented equation predictions and the experimental results obtained during this work on the AS4D/TC350 laminates with nondimensional thickness $\bar{t}$ =0.695 to check the validity of the presented equation for large indentation depths. The figure shows an excellent agreement between the equation predictions and the experimental results until the damage starts.

7.6 Discussion

The derived $\bar{F} - \bar{\alpha}$ relations introduced in Equation 7.11 and 7.13 can be used to predict the elastic force-indentation relationship (F-α) for any general composite laminate of finite thickness supported with fully support or hollow support boundary conditions. In this study, the FE results were fitted with two power equations:

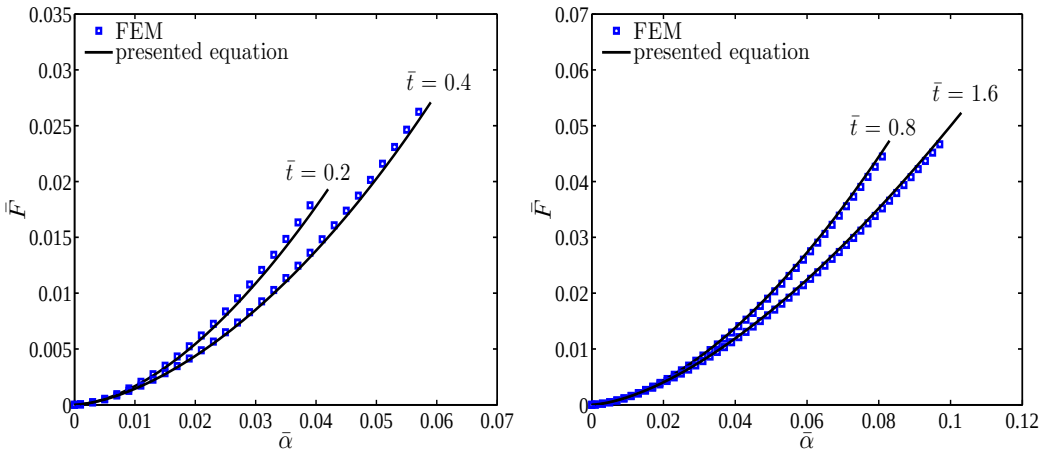

(a) $\bar{t} = 0.2$ and 0.4 **(b)** $\bar{t} = 0.8$ and 1.6

Fig. 7.10: Comparison between FEM results for AS4D/TC350 material and the presented equation predictions.

- Fully support

$$\bar{F} = \left(\frac{4}{3} + 0.5\bar{t}^{-1.35}\right)\bar{\alpha}_f^{\left(1.5+0.05\bar{t}^{-0.8}\right)} \tag{7.15}$$

- Hollow support

$$\bar{F} = \left[\left(\left(0.97 + 0.3\bar{t}^{-1.5}\right)\bar{\alpha}_h^{\left(1.5+0.03\bar{t}^{-1.2}\right)}\right)^{2.5} + \left(\left(1.05 + 1.5\bar{t}^{-2}\right)\bar{\alpha}_h^{\left(1.5+0.2\bar{t}^{-1.5}\right)}\right)^{2.5}\right]^{\frac{1}{2.5}} \tag{7.16}$$

Given the indenter radius, the laminate thickness, the boundary condition applied and the effective elastic modulus, the indentation response (F-α) can be easily computed through Equations 7.15 and 7.16.

For the hollow supported boundary condition, it is observed that Yang and Sun model predictions [118] deviate from the experimental data at the very beginning of the indentation and overestimate the indentation depth at a given contact force. In addition, the deviation becomes more significant as the contact force increases. Chen et al. model [121] shows a good agreement with the experimental data at the very beginning of the indentation. For large indentation, it overestimates the indentation depth at a given contact force at $\bar{t} = 0.315$ (see Figure 7.11a) and lower estimation of the indentation depth at a given force is predicted at $\bar{t} = 0.419$ and 0.63 (see Figure 7.11b and c). The prediction of the presented Equation 7.16 shows an excellent agreement with the experimental data for small and large indentation depths.

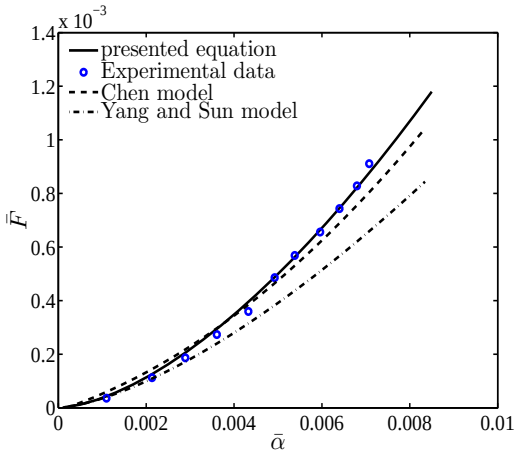

(a) Wu and Shyu [98] Experimental results for $\bar{t} = 0.315$

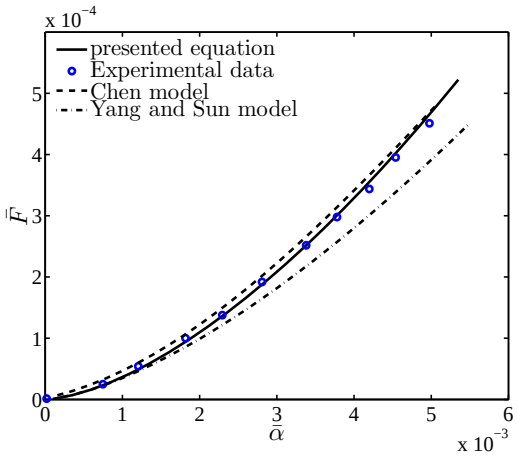

(b) Wu and Shyu [98] Experimental results for $\bar{t} = 0.419$

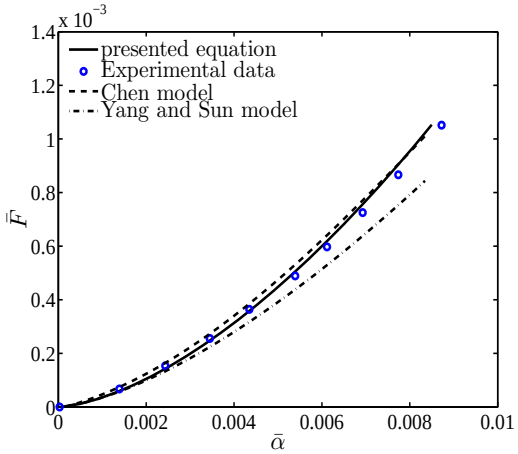

(c) Wu and Shyu [98] Experimental results for $\bar{t} = 0.63$

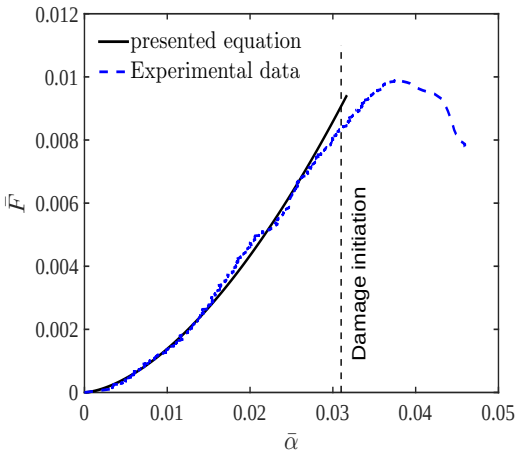

(d) AS4D/TC350 for $\bar{t} = 0.695$

Fig. 7.11: Comparison between presented equation predictions, experimental results, Chen et al. model [121] and Yang and Sun model [118].

It should be noted that the presented equations, Equations 7.15 and 7.16, are valid only for the elastic response of the composite laminates. In another word, these equations are valid to predict the indentation depth for composite laminates up to the damage initiation, Figures 7.5d and 7.11d. Because as previously reported by Wagih et al. [186], the response of the composite laminates can be divided into elastic response and damaged response without any kind of plasticity. Moreover, it was observed that before the first change in the laminate stiffness (first load drop in the load-displacement curve), there was no evidence on any kind of damage in the laminate. For the use of composite laminates in industrial applications, the prediction of the indentation depth in the elastic zone is important because after the damage starts, the damage size and the damage tolerance have much more importance than the indentation depth. It is valuable to mention that the elastic range for the hollow support case is much smaller than that for the fully supported

case. This is due to the effect of compressive forces due to bending in the hollow supported case which cause the damage to start earlier.

7.7 Conclusions

An elastic 2D axisymmetric contact model was implemented using a commercial FE software to simulate the elastic response of orthotropic composite laminates of finite thickness in contact with stiff indenter and supported with two different boundary condition: fully and hollow support. The FE model requires to define the three-dimensional effective elastic properties so a simple method was introduced to calculate these properties. Parametric studies were performed using the introduced FE model to investigate the effect of each parameter on the elastic response of indentation problem.

Two equations were derived to predict the response of an orthotropic composite laminate with finite thickness by normalizing the parameters influencing the problem and fitting of the normalized FE results. One of these equations is to predict the response of a specimen with fully supported boundary condition while the other is to predict the response of a specimen with hollow supported boundary condition. The predictions of the equations were validated by comparing the results with experimental results obtained during this study and those available from the literature. Moreover, the predictions of the equation of the hollow supported case were compared to the available analytical models. The predictions of the presented equation show excellent correlation with the experimental results. Based on the observations, the indentation response of orthotropic plate was found to be material independent and strongly dependent on the laminate thickness. There is no significant effect of the lamina thickness on the response of contact problem and the effect of the hole radius can be neglected for the hollow support experiment, as well.

8 Scaling laws

8.1 Introduction

In this chapter, a scaling approach based on a simplified analytical model and experimental results presented in Chapters 3, 4 and 5 and the experimental results available in the literature is presented for scaling quasi-isotropic composite laminate specimens under out-of-plane loading. The analytical model used in this study is developed and validated during this work. So, the aim of this chapter can be summarized as: analytical prediction of QSI response and the use of a small scale QSI test on a quasi-isotropic composite laminate to predict the response of large scale QSI and low-velocity impact tests.

8.2 Quasi-static indentation model

Based on the results presented in Chapters 3 and 4 and the available analytical models [21, 196], the plate response or load displacement response (F-u) of a composite laminate subjected to quasi-static indentation load can be defined by four different stages as shown in Figure 8.1 (a) and represented by a simplified schematic drawing as shown in Figure 8.1 (b). The first stage is the elastic response of the laminate which corresponds to the bending and contact responses. It is well known that the bending response depends on the in-plane dimensions. However, the contact response is independent of the in-plane dimensions [187]. At a certain load (F_{th}) damage onset is reached. In most laminates, it corresponds to a load drop in the load displacement response until F_{dn} [197], this is termed stage II. However, in other cases this load drop is not present and the damage threshold load is equal to the load after the damage initiation ($F_{\text{th}} = F_{\text{dn}}$) [186]. The third stage is related to the delamination growth. During this stage, stable delaminations grow between the interfaces of the laminate. The final stage is defined as the fiber breakage stage which corresponds to a large load drop in the load displacement curve.

8.2.1 Elastic Response

Considering the simplified mass structural model, Figure 8.1 (c), the plate response of a composite laminate of thickness h and circular in-plane dimension of radius R

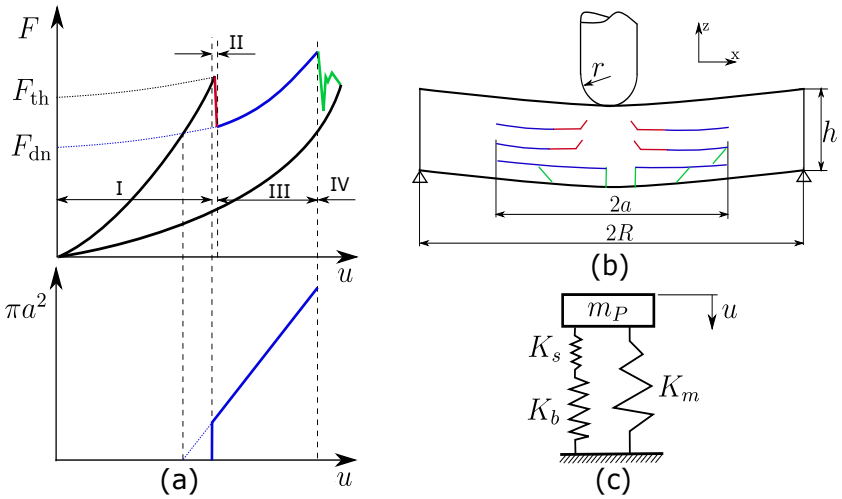

Fig. 8.1: Representation of the mechanical response and delamination area of a QSI test (a) the associated damage mechanisms (b) and a simplified mechanical model (c).

indented by hemispherical indenter of radius r, can be defined by an approximate solution as [198]:

$$F = Ku + K_{\mathrm{m}}u^3 \tag{8.1}$$

where K is the linear part of the stiffness (including the bending and shear stiffness) and K_{m} is the membrane stiffness. The linear part of the stiffness can be calculated by the combination of the bending and the shear compliances which can be expressed as:

$$K = (K_{\mathrm{b}}^{-1} + K_{\mathrm{s}}^{-1})^{-1} \tag{8.2}$$

where $K_{\mathrm{b}} = k_{\mathrm{b}}\frac{h^3}{R^2}$, $K_{\mathrm{s}} = k_{\mathrm{s}}h$ and $K_{\mathrm{m}} = k_{\mathrm{m}}\frac{h}{R^2}$, being k_{b} and k_{m} two constants that depend on the elastic properties, the geometry, and the boundary conditions, but not on the specimen size. Table 8.1 shows the expression for computing k_{b} and k_{m} for different boundary conditions [196]. k_{s} depends on the material properties and the geometry and can be computed as:

$$k_{\mathrm{s}} = \frac{4\pi G_{\mathrm{xz}}}{3}\frac{E_{\mathrm{x}}}{E_{\mathrm{x}} - 4\nu_{\mathrm{xz}}G_{\mathrm{xz}}}\left(\frac{4}{3} + \log\left(\frac{R}{r_{\mathrm{c}}}\right)\right)^{-1} \tag{8.3}$$

where E_{x}, G_{xz} and ν_{xz} are the elastic properties of the quasi-isotropic laminate (subscript x and z refer to the in-plane and out-of-plane directions, respectively) and r_{c} is the contact radius between the impactor and the plate [196]. With the aim of simplifying the calculation, r_c is considered as a constant value as suggested by Shivakumar et al. [196].

For rectangular or square laminate plates with in-plane dimensions $\beta \times \gamma$, the value of R can be computed as $\sqrt{\beta\gamma/\pi}$ [199].

Tab. 8.1: Determination of the k_b and k_m constants for different boundary conditions [196]. In the table B C refers to boundary condition, C refers to clamped support, S refers to simply supported, M refers to movable support and I refers to immovable support. x is the in-plane direction.

B C	k_b	k_m
C-M	$\frac{4\pi E_x}{3(1-\nu_x^2)}$	$\frac{191\pi E_x}{648}$
C-I	$\frac{4\pi E_x}{3(1-\nu_x^2)}$	$\frac{\pi E_x}{1-\nu_x}\frac{353-191\nu_x}{648}$
S-M	$\frac{4\pi E_x}{3(1-\nu_x)(3+\nu_x)}$	$\frac{\pi E_x}{(3+\nu_x)^4}\left(k_m^{CM}(1+\nu_x)^4+\frac{41}{27}(1+\nu_x)^3+\frac{32}{9}(1+\nu_x)^2+\frac{40}{9}(1+\nu_x)+\frac{8}{3}\right)$
S-I	$\frac{4\pi E_x}{3(1-\nu_x)(3+\nu_x)}$	$k_m^{SM}+\frac{2}{(1-\nu_x)(3+\nu_x)^4}\left(\frac{1}{8}(1+\nu_x)^4+(1+\nu_x)^3+4(1+\nu_x)^2+8(1+\nu_x)+8\right)$

The presence of n equally distributed circular delaminations of radius a produces a decrease of bending stiffness which can be expressed as [80]:

$$K_b^{-1}=\frac{R^2}{k_b h^3}-\frac{a^2}{k_{bc}h^3}+\frac{a^2(n+1)^2}{k_{bc}h^3}=\frac{1}{h^3}\left(\frac{R^2}{k_b}+\frac{n(n+2)a^2}{k_{bc}}\right) \tag{8.4}$$

where k_{bc} is the bending stiffness of a circular clamped plate. The first term represents the compliance of the plate of in-plane radius R without delamination, the second term represents the compliance of a circular plate of radius a without delamination and the last term represents the compliance of a circular plate of radius a with n equally distributed through the thickness circular delaminations.

Consequently, by Substituting Equations 8.2 and 8.4 in Equation 8.1, the elastic load-displacement response assuming n delaminations of radius a can be expressed as:

$$F=\frac{h^3}{R^2}\left(\frac{1}{k_b}+\frac{n(n+2)}{k_{bc}}\frac{a^2}{R^2}+\frac{1}{k_s}\frac{h^2}{R^2}\right)^{-1}u+k_m\frac{h}{R^2}u^3 \tag{8.5}$$

8.2.2 Delamination Growth

The load displacement curve when delaminations are growing can be determined by means of linear elastic fracture mechanics. The elastic energy (U) can be expressed as the area under the unloading curve and can be defined as:

$$U=\int F du=\frac{h^3}{2R^2}\left(\frac{1}{k_b}+\frac{n(n+2)}{k_{bc}}\frac{a^2}{R^2}+\frac{1}{k_s}\frac{h^2}{R^2}\right)^{-1}u^2+\frac{k_m h}{4R^2}u^4 \tag{8.6}$$

Applying linear elastic fracture mechanics, $G = \frac{-1}{2\pi a n}\frac{\partial U}{\partial a} = G_{\text{IIc}}$, the relation between the applied displacement and delamination radius during crack growth is governed by:

$$u = F_{\text{dn}}\frac{R^2}{h^3}\left(\frac{1}{k_{\text{b}}} + \frac{n(n+2)}{k_{\text{bc}}}\frac{a^2}{R^2} + \frac{1}{k_{\text{s}}}\frac{h^2}{R^2}\right) \tag{8.7}$$

where

$$F_{\text{dn}} = \sqrt{\frac{2\pi G_{\text{IIc}} k_{\text{bc}} h^3}{n+2}} \tag{8.8}$$

where G_{IIc} is the mode II interlaminar fracture toughness [81, 82, 95].

So, taking into account Equations 8.5 and 8.7, the load-displacement response when delaminations propagate can be expressed as:

$$F = F_{\text{dn}} + k_{\text{m}}\frac{h}{R^2}u^3 \tag{8.9}$$

Equation 8.5 defines the elastic response of the plate and it is valid for no delamination and constant radius delamination (black lines in Figure 8.1 (a)). When delaminations grow, the load displacement is defined by Equation 8.9 (blue line in Figure 8.1 (a)). Equation 8.7 defines the maximum plate displacement for a given delamination size and G_{IIc} value. Therefore, it is possible to define the projected delaminated area for a specific plate displacement as:

$$\pi a^2 = \frac{F_{\text{dn}}}{2nG_{\text{IIc}}}\left\langle u - \left(\frac{1}{k_{\text{b}}} + \frac{1}{k_{\text{s}}}\frac{h^2}{R^2}\right)\frac{R^2}{h^3}F_{\text{dn}}\right\rangle \tag{8.10}$$

where $< \bullet >$ are the Macauley brackets. According to this, the delamination area increases proportionally to the displacement with a slope of $F_{\text{dn}}/(2nG_{\text{IIc}})$.

The response of Equations 8.5 and 8.9 is equivalent to the model presented by Olsson [95]. A key point in the proposed model to define the load F_{dn} and the delamination area is to define the number of the delaminated interfaces, n.

8.2.3 Onset of delamination

During a QSI or impact test the load required for the damage threshold (F_{th}) is usually larger than the load after damage initiation (F_{dn}), promoting an unstable behavior with a sudden load drop.

According to Shivakumar and Elber [200] delaminations are initiated if the transverse shear stress is larger than the critical shear strength and these delaminations grow if the energy release rate is larger than the mode II fracture toughness of the interface.

The strength criterion to define the onset of cracking or delamination for hemispherical indenters is formulated as [97, 199]:

$$F_{\mathrm{S}} = \sqrt{\frac{\kappa \tau_{\mathrm{s}}^3 \pi^3 h^3 r}{E}} \tag{8.11}$$

where τ_{s} is the interlaminar shear strength of the laminate and E is the contact modulus which can be computed as $\frac{1}{E} = \frac{1-\nu_1^2}{E_1} + \frac{1-\nu_2^2}{E_2}$, where subscripts 1 and 2 refer to the indenter and the laminate, respectively. κ is a constant that depends on the stress distribution considered, parabolic: $\kappa = 16/9$ [199] or constant $\kappa = 6$ [97].

The process of delamination grow is defined by means of linear elastic fracture mechanics. The growth of delaminations approximately follows the sequence: a single delamination starts to grow in the middle of the laminate dividing it into two sublaminates. After this delamination, two delaminations grow at the middle of the two resulting sublaminates and this phenomenon is repeated until F_{dn} is reached. Applying Equation 8.8 with $n = 1$ the load required to growth the first delamination is defined as [80, 93]:

$$F_{\mathrm{d1}} = \sqrt{\frac{2\pi G_{\mathrm{IIc}} k_{\mathrm{bc}} h^3}{3}} \tag{8.12}$$

It must be pointed out that the indenter radius must influence the energy release rate somehow. The numerical models of Shivakumar and Elber [200] showed that, the energy release rate associated to delaminations smaller than the contact radius, is very small. This suggests that an enough shear stresses are necessary to produce matrix and interface damage of enough size to delamination growth. Therefore, a criterion for delamination threshold can be expressed as:

$$F_{\mathrm{th}} = \max\{F_{\mathrm{d1}}, F_{\mathrm{S}}\} \tag{8.13}$$

8.2.4 Energy balance

The elastic energy is defined by means of Equation 8.6. In the elastic region, when the displacement value is smaller than $u_{\mathrm{th}} = F_{\mathrm{th}}/K$ (with the stiffness defined in Equation 8.2), the total energy of the system is elastic and determined by Equation 8.6 with $a = 0$. After the threshold displacement is reached the total energy is the contribution of the elastic energy (U_E), the dissipated energy by delamination (U_D)

and in the case, $F_{\text{th}} > F_{\text{dn}}$, some energy that is assumed to be dissipated as elastic waves (U_K). The dissipated energy U_D, can be computed by multiplying Equation 8.10 by nG_{IIc} while U_K can be computed as the energy released in the unstable drop of loads between F_{th} and F_{dn}. Therefore the total energy can be expressed as: $U_T = U_E + U_D + U_K$, where:

$$U_E = \frac{F_{\text{dn}}}{2}u + \frac{k_m h}{4R^2}u^4, \quad U_D = \frac{F_{\text{dn}}}{2}\left(u - \frac{F_{\text{dn}}}{K}\right) = \pi a^2 n G_{\text{IIc}} \quad \text{and} \quad U_K = \frac{\langle F_{\text{th}} - F_{\text{dn}}\rangle^2}{2K} \tag{8.14}$$

8.3 Scaling effects

Because of the complexity of the impact problem, experimental data are needed to determine the extent of impact damage in particular material systems and structural geometries. Scaling of impact is of particular concern in the design of large composite structures, where the cost and the difficulty of full-scale impact testing is, in general, prohibitive. The emphasis in this section is on establishing scaling laws for QSI and impact tests.

As a preliminary step for scaling, it is mandatory to identify the geometrical parameters that influence the QSI and low-velocity impact response. The geometrical parameters that affect the response are the in-plane shape and size, the laminate and ply thicknesses and the indenter radius. In QSI and low-velocity impact tests, the response can be summarized as: the initial stiffness, the damage threshold load (F_{th}), the load after damage initiation (F_{dn}) and the damage size (πa^2) (see Figure 8.1(a)). In the following subsections the effect of each of the aforementioned geometrical parameters on each part of the QSI response will be studied to obtain a clear picture of the scaling laws involved.

Tab. 8.2: Summary of the parameters studied in experimental tests in the literature. In the table $\pi/8$ K3 means $[0/22.5/45/67.5/90/-67.5/-45/-22.5]_{2s}$ and LVI refers to low-velocity impact test.

Label	Ref.	Staking sequence	Test	R (mm)	h (mm)	r (mm)	t_p (mm)
A1	[68]	$[45/0/-45/90]_{ns}$	QSI	150 × 100	2 and 4	8	0.125
A2	[68]	$[45/0/-45/90]_{ns}$	QSI	150 × 100	4	8	0.125 and 0.25
E1	[201]	Woven GFRP	LVI	100 × 100	2.1, 4, 5.9 and 8.1	5	≈ 0.59-0.7
E2	[201]	Unidirectional GFRP	LVI	100 × 100	2.2, 4, 6.1 and 8	5	≈ 0.43-0.45
G1	[202]	$[45/0/-45/90]_{ns}$	LVI	150 × 100	3, 5.8 and 8.8	8	0.181
G2	[60]	$[45_m/0_m/-45_m/90_m]_{ns}$	LVI	150 × 100	5.8	8	0.181, 0.36 and 0.724
G3	[203]	$[0_2/90_2/(45/-45)_2]_s$	LVI	45 and 150 × 100	2.75	6.35	0.172
K1	[204]	$[0/45/90/-45]_{4s}$	LVI and QSI	25.4, 38.1 and 50.8	4	3.175 and 12.7	0.125
K2	[204]	$[0/90]_{8s}$	LVI and QSI	25.4, 38.1 and 50.8	4	3.175 and 12.7	0.125
K3	[204]	Lam. $\pi/8$	LVI and QSI	25.4, 38.1 and 50.8	4	3.175 and 12.7	0.125
S1	[61]	$[45/0/-45/90]_{3s}$	LVI	150 × 100	4.4	8	0.184
S2	[205]	Woven	LVI	25 and 50	3.3, 6.6, 9.8 and 12.4	5	0.66
W1	Ch3	$[45/0/-45/90]_{3s}$	QSI	25	4.4	6.35	0.184
W2	Ch4	$[(45/-45)/(0/90)]_{ns}$	QSI	150 × 100	4.5	8	0.08 and 0.16
Y1	[206]	$[0/90]_{ns}$	LVI	25, 50, 75 and 100	1.8, 2.5, 2.7 and 3.6	5	0.225
Y2	[206]	$[0/90]_{ns}$	LVI	50	2.7 and 3.6	2.3, 5, 6, 7.2 and 9.6	0.225

For a better understanding of the influence of the aforementioned geometrical parameters (specimen in-plane dimension, laminate and lamina thicknesses and indenter radius) different experimental results available in the literature are analyzed to highlight the influence of each parameter. Table 8.2 summarizes the experimental tests used in the present study. Special attention is paid for the test campaigns G1, G2, S1, W1 and W2 which was done by the researchers and the material is fully characterized.

8.3.1 Thickness effect

In general, a specific thickness of a laminate can be achieved by the repetition of a group of plies, or sublaminate, with specific orientations and keeping the thickness of the individual plies constant, sublaminate clustering, or by grouping or clustering different plies with the same orientation and increasing the ply thickness. Such a procedure is commonly referred as ply clustering. In the first case, sublaminate clustering, the ply thickness (t_p) is kept constant while the number of interfaces for delamination ($N = h/t_p - 2$, for symmetric laminates) is increased. In the second case, ply clustering, the ply thickness is increased but the number of interfaces for delamination remains constant.

(i) Damage threshold load (F_{th})

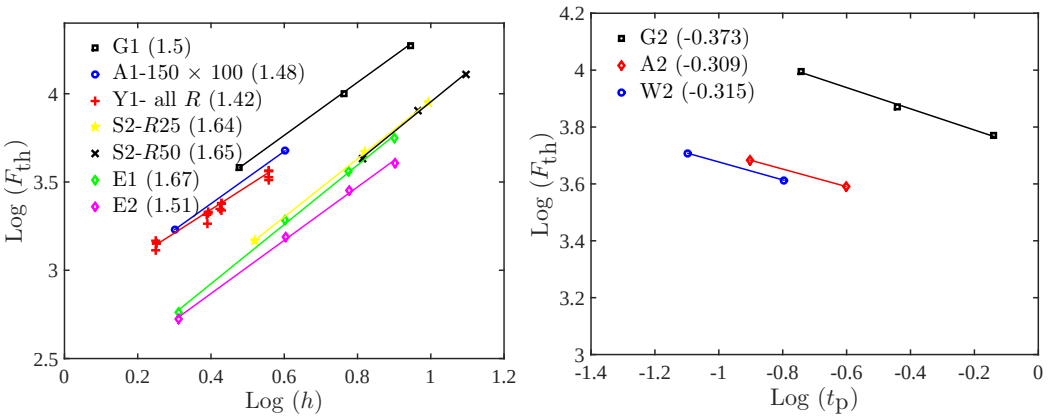

(a) Effect of laminate thickness. **(b)** Effect of lamina thickness.

Fig. 8.2: Effect of laminate thickness and lamina thickness on the damage threshold load. The data points correspond to the experimental results of the tests summarised in Table 8.2 and the lines are the linear fitting of this data. The legend includes the code of the test, the in-plane dimension and the slope of the fitting lines in (a) and the code of the test and the slope of the fitting lines in (b).

The damage threshold load (F_{th}) defines the maximum elastic load before delamination initiation. This load is defined in Equation 8.13 as the maximum of two criterion, a strength criterion (Equation 8.11) and a fracture mechanics criterion

(Equation 8.12). According both conditions the threshold load scales with laminate thickness as $F_{\text{th}} \propto h^{1.5}$. In Figure 8.2a several experimental results from bibliography (summarized in table 8.2) confirms this scaling law, this trend is very well experimentally validated by Schoeppner and Abrate [207]. It must be pointed out that the results presented in Figure 8.2a are from the same material and the thickness is increased by means of sublaminate scaling (constant t_p). In Figure 8.2b the effect of ply thickness is shown, for constant h, the damage threshold load decrease with respect to the ply thickness as $F_{\text{th}} \propto h^{-0.33}$.

(ii) Load after delamination initiation (F_{dn}) and number of delaminated interfaces

The load after the damage initiation (F_{dn}) characterizes the progression load for the growth of n equally distributed through-the-thickness circular delaminations. Based on LEFM analysis (Equation 8.8), this load is proportional to the laminate thickness and the number of delaminated interfaces according to $F_{\text{dn}} \propto \sqrt{h^3/(n+2)}$.

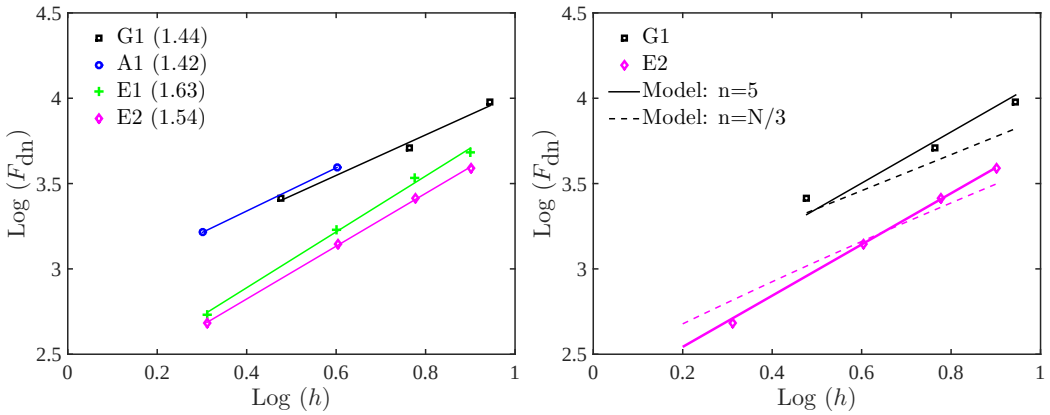

(a) Effect of laminate thickness. **(b)** Effect of lamina thickness.

Fig. 8.3: Effect of laminate thickness and lamina thickness on the load after damage initiation. The data points in (a) correspond to the experimental results of the tests summarised in Table 8.2 and the lines are the linear fitting of this data. The legend includes the code of the test and the slope of the fitting lines. The results in (b) are the experimental results of three different lamina thicknesses [60] and the prediction of the proposed model.

In Figure 8.3a the effect of laminate thickness on F_{dn} is shown. In all the cases the laminate thickness is increased by means of sublaminate clustering, i.e. the number of interfaces is increased while t_p is kept constant. The experimental results presented show a linear trend in a bi-logarithmic plot with a slope close to 1.5, this suggest a null influence of the number of interfaces available to delamination growth, i.e. n is constant and independent on N.

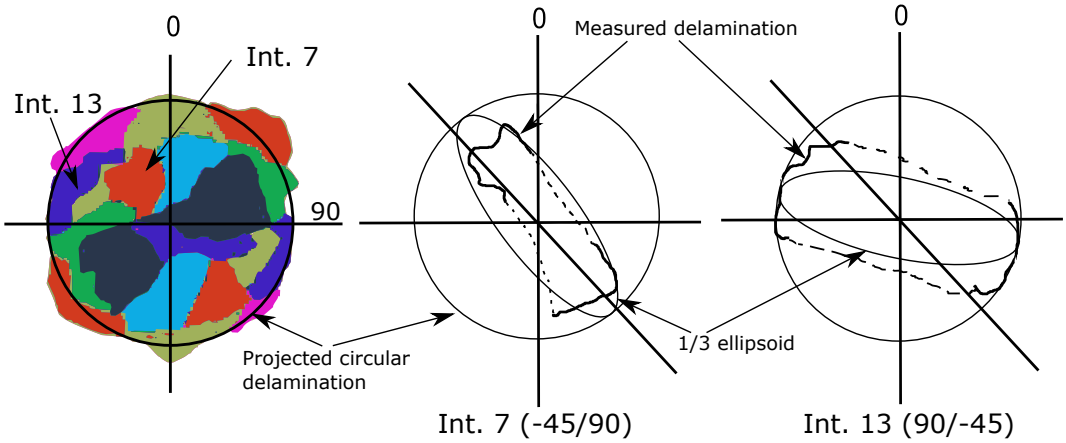

Fig. 8.4: C-scan projection of static indentation and true shape of delamination in interfaces 7 and 13 [186].

The projected delamination area of all interfaces is usually quite circular in quasi-isotropic laminates. When each delaminated interface is analyzed it can be observed that the shape of delamination is elliptical, with an aspect ratio of approximately 1/3, oriented in the direction of the fiber of the bottom and upper ply. In Figure 8.4 the C-scan of a statically indented quasi-isotropic laminate by Wagih et al. [186] is presented. While the projected delamination area is circular, the shape of each interface is oriented in the direction of the fiber (at the beginning of the upper ply and increasing the external displacement to the bottom ply). Due to this experimental evidence, Olsson [21, 95] suggest that the number of equivalent delaminations is about one third of the interfaces between plies: $n = N/3$. When considering this hypothesis the scaling law for delamination growth is expressed as: $F_{\text{dn}} \propto h\sqrt{3t_p/(1+4t_p/h)}$. In Figure 8.3b some experimental results of Figure 8.3a are reproduced again. The dotted lines correspond to the hypothesis $n = N/3$, while the solid lines correspond to n constant and independently on N. For the experimental results E2 from Evci [201] the best possible fit is defined while for the results G1 [202] the material properties Hexply AS4/8552 of table 8.3 are used. By considering the clamped bending stiffness of Table 8.1 ($k_{bc} = 226.1$GPa) and $n = 5$, the prediction is significantly better than considering $n = N/3 = 4.7, 10$ and 15.3 from the thinner to the thicker.

Tab. 8.3: Elastic and fracture properties of the ply.

Material	Ref.	E_{11} (GPa)	E_{22} (GPa)	G_{12} (GPa)	ν_{12}	G_{IIc} (N/mm)
Hexply AS4/8552	[60]	128	7.6	4.4	0.35	0.79
TeXtreme	[208]	69.1	69.1	4.0	0.03	1.09
AS4D/TC350	[61]	135.4	9.3	5.3	0.32	1.17

To clarify the scaling of number of delaminated interfaces the load displacement presented by González et al. [60, 202] and summarized as G1 and G2 in Table 8.2 are represented in Figure 8.5. All experiments are LVI tests performed according the ASTM D7136 [209] specifications. The specimen have a dimensions of 150×100 mm over a flat support with a 125×75 mm rectangular cut-out, with corresponds to an equivalent radius of $R = \sqrt{125 \times 75/\pi} = 54.63$ mm. The shear stiffness defined by equation 8.3 and the bending stiffness of Table 8.1 for simply supported are $k_s \approx 6.6$ GPa (for $r_c = r/2$) and $k_b = 90.29$ GPa, respectively. The determination of the membrane stiffness is approximated as $k_m = 23.79(2R/\gamma)^2 = 54.6$ GPa, where $\gamma = 75$ mm.

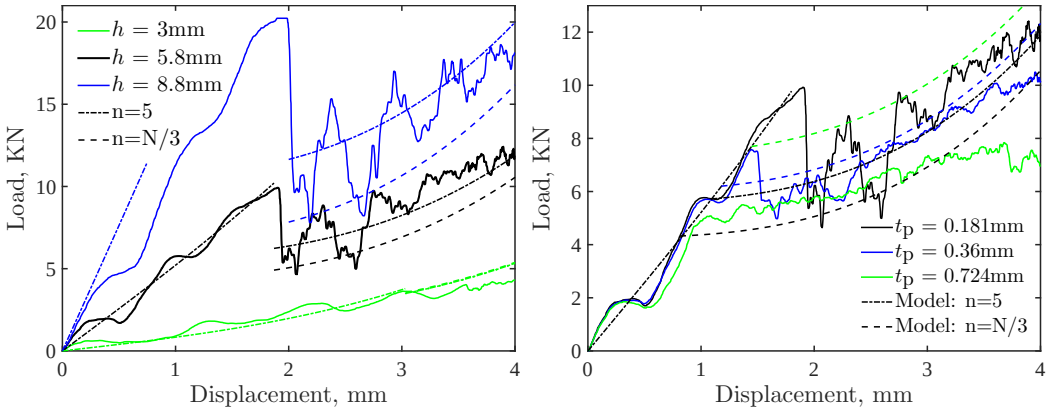

(a) Effect of laminate thickness. **(b)** Effect of lamina thickness.

Fig. 8.5: Effect of laminate and lamina thickness on the load displacement curve. The data points correspond to the experimental results of González et al. [60, 202] summarized as G1 and G2 in Table 8.2.

In Figure 8.5a the response of the impacted specimens G1 with different laminate thicknesses (h = 3, 5.8 and 8.8 mm) and constant ply thickness ($t = 0.181$ mm) are shown together with the model predictions considering; a constant number of delaminated interfaces ($n = 5$) and $n = N/3$. The response considering an increasing number of delaminated interfaces ($n = N/3$) tends to under predict the load to delamination growth when the laminate thickness increases.

The set of experiments G2 in table 8.2 have the same laminate thickness ($h = 5.8$ mm) with three different ply thicknesses: $t_p = 0.181$, 0.36 and 0.724 mm. The experimental results with the model predictions are represented in Figure 8.5b. For ply thicknesses of $t_p = 0.181$ and 0.36 mm, the global load displacement is almost the same except for the threshold load. For the thicker ply ($t_p = 0.724$ mm) the response after damage onset follows a linear response that does not fit to the model presented. This laminate have only eight plies which are not enough to fulfill the hypothesis of the model, furthermore they present extensive matrix cracking and the delamination shape is no longer circular but they are driven by the presence of the matrix cracking. For the ply thicknesses of $t_p = 0.181$ and 0.36 mm, F_{dn} is independent of the ply

thickness and the number of available interfaces for delamination (N). The same conclusions can be obtained by means of the experimental results presented by Abisset et al. [68] (A2 and W2 in table 8.2).

(iii) Projected delamination area

According to the model the projected delamination area increases linearly with the applied displacement as defined in Equation 8.10. In Figure 8.6, the projected delamination area for test results G1 and G2 are represented considering a constant number of delaminated interfaces $n = 5$ and $n = N/3$. The effect of the laminate thickness is shown in Figure 8.6a, the constant number of delaminations $n = 5$ shows a very good correlation with the experimental results while the hypothesis $n = N/3$ tends to under predict the response. The delamination area for the thinner laminate are collected beyond the point region of delamination growth and there are significative fibre damage. It is valuable noting that the slope of the delaminated area is proportional to $h^{1.5}$. In Figure 8.6b, the effect of ply thickness is shown, for $t_p = 0.181$ and 0.36 mm, the delamination area is quite similar (a little smaller for the thinner ply). For the thicker ply the delamination area has no longer a circular shape and the model described is not applicable. Again, considering $n = 5$ the prediction of the delaminated area for the thinner plies is better than $n = N/3$.

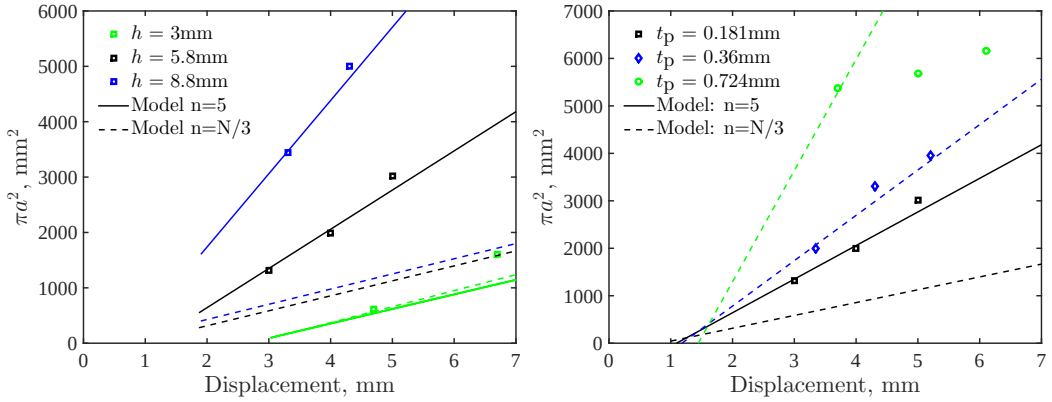

(a) Effect of laminate thickness. **(b)** Effect of lamina thickness.

Fig. 8.6: Effect of laminate and lamina thickness on the projected delamination area. The data points correspond to the experimental results of González et al. [60, 202] summarized as G1 and G2 in Table 8.2.

In figure 8.7, the load and the delamination area as a function of the applied displacement is presented from the results presented by the author in 4 (W2 in table 8.2) for laminates with two different ply thicknesses, 0.08 mm and 0.16 mm referred as UTP and TP. The material is TeXtreme plain weave with 20 mm wide yarn fabrics, manufactured by Oxeon AB and the number of plies for the TP and UTP ply thicknesses are 28 and 56 plies, respectively. The specimen have a dimensions

of 150 × 100 mm over a flat support with a 125 × 75 mm rectangular cut-out. This figure presents also experimental results for UTP laminate under LVI test at 20 J impact energy extracted from Soto et al. [210]. As shown in Figure 8.7a, the load-displacement curve predicted by the presented model correlates well with the experimental results for TP and UTP laminates considering $n = 5$. Again, the response considering an increasing number of delaminated interfaces ($n = N/3$) tends to under predict the load for both laminates.

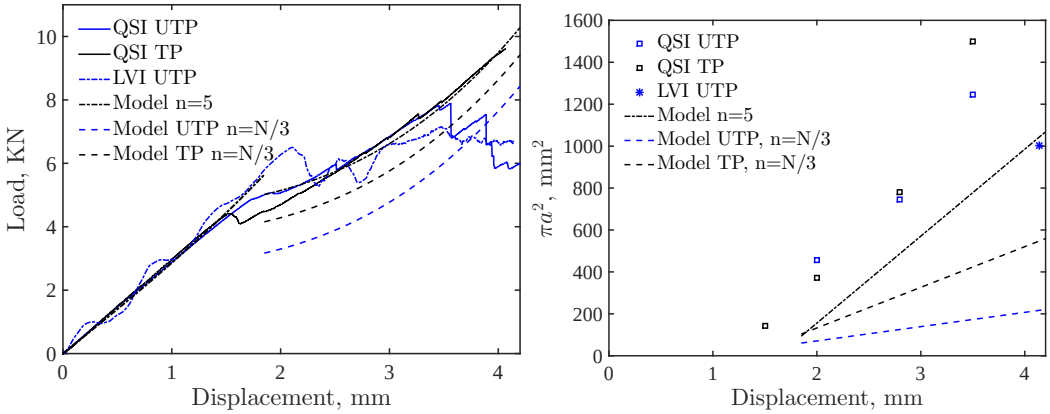

(a) Load displacement response. **(b)** Delamination area.

Fig. 8.7: Effect of the ply thickness. The data points correspond to the experimental results of 4 summarized as W2 in Table 8.2 for QSI results and numerical results of Soto et al. [210] for LVI results.

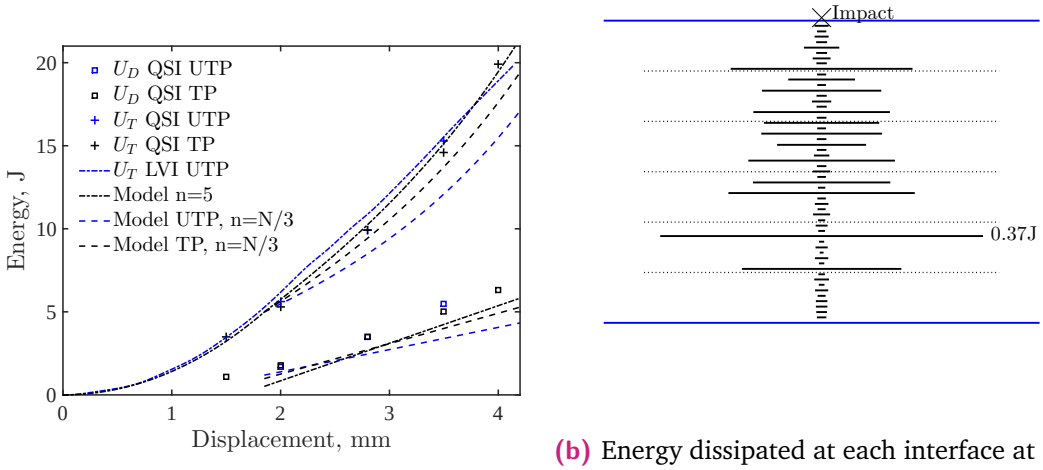

(a) Dissipated (U_D) and total (U_T) energy. **(b)** Energy dissipated at each interface at $u = 2.5$ mm [210].

Fig. 8.8: Energy balance and delaminated interfaces for TeXtreme material. In (b) the solid lines represent the delaminations positions presented by Soto et al. [210] and the dash lines represent the presented model prediction with $n = 5$.

Figure 8.8a shows the variation of the total and the dissipated energy for laminates TP and UTP under QSI 4 and LVI tests [210]. The figure reflects better correlation between the experimental results and the presented model prediction considering

$n = 5$ than considering $n = N/3$. According to the numerical results of Soto et al. [210] at a displacement of $u = 2.5$ mm the total energy is $E_T = 9.37$ J, the energy dissipated by delamination is 2.45 J and by interlaminar damage 0.38 J. The model used in Soto et al. [210] study is a high fidelity finite element model where all interfaces are modeled with cohesive elements and plies with continuum damage models. In Figure 8.8b the energy dissipated by each interface is shown. The top and bottom one sixth of the interfaces dissipates a very small amount of energy by delamination (most of interalaminar energy). Between them there are only twelve significantly delaminated interfaces (22% of the total number of interfaces) that dissipates 82% of the energy. The most delaminated interface is situated at three quarter of the laminate thickness and dissipates 0.37 J. In the same figure (with dotted lines) the model prediction with $n = 5$ delaminated interfaces is also shown. In this case each interface dissipates 0.41 J.

8.3.2 In-plane dimension (R)

The influence of the in-plane dimension on the damage threshold load is shown in Figure 8.9a. As shown in the figure, the experimental data can be fitted with almost horizontal lines in a bi-logarithmic plot with very low scatter. From this figure, it is clear that the in-plane dimension has no influence on the damage threshold. Similar observation were reported by Olsson [95] and Olsson et al. [79]. Figure 8.10b shows the influence of the in-plane dimension on the load after damage initiation, F_{dn}. As shown in the figure, the influence of the in-plane dimension can be also neglected since the slope for all the tested specimens is almost zero. It can be also observed in Figure 8.9 that there is no effect of the in-plane shape on F_{d1} and F_{dn}. In fact, the figure summarises the experimental data for two different in-plane shapes, circular and rectangular, with similar results.

The experimental results S1 and W1 in Table 8.2 are performed by Sebaey et al. [61] and Wagih et al. [186], respectively. Both tests are done with the same material (AS4D/TC350, see Table 8.3) and the same stacking sequence. Sebaey et al. [61] specimens are impacted following the ASTM D7136 [209] specifications while Wagih et al. [197] specimens are quasi-static indented using small circular fixture. In Figure 8.10, the load and delamination area are represented as a function of the applied displacement for both tests considering $n = 5$ and $n = N/3$. Again, the response considering $n = N/3$ tends to under predict the load and the delamination area for both tests.

8.3.3 Indenter radius (r)

The damage threshold expressed with Equation 8.13 is a combination of the load required to reach shear strength (Equation 8.11) and to grow a middle delamination

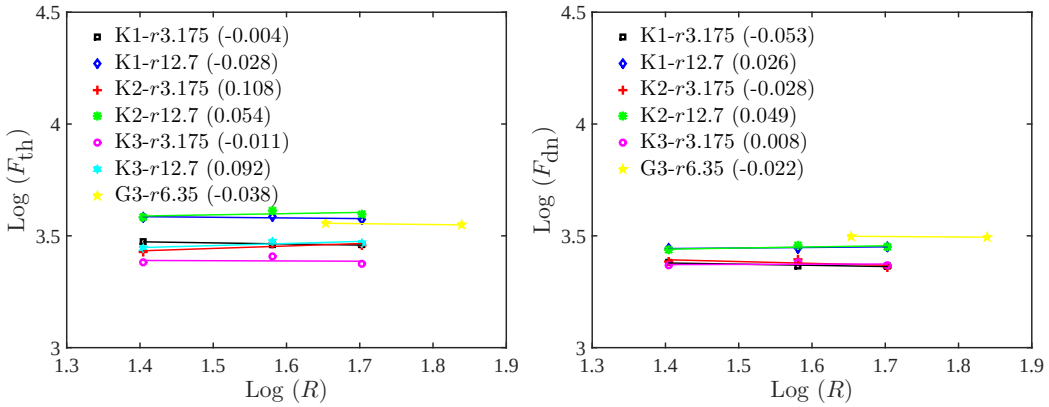

(a) Damage threshold load. **(b)** Load after damage initiation.

Fig. 8.9: Effect of the in-plane dimension on the damage threshold load and the load after the damage initiation. The data points correspond to the experimental results of the tests summarised in Table 8.2 and the lines are the linear fitting of this data. The legends include the code of the test, the indenter radius and the slope of the fitting lines in each case.

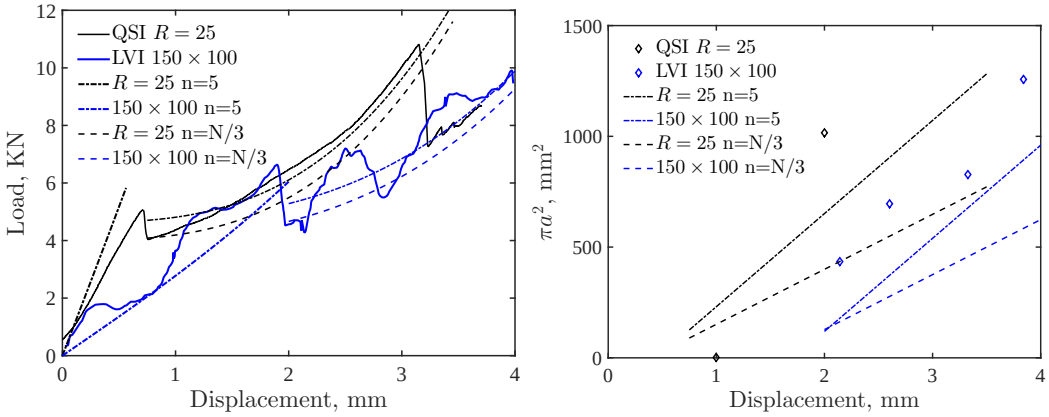

(a) Load displacement response. **(b)** Delamination area.

Fig. 8.10: Effect of in-plane size (R) on load-displacement response and delamination area.

according to fracture mechanics (Equation 8.12). The threshold load according to the shear criterion scales with indenter radius as $r^{1/2}$. For very small indenter radius, the shear criterion is fulfilled at loads smaller than the fracture mechanics criterion and the latter becomes dominant. On the other hand, for large indenter radii, the load is distributed in a larger zone and the external load to nucleate shear cracks is larger than the energy release rate for these cracks to grow. Therefore, for large indenter radii, the strength criterion becomes dominant.

Experimental results from Kwon and Sankar [204] (K1, K2 and K3 in Table 8.2), Wagih et al. [186] and Sebaey et al. [61] (W2 and S1) with two indenter radii shows an increment of damage threshold load with respect the indenter radius. The experimental results of Yang and Cantwell [206] are of special interest because

five indenter radii are considered. The damage threshold is plotted in Figure 8.11a in a bi-logarithmic scale. The dash lines have a slope equal to zero and fits the damage threshold load for small indenter radii. The solid lines have a slope equal to $1/2$ and fits the damage threshold loads of indenter radii larger than 4 mm. This transition radius, 4 mm, is defined by equaling the load obtained by Equations 8.11 and 8.12.

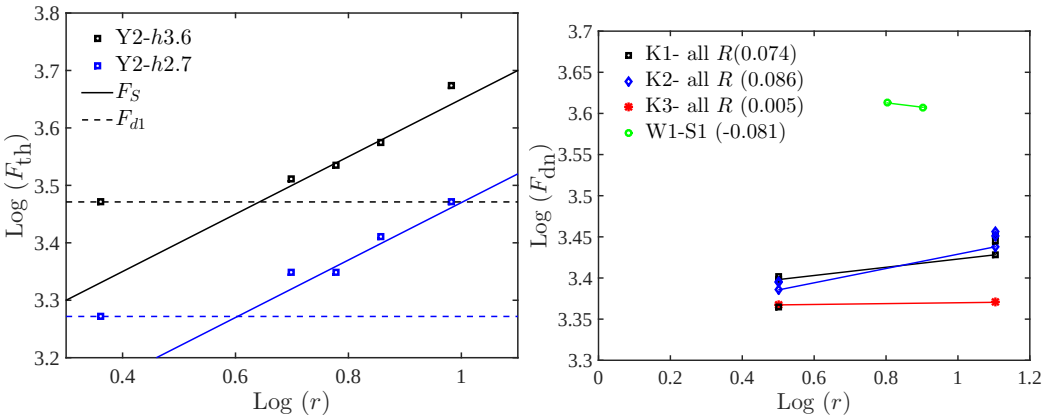

(a) Damage threshold load. **(b)** Load after damage initiation.

Fig. 8.11: Effect of indenter radius on the damage threshold load and the load after damage initiation. In (b), the legends include the code of the test and the slope of the fitting lines in each case.

The influence of the indenter radius on the load after damage initiation, F_{dn}, is shown in Figure 8.11b. From the figure, the influence of the indenter radius can be neglected since the slope of the linear fitting is close to zero and also because by the Saint Venant's principle, when the delamination radius is large enough the impactor radius does not influence the energy release rate due to delamination.

According to Equation 8.10, there is no influence of the indenter radius on the projected delamination area. The experimental results presented by Kwon et al. [204] confirm the fact that the indenter radius has no influence on the delamination area. In their results two different indenter radii, 3.175 and 12.7 mm, were considered, and the projected delamination area was almost equal for both radii.

8.4 Conclusions

The scaling of elastic properties with respect to specimen size are well defined by elasticity theory: the bending stiffness scales as h^3/R^2 and the membrane stiffness scales as h/R^2. The delamination response is defined by means of two loads, the damage threshold load (F_{th}) and the growth load (F_{dn}). Both loads are independent on the in-plane size (R) and scales with the laminate thickness as $h^{1.5}$ as predicted by analytical expressions presented in section 8.2. Based on the experimental

results, an increment of ply thickness reduces the damage threshold load according to $t_p^{-0.33}$, but it does not influence the damage growth load. The indenter radius does not influence the damage growth load, but it has an influence on the damage threshold load. According to the analytical models, the load required to reach the shear strength of the material scales with the indenter radius according to $r^{1/2}$. Experimental results show that as indenter radius increases, the damage threshold load increased, for large enough indenter radii. For small indenter radii, the damage threshold load becomes constant because, despite of the shear stress is larger than the material shear strength, the energy release rate is not enough to crack growth.

Experimental results show that delaminations grow in almost all interfaces with mismatch angles. However, these delaminations are of different size and with elliptical shapes with the major length in the direction of the fibers of the adjacent plies. The analytical model defined in section 8.2 requires the definition of n equivalent circular delaminations. This definition influences the propagation load (F_{dn}) and the delamination area. The experimental results analyzed concludes that n between 3 and 6 offers a good fitting to the progression load and delamination area for the great variety of results analyzed and it is independent of the number of interfaces of the laminate. The projected delamination area predicted by the presented analytical model increases linearly with the applied displacement and correlates well with the experimental results. The slope of the linear relation between delamination area and applied displacement scales only with ply thickness according to $h^{1.5}$.

The model and the results presented justify the use of small in-plane and out-of-plane coupons under static indentation tests to evaluate the response of large impacted structures.

Part III

Conclusions and future work

Conclusions and future work

9

9.1 Main Conclusions

The main objective of the present thesis is to provide a reliable scaling tool for composite laminates under out-of-plane loading. This main objective has been achieved by two research methodologies, experimental investigation and analytical modeling. Experimentally, for better understanding the damage mechanics, the damage sequence in composite laminates made of different fiber architectures has been analyzed. Moreover, the influence of different laminate design parameters on the damage resistance of composite laminates has been investigated. Analytically, a predictive model has been presented to predict the local indentation depth of indented/impacted composite laminates. Also, an analytical model has been presented to predict the global indentation response of composite laminates under out-of-plane loading. Finally, a scaling approach has been introduced based on the experimental investigations and the analytical model presented to predict the response of a larger in-plane and thickness specimen impacted by large indenter by testing a small scale coupon.

In light of the results and the discussions introduced in the previous chapters, the following conclusions can be drawn.

9.1.1 Damage sequence

A series of quasi-static indentation tests on quasi-isotropic carbon reinforced composite laminates with two different fiber architectures , UD plies and fabrics, have been performed to investigate the damage sequence during a low velocity impact event. The damage sequence in composite laminates made of both fiber architectures is quite similar. The damage sequence has been characterized by five stages. The first stage corresponds to the elastic response of the material, in which the load elastically increase by increasing the displacement without any evidence on damage. The second stage, the damage initiation, was characterized by a sudden drop in load related to the onset of matrix cracking, whereas no evidence of delaminations was observed at this stage for laminates made of UD plies. However, for fabric laminates, this load drop is related to matrix cracking and the onset of induced delaminations. The third stage, delamination propagation, was characterized by increasing the load monotonically by increasing the applied displacement at a lower slope than in the

first stage for both fiber architectures. As the loading continues, a large load drop in the load-displacement curve occurs due to the fiber breakage, fourth stage. The fives stage, perforation, during this stage, the fibers are sheared out to form a plug.

9.1.2 Effect of laminate design parameters

Two main laminate design parameters have been considered in this study, ply thickness and mismatch angle between adjacent plies. The influence of ply thickness has been studied by investigating laminates with two different ply thickness, 0.04 and 0.08 mm. The damage starts earlier in laminates with thick plies. However, the fiber breakage damage mechanism occurs earlier in laminates with thin plies. Before the fiber breakage, the projected delaminated area is smaller for laminates with thin-plies. However, after the fiber breakage, laminates with thin-plies show larger projected delaminated area.

The influence of mismatch angle has been studied by investigating laminates with three different mismatch angles, 15, 45 and 90°. As the mismatch angle decreased, the damage starts earlier. However, the maximum load capacity of the laminate is increased. The mismatch angle has no influence on the projected delaminated area. However, the number of delaminated interfaces is highly affected by the mismatch angle. The larger the mismatch angle is, the larger number of delaminated interfaces is.

Based on these studies, the effect of ply thickness and the effect of mismatch angle, hybrid laminates have been designed to improve the damage resistance of composite laminates by combining small and larger mismatch angles in the same laminates and also combining thin and thick plies in the same laminate. The maximum load capacity of the laminate is increased in the laminates with larger mismatch angle in the upper part of the laminate and also by using thick plies in the upper part of the laminate. Also, laminates with thicker plies in the upper part of the laminate show the best damage resistance between the tested laminates.

9.1.3 Prediction of indentation depth

An elastic 2D axisymmetric contact model was implemented using a commercial FE software to simulate the elastic response of orthotropic composite laminates of finite thickness in contact with stiff indenter and supported with two different boundary condition: fully and hollow support. Parametric studies were performed using the introduced FE model to investigate the effect of each parameter on the elastic response of indentation problem.

Two equations were derived to predict the response of an orthotropic composite laminate with finite thickness by normalizing the parameters influencing the problem

and fitting of the normalized FE results. One of these equations is to predict the response of a specimen with fully supported boundary condition while the other is to predict the response of a specimen with hollow supported boundary condition. The predictions of the equations were validated by comparing the results with experimental results. Based on the observations, the indentation response of orthotropic plate was found to be material independent and strongly dependent on the laminate thickness.

9.1.4 Scaling effects

An analytical model was introduced to predict the response of a composite laminate under quasi-static indentation load. The predicted load-displacement responses correlate well with the experimental results presented in the literature.

A scaling approach was presented to obtain the response of a composite laminate under out-of-plane loading. The presented approach was validated by comparison with the experimental results. The results show that the in-plane dimension and the in-plane shape have no influence on neither the damage threshold load nor the load after damage initiation. The damage threshold load and the load after damage initiation are scaled with the laminate thickness with a power of 1.5. The damage threshold load is scaled to the lamina thickness with a power of -1/3. The load after damage initiation is independent of the lamina thickness. The damage size is highly dependent of the laminate thickness.

The indenter radius significantly affects the damage threshold load. However, it has no influence on the load when the damage grows. According to the experimental results and the available analytical models built based on the interlaminar fracture toughness theory and the interlaminar shear stress theory, a new relation is proposed to relate the damage threshold load and the indenter radius. This relation might help for implementing an accurate analytical model for the prediction of the damage threshold load based on the interlaminar fracture toughness criteria and the interlaminar shear strength criteria.

9.2 Future work

The following topics are suggested for possible developments:

- Implementing an accurate analytical model to predict the damage threshold load based on the interlaminar fracture toughness criteria and the interlaminar shear strength criteria. This model can be implemented based on the proposed relation on this thesis.

- As shown in this thesis, using the relation between the projected delamination area and the displacement is a misleading parameter to judge the damage resistance of composite laminates. The projected delaminated area, the damage threshold load, the maximum load capacity and the dissipated energy should be taken into account for damage resistance evaluation. Hence, all this parameters might be included in a single coefficient to judge the damage resistance of composite laminates.

- However, damage tolerance is one of the most important parameters to judge composite laminates. The laminate design parameters which affect damage tolerance is still under doubt. Understanding the influence of the design parameters on the damage tolerance can help to get an optimum laminate design with improved damage resistance and damage tolerance.

- Composite parts in real applications are not only subjected to out-of-plane loads but also to in-plane loads such as tensile and compression. So, study the influence of the mismatch angle and the ply thickness on the damage assessment during in-plane loading is also important issue to get a robust design recommendation for composite laminates. This can be done by checking the effect of mismatch angle and ply-thickness on composite laminates under impact, unnotched tensile and compression and notched tensile and compression tests.

Part IV

Annex

1 Homogenization Model

The constitutive equation for ply i can be expressed in function of the transformed stiffness matrix, C, of the ply according to:

$$\begin{pmatrix} \sigma^i_{xx} \\ \sigma^i_{yy} \\ \sigma^i_{zz} \\ \sigma^i_{yz} \\ \sigma^i_{xz} \\ \sigma^i_{xy} \end{pmatrix} = \begin{bmatrix} \bar{C}^i_{11} & \bar{C}^i_{12} & \bar{C}^i_{13} & \bar{C}^i_{14} & \bar{C}^i_{15} & \bar{C}^i_{16} \\ \bar{C}^i_{21} & \bar{C}^i_{22} & \bar{C}^i_{23} & \bar{C}^i_{24} & \bar{C}^i_{25} & \bar{C}^i_{26} \\ \bar{C}^i_{31} & \bar{C}^i_{32} & \bar{C}^i_{33} & \bar{C}^i_{34} & \bar{C}^i_{35} & \bar{C}^i_{36} \\ \bar{C}^i_{41} & \bar{C}^i_{42} & \bar{C}^i_{43} & \bar{C}^i_{44} & \bar{C}^i_{45} & \bar{C}^i_{46} \\ \bar{C}^i_{51} & \bar{C}^i_{52} & \bar{C}^i_{53} & \bar{C}^i_{54} & \bar{C}^i_{55} & \bar{C}^i_{56} \\ \bar{C}^i_{61} & \bar{C}^i_{62} & \bar{C}^i_{63} & \bar{C}^i_{64} & \bar{C}^i_{65} & \bar{C}^i_{66} \end{bmatrix} \cdot \begin{pmatrix} \varepsilon^i_{xx} \\ \varepsilon^i_{yy} \\ \varepsilon^i_{zz} \\ \varepsilon^i_{yz} \\ \varepsilon^i_{xz} \\ \varepsilon^i_{xy} \end{pmatrix} \tag{1.1}$$

The transformed stiffness matrix can be obtained in function of the stiffness matrix of the ply, C, and the transformation matrices T_1 and T_2 as shown in [150].

$$[\bar{C}] = [T_1]^{-1}.[C].[T_2] \tag{1.2}$$

The stress and strain components can be expressed in two different groups. The first group corresponds to components that have the same strains, $\sigma_p = \{\sigma_{xx}, \sigma_{yy}, \sigma_{xy}\}$, and $\varepsilon_p = \{\varepsilon_{xx}, \varepsilon_{yy}, \varepsilon_{xy}\}$, therefore ε_p is equal for all plies. The second group corresponds to components that have the same stresses, $\sigma_s = \{\sigma_{yz}, \sigma_{xz}, \sigma_{zz}\}$, and $\varepsilon_s = \{\varepsilon_{yz}, \varepsilon_{xz}, \varepsilon_{zz}\}$, therefore σ_s is equal for all plies. x and y are the in-plane directions and z is the direction normal to the laminate plane.

The global stress of the first group and the global strain for the second group can be obtained as:

$$\sigma_p = \sum \frac{t^i}{t} \sigma^i_p \tag{1.3}$$

and

$$\varepsilon_s = \sum \frac{t^i}{t} \varepsilon^i_s \tag{1.4}$$

where t^i is the ply thickness and t is the global laminate thickness.

Then, the constitutive equation can be expressed as:

$$\sigma^i_p = \bar{C}^i_{pp} \varepsilon_p + \bar{C}^i_{ps} \varepsilon^i_s \tag{1.5}$$

and

$$\sigma_s = \bar{C}^i_{sp}\varepsilon_p + \bar{C}^i_{ss}\varepsilon^i_s \tag{1.6}$$

where $\bar{C}^i_{pp} = \begin{bmatrix} \bar{C}^i_{11} & \bar{C}^i_{12} & \bar{C}^i_{16} \\ \bar{C}^i_{21} & \bar{C}^i_{22} & \bar{C}^i_{26} \\ \bar{C}^i_{61} & \bar{C}^i_{62} & \bar{C}^i_{66} \end{bmatrix}$, $\bar{C}^i_{ps} = \begin{bmatrix} \bar{C}^i_{13} & \bar{C}^i_{14} & \bar{C}^i_{15} \\ \bar{C}^i_{23} & \bar{C}^i_{24} & \bar{C}^i_{25} \\ \bar{C}^i_{63} & \bar{C}^i_{64} & \bar{C}^i_{65} \end{bmatrix}$, $\bar{C}^i_{sp} = \begin{bmatrix} \bar{C}^i_{31} & \bar{C}^i_{32} & \bar{C}^i_{36} \\ \bar{C}^i_{41} & \bar{C}^i_{42} & \bar{C}^i_{46} \\ \bar{C}^i_{51} & \bar{C}^i_{52} & \bar{C}^i_{56} \end{bmatrix}$,
and $\bar{C}^i_{ss} = \begin{bmatrix} \bar{C}^i_{33} & \bar{C}^i_{34} & \bar{C}^i_{35} \\ \bar{C}^i_{43} & \bar{C}^i_{44} & \bar{C}^i_{45} \\ \bar{C}^i_{53} & \bar{C}^i_{54} & \bar{C}^i_{55} \end{bmatrix}$.

By substituting Equation 1.6 in Equation 1.5:

$$\sigma^i_p = \left[\bar{C}^i_{pp} - \bar{C}^i_{ps}(\bar{C}^i_{ss})^{-1}\bar{C}^i_{sp}\right]\varepsilon_p + \bar{C}^i_{ps}(\bar{C}^i_{ss})^{-1}\sigma_s \tag{1.7}$$

By introducing σ^i_p in Equation 1.3, the strain component of the laminate can be expressed as:

$$\varepsilon_p = M_{pp}\cdot\sigma_p + M_{ps}\cdot\sigma_s \tag{1.8}$$

where

$$M_{pp} = \left(\sum \frac{t^i}{t}\left[\bar{c}^i_{pp} - \bar{c}^i_{ps}(\bar{c}^i_{ss})^{-1}\bar{c}^i_{sp}\right]\right)^{-1}$$

and

$$M_{ps} = -M_{pp}\left(\sum \frac{t^i}{t}\bar{c}^i_{ps}(\bar{c}^i_{ss})^{-1}\right)$$

By extracting ε^i_s from Equation 1.6 and substituting by Equation 1.8 in the resulting equation:

$$\varepsilon_s = M_{ss}\cdot\sigma_s + M_{sp}\cdot\sigma_p \tag{1.9}$$

where

$$M_{sp} = -M_{pp}\cdot\left(\sum \frac{t^i}{t}\bar{c}^i_{ss}\cdot\bar{c}^i_{sp}\right)$$

and

$$M_{ss} = \sum \frac{t^i}{t}\bar{c}^i_{ss} - M_{ps}\left(\sum \frac{t^i}{t}\bar{c}^i_{ss}\cdot\bar{c}^i_{sp}\right)$$

Finally, the constitutive equation of the laminate can be expressed in this form:

$$\begin{pmatrix} \varepsilon_p \\ \varepsilon_s \end{pmatrix} = \begin{bmatrix} M_{pp} & M_{ps} \\ M_{sp} & M_{ss} \end{bmatrix}\cdot\begin{pmatrix} \sigma_p \\ \sigma_s \end{pmatrix} \tag{1.10}$$

Bibliography

[1] W. D. Callister and D. G. Rethwisch. *Materials science and engineering: an introduction*. Vol. 7. Wiley New York, 2007 (cit. on pp. 1, 2).

[2] M. F. Ashby and K. Johnson. *Materials and design: the art and science of material selection in product design*. Butterworth-Heinemann, 2013 (cit. on p. 2).

[3] V. R. Gowariker, N. V. Viswanathan, and J. Sreedhar. *Polymer science*. New Age International, 1986 (cit. on p. 2).

[4] L. A. Carlsson, D. F. Adams, and R. B. Pipes. *Experimental characterization of advanced composite materials*. CRC press, 2014 (cit. on p. 2).

[5] DDL Chung. *Composite materials science and applications*. second. Manchester: springer, 2010 (cit. on pp. 2, 3).

[6] A. K. Kaw. *Mechanics of composite materials*. CRC press, 2005 (cit. on p. 2).

[7] T. Pringle. *Preventing ramp and ground accidents, Transport Canada*. 2010 (cit. on pp. 3, 4).

[8] International Air Transportation Association et al. „Ground damage prevention programme targets 10 cost reduction“. In: *Industry Times* (2005) (cit. on p. 3).

[9] *Bird Strike, 2014 (website: http://www.dailymail.co.uk/news/article-1217035/Bird-strike-The-moment-200-starlings-sucked-passenger-jet-engine-off.html)*. Norm (cit. on p. 3).

[10] *Lufthansa perspectives on safe composite maintenance practices. Composite Damage Tolerence and Maintenance, Commercial Aircraft Composite Repair Committee (CACRC), Amsterdam, 2007*. Norm (cit. on p. 4).

[11] W. J. Cantwell and J. Morton. „Geometrical effects in the low velocity impact response of CFRP“. In: *Composite Structures* 12.1 (1989), pp. 39–59 (cit. on pp. 3, 13, 15, 17, 22).

[12] W. J. Cantwell and J. Morton. „Comparison of the low and high velocity impact response of CFRP“. In: *Composites* 20.6 (1989), pp. 545–551 (cit. on pp. 3, 13, 15, 21).

[13] W. J. Cantwell and J. Morton. „The influence of varying projectile mass on the impact response of CFRP“. In: *Composite Structures* 13.2 (1989), pp. 101–114 (cit. on pp. 3, 11, 13, 15, 18, 21).

[14]W. J. Cantwell and J. Morton. „Impact perforation of carbon fibre reinforced plastic“. In: *Composites Science and Technology* 38.2 (1990), pp. 119–141 (cit. on pp. 3, 13, 15, 21).

[15]W. J. Cantwell and J. Morton. „An assessment of the residual strength of an impact-damaged carbon fibre reinforced epoxy“. In: *Composite Structures* 14.4 (1990), pp. 303–317 (cit. on pp. 3, 13, 15, 21).

[16]W. J. Cantwell and J. Morton. „The impact resistance of composite materials-a review“. In: *Composites* 22.5 (1991), pp. 347–362 (cit. on pp. 3, 13, 15, 21).

[17]J. F. Doyle. *Wave propagation in structures*. Springer, 1989 (cit. on pp. 3, 13).

[18]B. V. Sankar. „Low-velocity impact response and damage in composite materials“. In: *Key Engineering Materials*. Vol. 120. Trans Tech Publ. 1996, pp. 549–582 (cit. on pp. 3, 13).

[19]R. Olsson. „Mass criterion for wave controlled impact response of composite plates“. In: *Composites Part A: Applied Science and Manufacturing* 31.8 (2000), pp. 879–887 (cit. on pp. 3, 13, 14, 18–20).

[20]R. Olsson. „Closed form prediction of peak load and delamination onset under small mass impact“. In: *Composite Structures* 59.3 (2003), pp. 341–349 (cit. on pp. 3, 13, 18, 20, 24, 39).

[21]R. Olsson. „Analytical prediction of damage due to large mass impact on thin ply composites“. In: *Composites Part A: Applied Science and Manufacturing* 72 (2015), pp. 184–191 (cit. on pp. 3, 13, 17, 19–21, 39, 43, 47, 123, 131).

[22]A. S. Yigit and A. P. Christoforou. „Limits of asymptotic solutions in low-velocity impact of composite plates“. In: *Composite Structures* 81.4 (2007), pp. 568–574 (cit. on pp. 3, 13, 14).

[23]W. Goldsmith. *Impact*. Courier Corporation, 2001 (cit. on p. 11).

[24]C. T. Sun and S. Chattopadhyay. „Dynamic response of anisotropic laminated plates under initial stress to impact of a mass“. In: *Journal of Applied Mechanics* 42.3 (1975), pp. 693–698 (cit. on p. 11).

[25]P. W. R. Beaumont, P. G. Riewald, and C. Zweben. „Foreign object impact damage to composites“. In: *Astm Stp* 568 (1974), p. 134 (cit. on p. 11).

[26]M. J. Pavier and M. P. Clarke. „Experimental techniques for the investigation of the effects of impact damage on carbon-fibre composites“. In: *Composites Science and Technology* 55.2 (1995), pp. 157–169 (cit. on p. 11).

[27]G. Clark. „Modelling of impact damage in composite laminates“. In: *Composites* 20.3 (1989), pp. 209–214 (cit. on pp. 11, 15).

[28]S. Abrate. „Impact on laminated composite materials“. In: *Applied Mechanics Reviews* 44.4 (1991), pp. 155–190 (cit. on pp. 11, 15, 17).

[29]T. Ishikawa, S. Sugimoto, M. Matsushima, and Y. Hayashi. „Some experimental findings in compression-after-impact (CAI) tests of CF/PEEK (APC-2) and conventional CF/Epoxy flat plates“. In: *Composites Science and Technology* 55.4 (1995), pp. 349–363 (cit. on p. 11).

[30]S. A. Hitchen and R. M. J. Kemp. „The effect of stacking sequence on impact damage in a carbon fibre/epoxy composite“. In: *Composites* 26.3 (1995), pp. 207–214 (cit. on pp. 11, 67, 68).

[31]C. Scarponi and G. Briotti. „Ultrasonic technique for the evaluation of delaminations on CFRP, GFRP, KFRP composite materials“. In: *Composites Part B: Engineering* 31.3 (2000), pp. 237–243 (cit. on p. 11).

[32]R. L. Sierakowski and S. K. Chaturvedi. „Dynamic loading and characterization of fiber-reinforced composites“. In: (1997) (cit. on pp. 11, 12, 15, 16).

[33]R. Olsson. „Impact response of composite laminates: a guide to closed form solutions“. In: *FFA TN 1992-33. Tech. Rep.; The Aeronautical Research Institute of Sweden* (1993) (cit. on pp. 12–14, 18, 20).

[34]P. Robinson and G. A. O. Davies. „Impactor mass and specimen geometry effects in low velocity impact of laminated composites“. In: *International Journal of Impact Engineering* 12.2 (1992), pp. 189–207 (cit. on p. 13).

[35]S. Abrate. „Impact on laminated composite materials“. In: *Applied Mechanics Reviews* 44 (1991) (cit. on p. 13).

[36]P. O. Sjoblom, J. T. Hartness, and T. M. Cordell. „On low-velocity impact testing of composite materials“. In: *Journal of Composite Materials* 22.1 (1988), pp. 30–52 (cit. on p. 13).

[37]C. Sridhar and K. P. Rao. „Estimation of low-velocity impact damage in laminated composite circular plates using nonlinear finite element analysis“. In: *Computers & structures* 54.6 (1995), pp. 1183–1189 (cit. on p. 13).

[38]D. Delfosse and A. Poursartip. „Energy-based approach to impact damage in CFRP laminates“. In: *Composites Part A: Applied Science and Manufacturing* 28.7 (1997), pp. 647–655 (cit. on p. 13).

[39]L. S. Sutherland and C. G. Soares. „The use of quasi-static testing to obtain the low-velocity impact damage resistance of marine GRP laminates“. In: *Composites Part B: Engineering* 43.3 (2012), pp. 1459–1467 (cit. on p. 14).

[40]Stephen R Swanson. „Limits of quasi-static solutions in impact of composite structures“. In: *Composites Engineering* 2.4 (1992), pp. 261–267 (cit. on p. 14).

[41]Ronald B Bucinell, Ralph J Nuismer, and Jim L Koury. „Response of composite plates to quasi-static impact events“. In: *Composite Materials: Fatigue and Fracture (Third Volume)*. ASTM International, 1991 (cit. on p. 14).

[42]B. V. Sankar and Y. S. Kwon. „Indentation-flexure and low-velocity impact damage in graphite epoxy laminates“. In: *Journal of Composites, Technology and Research* 15.2 (1993), pp. 101–111 (cit. on p. 14).

[43]S. Abrate. *Impact on composite structures*. Cambridge university press, 2005 (cit. on pp. 14, 93).

[44]S. Guinard, O. Allix, D. Guédra-Degeorges, and A. Vinet. „A 3D damage analysis of low-velocity impacts on laminated composites“. In: *Composites Science and Technology* 62.4 (2002), pp. 585–589 (cit. on p. 14).

[45]C. Bouvet, S. Rivallant, and J. Barrau. „Low velocity impact modeling in composite laminates capturing permanent indentation“. In: *Composites Science and Technology* 72.16 (2012), pp. 1977–1988 (cit. on p. 14).

[46]L. Lammerant and I. Verpoest. „Modelling of the interaction between matrix cracks and delaminations during impact of composite plates“. In: *Composites Science and Technology* 56.10 (1996), pp. 1171–1178 (cit. on p. 14).

[47]Z. Guan, W. He, J. Chen, and L. Liu. „Permanent indentation and damage creation of laminates with different composite systems: An experimental investigation“. In: *Polymer Composites* 35.5 (2014), pp. 872–883 (cit. on p. 14).

[48]H. Y. Choi and F. Chang. „A model for predicting damage in graphite/epoxy laminated composites resulting from low-velocity point impact“. In: *Journal of Composite Materials* 26.14 (1992), pp. 2134–2169 (cit. on pp. 14, 15).

[49]A. Forghani and R. Vaziri. „Computational modeling of damage development in composite laminates subjected to transverse dynamic loading“. In: *Journal of Applied Mechanics* 76.5 (2009), p. 051304 (cit. on p. 14).

[50]F. Cesari, V. Dal Re, G. Minak, and A. Zucchelli. „Damage and residual strength of laminated carbon–epoxy composite circular plates loaded at the centre“. In: *Composites Part A: Applied Science and Manufacturing* 38.4 (2007), pp. 1163–1173 (cit. on pp. 14, 18).

[51]J. Sirichantra, S. L. Ogin, and D. A. Jesson. „The use of a controlled multiple quasi-static indentation test to characterise through-thickness penetration of composite panels“. In: *Composites Part B: Engineering* 43.2 (2012), pp. 655–662 (cit. on p. 14).

[52]E. Abisset, F. Daghia, X. C. Sun, M. R. Wisnom, and S. R. Hallett. „Interaction of inter- and intralaminar damage in scaled quasi-static indentation tests: Part 1–Experiments“. In: *Composite Structures* 136 (2016), pp. 712–726 (cit. on pp. 14, 88).

[53]X. C. Sun, M. R. Wisnom, and S. R. Hallett. „Interaction of inter-and intralaminar damage in scaled quasi-static indentation tests: Part 2–Numerical simulation“. In: *Composite Structures* 136 (2016), pp. 727–742 (cit. on p. 14).

[54]F. J. Bradshaw, G. Dorey, and G. R. Sidey. *Impact resistance of carbon fiber resin-forced plastics*. Tech. rep. Technical report No: 72240. Royal Aircraft Estabblishment, Franborough, 1973 (cit. on pp. 14, 15).

[55]P. Lagace. „Impact damage resistance of several laminated material systems“. In: *34 th AIAA/ASME/ASCE/AHS/ASC Structures, Structural Dynamics, and Materials Conference*. 1993, pp. 1863–1872 (cit. on p. 15).

[56]G. Zhou. „Damage mechanisms in composite laminates impacted by a flat-ended impactor“. In: *Composites Science and Technology* 54.3 (1995), pp. 267–273 (cit. on p. 15).

[57]G. A. O. Davies, D. Hitchings, and G. Zhou. „Impact damage and residual strengths of woven fabric glass/polyester laminates“. In: *Composites Part A: Applied Science and Manufacturing* 27.12 (1996), pp. 1147–1156 (cit. on p. 15).

[58]G. A. O. Davies and X. Zhang. „Impact damage prediction in carbon composite structures“. In: *International Journal of Impact Engineering* 16.1 (1995), pp. 149–170 (cit. on p. 15).

[59]T. A. Sebaey, E. V. González, C. S. Lopes, et al. „Damage resistance and damage tolerance of dispersed CFRP laminates: Effect of the mismatch angle between plies“. In: *Composite Structures* 101 (2013), pp. 255–264 (cit. on pp. 15, 20, 33, 41).

[60]E. V. González, P. Maimí, P. P. Camanho, C. S. Lopes, and N. Blanco. „Effects of ply clustering in laminated composite plates under low-velocity impact loading“. In: *Composites Science and Technology* 71.6 (2011), pp. 805–817 (cit. on pp. 15, 18, 20, 39–41, 47, 48, 86, 97, 128, 130–133).

[61]T. A. Sebaey, E. V. González, C. S. Lopes, et al. „Damage resistance and damage tolerance of dispersed CFRP laminates: Effect of the mismatch angle between plies“. In: *Composite Structures* 101 (2013), pp. 255–264 (cit. on pp. 15, 18, 20, 40, 67, 68, 78, 86, 91, 128, 131, 135, 136).

[62]M. O. W. Richardson and M. J. Wisheart. „Review of low-velocity impact properties of composite materials“. In: *Composites Part A: Applied Science and Manufacturing* 27.12 (1996), pp. 1123–1131 (cit. on p. 16).

[63]S. P. Joshi and C. T. Sun. „Impact induced fracture in a laminated composite“. In: *Journal of Composite Materials* 19.1 (1985), pp. 51–66 (cit. on pp. 16, 18).

[64]H. Y. Choi, H. T. Wu, and F. Chang. „A new approach toward understanding damage mechanisms and mechanics of laminated composites due to low-velocity impact: Part II-analysis“. In: *Journal of Composite Materials* 25.8 (1991), pp. 1012–1038 (cit. on pp. 17, 18, 20).

[65]N. Takeda, R. L. Sierakowski, and L. E. Malvern. „Transverse cracks in glass/epoxy cross-ply laminates impacted by projectiles“. In: *Journal of Materials Science* 16.7 (1981), pp. 2008–2011 (cit. on p. 17).

[66]C. J. Jih and C. T. Sun. „Prediction of delamination in composite laminates subjected to low velocity impact“. In: *Journal of Composite Materials* 27.7 (1993), pp. 684–701 (cit. on pp. 17, 20).

[67]S. W. R. Lee and C. T. Sun. „A quasi-static penetration model for composite laminates“. In: *Journal of Composite Materials* 27.3 (1993), pp. 251–271 (cit. on p. 17).

[68]E. Abisset, F. Daghia, X. C. Sun, M. R. Wisnom, and S. R. Hallett. „Interaction of inter- and intralaminar damage in scaled quasi-static indentation tests: Part 1–Experiments“. In: *Composite Structures* 136 (2016), pp. 712–726 (cit. on pp. 17, 29, 128, 133).

[69]T. Yokozeki, Y. Aoki, and T. Ogasawara. „Experimental characterization of strength and damage resistance properties of thin-ply carbon fiber/toughened epoxy laminates“. In: *Composite Structures* 82.3 (2008), pp. 382–389 (cit. on pp. 17, 47, 48).

[70]D. J. Bull, L. Helfen, I. Sinclair, S. M. Spearing, and T. Baumbach. „A comparison of multi-scale 3D X-ray tomographic inspection techniques for assessing carbon fibre composite impact damage“. In: *Composites Science and Technology* 75 (2013), pp. 55–61 (cit. on p. 17).

[71]D. Liu and L. E. Malvern. „Matrix cracking in impacted glass/epoxy plates“. In: *Journal of Composite Materials* 21.7 (1987), pp. 594–609 (cit. on p. 17).

[72]L. E. Malvern, N. Takeda, and R. L. Sierakowski. „Microscopic observations of cross sections of impacted composite laminates“. In: *Journal of Composites, Technology and Research* 4.2 (1982), pp. 40–44 (cit. on p. 17).

[73]H. T. Wu and G. S. Springer. „Measurements of matrix cracking and delamination caused by impact on composite plates“. In: *Journal of Composite Materials* 22.6 (1988), pp. 518–532 (cit. on pp. 17, 18).

[74]S. Abrate. *Impact on composite structures*. 1998 (cit. on pp. 17, 18, 21).

[75]F. W. Crossman and A. S. D. Wang. „The dependence of transverse cracking and delamination on ply thickness in graphite/epoxy laminates“. In: *Damage in Composite Materials* (1982), pp. 118–139 (cit. on pp. 17, 47).

[76]R. Amacher, J. Cugnoni, J. Botsis, et al. „Thin ply composites: Experimental characterization and modeling of size-effects“. In: *Composites Science and Technology* 101 (2014), pp. 121–132 (cit. on pp. 17, 43, 47, 48, 56, 60).

[77]S. Sihn, R. Y. Kim, K. Kawabe, and S. W. Tsai. „Experimental studies of thin-ply laminated composites“. In: *Composites Science and Technology* 67.6 (2007), pp. 996–1008 (cit. on pp. 17, 47, 48).

[78]H. Saito, M. Morita, K. Kawabe, et al. „Effect of ply-thickness on impact damage morphology in CFRP laminates“. In: *Journal of Reinforced Plastics and Composites* 30.13 (2011), pp. 1097–1106 (cit. on pp. 17, 47, 48, 60).

[79]R. Olsson, M. V. Donadon, and B. G. Falzon. „Delamination threshold load for dynamic impact on plates“. In: *International Journal of Solids and Structures* 43.10 (2006), pp. 3124–3141 (cit. on pp. 17–20, 135).

[80]G. A. O. Davies, X. Zhang, G. Zhou, and S. Watson. „Numerical modelling of impact damage“. In: *Composites* 25.5 (1994), pp. 342–350 (cit. on pp. 17, 19, 125, 127).

[81]H. Suemasu and O. Majima. „Multiple delaminations and their severity in nonlinear circular plates subjected to concentrated loading“. In: *Journal of composite materials* 32.2 (1998), pp. 123–140 (cit. on pp. 18–20, 40, 126).

[82]H. Suemasu and O. Majima. „Multiple delaminations and their severity in circular axisymmetric plates subjected to transverse loading“. In: *Journal of Composite Materials* 30.4 (1996), pp. 441–453 (cit. on pp. 18–20, 40, 126).

[83]A. J. Lesser. „Effect of resin crosslink density on the impact damage resistance of laminated composites“. In: *Polymer composites* 18.1 (1997), pp. 16–27 (cit. on pp. 18, 39, 56).

[84]T. Shyr and Y. Pan. „Impact resistance and damage characteristics of composite laminates“. In: *Composite Structures* 62.2 (2003), pp. 193–203 (cit. on pp. 18, 39, 41, 56, 67).

[85]A. J. Lesser and A. G. Filippov. „Mechanisms governing the damage resistance of laminated composites subjected to low-velocity impacts“. In: *International Journal of Damage Mechanics* 3.4 (1994), pp. 408–432 (cit. on pp. 18, 39).

[86]W. Cui and M. R. Wisnom. „A combined stress-based and fracture-mechanics-based model for predicting delamination in composites“. In: *Composites* 24.6 (1993), pp. 467–474 (cit. on p. 18).

[87]C. A. Ross and R. L. Sierakowski. „Studies on the impact resistance of composite plates“. In: *Composites* 4.4 (1973), pp. 157–161 (cit. on p. 18).

[88]N. Takeda, R. L. Sierakowski, C. A. Ross, and L. E. Malvern. „Delamination-crack propagation in ballistically impacted glass/epoxy composite laminates“. In: *Experimental Mechanics* 22.1 (1982), pp. 19–25 (cit. on p. 18).

[89]D. Liu. „Impact-induced delamination-a view of bending stiffness mismatching“. In: *Journal of Composite Materials* 22.7 (1988), pp. 674–692 (cit. on p. 18).

[90]F. Chang, H. Y. Choi, and S. Jeng. „Study on impact damage in laminated composites“. In: *Mechanics of Materials* 10.1-2 (1990), pp. 83–95 (cit. on p. 18).

[91]S. Liu, Z. Kutlu, and F. Chang. „Matrix cracking and delamination in laminated composite beams subjected to a transverse concentrated line load“. In: *Journal of Composite Materials* 27.5 (1993), pp. 436–470 (cit. on p. 18).

[92]A. C. Garg. „Delamination-a damage mode in composite structures“. In: *Engineering Fracture Mechanics* 29.5 (1988), pp. 557–584 (cit. on p. 18).

[93]G. A. O. Davies and P. Robinson. „Predicting failure by debonding/delamination“. In: *AGARD, Debonding/Delamination of Composites 28 p(SEE N 93-21507 07-24)* (1992) (cit. on pp. 19, 127).

[94]H. Suemasu, S. Kerth, and M. Maier. „Indentation of spherical head indentors on transversely isotropic composite plates“. In: *Journal of Composite Materials* 28.17 (1994), pp. 1723–1739 (cit. on p. 19).

[95]R. Olsson. „Analytical prediction of large mass impact damage in composite laminates“. In: *Composites Part A: Applied Science and Manufacturing* 32.9 (2001), pp. 1207–1215 (cit. on pp. 19, 20, 126, 131, 135).

[96]G. A. Schoeppner and S. Abrate. „Delamination threshold loads for low velocity impact on composite laminates“. In: *Composites Part A: Applied Science and Manufacturing* 31.9 (2000), pp. 903–915 (cit. on pp. 19, 39).

[97]L. S. Sutherland and C. G. Soares. „Contact indentation of marine composites“. In: *Composite Structures* 70.3 (2005), pp. 287–294 (cit. on pp. 19, 127).

[98]Enboa Wu and Kae Shyu. „Response of composite laminates to contact loads and relationship to low-velocity impact“. In: *Journal of Composite Materials* 27.15 (1993), pp. 1443–1464 (cit. on pp. 20, 27, 111, 119, 121).

[99]L. E. Doxsee, P. Rubbrecht, L. Li, I. Verpoest, and M. Scholle. „Delamination growth in composite plates subjected to transverse loads“. In: *Journal of Composite Materials* 27.8 (1993), pp. 764–781 (cit. on p. 20).

[100]H. Razi and A. S. Kobayashi. „Delamination in cross-ply laminated composite subjected to low-velocity impact“. In: *AIAA journal* 31.8 (1993), pp. 1498–1502 (cit. on p. 20).

[101]F. J. Guild, P. J. Hogg, and J. C. Prichard. „A model for the reduction in compression strength of continuous fibre composites after impact damage“. In: *Composites* 24.4 (1993), pp. 333–339 (cit. on p. 20).

[102]K. Levin. „Characterization of delamination and fiber fractures in carbon fiber reinforced plastics induced from impact“. In: *Mechanical behaviour of materials- VI* (1992), pp. 519–524 (cit. on p. 20).

[103]G. Belingardi and R. Vadori. „Low velocity impact tests of laminate glass-fiber-epoxy matrix composite material plates“. In: *International Journal of Impact Engineering* 27.2 (2002), pp. 213–229 (cit. on p. 21).

[104]P. Sjoblom. „Simple design approach against low-velocity impact damage“. In: *Advanced Materials Technology* 87 (1987), pp. 529–539 (cit. on p. 21).

[105]M. Aktaş, C. Atas, and R. İçten B. M.and Karakuzu. „An experimental investigation of the impact response of composite laminates“. In: *Composite Structures* 87.4 (2009), pp. 307–313 (cit. on pp. 22, 23).

[106]G Caprino, V Lopresto, C Scarponi, and G Briotti. „Influence of material thickness on the response of carbon-fabric/epoxy panels to low velocity impact“. In: *Composites Science and Technology* 59.15 (1999), pp. 2279–2286 (cit. on pp. 22, 24, 80).

[107]A. M. El-Habak. „Effect of impact perforation load on GFRP composites“. In: *Composites* 24.4 (1993), pp. 341–345 (cit. on p. 22).

[108]D. Liu, B. B. Raju, and X. Dang. „Impact perforation resistance of laminated and assembled composite plates“. In: *International Journal of Impact Engineering* 24.6 (2000), pp. 733–746 (cit. on p. 22).

[109]G Caprino and V Lopresto. „On the penetration energy for fibre-reinforced plastics under low-velocity impact conditions“. In: *Composites Science and Technology* 61.1 (2001), pp. 65–73 (cit. on p. 23).

[110]A. K. Singh, B. D. Davidson, D. P. Eisenberg, M. W. Czabaj, and A. T. Zehnder. „Damage characterization of quasistatically indented composite sandwich structures“. In: *Journal of Composite Materials* 0 (2012), pp. 1–19 (cit. on p. 24).

[111]H. Hertz. *Miscellaneous Papers by H. Hertz*. London, U.K.: Macmillan, 1896 (cit. on p. 24).

[112]K. L. Johnson. *Contact mechanics*. Cambridge: Cambrigde university press, 1985 (cit. on p. 25).

[113]A. E. Green and W. Zerna. *Theoretical Elasticity*. Oxford: Oxford University press, 1954 (cit. on pp. 25, 28).

[114]S. G. Leknitskii. *Theory of Elasticity os an Anisotropic Elastic Body*. San Francisco: Holden-Day, 1963 (cit. on pp. 25, 28).

[115]VA Sveklo. „Boussinesq type problems for the anisotropio half-space“. In: *Journal of Applied Mathematics and Mechanics* 28.5 (1964), pp. 1099–1105 (cit. on p. 25).

[116]M. Dahan and J. Zakara. „Elastic contact between a sphere and a semi-infinite trasversely isotropic body“. In: *International Journal of Solids and Structures* 13.3 (1977), pp. 229–238 (cit. on p. 25).

[117]J. R. Turner. „Contact on a transversaly isotropic half-space or between two transversaly isotropic bodies“. In: *International Journal of Solids and Structures* 16.5 (1980), pp. 409–419 (cit. on pp. 25, 26, 107, 109).

[118]S. C. Yang and C. T. Sun. *Indentation law for composite laminates*. Tech. rep. Purdue university, NASA CR-165460, CML 81-1. Aeronautics and Astronautics, West Lafayette, Indiana, 1981 (cit. on pp. 25, 27, 119–121).

[119]S. R. Swanson. „Hertzian contact of orthotropic materials“. In: *International Journal of Solids and Structures* 41 (2004) (cit. on pp. 25, 107).

[120]L. B. Greszczuk. „Damage in composite materials due to low velocity impact“. In: *Impact Dynamics* (1982), pp. 55–94 (cit. on p. 26).

[121]P. Chen, X. Junjie, and S. Zhen. „Thickness effect on the contact behavior of a composite laminate indented by a rigid sphere“. In: *Mechanics of Materials* 40.4 (2008), pp. 183–194 (cit. on pp. 27, 117, 119–121).

[122]Enboa Wu and Ching-Shih Yen. „The contact behavior between laminated composite plates and rigid spheres“. In: *Journal of Applied Mechanics* 61.1 (1994), pp. 60–66 (cit. on p. 28).

[123]CC Chao and CY Tu. „Three-dimensional contact dynamics of laminated plates: Part 1. Normal impact“. In: *Composites Part B: Engineering* 30.1 (1999), pp. 9–22 (cit. on p. 28).

[124]NJ Pagano. „Exact moduli of anisotropic laminates“. In: *Mechanics of composite materials*. Ed. by J.N. Reddy. Vol. 34. Springer Netherlands, 1994, pp. 210–231 (cit. on pp. 28, 108).

[125]BV Sankar. „Smooth indentation of orthotropic beams“. In: *Composites Science and Technology* 34.2 (1989), pp. 95–111 (cit. on p. 28).

[126]Douglas Scott Cairns and Paul A Lagace. „Thick composite plates subjected to lateral loading“. In: *Journal of Applied Mechanics* 54.3 (1987), pp. 611–616 (cit. on p. 28).

[127]Stephen R Swanson. „Contact deformation and stress in orthotropic plates“. In: *Composites Part A: Applied Science and Manufacturing* 36.10 (2005), pp. 1421–1429 (cit. on p. 28).

[128]Han Soo Jung. „Finite element modeling of static indentation damage in laminated composites“. In: *Ph.D. Thesis, Florida University*. 1991 (cit. on p. 28).

[129]Qiang Ye, Pu Hui Chen, and Zhen Shen. „Prediction Method of the Dent Depth of Composite Laminates Subjected to Quasi-Static Indentation“. In: *Advanced Materials Research* 328 (2011), pp. 1483–1486 (cit. on p. 28).

[130]K. Varadi, Z. Neder, K. Friedrich, and J. Flockb. „Finite-element analysis of a polymer composite subjected to ball indentation“. In: *Composites Science and Technology* 59.2 (1999), pp. 4271–281 (cit. on p. 28).

[131]K. W. Gan, M. R. Wisnom, and S. R. Hallett. „An approximate model of cylindrical and spherical contact on composite laminates of finite thickness“. In: *Composite Structures* 103 (2013), pp. 136–142 (cit. on pp. 28, 62, 111).

[132]C. T. Sun and S. C. Yang. *Contact law and impact response of laminated composites*. Tech. rep. Purdue university, NASA CR-159884, CML 80-1. Aeronautics and Astronautics, West Lafayette, Indiana, 1980 (cit. on pp. 28, 111).

[133]S. C. Yang and C. T. Sun. *Indentation law for composite laminates*. Tech. rep. Purdue university, NASA CR-165460, CML 81-1. Aeronautics and Astronautics, West Lafayette, Indiana, 1981 (cit. on p. 28).

[134]A. W. Crook. „A study of some impacts between metal bodies by a piezo-electric method“. In: *Proceedings of the Royal Society of London A: Mathematical, Physical and Engineering Sciences*. Vol. 212. 1110. The Royal Society. 1952, pp. 377–390 (cit. on p. 28).

[135]Zdeněk P Bažant and Er-Ping Chen. „Scaling of structural failure“. In: *Applied Mechanics Reviews* 50.10 (1997), pp. 593–627 (cit. on p. 29).

[136]M. R. Wisnom, S. R. Hallett, and C. Soutis. „Scaling effects in notched composites“. In: *Journal of Composite Materials* 44.2 (2009), pp. 195–210 (cit. on pp. 29, 47).

[137]Pere Maimí, Emilio V González, Narcís Gascons, and Lluís Ripoll. „Size effect law and critical distance theories to predict the nominal strength of quasibrittle structures“. In: *Applied Mechanics Reviews* 65.2 (2013), pp. 020802–1–16 (cit. on p. 29).

[138]MR Wisnom, B Khan, and SR Hallett. „Size effects in unnotched tensile strength of unidirectional and quasi–isotropic carbon/epoxy composites“. In: *Composite Structures* 84.1 (2008), pp. 21–28 (cit. on p. 29).

[139]MR Wisnom. „Size effects in the testing of fibre-composite materials“. In: *Composites Science and Technology* 59.13 (1999), pp. 1937–1957 (cit. on p. 29).

[140]Karen E Jackson, Sotiris Kellas, and John Morton. „Scale effects in the response and failure of fiber reinforced composite laminates loaded in tension and in flexure“. In: *Journal of Composite Materials* 26.18 (1992), pp. 2674–2705 (cit. on p. 29).

[141]J Andre Lavoie, Costas Soutis, and John Morton. „Apparent strength scaling in continuous fiber composite laminates“. In: *Composites Science and Technology* 60.2 (2000), pp. 283–299 (cit. on p. 29).

[142]Zdenek P Bažant, Isaac M Daniel, and Zhengzhi Li. „Size effect and fracture characteristics of composite laminates“. In: *Journal of Engineering Materials and Technology* 118.3 (1996), pp. 317–324 (cit. on p. 29).

[143]C Soutis, J Lee, and C Kong. „Size effect on compressive strength of T300/924C carbon fibre-epoxy laminates“. In: *Plastics, Rubber and Composites* 31.8 (2002), pp. 364–370 (cit. on p. 29).

[144]BG Green, MR Wisnom, and SR Hallett. „An experimental investigation into the tensile strength scaling of notched composites“. In: *Composites Part A: Applied Science and Manufacturing* 38.3 (2007), pp. 867–878 (cit. on p. 29).

[145]John Morton. „Scaling of impact-loaded carbon-fiber composites“. In: *AIAA journal* 26.8 (1988), pp. 989–994 (cit. on p. 29).

[146]Y Qian, SR Swanson, RJ Nuismer, and RB Bucinell. „An experimental study of scaling rules for impact damage in fiber composites“. In: *Journal of Composite Materials* 24.5 (1990), pp. 559–570 (cit. on p. 29).

[147]Bhavani V Sankar. „Scaling of low-velocity impact for symmetric composite laminates“. In: *Journal of Reinforced Plastics and Composites* 11.3 (1992), pp. 296–309 (cit. on p. 29).

[148]Dahsin Liu, Basavaraju B Raju, and Xinglai Dang. „Size effects on impact response of composite laminates“. In: *International journal of Impact Engineering* 21.10 (1998), pp. 837–854 (cit. on p. 29).

[149]*Standard Test Method for Measuring Damage Resistance of Fiber-Reinforced Polymer-Matrix Composite to Concentrated Quasi-Static Indentation*. Norm. 2004 (cit. on pp. 34, 49, 69, 87, 112).

[150]C. T. Herakovich. *Mechanics of fibrous composites*. Wiley New York, 1998 (cit. on pp. 35, 108, 147).

[151]D. D. Symons. „Characterisation of indentation damage in 0/90 lay-up T300/914 CFRP“. In: *Composites Science and Technology* 60.3 (2000), pp. 391–401 (cit. on p. 40).

[152]P. Chen, Z. Shen, J. Xiong, et al. „Failure mechanisms of laminated composites subjected to static indentation“. In: *Composite structures* 75.1 (2006), pp. 489–495 (cit. on p. 41).

[153]G. Guillamet, A. Turon, J. Costa, et al. „Damage occurrence at edges of non-crimp-fabric thin-ply laminates under off-axis uniaxial loading“. In: *Composites Science and Technology* 98 (2014), pp. 44–50 (cit. on pp. 43, 47, 56, 67).

[154]E. Abi Abdallah, C. Bouvet, S. Rivallant, B. Broll, and J. Barrau. „Experimental analysis of damage creation and permanent indentation on highly oriented plates“. In: *Composites Science and Technology* 69 (2009), pp. 1238–45 (cit. on p. 45).

[155]A. Parvizi, K. W. Garrett, and J. E. Bailey. „Constrained cracking in glass fibre-reinforced epoxy cross-ply laminates“. In: *Journal of Materials Science* 13.1 (1978), pp. 195–201 (cit. on p. 47).

[156]G. J. Dvorak and N. Laws. „Analysis of progressive matrix cracking in composite laminates II. First ply failure“. In: *Journal of Composite Materials* 21.4 (1987), pp. 309–329 (cit. on p. 47).

[157]P. P. Camanho, C. G Dávila, S. T. Pinho, L. Iannucci, and P. Robinson. „Prediction of in situ strengths and matrix cracking in composites under transverse tension and in-plane shear“. In: *Composites Part A: Applied Science and Manufacturing* 37.2 (2006), pp. 165–176 (cit. on p. 47).

[158]P. Maimí, P. P. Camanho, J. A. Mayugo, and A. Turon. „Matrix cracking and delamination in laminated composites. Part I: Ply constitutive law, first ply failure and onset of delamination“. In: *Mechanics of Materials* 43.4 (2011), pp. 169–185 (cit. on p. 47).

[159]T. K. O'Brien. „Analysis of local delaminations and their influence on composite laminate behavior“. In: *Delamination and debonding of materials, ASTM STP* 876 (1985), pp. 282–297 (cit. on p. 47).

[160]L. Zubillaga, A. Turon, P. Maimí, et al. „An energy based failure criterion for matrix crack induced delamination in laminated composite structures“. In: *Composite Structures* 112 (2014), pp. 339–344 (cit. on p. 47).

[161]J. E. Bailey, P. T. Curtis, and A. Parvizi. „On the transverse cracking and longitudinal splitting behaviour of glass and carbon fibre reinforced epoxy cross ply laminates and the effect of Poisson and thermally generated strain“. In: *Proceedings of the Royal Society of London. A. Mathematical and Physical Sciences* 366.1727 (1979), pp. 599–623 (cit. on p. 47).

[162]Y. Nishikawa, K. Okubo, T. Fujii, and K. Kawabe. „Fatigue crack constraint in plain-woven CFRP using newly-developed spread tows“. In: *International Journal of Fatigue* 28.10 (2006), pp. 1248–1253 (cit. on p. 47).

[163]T. Yokozeki, A. Kuroda, A. Yoshimura, T. Ogasawara, and T. Aoki. „Damage characterization in thin-ply composite laminates under out-of-plane transverse loadings“. In: *Composite Structures* 93.1 (2010), pp. 49–57 (cit. on pp. 47, 56).

[164]*Aerospace Series. Carbon Fibre Laminates. Determination of th Fiber, Resin and Void Contents*. Norm. 1998 (cit. on p. 48).

[165]*Standard test method for measuring the damage resistance of a fiber-reinforced polymer matrix composite to a drop-weight impact event*. Norm. 2012 (cit. on p. 48).

[166]M. J. Laffan, S. T. Pinho, P. Robinson, and L. Iannucci. „Measurement of the in situ ply fracture toughness associated with mode I fibre tensile failure in FRP. Part II: Size and lay-up effects“. In: *Composites Science and Technology* 70.4 (2010), pp. 614–621 (cit. on pp. 58, 60).

[167]P. Robinson, E. Greenhalgh, and S. Pinho. *Failure mechanisms in polymer matrix composites: Criteria, testing and industrial applications*. Elsevier, 2012 (cit. on p. 65).

[168]GA Bibo, PJ Hogg, and M Kemp. „Mechanical characterisation of glass-and carbon-fibre-reinforced composites made with non-crimp fabrics“. In: *Composites Science and Technology* 57.9 (1997), pp. 1221–1241 (cit. on p. 67).

[169]S. W. Tsai and A. T. Nettles. „Representative test data on bi-angle thin-ply NCF“. In: *JEC composites* 68 (2011), pp. 62–63 (cit. on p. 67).

[170]Stepan V Lomov. *Non-crimp fabric composites: manufacturing, properties and applications*. Elsevier, 2011 (cit. on p. 67).

[171]A Arteiro, G Catalanotti, J Xavier, and PP Camanho. „Notched response of non-crimp fabric thin-ply laminates“. In: *Composites Science and Technology* 79 (2013), pp. 97–114 (cit. on p. 67).

[172]B Yang, V Kozey, S Adanur, and S Kumar. „Bending, compression, and shear behavior of woven glass fiber–epoxy composites“. In: *Composites Part B: Engineering* 31.8 (2000), pp. 715–721 (cit. on p. 67).

[173]GA Bibo, PJ Hogg, R Backhouse, and A Mills. „Carbon-fibre non-crimp fabric laminates for cost-effective damage-tolerant structures“. In: *Composites Science and Technology* 58.1 (1998), pp. 129–143 (cit. on p. 67).

[174]F Chen and JM Hodgkinson. „Impact behaviour of composites with different fibre architecture“. In: *Proceedings of the Institution of Mechanical Engineers, Part G: Journal of Aerospace Engineering* 223.7 (2009), pp. 1009–1017 (cit. on p. 67).

[175]Edgar Fuoss, Paul V Straznicky, and Cheung Poon. „Effects of stacking sequence on the impact resistance in composite laminates: Part I parametric study“. In: *Composite Structures* 41.1 (1998), pp. 67–77 (cit. on p. 67).

[176]CS Lopes, O Seresta, Y Coquet, et al. „Low-velocity impact damage on dispersed stacking sequence laminates. Part I: Experiments“. In: *Composites Science and Technology* 69.7 (2009), pp. 926–936 (cit. on pp. 67, 68).

[177]Hai-Po Cui, Wei-Dong Wen, and Hai-Tao Cui. „An integrated method for predicting damage and residual tensile strength of composite laminates under low velocity impact“. In: *Computers & Structures* 87.7 (2009), pp. 456–466 (cit. on p. 67).

[178]CKL Davies, S Turner, and KH Williamson. „Flexed plate impact testing of carbon fibre-reinforced polymer composites“. In: *Composites* 16.4 (1985), pp. 279–285 (cit. on pp. 67, 78).

[179]C Soutis and PT Curtis. „Prediction of the post-impact compressive strength of CFRP laminated composites“. In: *Composites Science and Technology* 56.6 (1996), pp. 677–684 (cit. on pp. 67, 78).

[180]MV Hosur, CRL Murthy, TS Ramamurthy, and Anita Shet. „Estimation of impact-induced damage in CFRR laminates through ultrasonic imaging“. In: *NDT & E International* 31.5 (1998), pp. 359–374 (cit. on pp. 67, 68).

[181]C Huchette. „Analyse multiéchelle des interactions entre fissurations intralaminaire et interlaminaire dans les matériaux composites stratifiés“. PhD thesis. Thèse de l'université de Paris VI, 2005 (cit. on p. 68).

[182]A Wagih, P Maimí, N Blanco, and EV González. „Scaling effects of composite laminates under out-of-plane loading“. In: *Journal of Composite Materials* Submitted (2017) (cit. on pp. 68, 72, 78, 85, 91).

[183]F Aymerich and M Serra. „Optimization of laminate stacking sequence for maximum buckling load using the ant colony optimization (ACO) metaheuristic“. In: *Composites Part A: Applied Science and Manufacturing* 39.2 (2008), pp. 262–272 (cit. on pp. 69, 86).

[184]Singiresu S Rao and SS Rao. *Engineering optimization: theory and practice*. John Wiley & Sons, 2009 (cit. on pp. 69, 86).

[185]G Guillamet. „Improved delamination resistance of this-ply based laminates: An experimental and numerical study“. PhD thesis. Thèse de l'université de Girona, 2016 (cit. on p. 69).

[186]A Wagih, P Maimí, N Blanco, and J Costa. „A quasi-static indentation test to elucidate the sequence of damage events in low velocity impacts on composite laminates“. In: *Composites Part A: Applied Science and Manufacturing* 82 (2016), pp. 180–189 (cit. on pp. 78, 80, 88, 89, 91, 93, 94, 121, 123, 131, 135, 136).

[187]A Wagih, P Maimí, N Blanco, and D Trias. „Predictive model for the spherical indentation of composite laminates with finite thickness“. In: *Composite Structures* 153 (2016), pp. 468–477 (cit. on pp. 80, 123).

[188]Giancarlo Caprino and Valentina Lopresto. „The significance of indentation in the inspection of carbon fibre-reinforced plastic panels damaged by low-velocity impact“. In: *Composites Science and Technology* 60.7 (2000), pp. 1003–1012 (cit. on p. 80).

[189]A Wagih, P Maimí, R.P. Issac, et al. „Effect of mismatch angle on the resonse of thin-ply non-crimp fabric laminates under out-of-plane loading“. In: *Preparing for submission* (2017) (cit. on pp. 91, 102).

[190]DJ Bull, SM Spearing, and I Sinclair. „Observations of damage development from compression-after-impact experiments using ex situ micro-focus computed tomography“. In: *Composites Science and Technology* 97 (2014), pp. 106–114 (cit. on p. 102).

[191]C.T. Sun and S. Li. „Three-dimensional effective elastic constants for thick laminates“. In: *Journal of Composite Materials* 22.7 (1988), pp. 629–639 (cit. on p. 108).

[192]Ajit K Roy and Stephen W Tsai. „Three-dimensional effective moduli of orthotropic and symmetric laminates“. In: *Journal of Applied Mechanics* 59.1 (1992), pp. 39–47 (cit. on p. 108).

[193]Edgar Buckingham. „On physically similar systems; illustrations of the use of dimensional equations“. In: *Physical Review* 4.4 (1914), pp. 345–376 (cit. on p. 109).

[194]MD Gilchrist, A.J. Kinlochb, F.L. Matthewsc, and S.O. Osiyemib. „Mechanical performance of carbon-fibre and glass-fibre reinforced epoxy I-beams.1. Mechanical behaviour“. In: *Composites Science and Technology* 56.1 (1996), pp. 37–53 (cit. on p. 111).

[195]JY Zhang, TX Yu, JK Kim, and GX Sui. „Static indentation and impact behaviour of reformed bamboo/aluminium laminated composites“. In: *Composite Structures* 50.2 (2000), pp. 207–216 (cit. on p. 113).

[196]KN Shivakumar, Wolf Elber, and W Illg. „Prediction of impact force and duration due to low-velocity impact on circular composite laminates“. In: *Journal of Applied Mechanics* 52.3 (1985), pp. 674–680 (cit. on pp. 123–125).

[197]A. Wagih, P. Maimí, N. Blanco, and J. Costa. „A quasi-static indentation test to elucidate the sequence of damage events in low velocity impacts on composite laminates“. In: *Composites Part A: Applied Science and Manufacturing* 82 (2016), pp. 180–189 (cit. on pp. 123, 135).

[198]Stephen Timoshenko, Sergius Woinowsky-Krieger, and S Woinowsky-Krieger. *Theory of plates and shells*. Vol. 2. McGraw-hill New York, 1959 (cit. on p. 124).

[199]Robin Olsson. „Engineering method for prediction of impact response and damage in sandwich panels“. In: *Journal of Sandwich Structures and Materials* 4.1 (2002), pp. 3–29 (cit. on pp. 124, 127).

[200]KN Shivakumar and Wolf Elber. *Delamination growth analysis in quasi-isotropic laminates under loads simulating low-velocity impact*. National Aeronautics and Space Administration, Langley Research Center, 1984 (cit. on p. 127).

[201]Celal Evci. „Thickness-dependent energy dissipation characteristics of laminated composites subjected to low velocity impact“. In: *Composite Structures* 133 (2015), pp. 508–521 (cit. on pp. 128, 131).

[202]EV González. „Simulation of interlaminar and intralaminar damage in polymer-based composites for aeronautical applications under impact loading“. PhD thesis. Universitat de Girona, 2010 (cit. on pp. 128, 131–133).

[203]Daniele Ghelli and Giangiacomo Minak. „Low velocity impact and compression after impact tests on thin carbon/epoxy laminates“. In: *Composites Part B: Engineering* 42.7 (2011), pp. 2067–2079 (cit. on p. 128).

[204]Young S. Kwon and Bhavani V. Sankar. *Indentation-flexure and low-velocity impact damage in Graphite/Epoxy laminates*. Tech. rep. NASA contractor report 18624. University of Florida, Gainesville, Florida, 1992 (cit. on pp. 128, 136, 137).

[205]LS Sutherland and C Guedes Soares. „Impact characterisation of low fibre-volume glass reinforced polyester circular laminated plates“. In: *International Journal of Impact Engineering* 31.1 (2005), pp. 1–23 (cit. on p. 128).

[206]FJ Yang and WJ Cantwell. „Impact damage initiation in composite materials“. In: *Composites Science and Technology* 70.2 (2010), pp. 336–342 (cit. on pp. 128, 136).

[207]G A Schoeppner and S Abrate. „Delamination threshold loads for low velocity impact on composite laminates“. In: *Composites Part A: applied science and manufacturing* 31.9 (2000), pp. 903–915 (cit. on p. 130).

[208]R Olsson, A André, and P Hellström. „Analytical Modelling and FE Simulation of Impact Response and Damage Growth in a Thin-Ply Laminate“. In: *20th International Conference on Composite Materials ICCM-20* July (2015), pp. 19–24 (cit. on p. 131).

[209]ASTM D7136/D7136M-12. *Standard Test Method for Measuring the Damage Resistance of a Fiber-Reinforced Polymer Matrix Composite to a Drop-Weight Impact Event*. Tech. rep. 2005, pp. 1–16 (cit. on pp. 132, 135).

[210]Albert Soto, EV González, Pere Maimí, et al. „Low velocity impact and compression after impact simulation of thin ply laminates“. In: *Composites - Part A: Applied Science and Manufacturing* Submitted (2018) (cit. on pp. 134, 135).